



HAL
open science

Dehydrogenation mechanisms of methyl-cyclohexane on γ -alumina supported platinum subnanometric-clusters : DFT coupled with experimental kinetics and kinetic modelling

Wei Zhao

► **To cite this version:**

Wei Zhao. Dehydrogenation mechanisms of methyl-cyclohexane on γ -alumina supported platinum subnanometric-clusters : DFT coupled with experimental kinetics and kinetic modelling. Other. Université de Lyon, 2017. English. NNT : 2017LYSEN052 . tel-01827240

HAL Id: tel-01827240

<https://theses.hal.science/tel-01827240>

Submitted on 2 Jul 2018

HAL is a multi-disciplinary open access archive for the deposit and dissemination of scientific research documents, whether they are published or not. The documents may come from teaching and research institutions in France or abroad, or from public or private research centers.

L'archive ouverte pluridisciplinaire **HAL**, est destinée au dépôt et à la diffusion de documents scientifiques de niveau recherche, publiés ou non, émanant des établissements d'enseignement et de recherche français ou étrangers, des laboratoires publics ou privés.



Numéro National de Thèse : 2017LYSEN052

THESE de DOCTORAT DE L'UNIVERSITE DE LYON
opérée par
l'Ecole Normale Supérieure de Lyon

Ecole Doctorale N° 206
Ecole Doctorale de Chimie (Chimie, Procédés, Environnement)

Discipline : Chimie

Soutenue publiquement le 09/11/2017, par :
Wei ZHAO

**Dehydrogenation mechanisms of methyl-cyclohexane on
 γ -alumina supported platinum subnanometric-clusters : DFT
coupled with experimental kinetics and kinetic modelling**

Mécanismes de déshydrogénation du méthyl-cyclohexane catalysée par
des agrégats sub-nanométriques de platine supportés sur alumine gamma:
études couplées DFT, cinétique expérimentale et modélisation cinétique

Devant le jury composé de :

Monica Calatayud, Maître de conférences, Université Pierre et Marie Curie, Paris VI	Rapporteuse
Guy Marin, Professeur à l'Université de Gent, Belgique	Rapporteur
Jean-François Paul, Professeur à l'Université de Lille 1	Examineur
Philippe Sautet, Professeur à l'Université de Californie, Los Angeles, États Unis - Directeur de Recherches au CNRS, Ecole Normale Supérieure de Lyon)	Directeur de thèse
Pascal Raybaud, H.D.R., IFP Energies nouvelles	Co-Encadrant de thèse
Céline Chizallet, H.D.R., IFP Energies nouvelles	Co-Encadrante de thèse

TABLE OF CONTENTS

CHAPTER I – INTRODUCTION

References	5
------------------	---

CHAPTER II – STATE OF THE ART AND STRATEGY OF THE THESIS

1. Reactions taking place in catalytic reforming	8
1.1 Nature of the reactions	8
1.2 Thermodynamics of the reactions	10
2. Catalyst.....	12
2.1 The catalyst support.....	13
2.2 The Pt/ γ -Al ₂ O ₃ based catalysts.....	14
3. Kinetic studies on dehydrogenation of methyl-cyclohexane into toluene	17
3.1 Overview of experimental kinetic studies	17
3.2 Focus on the kinetic model of Van Trimpont et al. and Verstraete.....	18
3.2.1 Hougen Watson reaction rate equations	18
3.2.2 Kinetic fitting parameters and reaction rate evolution as a function of hydrogen partial pressure	24
4. Models of reforming catalysts and related reactivity from DFT calculations.....	29
4.1 The γ -alumina support.....	29
4.2 The Pt ₁₃ / γ -Al ₂ O ₃ model	30
4.3 Investigation of C-H and C-C bond breaking on the Pt ₁₃ / γ -Al ₂ O ₃ model.....	32
4.4 DFT investigations of the hydrogenation of benzene into cyclohexane on Pt(111)	34
5. Open questions and strategy of the thesis	38
References	41

CHAPTER III – COMPUTATIONAL AND EXPERIMENTAL METHODOLOGY

1. <i>Ab initio</i> molecular modeling	44
1.1 Density functional theory (DFT).....	45
1.1.1 The Hohenberg-Kohn theorems	45
1.1.2 The Kohn-Sham equations	47
1.1.3 Exchange-correlation functionals	49
1.2 Molecular modeling	52
1.2.1 Plane waves and periodic boundary conditions	52
1.2.2 Pseudo-potentials and PAW method.....	53
1.2.3 Geometry optimization.....	55
1.2.4 <i>Ab initio</i> Molecular Dynamics	58
1.2.5 Nudged Elastic Band Method.....	59
1.3 Thermodynamic calculations	62
1.3.1 Expression of enthalpic and entropic terms according to statistical thermodynamics	62
1.3.2 Vibrational frequencies calculations	66
2. Catalytic experiment	72
2.1 Methodology and experimental techniques.....	73
2.1.1 Catalyst preparation and characterization	73
2.1.2 Catalytic test set-up	79
2.1.3 Reaction conditions	85
2.2 Experimental protocol of catalytic tests	88
2.2.1 Catalyst activation	88
2.2.2 Thermal profile inside the reactor	88
2.2.3 Reactant conversion and mass balance calculations	90

2.2.4 Reaction kinetics calculations	97
References	101
Appendix-III	104
1. Quantum chemistry	104
1.1 – The Schrödinger equation	104
1.2 – The Born Oppenheimer approximation.....	105
1.3 - Variational principle for the ground state	106
2. Granulometry study for the employed catalyst	108

**CHAPTER IV – KINETICS OF METHYLCYCLOHEXANE
DEHYDROGENATION ON ULTRA-DISPERSED Pt/Al₂O₃
CATALYSTS: ELEMENTARY STEPS FROM AB INITIO
CALCULATIONS**

Introduction	109
1. Atomistic model of the catalyst	110
2. Preliminary investigation on the stability of C₇H₁₂ intermediates.....	112
2.1 Respective stability of C ₇ H ₁₂ radical and non-radical intermediates.....	113
2.2 Analysis of the adsorption modes of 4-methyl-cyclohexene with respect to ethylene, comparison with Pt(111)	116
3. Adsorption of 4-methylcyclohexene on Pt₁₃H₆/γ-Al₂O₃ (100): static and molecular dynamics investigation	118
3.1 Stability of the adsorbed intermediate on Pt ₁₃ H ₆ /γ-Al ₂ O ₃ as a function of the adsorption site	118
3.2 Static conformation analysis for the adsorption of 4-MCHe on the V3 site	120
3.3 Molecular Dynamics conformational analysis of the adsorption of 4-MCHe on the V3 site	123

4. Stability of other intermediates along the dehydrogenation pathway, comparison with Pt(111) surface	128
5. Effect of the functional : PBE vs. PBE-dDsC	133
5.1 Effect of the functional on the MCH physisorption step.....	134
5.2 PBE-dDsC impact on adsorption configuration for the dehydrogenated intermediates	135
5.3 PBE-dDsC impact on dehydrogenation energies of various intermediates	136
6. Detailed reaction mechanism and free energy profiles of methyl-cyclohexane dehydrogenation over Pt₁₃H₆/γ-Al₂O₃ (100) with the PBE-dDsC functional.....	138
6.1 General feature on temperature influence	139
6.2 Methyl-cyclohexane adsorption and toluene desorption.....	143
6.3 C-H bond cleavage	145
6.4 Cluster reconstruction.....	150
6.5 H atom migration.....	154
6.6 H ₂ desorption.....	155
7. Effect of the functional on the Gibbs free energy profile over Pt₁₃H₆/γ-Al₂O₃ (100): PBE vs PBE-dDsC	156
8. Detailed reaction mechanism and free energy profile of methyl-cyclohexane dehydrogenation over the Pt(111) surface	159
8.1 Reaction mechanisms of methyl-cyclohexane dehydrogenation over the Pt(111) surface at the PBE-dDsC level.....	159
8.2 General feature on temperature influence and detailed reaction pathway over Pt(111) at the PBE-dDsC level.....	161
8.3 Comparison of Gibbs free energy profiles on Pt(111) with PBE-dDsC and PBE functionals	167
9. Comparaision of Gibbs free energy profiles on Pt (111) and on Pt₁₃H₆/γ-Al₂O₃ (100) with the PBE-dDsC functional	168
Conclusions and perspectives	170
References	173

Appendix-IV.....	175
1. Comparison on different adsorption modes of MCH _e and ethylene, and effect of hydrogen coverage	175
2. Decomposition of the dehydrogenation energy for adsorbed 4-methyl-cyclohexene before and after MD	178
3. Detailed thermodynamics for reaction path on Pt ₁₃ H ₆ /γ-Al ₂ O ₃ (100) cluster at different temperatures at the PBE-dDsC level.....	180
4. BEP linear relationship study of sequential C-H bond cleavage for methyl-cyclohexane dehydrogenation over Pt ₁₃ H ₆ /γ-Al ₂ O ₃ (100) cluster and Pt(111) surface at 625 K at the PBE-dDsC level	181
5. NEB investigation of the first H ₂ desorption step	182
6. Detailed thermodynamics study for reaction path on Pt ₁₃ H ₆ /γ-Al ₂ O ₃ (100) cluster at the PBE level.....	183
7. Detailed thermodynamic data for reaction path on Pt(111) surface at different temperatures at the PBE-dDsC level.....	185
8. Comparison of free energy profiles between the cluster and Pt(111) at the PBE level	186

CHAPTER V – REACTION KINETICS FOR THE DEHYDROGENATION OF METHYLCYCLOHEXANE INTO TOLUENE ON A Pt/Al₂O₃ CATALYST

1. Catalytic experiment	189
1.1 Temperature effect	189
1.2 WHSV effect.....	193
1.3 MCH and H ₂ partial pressures effects	196
1.4 Conclusions and Perspectives	200
2. Kinetic modelling investigation.....	201

2.1 Power-law kinetic model.....	201
2.1.1 Variations of the reaction rate as a function of space time	201
2.1.2. Impact of MCH and H ₂ partial pressures	206
2.2 Langmuir Hinshelwood mechanistic models	210
2.2.1. Individual steps and rate constants from DFT.....	210
2.2.2. Rate limiting steps	212
2.2.3. TOF-determining intermediates (TDI) and transition states (TDTS)	213
2.3 LH kinetic models based on a single rate determining elementary step without explicit consideration of adsorption competition with adsorbed atomic hydrogen.....	216
2.3.1 RDS-(I) model: irreversible rate-determining step (5).....	216
2.3.2 RDS-(II) model: reversible rate-determining step (5).....	222
2.3.3 RDS-(III) model: reversible rate-determining step (13).....	224
2.3.4 Arrhenius plot and Eyring plot for models RDS-(I), (II) and (III).....	229
2.4 LH kinetic models based on a single rate determining elementary step including explicit consideration of adsorption competition with adsorbed atomic hydrogen.....	232
2.4.1 RDS-(IV) model: rate-determining step (5)	233
2.4.2 RDS-(V) model: reversible rate-determining step (5).....	236
2.4.3 RDS-(VI) model: reversible rate-determining step (13)	243
2.4.4 TDTS-(II) model: reversible rate-determining step (11).....	249
2.4.5 TDTS-(III) model: reversible rate-determining step (15)	254
2.4.6 Sensibility analysis for the RDS-(VI) model	258
2.4.7 Arrhenius plot and Eyring plot for the Langmuir Hinshelwood kinetic models ...	262
2.5. Conclusion and perspectives	263
References	265

CHAPTER VI – CONCLUSIONS AND PERSPECTIVES

1. Conclusions	266
1.1 <i>Ab initio</i> dehydrogenation mechanisms of methyl-cyclohexane over Pt ₁₃ H ₆ / γ -Al ₂ O ₃ (100) cluster and Pt (111) surface	266
1.2 Kinetics for dehydrogenation reaction on γ -alumina supported platinum catalyst	268
2. Perspectives.....	270
References	273

CHAPTER I – INTRODUCTION

In 2015, crude oil represents 32% of the global energy resources, which in fact is the first source of energy for the whole planet.^{1,2} In 2016, the world production of oil (crude oil, shale oil, oil sands and natural gas liquids) was about 92150 thousand barrels (4382 million tonnes) daily and the consumption about 96558 thousand barrels (4418 million tonnes) daily.³ The petroleum refining processes are used in petroleum refineries (or oil refineries) to transform crude oil into useful products such as liquefied petroleum gas (LPG), gasoline, jet fuel (kerosene is a jet fuel), diesel oil and fuel oils. Catalytic reforming is one of the main processes in the refining industry aiming at the transformation of petroleum fractions with a low research Octane Number into a high octane reformat, a major blending fuel for gasoline motors and an important source of aromatic hydrocarbons, while valuable co-product is hydrogen.⁴⁻⁶ The aromatic hydrocarbons produced are of interest for petrochemicals. Mainly, targeted reactions in catalytic reforming are dehydrogenation, dehydrocyclization and alkane isomerizations.⁷⁻⁹

During the 1950s and 1960s, platinum on chlorinated or non-chlorinated alumina catalysts were employed almost exclusively in commercial reforming units.^{8,10} The outstanding performance of these catalysts led to the wide applications of catalytic reforming in petroleum refineries. This kind of catalyst operates in a bi-functional way. The superior activation properties of platinum for C-H bond and low activity for C-C bond cleavage also makes the platinum based catalyst on γ -alumina a popular choice for the non-oxidative dehydrogenation of light olefins.¹¹ Alumina proves to be the most suitable acid support required for cyclisation and isomerization reactions, where chlorine changes the acidity of the support.^{5,12-14} Early study of Parera et al.¹² suggested that a 0.8-0.9% chlorinated alumina shows a good selectivity and activity for n-

Heptane reforming. Platinum catalyzes the dehydrogenation-hydrogenation reactions. The dehydrogenation of hydrocarbons by platinum is generally considered to be structure sensitive, which means that the control of the size and shape of platinum particles is of high importance in reforming.^{8,15,16} In industrial catalysts, the size of the platinum nanoparticles is thus close or even smaller than 1 nanometer^{7,17-19} with a very high dispersion close to 100%. From the late 1960s to the present the platinum on alumina catalysts have largely been replaced in commercial practice by catalysts containing platinum and a second metallic element, such as tin or rhenium, to improve the selectivity to aromatics and reduce deactivation of catalysts by coke formation.

Due to the high level of complexity inherent to the reaction networks involved in naphtha reforming, model reactions have to be chosen for a better understanding of the catalytic properties.²⁰⁻²⁵ A very popular one is the reforming of n-heptane, which already give rise to many reactions and products, as isomerization, dehydrogenation, dehydrocyclization but also alkane cracking, hydrogenolysis and coking may concomitantly occur.^{4,7,20} We will focus on the mechanism of a more simple but essential reaction: dehydrogenation of methyl-cyclohexane to toluene. Thus, this reaction aims at probing predominantly the catalytic properties of the metallic active phase with respect to its dehydrogenation function in absence of any secondary reactions such as hydrogenolysis or cracking. It has also been the subject of numerous experimental kinetic investigations on mono- or bi-metallic platinum based catalysts,^{16,25-35} sometimes together with kinetic modeling.^{27,29-31} However, some debates remains about the relevant mechanism, rate determining step and corresponding kinetic parameters.

Detailed knowledge on the mechanisms taking place during methylcyclohexane dehydrogenation on supported platinum particles is required to obtain a high degree of control for reactivity and selectivity, which by the way is known to depend a lot on operating conditions

(temperature, pressure of H₂ and hydrocarbons²³). We propose here to investigate the reactivity of those nanoparticles, in a first step mono-metallic platinum nano-aggregates, by quantum simulations based on the density functional theory (DFT). In the literature, regarding DFT modeling aspect, model Pt (111) surfaces at low hydrogen coverage have been extensively used for the modeling of the hydrogenation/dehydrogenation reaction³⁶⁻⁴⁷ involving small alkene molecules (ethylene or propene)^{15,36,44,48-51} and aromatics (such as benzene).^{40-42,52-54} Aiming at a more innovative and realistic approach, we propose here to simulate the catalytic system using models developed in the past at IFP Energies nouvelles for subnanometric particles supported on γ -alumina.⁵⁵⁻⁵⁹ The influence of the partial pressure of hydrogen will be taken into account. Comparison with the Pt (111) surface will be performed. A promising approach for the validation of the mechanisms and rate constants obtained *ab initio* is multi-scale modeling, performed by integration of the data calculated *ab initio* in higher-scale models.⁶⁰ Comparison with careful experiments is fruitful to get unedited information about the reaction mechanisms at the atomic scale. This combined experimental and multi-scale modeling methodology was applied recently to several kinds of catalytic systems,^{53,61,62} and will be the object of some trials in the present work.

Chapter I proposes a literature analysis of the current state of knowledge for the catalytic systems under investigation and reactions of interest, and also an overview on the relevant modeling achievement of the catalyst properties. A methodology part follows in Chapter II, setting the theoretical background employed, as well as the experimental details for the catalytic tests performed. In Chapter III, we report the results obtained in the DFT simulations of methylcyclohexane dehydrogenation, on a Pt₁₃/ γ -Al₂O₃(100) model developed previously.^{14,55-57,63} In Chapter IV, we report a combined experimental and simulation kinetic study of

methylcyclohexane dehydrogenation. We establish kinetic models of Langmuir-Hinshelwood (LH) type, fully parameterized by *ab initio* kinetic constants of the mechanistic model, in comparison with kinetic experimental data obtained currently at IFPEN on a relevant non-chlorinated platinum based catalyst. These models were examined for the validation in aspect of several kinetic descriptors: the evolution of reaction rates as a function of operational conditions at the initial reaction state or during the reaction course, and also the apparent reaction activation energy. These achievements open perspectives in terms of variation of the hydrogen content on the particle, the improvements on the mechanistic model and also the discussions on the containment of employed LH models, while the micro-kinetic modeling is fully expected to be pursued in the future, as will be presented in the last section of the manuscript.

References

- (1) Oil Information Overview (2017 edition) accessed 09/15/2017, Page 3. <http://www.iea.org/publications/freepublications/publication/OilInformation2017Overview.pdf>.
- (2) World Energy Balances 2017 Overview accessed 09/15/2017, Page 3. <http://www.iea.org/publications/freepublications/publication/WorldEnergyBalances2017Overview.pdf>.
- (3) Source BP statistical review 2016 accessed 09/15/2017, Page 14-17. <http://www.bp.com/en/global/corporate/energy-economics/statistical-review-of-world-energy.html>.
- (4) Leprince, P. *3 Procédés de Transformation. Chap.4 Reformage Catalytique*, 105-169; Technip, 1998.
- (5) Gjervan, T.; Prestvik, R.; Holmen A. *Basic Principles in Applied Catalysis. Catalytic Reforming*, 125-158; Springer, 2004.
- (6) Rahimpour, M. R.; Jafari, M.; Iranshahi, D. *Appl. Energy* **2013**, *109*, 79–93.
- (7) Sinfelt, J. H. in: G. Ertl, E. Knözinger, J. Weitkamp (Eds.), *Handbook of Heterogeneous Catalysis*, Wiley, Weinheim, 1997, 1939–1955.
- (8) Sinfelt, J. H. *Bifunctional Catalysis*, in *Advances in Chemical Engineering*; Academic Press, 1964.
- (9) Little, D. M. *Catalytic Reforming 2 (Oklahoma)*; Pennwell Publ Co., 1985.
- (10) Boitiaux, J. P.; Devés, J. M.; Didillon, B.; Marcilly, C. R. *Catalytic Reforming of Naphtha. Catalyst Preparation*; Marcel Dekker, Inc., 1995.
- (11) Sattler, J. H. B.; Ruiz-Martinez, J.; Santillan-Jimenez, E.; Weckhuysen, B. M. *Chem. Rev.* **2014**, *114*, 10613–10653.
- (12) Figoli, N. S.; Sad, M. R.; Beltramini, J. N.; Jabioski, E. L.; Parera, J. M. *Ind. Eng. Chem. Prod. Res. Dev* **1980**, *19*, 545–551.
- (13) Keogh, R. A.; Sparks, D. E.; Thomas, G. A.; Davis, B. H. *ACS, Division of Fuel Chemistry, Preprints* **1992**, *37* (1895-1902).
- (14) Digne, M.; Raybaud, P.; Sautet, P.; Guillaume, D.; Toulhoat, H. *J. Am. Chem. Soc.* **2008**, *130*, 11030–11039.
- (15) Zhu, J.; Yang, M. L.; Yu, Y. D.; Zhu, Y. A.; Sui, Z. J.; Holmen, A.; Chen, D. *ACS Catal.* **2015**, *5*, 6310–6319.
- (16) Rochefort, A. *J. Catal.* **1992**, *138*, 482–490.
- (17) Ma, A. Z. *Sci Sin Chim* **2014**, *44*, 25.
- (18) Ahmed, F.; Alam, M. K.; Suzuki, A.; Koyama, M.; Tsuboi, H.; Hatakeyama, N.; Miyamoto, A. *J. Phys. Chem. C* **2009**, *113*, 15676–15683.
- (19) Jahel, A. N.; Moizan-Baslé, V.; Chizallet, C.; Raybaud, P.; Olivier-Fourcade, J.; Jumas, J. C.; Avenier, P.; Lacombe, S. *J. Phys. Chem. C* **2012**, *116*, 10073–10083.
- (20) Beltramini, J.; Trimm, D. L. *Appl. Catal.* **1987**, *31*, 113–118.
- (21) Myers, C. G.; Lang, W. H.; Weisz, P. B. *Ind. Eng. Chem. Res.* **1961**, *53*, 299–302.
- (22) Sinfelt, J. H. *J. Mol. Catal. A* **2000**, *163*, 123–128.
- (23) Bond, G. C.; Cunningham, R. H. *J. Catal.* **1997**, *166*, 172–185.

- (24) Liu, X.; Lang, W. Z.; Long, L. L.; Hu, C. L.; Chu, L. F.; Guo, Y. J. *Chem. Eng. J.* **2014**, *247*, 183–192.
- (25) Touzani, A.; Klvana, D.; Belanger, G. *Stud. Surf. Sci. Catal.* **1984**, *19*, 357–364.
- (26) Sinfelt, H. J.; Hurwitz, H.; Shulman, R. A. *J. Phys. Chem.* **1960**, *64*, 1559–1562.
- (27) Van Trimpont, P. A.; Marin, G. B.; Froment, G. F. *Ind. Eng. Chem. Fundam.* **1986**, *25*, 544–553.
- (28) Rochefort, A.; Le Peltier, F.; Boitiaux, J. P. *J. Catal.* **1994**, *145*, 409–415.
- (29) Verstraete, J. Thesis : Kinetische Studie van de Katalytische Reforming van Nafta over een Pt-Sn/Al₂O₃ Katalysator, Universiteit Gent, 1997.
- (30) Usman, M.; Cresswell, D.; Garforth, A. *Ind. Eng. Chem. Res.* **2012**, *51*, 158–170.
- (31) Alhumaidan, F.; Cresswell, D.; Garforth, A. *Ind. Eng. Chem. Res.* **2011**, *50*, 2509–2522.
- (32) Boudart, M. *AIChE J.* **1956**, *2*, 62–64.
- (33) Wolf, E. E.; Petersen E. E. *J. Catal.* **1977**, *46*, 190–203.
- (34) Garcia de la banda, J. F.; Corma, A., Melo, F. V. *Appl. Catal.*, 1986, 103–121.
- (35) Rodríguez, M. A.; Ancheyta, J. *Fuel* **2011**, *90*, 3492–3508.
- (36) Steininger, H.; Ibach, H.; Lehwald, S. *Surf. Sci.* **1982**, *117*, 685–698.
- (37) Hem, F. C.; Diaz, A. L.; Bussell, M. E.; Hugenschmidt, M. B.; Domagala, M. E.; Campbell, C. T. *J. Phys. Chem. B* **1992**, *96*, 5965–5974.
- (38) Watwe, R. M.; Ramchandra, M.; Cortright, R. D.; Nørsko, J. K.; Dumesic, J. A. *J. Phys. Chem. B* **2000**, *104*, 2299–2310.
- (39) Valcárcel, A.; Clotet, A.; Ricart, J. M.; Delbecq, F.; Sautet, P. *Surf. Sci.* **2004**, *549*, 121–133.
- (40) Morin, C.; Simon, D.; Sautet, P. *J. Phys. Chem. B* **2004**, *108*, 5653–5665.
- (41) Saeys, M.; Reyniers, M.; Thybaut, J.; Neurock, M.; Marin, G. B. *J. Phys. Chem. B* **2005**, *109*, 2064–2073.
- (42) Morin, C.; Simon, D.; Sautet, P. *Surf. Sci.* **2006**, *600*, 1339–1350.
- (43) Becker, C.; Haubrich, J.; Wandelt, K.; Delbecq, F.; Loffreda, D.; Sautet, P. *J. Phys. Chem. C* **2008**, *112*, 14693–14695.
- (44) Chen, Y.; Vlachos, D. G. *J. Phys. Chem. C* **2010**, *114*, 4973–4982.
- (45) Gautier, S.; Steinmann, S. N.; Michel, C.; Fleurat-Lessard, P.; Sautet, P. *Phys. Chem. Chem. Phys.* **2015**, *17*, 28921–28930.
- (46) Wang, B.; Froment, G. F. *Catal. Lett.* **2017**, *147*, 663–673.
- (47) Watwe, R. M.; Spiewak, B. E.; Cortright, R. D.; Dumesic, J. A. *J. Catal.* **1998**, *180*, 184–193.
- (48) Neurock, M.; van Santen, R. A. *J. Phys. Chem. B* **2000**, *104*, 11127–11145.
- (49) Aleksandrov, H. A.; Moskaleva, L. V.; Zhao, Z. J.; Basaran, D.; Chen, Z. X.; Mei, D. H.; Rösch, N. *J. Catal.* **2012**, *285*, 187–195.
- (50) Breinlich, C.; Haubrich, J.; Becker, C.; Valcarcel, A.; Delbecq, F.; Wandelt, K. *J. Catal.* **2007**, *251*, 123–130.
- (51) Okada, T.; Kim, Y.; Sainoo, Y.; Komeda, T.; Trenary, M.; Kawai, M. *J. Phys. Chem. Lett.* **2011**, *2*, 2263–2266.

- (52) Canduela-Rodriguez, G.; Sabbe, M. K.; Reyniers, M. F.; Joly, J. F.; Marin, G. B. *Phys. Chem. Chem. Phys.* **2014**, *16*, 23754–23768.
- (53) Sabbe, M. K.; Canduela-Rodriguez, G.; Reyniers, M. F.; Marin, G. B. *J. Catal.* **2015**, *330*, 406–422.
- (54) Ma, H. Y.; Wang, G. C. *J. Catal.* **2011**, *281*, 63–75.
- (55) Hu, C. H.; Chizallet, C.; Mager-Maury, C.; Corral-Valero, M.; Sautet, P.; Toulhoat, H.; Raybaud, P. *J. Catal.* **2010**, *274*, 99–110.
- (56) Mager-Maury, C.; Bonnard, G.; Chizallet, C.; Sautet, P.; Raybaud, P. *ChemCatChem* **2011**, *3*, 200–207.
- (57) Chizallet, C.; Raybaud, P. *Catal. Sci. Technol.* **2014**, *4*, 2797.
- (58) Gorczyca, A.; Moizan, V.; Chizallet, C.; Proux, O.; Del Net, W.; Lahera, E.; Hazemann, J. L.; Raybaud, P.; Joly, Y. *Angew. Chem. Int. Ed.* **2014**, *53*, 12426–12429.
- (59) Mager-Maury, C.; Chizallet, C.; Sautet, P.; Raybaud, P. *ACS Catal.* **2012**, *2*, 1346–1357.
- (60) Saliccioli, M.; Stamatakis, M.; Caratzoulas, S.; Vlachos, D. G. *Chem. Eng. Sci.* **2011**, *66*, 4319–4355.
- (61) John, M.; Alexopoulos, K.; Reyniers, M. F.; Marin, G. B. *J. Catal.* **2015**, *330*, 28–45.
- (62) Larmier, K.; Nicolle, A.; Chizallet, C.; Cadran, N.; Maury, S.; Lamic-Humblot, A.-F.; Marceau, E.; Lauron-Pernot, H. *ACS Catal.* **2016**, *6*, 1905–1920.
- (63) Raybaud, P.; Chizallet, C.; Mager-Maury, C.; Digne, M.; Toulhoat, H.; Sautet, P. *J. Catal.* **2013**, *308*, 328–340.

CHAPTER II – STATE OF THE ART AND STRATEGY OF THE THESIS

1. Reactions taking place in catalytic reforming

1.1 Nature of the reactions

Catalytic reforming involves the transformation of low-octane hydrocarbons boiling in the gasoline range into more valuable high-octane gasoline components, such as aromatics and highly branched paraffins, without significantly changing their carbon numbers (Figure II-1). Targeted reactions leading to the formation of aromatic hydrocarbons involve dehydrogenation, cyclization (dehydrocyclization), isomerization, whereas unwished reactions are hydrogenolysis and coking.¹⁻⁶ They are illustrated in the following on the example of n-heptane and toluene molecules as reactants.

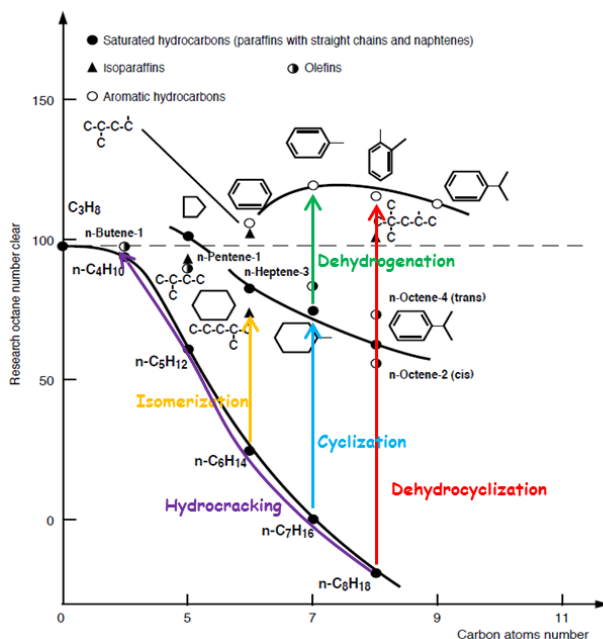
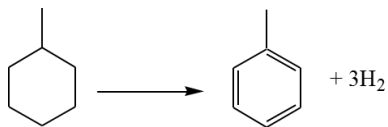


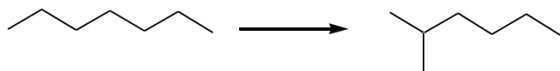
Figure II- 1 Research Octane Number of different hydrocarbons (paraffins, olefins, naphthenes and aromatics) and different reforming reactions (adapted from¹)

Targeted reaction:

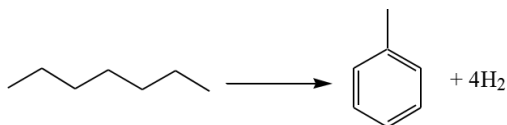
(1) Dehydrogenation



(2) Isomerization



(3) Aromatization (cyclization and dehydrogenation, so called dehydrocyclization)

**Unwished reaction:**

(4) Hydrogenolysis:



(5) coking:



The reforming catalyst is a bifunctional catalyst⁴ with a metal function for hydrogenation and dehydrogenation reactions and an acid function for hydrocarbon rearrangements. Both the metal

and acid sites are dispersed on the surface of the support. The two catalyst functions interact with olefins, which are key intermediates in the reaction network.

The first three reactions (1)-(3) lead to higher octane number products whereas the last two reactions (4) and (5) are undesirable since they decrease the yield of gasoline. In fact, under reforming conditions, the bi-functional acid catalyzed cyclization pathway is dominant.⁷⁻¹⁰ In the 1930s, the early thinking materialized as the Twigg mechanism¹¹ which implies that cyclization leads to an adsorbed cyclohexane, which means the dehydrogenation to form the aromatic occurred after ring formation. Many of the early mechanistic studies were based on kinetic measurements, which will be presented in the following part. It should however be realized that the reaction network is in fact much more complex, with a large number of reactants that may lead to over 100 reaction products.

In this thesis work, as we mentioned in the general introduction part, we will basically focus on the dehydrogenation of methyl-cyclohexane to toluene, which is one of the key reaction in catalytic reforming.

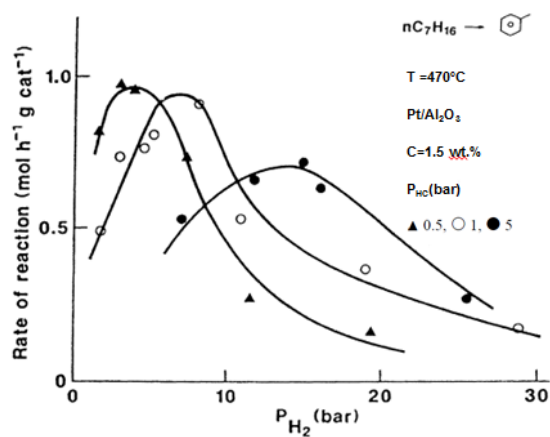
1.2 Thermodynamics of the reactions

The petroleum naphtha fractions consist of hydrocarbons having boiling points within the approximate range of 60-180°C. Reaction temperatures of 425-525°C and pressures of 10-35 atm are employed in the process. Paraffin dehydrogenation is strongly endothermic while hydrocracking and hydrogenolysis are exothermic (Table II-1). Thus, in practice, the employed temperature is around 500°C in the reactors.

Table II- 1 Thermodynamic data, at 500°C, of typical reforming reactions with C6 and C7 hydrocarbons ²

Reaction type	Reaction	$\Delta_r H^\circ$ (kJ/mol)
Dehydrogenation	Methylcyclohexane \rightleftharpoons Toluene + 3 H ₂	216
Dehydrocyclization	n-Heptane \rightleftharpoons Toluene + 4 H ₂	252
Hydrocracking	n-Heptane + H ₂ \rightleftharpoons Propane + n-butane	-52
Hydrogenolysis	n-Heptane + H ₂ \rightleftharpoons Methane + n-hexane	-62

The dehydrogenation and dehydrocyclization reactions produce hydrogen during the process, which makes a low hydrogen partial pressure beneficial to thermodynamics. However, at high temperatures and low hydrogen partial pressure, formation of coke on the surface of the catalyst occurs, which leads to a decrease of the catalyst activity. This is the usual explanation given for maximum curves such as the one shown in Figure II-2,¹² for *n*-heptane dehydrocyclization rate versus hydrogen pressure. Similar patterns were obtained by Rohrer et al. et Bond et al..¹³⁻¹⁸

Figure II- 2 Rate of dehydrocyclization versus hydrogen pressure for various hydrocarbon pressures¹²

For the investigations dealing with the effect of the hydrogen partial pressure on the activity in dehydrogenation of methyl-cyclohexane to toluene, the total pressure and the hydrogen partial pressure for this reaction remains really variable.^{4,13,19–23} The total pressure varies from 1.5 to 30 bar; hydrogen partial pressure varies between 1.1 and 20 bar; the $P(\text{H}_2)/P(\text{HC})$ ratio ranges from 1.5 to 30. And these pressure values highly depend on the nature of the catalyst. The mono- or bi-metallicity of the catalyst and also the composition of the alloy can change a lot on the choice of the reaction pressure as well.^{1,2,4} The optimal operating conditions in this work by using Pt supported on non-chlorinated gamma alumina for the dehydrogenation of methyl-cyclohexane to toluene employ a temperature range of 320-380°C, a total pressure of 12 bar and a $P(\text{H}_2)/P(\text{HC})$ of 15, the reason of this condition choice will be explained in next chapter.

2. Catalyst

The reforming catalyst as we presented is a bifunctional catalyst, which consists of γ -alumina support for its acidic function and metal component for the dehydrogenation (or hydrogenation) function. This metal is usually chosen among the noble metals as platinum. Nowadays, bi-metallic catalyst are made by platinum combined with a second noble metal such as rhenium^{20,24–26}, iridium^{27,28} or tin^{7,29–31} to provide a better stability and selectivity.^{2,4}

2.1 The catalyst support

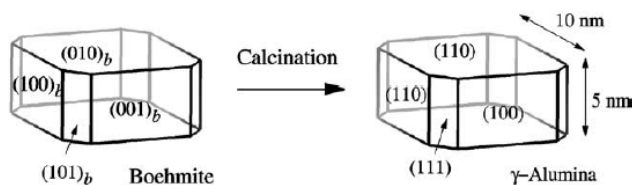


Figure II- 3 Transformation of boehmite into γ -alumina nanoparticles with the corresponding surface orientations³²

γ -Al₂O₃ is obtained from boehmite by calcination in air or vacuum.^{33–35} The γ -Al₂O₃ particle morphology is directly inherited from the equilibrium morphology of boehmite particles (Figure II-3). The most common shape of a boehmite nanoparticle is rhombohedral: the predominant (010) surface is referred to as the basal surface, while three types of edge surfaces (100), (001), and (101) may be exposed. Once the topotactic transformation is done, the crystallographic orientation using a spinel-type indexation, the topology of γ -alumina surfaces can be classified according to the oxygen atom sublattice: the (100) surface exhibits a square oxygen atom sublattice, the (110) a rectangular one and the (111) a hexagonal one. The (110) surface corresponds to the predominant area between 70 and 83%^{36,37}. The (100) surface is less abundant and accounts for 17%, according to Ref.³⁶. The (111) surface can be exposed, too, but its importance depends on the synthesis conditions³⁷.

In order to enhance its acidity and activate the catalyst, the γ -Al₂O₃ is chlorinated³⁸. However, it's important to choose a balanced acidity with chlorine, in order to enhance the desirable reforming reaction like isomerization and also to hinder the non-desirable reaction such as hydrocracking³⁹. Gates et al.⁴⁰ revealed that by increasing the acidity of the support with a high chlorine content will give rise to excessive undesired hydrocracking, while a low content

leads to low activity for isomerization and dehydrocyclization. So, an optimal chlorine concentration must be chosen. Generally, a dose of 0.8-0.9% chlorine is proposed to present a good selectivity and activity of catalyst and incites a minimum coke formation during the reforming.⁴¹ In addition, it is also observed experimentally that chlorine may prevent the sintering of Pt nano-clusters^{39,42,43}. In the recent DFT theoretical study of Mager-Maury et al.⁴⁴, this peculiar effect of the chlorination was explained as limiting the sintering of metallic phase by acting as a surface ligand and helping stabilizing its optimal dispersion.

2.2 The Pt/ γ -Al₂O₃ based catalysts

Platinum (Pt) supported on γ -alumina is the most used reforming catalyst.^{4,5,13,14,38,45-47} It is favored for Pt to be the active phase of the catalyst because of its high activity and good selectivity for dehydrogenation, compared to the other noble metals. Table II-2, extracted from ref.², compares the activity of different catalyst supported on alumina, silica or silica-alumina for dehydrogenation of cyclohexane to benzene. Compared to the other mono- metallic catalyst such as palladium (Pd), iridium (Ir) and rhodium (Rh), Pt catalyst presents obviously a superior activity level.

Table II- 2 Cyclohexane dehydrogenation activities of supported metal and metal oxide catalysts ²

Catalyst, wt%	Dehydrogenation activity (μ moles benzene/g catalyst/s)
34% Cr ₂ O ₃ cogelled with Al ₂ O ₃	0.5
10% MoO ₃ coprecipitated with Al ₂ O ₃	3
5% Ni on Al ₂ O ₃ or SiO ₂ -Al ₂ O ₃	13
5% Co on Al ₂ O ₃	13
0.5% Ir on Al ₂ O ₃	190
1% Pd on Al ₂ O ₃	200
5% Ni on SiO ₂	320
1% Rh on Al ₂ O ₃	890
0.5% Pt on Al ₂ O ₃ or SiO ₂ -Al ₂ O ₃	1400-4000

*differential flow reactor at 427°C, 6.8 atm, H₂/HC=6 (mole ratio), activity determined after 30 min on stream, pre-treated with H₂ at reaction conditions.

However, platinum on alumina catalysts have largely been replaced in commercial practice by catalysts containing platinum and a second metallic element. Among them all, three of such bimetallic catalyst systems that have been employed extensively in commercial reformers are platinum-rhenium,^{20,24–26,48} platinum-iridium^{27,28} and platinum-tin.^{7,29–31} The application of these bi-metallic catalysts in reforming has resulted in major improvements of the selectivity of the major products like aromatic hydrocarbons, and also in the reduction of deactivation of catalysts by coke formation.^{25,28–30} For instance, Pt-Sn bimetallic catalyst exhibits an increase on the catalyst selectivity and stability and a decrease on hydrogenolysis.^{30,31,49–55} To explain these phenomena, some studies show that an electronic effect has been provoked from Sn to Pt, which makes Pt inhibit part of its activity and become more stable during the reaction.^{30,48,52–55} While others consider a geometric effect that either the Sn atoms help to divide the Pt particles into smaller clusters, or the existence of these Pt-Sn alloy dilutes and blocks Pt atoms, thus changes its

activity.^{49–51} Meanwhile, a combination effect of the electronic and geometric effect has also been proposed.⁵⁶

The mono metallic Pt catalyst is ultra-dispersed on the porous alumina support, possibly atomically deposited due to its high cost. In industrial catalysts, the size of the platinum nanoparticles is thus close or even smaller than 1 nanometer with a very high dispersion close to 100%. High activity and high dispersion require only small amounts of platinum and the current commercial catalysts typically contain in the order of 0.2-0.4 wt% of platinum and the metal particle size can vary in the range 0.8 to 2.5 nm.^{16,27,57,58} Figure II-4(a)²⁷ shows selected STEM (scanning transmission electron microscopy) images of reduced monometallic Pt/ γ -Al₂O₃-Cl (0.3 wt% Pt; 0.98 wt% Cl). The monometallic catalysts show a narrow particle size distribution between 0.6 and 2.5 nm, which is about 10-20 atoms per particle. Figure II-4(b)²⁷ depicts the STEM image of reduced bimetallic PtSn/ γ -Al₂O₃-Cl (0.3 wt% Pt; 0.32 wt% Sn; 0.98 wt% Cl). The bimetallic particles size range on the reduced catalysts between 0.7 nm and 3.5 nm. The average particle size is determined at 1.5 nm.

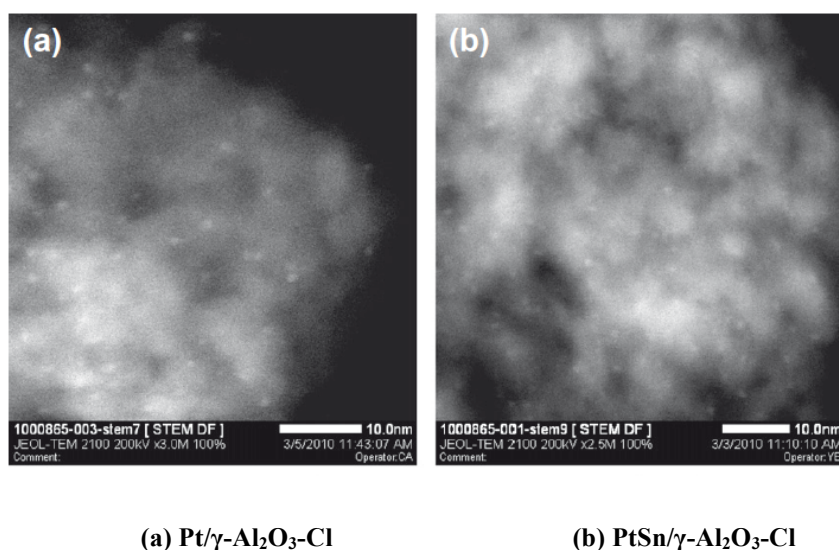


Figure II- 4 Selected STEM images of reduced catalysts: (a) Pt/Al₂O₃-Cl (b) PtSn/Al₂O₃-Cl²⁷

3. Kinetic studies on dehydrogenation of methyl-cyclohexane into toluene

3.1 Overview of experimental kinetic studies

Focusing on the mechanism and kinetics of dehydrogenation of methyl-cyclohexane on toluene, different studies by using experimental or kinetic fitting modeling methods have been reported. Sinfelt et al.¹³ studied the reaction kinetics over a 0.3 w% platinum-on-alumina catalyst in the 315 to 372°C temperature range, at methyl-cyclohexane partial pressures ranging from 0.07 to 2.2 atmospheres and hydrogen pressures ranging from 1.1 to 4.1 atmospheres. The reaction was found to be nearly zero order with respect to methyl-cyclohexane (MCH) and hydrogen (H₂) over the range of conditions studied. The apparent activation energy for the reaction was found to be 138 kJ/mol. The near zero order behavior of the reaction suggests that the active catalyst sites are heavily covered with adsorbed molecules or radicals at reaction conditions. Bournonville et al.¹² used the catalyst 0.35 wt% Pt-0.20 wt% Sn on γ -Al₂O₃ to investigate the reaction kinetics, over the temperature range 300-450°C, at methyl-cyclohexane partial pressures ranging from 0.02 to 0.2 atmospheres and hydrogen pressures ranging from 0.8 to 0.98 atmospheres. They found the same reaction orders near zero for both MCH and H₂ and an apparent activation energy of 116 kJ/mol, which is very closed to the value Touzani et al.⁵⁹ obtained. These two studies are based on a simple kinetic scheme without considering the intermediate steps. Alhumaidan et al.²² obtained the partial reaction orders to methyl-cyclohexane and hydrogen equal -0.05 and -0.41, respectively by fitting the experimental data on a Power-law kinetic model. Van Trimpont et al.²⁰ applied a single site surface reaction mechanism by applying the Langmuir-Hinshelwood-Hougen-Watson (LHHW) mechanism and fitting modeling. They proposed the reaction rate-determining step is the dehydrogenation of methyl-cyclohexadiene into toluene. The activation energy obtained by kinetic fitting is 180 kJ/mol. Usman et al.²³

performed the same single site LHHW mechanism and they found the dehydrogenation of the first hydrogen molecule as the rate-determining step and an activation energy of 39.3 kJ/mol. Finally, Verstraete⁶⁰ in his thesis by using the same kind of mechanism as van Trimont, also compared the fitting results with experimental results and found a good match, in the case of platinum, platinum-tin and platinum-rhenium catalysts.

3.2 Focus on the kinetic model of Van Trimont et al. and Verstraete

3.2.1 Hougen Watson reaction rate equations

As suggested by Langmuir in 1921 and further developed by Hinshelwood in 1926, the Langmuir Hinshelwood Hougen Watson (LHHW) model⁶¹⁻⁶³ provides a mechanistic analysis that describes the elementary steps of surface catalytic reactions. It is one of the most commonly used approach to solve the reaction kinetics, by assuming that the reactant diffusion on the catalyst surface can be neglected. If so, the reaction rates depend on the chemisorption/desorption steps (obeying Langmuir formalism) and on the surface reaction steps. Furthermore, the derivation of rate equations assumes the existence of a rate-determining step, whereas the other elementary steps are in pseudo-equilibrium. In addition, the total concentration of surface active sites, which is the sum of the concentration of all surface species including the adsorbed reactants, products, and vacant sites, is assumed to be constant (thanks the equation of sites conservation). This LHHW model allows us to describe the surface catalytic process and the rate equations derived from the mechanistic model, more or less adequately according to the relevance of the approximations.

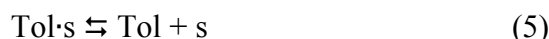
In the reference work of Van Trimont²⁰ et al. in 1986, the reaction mechanism of the dehydrogenation of methyl-cyclohexane on toluene was investigated by a LHHW kinetic method

and kinetic parameters were proposed, fitted on experimental data obtained on alumina supported sulfided platinum catalyst. One decade later in 1997, these mechanisms and kinetic parameters were revisited and extended by Verstraete⁶⁰ who determined about 20 reaction rates including the earlier model of Van Trimont in order to apply it on alumina supported platinum-tin catalyst as a function of reaction conditions (hydrogen partial pressure in particular). One intriguing result of the thesis of Verstraete is that a maximum of the rate as a function of the hydrogen partial pressure, can be obtained from a model without including any equation related to coke formation at low hydrogen partial pressure. This trend agrees with the one observed during the experiments. It must be underlined that such a trend exhibiting a maximum was reported by numerous experimental kinetic studies involving either dehydrogenation, dehydrocyclisation, hydrogenolysis reactions.¹⁴⁻¹⁸

At this stage, it is surprising that by only using mathematic fitting results and kinetic model without including coke formation in his mechanistic model, this experimental phenomenon seems to be explicitly arisen. However, in both works,^{20,60} the chemical origins of such a maximum, which cannot be reproduced by a power law rate equation as shown previously, have never been developed in details.

As a preliminary analysis to our work, and in order to better understand this mechanism and the possible kinetic models of methyl-cyclohexane dehydrogenation, we propose to review in what follows the works by Van Trimont²⁰. Three kinds of models were proposed by the authors, leading to successive simplifications: (I) a dual-site sequence, with generation of surface hydrogen atoms on another site (although similar in nature) than the dehydrogenated species, (II) a dual-site sequence, with generation of adsorbed molecular dihydrogen in single steps, (III) a single-site sequence, with formation of gaseous H₂ in single steps. After the analysis of all the

possibilities in terms of sequence and rate limiting step, the authors concluded that the most relevant scheme is the dual-site reactions sequence, with generation of adsorbed H_2 , where step (4) is the rate limiting step, which is presented here :



With MCH = methyl-cyclohexane in gas phase; s = active site; MCH·s = methyl-cyclohexane surface species on the active site; MCHe·s = methyl-cyclohexene surface species on the active site; MCHde·s = methyl-cyclohexadiene surface species on the active site; Tol·s = toluene surface species on the active site; Tol = toluene in gas phase; H₂·s = dihydrogen surface species on the active site; H₂ = dihydrogen in gas phase.

The rate-determining step of the reaction on the surface is indicated as the elementary step (4). All LHHW rate equations are thus re-established here in this work, in order to achieve the final reaction rate expression mentioned in their work, by understanding each of the hypotheses they made.

The reaction rate is expressed according to the rate-determining step (ES: elementary step) :

$$ES (4) : \quad r = k_4 [MCHde \cdot s][s] - k_{-4} [Tol \cdot s][H_2 \cdot s] \quad \text{Equation (II-1)}$$

The equation of sites conservation is the following :

$$\text{SS-1: } [MCH \cdot s] + [MCHe \cdot s] + [MCHde \cdot s] + [Tol \cdot s] + [H_2 \cdot s] + [s] = 1 \quad \text{Equation (II-2)}$$

The reaction equilibrium constants are established for each elementary step (ES) except for the rate determining step (4) :

$$\text{ES (1) : } K_1 = \frac{[MCH \cdot s]}{P_{MCH} \cdot [s]} \Rightarrow [MCH \cdot s] = K_1 P_{MCH} [s] \quad \text{Equation (II-3)}$$

$$\text{ES (6) : } K_6 = \frac{P_{H_2} \cdot [s]}{[H_2 \cdot s]} \Rightarrow [H_2 \cdot s] = \frac{P_{H_2} [s]}{K_6} \quad \text{Equation (II-4)}$$

$$\begin{aligned} \text{ES (2) : } K_2 &= \frac{[MCHe \cdot s][H_2 \cdot s]}{[MCH \cdot s][s]} \Rightarrow \\ [MCHe \cdot s] &= \frac{K_2 [MCH \cdot s][s]}{[H_2 \cdot s]} = \frac{K_1 K_2 K_6 P_{MCH} [s]}{P_{H_2}} \end{aligned} \quad \text{Equation (II-5)}$$

$$\begin{aligned} \text{ES (3) : } K_3 &= \frac{[MCHde \cdot s][H_2 \cdot s]}{[MCHe \cdot s][s]} \Rightarrow \\ [MCHde \cdot s] &= \frac{K_3 [MCHe \cdot s][s]}{[H_2 \cdot s]} = \frac{K_1 K_2 K_3 K_6^2 P_{MCH} [s]}{P_{H_2}^2} \end{aligned} \quad \text{Equation (II-6)}$$

$$\text{ES (5) : } K_5 = \frac{P_{Tol} \cdot [s]}{[Tol \cdot s]} \Rightarrow [Tol \cdot s] = \frac{P_{Tol} [s]}{K_5} \quad \text{Equation (II-7)}$$

Combining equations ES (1), (2), (3), (5), (6) and SS-1, we deduce the expression of the unknown variable $[s]$:

$$\text{SS-2 : } [s] = \frac{1}{1 + K_1 P_{MCH} + \frac{K_1 K_2 K_6 P_{MCH}}{P_{H_2}} + \frac{K_1 K_2 K_3 K_6^2 P_{MCH}}{P_{H_2}^2} + \frac{P_{Tol}}{K_5} + \frac{P_{H_2}}{K_6}} \quad \text{Equation (II-8)}$$

Thus the apparent reaction rate can be expressed as follows :

$$\begin{aligned}
 \text{RDS-1 : } \quad r &= \frac{k_4 K_1 K_2 K_3 K_6^2 P_{MCH} [s]^2}{P_{H_2}^2} - \frac{k_{-4} P_{Tol} P_{H_2} [s]}{K_5 K_6} \\
 \Rightarrow \quad r &= \frac{k_4 K_1 K_2 K_3 K_6^2 P_{MCH} - \frac{k_{-4}}{K_5 K_6} P_{Tol} P_{H_2}^3}{P_{H_2}^2 \left(1 + K_1 P_{MCH} + \frac{K_1 K_2 K_6 P_{MCH}}{P_{H_2}} + \frac{K_1 K_2 K_3 K_6^2 P_{MCH}}{P_{H_2}^2} + \frac{P_{Tol}}{K_5} + \frac{P_{H_2}}{K_6} \right)^2} \quad \text{Equation (II-9)}
 \end{aligned}$$

In Equation (II-9), assuming that the desorption of hydrogen and toluene are very fast and quantitative elementary steps, both terms $\frac{P_{Tol}}{K_5}$ and $\frac{P_{H_2}}{K_6}$ can be neglected with respect to 1. Note that this approximation is the one used by Van Trimpont et al. to simplify the number of parameters to be fitted experimentally.

The term $\frac{K_1 K_2 K_6 P_{MCH}}{P_{H_2}}$ is also omitted in the final expression of rate equation given by Van

Trimpont et al.. Somehow, this simplification is given no explanation in their work. However, in the work of Verstraete, it is found that on the same fitting model for the dehydrogenation reaction on Pt-Sn/Al₂O₃, during the first discrimination step for the parameter estimations, the parameters K_5 and K_6 are significantly negative. Therefore, for the second discrimination step, these parameters that could not be relevantly determined were set to zero (or neglected) and the remaining parameters were re-estimated. That could probably explain the fact that the term $\frac{K_1 K_2 K_6 P_{MCH}}{P_{H_2}}$ is omitted because of being significantly negative. Note that this appears to be in

contradiction with the first hypothesis according to which $\frac{P_{Tol}}{K_5}$ and $\frac{P_{H_2}}{K_6}$ are negligible. On the

other hand, that could also be considered as the reason that both terms $\frac{P_{Tol}}{K_5}$ and $\frac{P_{H_2}}{K_6}$ are

eliminated in the final rate equation expression. Note that neglecting $\frac{K_1 K_2 K_6 P_{MCH}}{P_{H_2}}$ means that

[MCHe·s] is negligible.

Meanwhile, the term $K_1 K_2 K_3 K_6^2$ can be treated as the equilibrium constant for the sum of Equation (II-3) +(II-4) +(II-5) + 2(II-6), which corresponds to the reaction :



So we have,

$$K_1 K_2 K_3 K_6^2 = \frac{[\text{MCHde} \cdot \text{s}] P_{H_2}^2}{P_{MCH} [\text{s}]} = K_{\text{MCHde}}$$

Equation (II-10)

where K_{MCHde} will be considered as the reaction equilibrium constant for the formation of the adsorbed methyl-cyclohexadiene intermediate.

In addition, at reaction equilibrium, $K_4 = \frac{k_4}{k_{-4}}$, so the term $\frac{k_{-4}}{K_5 K_6}$ in Equation (II-9) is identical to $\frac{k_4}{K_4 K_5 K_6}$.

Using a similar method as before, we can easily show that $K_4 K_5 K_6 = \frac{P_{Tol} P_{H_2} [s]}{[\text{MCHde} \cdot \text{s}]} = \frac{P_{Tol} P_{H_2}^3}{K_{\text{MCHde}} P_{MCH}}$. For the dehydrogenation reaction in gas phase at equilibrium, we define :

$$K_{\text{MCH} \rightarrow \text{Tol}} = \frac{P_{Tol} P_{H_2}^3}{P_{MCH}}$$

$$\Rightarrow \frac{k_{-4}}{K_5 K_6} = \frac{k_4 K_{MCHde}}{K_{MCH \rightarrow Tol}}$$

Equation (II-11)

Finally, replacing the terms $K_1 K_2 K_3 K_6^2$ and $\frac{k_{-4}}{K_5 K_6}$ by Equation (II-10) and (II-11), and as

$K_1 = K_{MCH}$ (equilibrium constant for the formation of the adsorbed MCH intermediate), we

express the apparent reaction rate equation from Equation (II-9) as follows :

$$\text{RDS-2 : } r_{MCH \rightarrow Tol} = \frac{k_4 K_{MCHde} (P_{MCH} - \frac{P_{Tol} P_{H_2}^3}{K_{MCH \rightarrow Tol}})}{P_{H_2}^2 (1 + K_{MCH} P_{MCH} + \frac{K_{MCHde} P_{MCH}}{P_{H_2}^2})^2} = \frac{k_{MCH \rightarrow Tol} (P_{MCH} - \frac{P_{Tol} P_{H_2}^3}{K_{MCH \rightarrow Tol}})}{P_{H_2}^2 (1 + K_{MCH} P_{MCH} + \frac{K_{MCHde} P_{MCH}}{P_{H_2}^2})^2}$$

Equation (II-12)

where $k_4 K_{MCHde} = k_{MCH \rightarrow Tol}$. Equation (II-12) is precisely the rate equation reported by Van

Trimpont et al. We are now aware of the assumptions behind this model.

3.2.2 Kinetic fitting parameters and reaction rate evolution as a function of hydrogen partial pressure

In the work of Van Trimpont, the pre-exponential factors, reaction enthalpies and activation energies involved in the Equation (II-12) have been determined to best fit the experimental data at a reaction temperature of 623 K. The fitting data are presented in terms of pre-factors and activation energies for each term in Equation (II-12), via the Arrhenius equation (Table II-3).

Table II- 3 Kinetic rate and equilibrium constants fitted for the LHHW dual site surface reaction mechanism at 623 K in the work of Van Trimpont²⁰

Kinetic Paramters	Rate equation II-4
$A_{MCH \rightarrow Tol}$, kmol bar ⁿ /(kg of cat.h)	2.60E+16
$E_{MCH \rightarrow Tol}$, kJ/mol	180
$k_{MCH \rightarrow Tol}$, kmol barⁿ/(kg of cat.h)	19.34
A_{MCH} , bar ⁻¹	5.10E+05
ΔH_{MCH} , kJ/mol	75
K_{MCH}, bar⁻¹	0.28
A_{MCHde} , bar ⁿ	1.47E+10
ΔH_{MCHde} , kJ/mol	100
K_{MCHde}, barⁿ	63.38
ΔH^\ddagger , kJ/mol	76
ΔS^\ddagger , J/(mol K)	-114
$K_{MCH \rightarrow Tol}$	7.43E-13

Note : (1) The values in black were taken from the Table V and VII for the rate equation II (4) in Ref.20;
(2) The values in blue were recalculated in this work from the corresponding parameters given by Table V and VII for the rate equation II (4) in Ref.20.

Therefore, the initial reaction rate ($P_{Tol} = 0$ bar) depending on hydrogen partial pressure at constant methyl-cyclohexane partial pressure of 0.5 bar and temperature of 623 K can be easily plotted by employing the Equation (II-12) with constants given in Table II-3, as shown in Figure II-5.

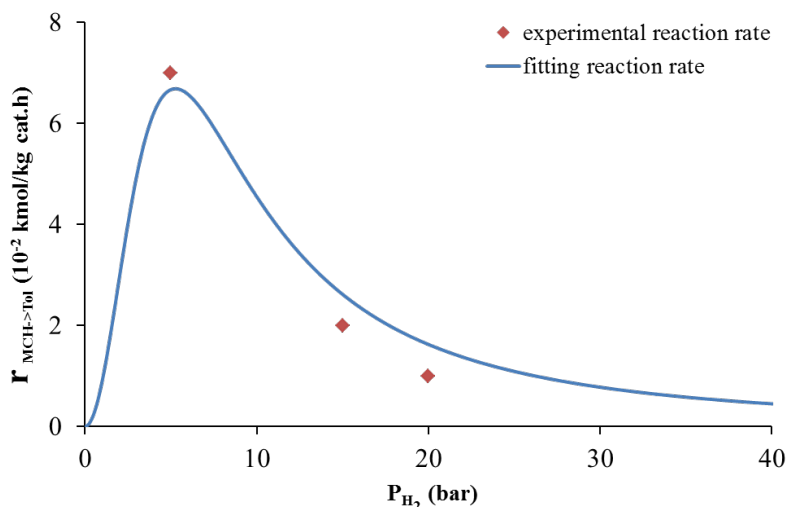


Figure II- 5 Influence of hydrogen partial pressure on initial dehydrogenation reaction rate related to the work of Van Trimpont²⁰

The experimental points from the same study were also added to compare with the fitting reaction rate. As we see in Figure II-5, the experimental operation conditions did not explore the very low hydrogen partial pressure regime. Nevertheless, the best-fitted kinetic model reveals an optimum value for P_{H_2} close to 5 bars.

Here a supplementary study is carried out, which was not plotted in the original work of Van Trimpont, in order to help us better understand this maximum value of P_{H_2} in Figure II-5. It involves an analysis of the coverage of relevant surface species, methyl-cyclohexane [MCH·s], methyl-cyclohexadiene [MCHde·s], free active site [s] and the product of [MCHde·s] [s], as a function of the hydrogen partial pressure P_{H_2} , illustrated in Figure II-6. The coverage of surface hydrogen atom [H₂·s] and adsorbed toluene [Tol·s] are neglected in this modelling, as K_5 and K_6 are omitted as explained before. Also [MCHe·s] was neglected in the model. As mentioned in the work of Van Trimpont, the methyl-cyclohexadiene is considered as the most abundant surface

intermediate during the reaction as it is the reactant of the rate limiting step (step (4)). This is well rendered by Figure II-6, provided the hydrogen pressure does not exceed 15 bars.

Moreover, for $P_{\text{Tot}} = 0$ bar as considered here, and starting from equation (ES4), the rate equation can be rewritten as: $r = k_4 [MCHde \cdot s][s]$

From this expression, it is clear that high amounts of both adsorbed MCHde·s and s are required to obtain significant rate values. Comparing figures II-5 and II-6, it turns out that in the framework of this model, the rate is null at zero $P(H_2)$ due to the absence of free sites s, needed for the dehydrogenation reaction, those sites being saturated by MCHde in these conditions. At reverse, at high partial pressure of hydrogen, the fact that the rate tends to zero is due to the vanishing of [MCHde·s], with a predominance of free sites. This is however not explained by a competition of MCHde with adsorbed H_2 in this model, at $[H_2]$ is neglected in any case. This is rather due to thermodynamic aspects, the equilibrium for the formation of MCHde·s being shifted to the left at high partial pressures of H_2 . At intermediate $P(H_2)$ values, the [MCHde·s][s] product exhibits positive values, with a maximum close to 5.2 bars.

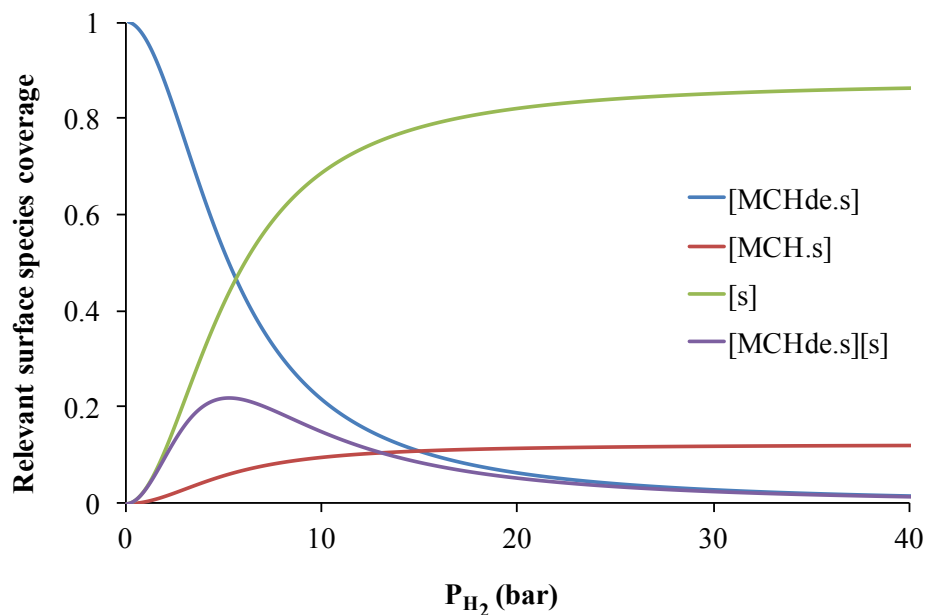


Figure II- 6 Coverage of relevant surface species: methyl-cyclohexadiene (blue line), methyl-cyclohexane (red line), free active sites (green line) and the product of methyl-cyclohexadiene and free active sites (purple line), as a function of hydrogen partial pressure related to the work of Van Trimpont²⁰

However, at this stage, the chemical relevance of the set of hypotheses made to reach this result have to be discussed. Assuming that $[H_2]$ is negligible may not hold true in the high $P(H_2)$ regime, in particular in the absence of any other adsorbed hydrocarbon compound in significant amount. Moreover, considering its high level of unsaturation, assuming that $[Tol\cdot s]$ is negligible too might be a strong assumption. Finally, the hypothesis according to which $[MCHe\cdot s]$ can be neglected needs to be justified.

4. Models of reforming catalysts and related reactivity from DFT calculations

The understanding at the atomic scale (in a range of 0.8-1 nm) of catalytic properties of mono- and bi-metallic nano-aggregates highly-dispersed on γ -alumina is needed for controlling reactivity and selectivity in catalytic reforming. Quantum molecular modeling (ab initio calculations) has become very successful to understand the properties of platinum metallic nano-aggregates supported by gamma-alumina. A growing number of studies is reported on quantum modeling of these metallic systems by applying density function theory (DFT), which have dealt with alkene dehydrogenation and hydrogenolysis mechanisms occurring either on infinite surface of platinum⁶⁴⁻⁶⁷ or Pt clusters.^{46,68} Considerable progresses have been made at IFPEN in this important area of research, which has concerned the description of γ -alumina-supported metallic particles in the catalytic reforming context, from 2002.⁶⁹⁻⁷²

4.1 The γ -alumina support

Digne et al.^{32,73}, using Density Functional Theory, built the first realistic models of γ -Al₂O₃ (110), (100) and (111) surfaces, taking into account of temperature effects on hydroxyl surface coverage. These surface models were derived from the bulk model of Krokidis et al.,⁷⁴ obtained by simulating dehydration process of boehmite into γ -alumina. The selected models are validated for representing the active surface of γ -alumina catalyst because of the correct surface density and vibrational properties of hydroxyl groups as compared with experiments.⁷⁵ The precise nature of the acid surface sites (concentrations and strengths) is also determined. The acid strengths are quantified by simulating the adsorption of relevant probe molecules such as CO and pyridine in correlation with surface electronic properties. The γ -alumina (100) surface with different hydroxyl coverage (0 or 8.8) is shown in Figure II-7.

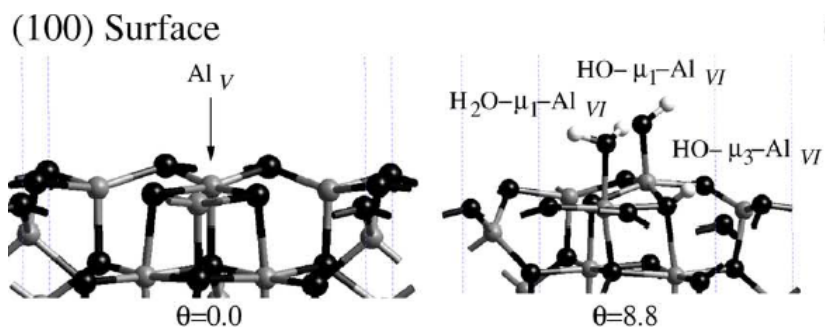


Figure II- 7 Relaxed configurations of γ - $\text{Al}_2\text{O}_3(100)$ surfaces for different hydroxyl coverages (θ in OH nm^{-2}). Al_n stands for aluminum atoms surrounded by n oxygen atoms, and $\text{HO}-\mu_m$ for OH groups linked to m aluminum atoms. Black balls, oxygen atoms. Gray balls, aluminum atoms. White balls, hydrogen atoms. ³²

4.2 The $\text{Pt}_{13}/\gamma\text{-Al}_2\text{O}_3$ model

Relying on the previous DFT surface model of $\gamma\text{-Al}_2\text{O}_3$,^{32,76,77} Hu et al.⁷⁸ investigated the interaction between Pt_{13} clusters with various shapes and dehydrated (100) and hydroxylated (110) $\gamma\text{-Al}_2\text{O}_3$ surfaces, in order to elucidate the nature of metal-support interaction on an atomic scale. They found that despite only 20% of surface orientation is exposed for the (100) surface by alumina platelets, flat lying bi-planar (BP) platinum clusters with strong interaction energies are stabilized on the dehydrated (100) surface, whereas clusters with a three-dimensional morphology are favored by the hydroxyl groups of the (110) surface.

Then, Mager-Maury et al.⁷⁹ provided an atomic-scale model for the $\text{Pt}_{13}/\text{Al}_2\text{O}_3(100)$ system, taking into account operating conditions⁷⁹ (temperature, hydrogen partial pressure). They found that the biplanar structure has a strong affinity towards hydrogen. The increase of hydrogen coverage above 18 H atoms per cluster ($\text{H}/\text{Pt} > 1.4$) induces a reconstruction from a BP to a cuboctahedral (CUB, Figure II-8 (b)) morphology. This reconstruction is driven by the ability of

the CUB structure to adsorb a significant amount of hydrogen with moderate deformation cost. Moreover, in reaction conditions such as catalytic reforming ($T \approx 800\text{K}$ and $P(\text{H}_2) \approx 10$ bar), the particle remains biplanar and retains its metallic character, with moderate H/Pt ratio (0.5-1), which is shown in Figure II-8 (b). Such investigation was later transposed to the $\gamma\text{-Al}_2\text{O}_3$ (110) orientation, and compared with experimental High Resolution XANES (X-Ray Absorption near Edge Structure) assigned by DFT XANES calculations.⁸⁰ It shows that qualitatively, the models proposed are valid, but that the amount of adsorbed H is likely slightly overestimated by DFT calculations in given operating conditions. Note that the multi-metallicity of the clusters was also investigated in the case of the platinum-tin system.^{57,81}

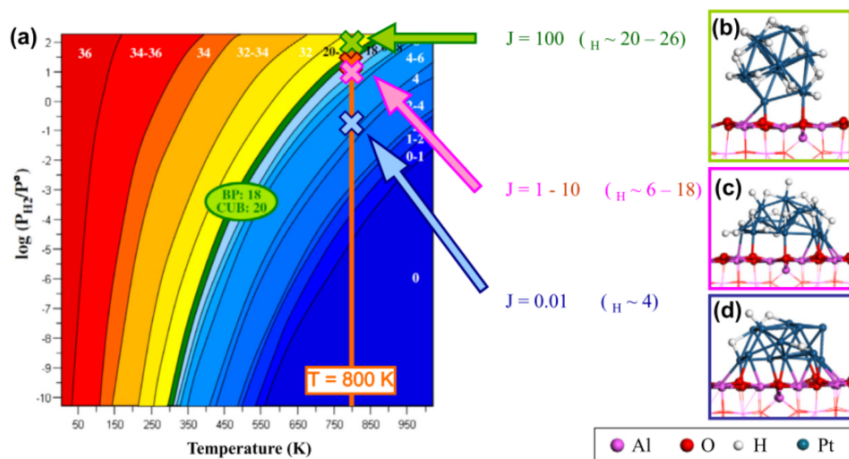


Figure II- 8 (a) Thermodynamic diagram depicting the hydrogen coverage on supported Pt_{13} clusters as a function of $P(\text{H}_2)$. Operating conditions considered for the interaction with hydrocarbons are shown and the stable hydrogenated particles depicted in (b) 20 hydrogen atoms, (c) 18 hydrogen atoms, (d) 4 hydrogen atoms. J stands for the $P(\text{H}_2)/P(\text{C}_2\text{H}_6)$ ratio. The number of H atoms per cluster is reported on each colored region of the diagram.^{79,69}

4.3 Investigation of C-H and C-C bond breaking on the Pt₁₃/ γ -Al₂O₃ model

In Mager-Maury's PhD thesis,⁶⁹ *ab initio* calculations of the thermodynamic profiles for the reaction pathways of dehydrogenation and of hydrogenolysis catalyzed by platinum particles were performed, in order to determine the evolution of the nature of hydrocarbon intermediates C_xH_y (x=1 or 2 and 0 ≤ y ≤ 5), which is formed on activation of ethane (C₂H₆) on supported Pt₁₃ clusters at variable hydrogen coverage θ_H . Symmetric (one H removed on each carbon atom) and dissymmetric (H removed first on the same carbon atom) dehydrogenation reaction paths were compared. The symmetric dehydrogenation (C-H bond scission) of ethane into valuable olefinic intermediates (e.g. ethylene), and dissymmetric dehydrogenation into dormant species (e.g. ethylidyne) were investigated. The impact of the $J = P(\text{H}_2)/P(\text{ethane})$ ratio ($J = 0.01, 1, 10$ and 100) was also studied. Intermediate J values between 1 and 10 correspond to an optimal thermodynamic balance favoring dehydrogenation while avoiding the C–C bond scission leading to coke precursors or surface carbide.

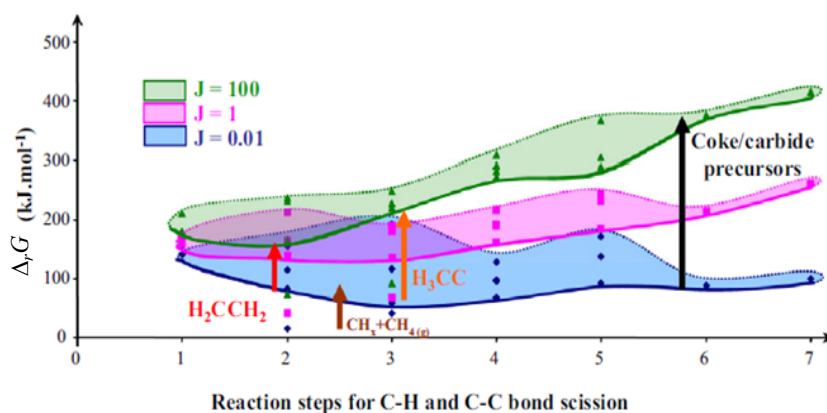


Figure II- 9 $\Delta_r G$ of all intermediates involved in dehydrogenation and/or C–C bond scission steps including hydrogenolysis for $J = 0.01, 1$ and 100 , respectively. Envelopes are drawn following the stability of each carbonaceous species: the blue ($J = 0.01$), pink ($J = 1$), and green ($J = 100$) envelopes encompass the carbonaceous species (except desorbed methane) for the corresponding J . Evolution of

stability of key intermediates are highlighted by the red, brown, orange, and black arrows for ethylene H_2CCH_2 , desorption of methane $\text{CH}_x + \text{CH}_4$ (g), ethylidyne H_3CC and coke/carbide precursors [(CH)(C) and (C)(C)], respectively. The size of arrows is proportional to $\Delta_r G(J = 100) - \Delta_r G(0.01)$, corresponding to the thermodynamic sensitivity of adsorbed species as a function of reaction conditions.⁶⁹

In Figure II-9, the shape and position of the envelope (blue-red-green) varies from large width (blue) to narrow width (green) reveals that the stability of the different intermediates decreases when increasing $P(\text{H}_2)$. For a given reaction step, the selectivity of the system can be thermodynamically switched from the formation of one adsorbed intermediate to another one just by increasing/decreasing the $P(\text{H}_2)$. At low J values, the olefin intermediates (e.g. ethylene) are more thermodynamically favored. From a more general point of view, the hydrogen coverage impacts significantly not only the surface morphology, but also for the choice of reaction pathways. As a consequence, DFT study quantified the interval of process conditions to be used for favoring moderate dehydrogenation of alkanes into olefins. It also gives a rational explanation of the thermodynamic optima in hydrogen pressure for maximizing either dehydrogenation or hydrogenolysis and avoiding coke formation catalyzed by platinum clusters highly dispersed on γ -alumina.

So far, no investigation was ever performed by DFT calculations, regarding the dehydrogenation of methyl-cyclohexane into toluene on supported platinum clusters. Extending the literature search to investigations performed on the Pt(111) surface, it appears that to the best of our knowledge, this reaction was not investigated either. A related reverse reaction, namely the hydrogenation of benzene into cyclohexane, was however the object of several studies, which can be a rich source of information for our own study.

4.4 DFT investigations of the hydrogenation of benzene into cyclohexane on Pt(111)

The catalytic hydrogenation of benzene to cyclohexane is an important relevant reaction to many critical steps in petroleum industry. Nevertheless, the dominant reaction path for benzene hydrogenation is still not clear in the literature. Considering this reaction is very similar to the reverse reaction of the dehydrogenation of methyl-cyclohexane to toluene, it becomes interesting in our case to be inspired by those existing DFT calculations focused on this similar reverse reaction. However, in the literature, most of those calculations have been done on the Pt (111) surface, instead of the Pt/ γ -Al₂O₃ cluster. So in the present work, a parallel study to investigate the dehydrogenation of methyl-cyclohexane to toluene on Pt (111) surface will be required in order to make a closer comparison with Pt cluster.

Saeys et al.^{82,83} used a Pt (111) catalyst modeled by a two-layer Pt₂₂ cluster with 14 atoms in the top layer. By using the Horiuti-Polanyi mechanism⁸⁴ that involves the consecutive addition of hydrogen atoms, the authors proposed a dominant reaction path where the hydrogenation happens in a meta position of methylene group by forming 1,2,3,5-tetrahydrobenzene, 1,3,5-trihydrobenzene and 1,3-dihydrobenzene as reaction intermediates. Cyclohexadiene and cyclohexene are not found to be formed along this proposed dominant pathway.

Morin et al.⁸⁵ used an extended slab model of the Pt (111) surface for their calculation on hydrogenation of benzene to cyclohexene. They found that the reaction path through a meta position as Saeys et al. proposed and the one through the cyclohexadiene and cyclohexene, the two are very competitive. It is found that the 1,3-cyclohexadiene is less stable than 1,3-dihydrobenzene, while cyclohexene is more stable than 1,3,5-trihydrobenzene on the surface. Ma et al.⁸⁶ investigated the dehydrogenation of 1,3-cyclohexadiene to benzene on Pt (111) and they found for the same intermediates configuration with closed adsorption energy as Saeys et al. and

Morin et al. found. Sabbe et al.⁸⁷ employed microkinetic simulation based on periodic DFT calculations for the full network of benzene hydrogenation on Pt (111) at a hydrogen coverage of 0.44 ML at industrial hydrogenation condition ($p_B = 0.1\text{--}0.6$ bar; $p_{H_2} = 0.5\text{--}6$ bar; $T = 400\text{--}500$ K). They found the ortho pathway, via cyclohexene, 1,2,3-trihydrobenzene and 1,3-dihydrobenzene, is identified as dominant path, partially different from what Saeys et al. proposed.

The adsorption energy of the relevant intermediates for these four studies are compared and shown in Table II-4. The results of Sabbe et al. and Morin et al. are very close while Sabbe et al. and Ma et al. presented higher and lower adsorption energy values, respectively.

Table II- 4 Comparison of the adsorption energies obtained by four DFT studies for benzene hydrogenation on Pt (111) or Pt₂₂ cluster.^{82,85,87,86}

Species	ΔE_{ads} (kJ/mol) ^{1,4}			
	Sabbe et al.	Morin et al.	Saeys et al. ²	Ma et al. ³
Benzene	-68(fcc 3 π)	-65(fcc 3 π)	-71(fcc 3 π)	-45(fcc 3 π)
	---	-87(bri 2 π 2 σ)	-102(bri 2 π 2 σ)	-77(bri 2 π 2 σ)
monohydrobenzene	-100	-99	-125	---
1,3-cyclohexadiene	-135	-133	-151	---
1,3-dihydrobenzene	-140	-140	-167	---
1,4-cyclohexadiene	-122	-120	-141	---
1,2,3-trihydrobenzene	-169($\sigma\pi$)	-173($\sigma\pi$)	-210($\sigma\pi$)	---
	-177($\sigma\sigma\sigma$)	-179($\sigma\sigma\sigma$)	---	---
1,2,4-trihydrobenzene	-161	-165	-194	---
1,3,5-trihydrobenzene	-164	-168	-199	---
cyclohexene	-204	-200	-228	---
1,2,3,5-tetrahydrobenzene	-189	-191	-216	---
1,2,4,5-tetrahydrobenzene	-172	---	-180	---
cyclohexyl	-240	---	-257	---
cyclohexane	-295	---	-323	---

¹ all the values are calculated by equation : $\Delta E_{\text{ads}}(\text{BH}_{n,\text{ads}}) = E_{\text{el}}(\text{BH}_{n,\text{ads}}) - E_{\text{el,Benzene,g}} - \frac{n}{2}E_{\text{H}_2,\text{g}} - E_{\text{el,cat}}$

² the energies presented here are recalculated by Sabbe et al. using the same equation in ¹ and the results in ref. ⁸²

³ the energies presented here are also calculated by using the same equation in ¹ and the results in ref. ⁸⁶ for the rest adsorption energy of intermediates cannot be recalculated due to the lack of data.

⁴ Sabbe et al., Morin et al., and Ma et al. used PW91 functional for these calculations; Saeys et al. used BP86.

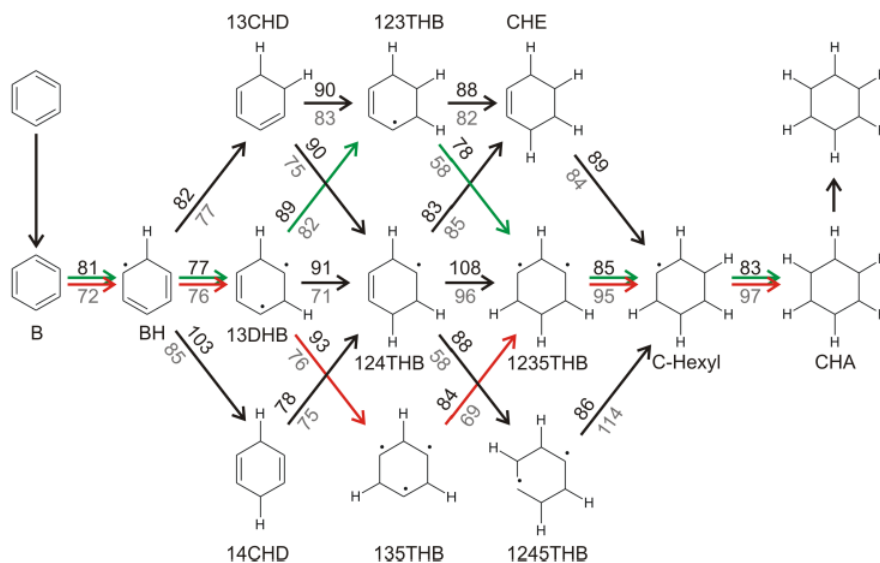


Figure II- 10 Electronic barriers for all the possible reaction steps of the hydrogenation of benzene (kJ/mol), with indication of the minimum energy path found by Sabbe et al. ⁸⁷ (green) and the path identified by Saeys on Pt₂₂ clusters ⁸² (red). Energy barrier for forward reaction (black), for reverse reaction (grey).

Figure II-10 extracted from the publication of Sabbe et al. ⁸⁷ shows the electronic activation energy for all the elementary steps of the reaction network, in forward and reverse

directions. It can be thus derived from this figure the dominant reaction pathway marked in green proposed by Sabbe et al., which does not involve of the methyl-cyclohexene or methyl-cyclohexadiene as intermediates. For this reaction path, the rate-limiting step is the hydrogenation from 1,3-dihydrobenzene to 1,2,3-tetrahydrobenzene with an activation energy of 89 kJ/mol, only 4 kJ/mol lower than the one to 1,3,5-tetrahydrobenzene via red pathway. It is also noted by Sabbe et al. that these barriers (77-108 kJ/mol) are much higher than experimental observation results, which gives an energy range of 50-74 kJ/mol.⁸⁷ Nevertheless, if we look at the reverse path, for the dehydrogenation reaction, the reaction passes through cyclohexene and then 1,2,3- tetrahydrobenzene. After that, there are two possibilities for the following path, either the reaction via the 1,3-cyclohexadiene to monohydrobenzene, or the reaction via 1,3-dihydrobenzene to BH, these two energy barriers have only a difference of 1 kJ/mol.

5. Open questions and strategy of the thesis

So far, the importance of investigating the selectivity and activity of this metallic nano-aggregate under the reforming condition has been emphasized. The lack of knowledge for describing the complex reactions during the catalytic reforming and elucidating the reaction mechanism from thermodynamic and kinetic points of view, encourages us (i) to focus on a model reaction, namely dehydrogenation of methylcyclohexane into toluene, (ii) to use modern quantum chemistry approaches, such as *ab initio* DFT methods for our investigation, in combination with experiments and multi-scale modeling approaches.

By using *ab initio* DFT methods, many questions have been regarding the nature of the model catalyst Pt/ γ -Al₂O₃, which gives a robust basic starting point for our reactivity investigation. Based on these achievements, the dehydrogenation reaction path for some small molecules like ethane adsorbed on the cluster were investigated, by establishing the thermodynamic profile under the condition of the reforming and considering the effect of hydrogen pressure on this reaction. According to these works, a biplanar morphology cluster consisted of 13 platinum atoms and 6 hydrogen atoms is chosen to be the model cluster (Pt₁₃H₆/ γ -Al₂O₃) to undertake our study, this choice will be explained later in this work. Meanwhile, the relevant theoretical studies of benzene hydrogenation over metal slab model surface Pt (111) using *ab initio* DFT methods provided the reaction mechanism regarding the kinetics of the reaction pathway. All this being considered, there is a lack of knowledge about the elementary steps for methyl-cyclohexane dehydrogenation on supported platinum, which is the goal of the present work.

Besides, existing studies now for the kinetics of dehydrogenation reaction are limited to the fitting of experimental results and have not yet used *ab initio* methods to investigate the kinetics of these reaction mechanisms. Further, there still exists a disagreement on the determination of the rate-limiting step by using these modeling fitting approaches. We propose here to build a kinetic model from *ab initio* calculations to give a robust atomistic basis to the model.

However, the dehydrogenation of methyl-cyclohexane to toluene involves numerous possibilities for the reaction network and thus numerous intermediates appear. It is unrealistic to study all of them one by one. To overcome that, our strategy is to focus on some relevant intermediates starting from the C_7H_{12} over $Pt_{13}H_6/\gamma-Al_2O_3$ system. Firstly, we will compare their stability, in order to identify the most stable configurations. All this work and hypothesis in this part aims at providing a final logic and a complete reaction pathway. Then all Gibbs free energy of absorbed intermediates and transition states and the activation energy for the elementary steps along this reaction pathway will be calculated. A similar study has been also consistently adopted on the ideal Pt (111) surface, for the sake of the comparison between these two model systems and in order to deduce the peculiar behaviors of our supported nano-cluster system.

Then, based on these thermodynamic and kinetic *ab initio* results, a kinetic model on the reaction path will be established. The *ab initio* kinetic rate constants will be incorporated into the Langmuir-Hinshelwood (LH) mechanism based kinetic models, relying on the stepwise dehydrogenation mechanistic models. Several LH kinetic models will be compared by assuming different rate-determining steps regarding the corresponding mechanistic model. Several relevant features will be thus defined at this stage: the initial reaction rates and surface species coverage as a function of reaction conditions, particularly hydrogen partial pressures and methyl-cyclohexane

partial pressure; the reaction rates and surface species coverage as a function of methyl-cyclohexane conversion to toluene; the apparent reaction activation enthalpy.

Meanwhile, we will perform experimental catalytic tests of methyl-cyclohexane dehydrogenation on a model catalyst Pt/Al₂O₃ without chlorine to allow us to measure the catalytic activity over a large range of space time and reaction conditions (hydrogen or methyl-cyclohexane partial pressures), as well as activation enthalpies and entropies that can be compared to the *ab initio* kinetic model. The comparison between the modeling results and experimental results will allow us to have a better understanding on the reactivity of this catalyst for the reaction under study, which is the objective of this thesis, and justify some refinements to be brought to the *ab initio* mechanistic investigation.

References

- (1) Leprince, P. 3 *Procédés de Transformation. Chap.4 Reformage Catalytique*, 105-169; Technip, 1998.
- (2) Gjervan, T.; Prestvik, R.; Holmen A. *Basic Principles in Applied Catalysis. Catalytic Reforming*, 125-158; Springer, 2004.
- (3) Davis, B. H. *Catal. Today* **1999**, *53*, 443–516.
- (4) Sinfelt, J. H. *Bifunctional Catalysis, in Advances in Chemical Engineering*; Academic Press, 1964.
- (5) Myers, C. G.; Lang, W. H.; Weisz, P. B. *Ind. Eng. Chem. Res.* **1961**, *53*, 299–302.
- (6) Rahimpour, M. R.; Jafari, M.; Iranshahi, D. *Appl. Energy* **2013**, *109*, 79–93.
- (7) Srinivasan, R.; Davis, B. H. *Platinum Metals Rev.* **1991**, *36*, 151–163.
- (8) Orchin, M.; Reggel, L.; Friedel, R. A. *J. Am. Chem. Soc.* **1948**, *71*, 2743–2746.
- (9) Steiner, A. H. *Catalysis*, *4*, 529; P.H. Emmett, Ed., 1957.
- (10) Hanch, C. *Chem. Revs* **1953**, *53*, 353–396.
- (11) Eley, D. D.; Twigh, G. H.; Frank, F. C.; Schultze, G. R.; Steiner, H.; Salomon, G.; Hoog, H.; Waterman, H. I. *Trans. Faraday Soc.* **1939**, *35*, 1006–1012.
- (12) Bournonville, J. P.; Franck, J. P. *Hydrogen and catalytic reforming In : Hydrogen effect in catalysis*, 653-677; Marcel Dekker, Inc., 1987.
- (13) Sinfelt, H. J.; Hurwitz, H.; Shulman, R. A. *J. Phys. Chem.* **1960**, *64*, 1559–1562.
- (14) Bond, G. C.; Cunningham, R. H. *J. Catal.* **1997**, *166*, 172–185.
- (15) Sinfelt, J. H. *Advances in Catal.* **1973**, *23*, 91–119.
- (16) Sinfelt, J. H. in: G. Ertl, E. Knözinger, J. Weitkamp (Eds.), *Handbook of Heterogeneous Catalysis*, Wiley, Weinheim, 1997, 1939–1955.
- (17) Franck, J. P. in Imelik, B.; Martin, G. A.; Renouprez, A. J. *Fundamental and Industrial Aspects of Catalysis by Metals*, 412; CNRS, 1984.
- (18) Bond, G. C. *Catal. Today* **1999**, *49*, 41–48.
- (19) Van Trimpont, P. A. Mari, G. B. Froment, G. F. *Appl. Catal.* **1985**, *17*, 161–173.
- (20) Van Trimpont, P. A.; Marin, G. B.; Froment, G. F. *Ind. Eng. Chem. Fundam.* **1986**, *25*, 544–553.
- (21) Van Trimpont, P. A.; Marin, G. B.; Froment, G. F. *Ind. Eng. Chem. Res.* **1988**, *27*, 51–57.
- (22) Alhumaidan, F.; Cresswell, D.; Garforth, A. *Ind. Eng. Chem. Res.* **2011**, *50*, 2509–2522.
- (23) Usman, M.; Cresswell, D.; Garforth, A. *Ind. Eng. Chem. Res.* **2012**, *51*, 158–170.
- (24) Carter, J. L.; Mcvicker, G. B.; Wissman, W.; Kmak, W. S.; Sinfelt, J. H. *Appl. Catal.* **1982**, *3*, 327–346.
- (25) Jothimurugesan, K.; Nayak, A. K.; Mehta, G. K.; Rai, K. N.; Bhatia, S.; Srivastava, R. D. *AIChE J.* **1985**, *31*, 1997–2007.
- (26) Fung, A. S.; Kelley, M. J.; Koningsberger, D. C.; Gates, B. C. *J. Am. Chem. Soc.* **1997**, *119*, 5877–5887.
- (27) Jahel, A.; Avenier, P.; Lacombe, S.; Olivier-Fourcade, J.; Jumas, J. C. *J. Catal.* **2010**, *272*, 275–286.
- (28) Macleod, N.; Fryer, J. R.; Stirling, D.; Webb, G. *Catal. Today* **1998**, *46*, 37–54.
- (29) Muller, A. C. *J. Catal.* **1979**, *72*, 65–72.
- (30) Burch, R.; Garla, L. *J. Catal.* **1981**, *71*, 360–372.
- (31) Siri, G. J.; Bertolini, G. R.; Casella, M. L.; Ferretti, O. A. *Mater. Lett.* **2005**, *59*, 2319–2324.

- (32) Digne, M. *J. Catal.* **2004**, *226*, 54–68.
- (33) Zhu, H. Y.; Gao, X. P.; Song, D. Y.; Ringer, P. R.; Frost, L. *Micro. Meso. Mat.* **2005**, *85*, 226–233.
- (34) Kuang, D. B.; Fang, Y. P.; Liu, H. Q.; Frommen, C.; Fenske, D. *J. Mater. Chem.* **2003**, *13*, 660–662.
- (35) Kaya, C.; He, J. Y.; Gu, X.; Butler, E. G. *Micro. Meso. Mater.* **2002**, *54*, 37–49.
- (36) Beaufils, J. P.; Barbaux, Y. *J. Chim. Phys.* **1981**, *78*, 347–352.
- (37) Nortier, P., Fourre, P., Mohammed Saad, A. B., Saur, O., and Lavalley. *J. C., Appl. Catal* **1990**, *61*, 141–160.
- (38) Boitiaux, J. P.; Devés, J. M.; Didillon, B.; Marcilly, C. R. *Catalytic Reforming of Naphtha. Catalyst Preparation*; Marcel Dekker, Inc., 1995.
- (39) Peri, J. B. *J. Phys. Chem. B* **1965**, *69*, 220–230.
- (40) Gates, B. C.; Katzer, J. R.; Schuit, G. *Chemistry of catalytic processes*; McGraw-Hill Book Company, 1978.
- (41) Figoli, N. S.; Sad, M. R.; Beltramini, J. N.; Jabioski, E. L.; Parera, J. M. *Ind. Eng. Chem. Prod. Res. Dev* **1980**, *19*, 545–551.
- (42) Berdala, J.; Freund, E. *J. Phys. Colloques* **1986**, *47*, 269–272.
- (43) Lynch, J. *Oil Gas Sci. Technol. – Rev. IFP* **2002**, *57*, 281–305.
- (44) Mager-Maury, C.; Chizallet, C.; Sautet, P.; Raybaud, P. *ACS Catal.* **2012**, *2*, 1346–1357.
- (45) Jossens, L.; Petersen E. E. *J. Catal.* **1982**, *73*, 377–386.
- (46) Vajda, S.; Pellin, M. J.; Greeley, J. P.; Marshall, C. L.; Curtiss, L. A.; Ballentine, G. A.; Elam, J. W.; Catillon-Mucherie, S.; Redfern, P. C.; Mehmood, F.; Zapol, P. *Nature Mater.* **2009**, *8*, 213–216.
- (47) Ritchie, A. W.; Nixon, A. C. *Ind. Eng. Chem. Prod. Res. Dev* **1966**, *5*, 59.
- (48) Burch, H. I.; Petersen, E. E. *J. Catal.* **1982**, *77*, 43–52.
- (49) Coq, B.; Figueras, F. *J. Catal.* **1984**, *85*, 197–205.
- (50) Li, Y. X.; Klaubunde, K. J. *J. Catal.* **1991**, *126*, 173–186.
- (51) Paál, Z.; Gyory, A.; Uszkurat, I.; Olivier, S.; Gurin, M.; Kappenstein, C. *J. Catal.* **1997**, *168*, 164–175.
- (52) Sexton, B. A.; Hughes, A. E.; Foger, K. *J. Catal.* **1984**, *88*, 466–477.
- (53) Parera, J. M.; Beltramini, J. N.; Querini, C. A.; Martinelli, E. E.; Churin, E. J.; Aloe, P. E.; Figoli, N. S. *J. Catal.* **1986**, *99*, 39–52.
- (54) Xu, C.; Tsai, Y. L.; Koel, B. E. *J. Phys. Chem. B* **1994**, *98*, 585–593.
- (55) Siri, G. J.; Ramallo-López, J. M.; Casella, M. L.; Fierro, J. L.; Requejo, F. G.; Ferretti, O. A. *Appl. Catal. A* **2005**, *278*, 239–249.
- (56) Dautzenberg, F. M.; Helle, J. N.; Bileon, P.; Sachtler, W. *J. Catal.* **1980**, *63*, 112–118.
- (57) Jahel, A. N.; Moizan-Baslé, V.; Chizallet, C.; Raybaud, P.; Olivier-Fourcade, J.; Jumas, J. C.; Avenier, P.; Lacombe, S. *J. Phys. Chem. C* **2012**, *116*, 10073–10083.
- (58) Ma, A. *Z. Sci Sin Chim* **2014**, *44*, 25.
- (59) Touzani, A.; Klvana, D.; Belanger, G. *Stud. Surf. Sci. Catal.* **1984**, *19*, 357–364.
- (60) Verstraete, J. Thesis : Kinetische Studie van de Katalytische Reforming van Nafta over een Pt-Sn/Al₂O₃ Katalysator, Universiteit Gent, 1997.
- (61) Langmuir I. *J. Am. Chem. Soc.* **1919**, *38*, 1145–1156.
- (62) Hinshelwood, C. N. *The Kinetics of Chemical Change*; Clarendon, 1940.
- (63) Hougen, O. A.; Watson, K. M. *Chemical Process Principles, Vol. III*; Wiley, 1943.
- (64) Zhao, Z. J.; Moskaleva, L. V.; Aleksandrov, H. A.; Basaran, D.; Rösch, N. *J. Phys. Chem. C* **2010**, *114*, 12190–12201.

- (65) Aleksandrov, H. A.; Moskaleva, L. V.; Zhao, Z. J.; Basaran, D.; Chen, Z. X.; Mei, D. H.; Rösch, N. *J. Catal.* **2012**, *285*, 187–195.
- (66) Kua, J.; Goddard, W. A. *J. Phys. Chem. B* **1998**, *102*, 9492–9500.
- (67) Watwe, R. M.; Ramchandra, M.; Cortright, R. D.; Nørsko, J. K.; Dumesic, J. A. *J. Phys. Chem. B* **2000**, *104*, 2299–2310.
- (68) Watwe, R. M.; Spiewak, B. E.; Cortright, R. D.; Dumesic, J. A. *J. Catal.* **1998**, *180*, 184–193.
- (69) Raybaud, P.; Chizallet, C.; Mager-Maury, C.; Digne, M.; Toulhoat, H.; Sautet, P. *J. Catal.* **2013**, *308*, 328–340.
- (70) Chizallet, C.; Raybaud, P. *Catal. Sci. Technol.* **2014**, *4*, 2797–2813.
- (71) Avenier, P.; Bazer-Bachi, D.; Bazer-Bachi, F.; Chizallet, C.; Deleau, F.; Diehl, F.; Gornay, J.; Lemaire, É.; Moizan-Basle, V.; Plais, C.; Raybaud, P.; Richard, F.; Lacombe, S. *Oil Gas Sci. Technol. - Rev. IFPEN* **2016**, *71*, 41–59.
- (72) Chizallet, C. *L'Act. Chim.* **2017**, *417*, 34–39.
- (73) Digne, M.; Sautet, P.; Raybaud, P.; Euzen, P.; Toulhoat, H. *J. Catal.* **2002**, *211*, 1–5.
- (74) Krokidis, X.; Raybaud, P.; Gobichon, A. E.; Rebours, B.; Euzen, P.; Toulhoat, H. *J. Phys. Chem. B* **2001**, *105*, 5121–5130.
- (75) Lagauche, M.; Larmier, K.; Jolimaitre, E.; Barthelet, K.; Chizallet, C.; Favergeon, L.; Pijolat, M. *J. Phys. Chem. C* **2017**, *121*, 16770–16782.
- (76) Digne, M.; Raybaud, P.; Sautet, P.; Guillaume, D.; Toulhoat, H. *J. Am. Chem. Soc.* **2008**, *130*, 11030–11039.
- (77) Digne, M.; Sautet, P.; Raybaud, P.; Euzen, P.; Toulhoat, H. *J. Catal.* **2002**, *211*, 1–5.
- (78) Hu, C. H.; Chizallet, C.; Mager-Maury, C.; Corral-Valero, M.; Sautet, P.; Toulhoat, H.; Raybaud, P. *J. Catal.* **2010**, *274*, 99–110.
- (79) Mager-Maury, C.; Bonnard, G.; Chizallet, C.; Sautet, P.; Raybaud, P. *ChemCatChem* **2011**, *3*, 200–207.
- (80) Gorczyca, A.; Moizan, V.; Chizallet, C.; Proux, O.; Del Net, W.; Lahera, E.; Hazemann, J. L.; Raybaud, P.; Joly, Y. *Angew. Chem. Int. Ed.* **2014**, *53*, 12426–12429.
- (81) Gorczyca, A. Thesis : Caractérisation de catalyseurs métalliques supportés par spectroscopie XANES, apports du calcul quantique dans l'interprétation des spectres expérimentaux. research thesis, Université Joseph Fournier de Grenoble & IFPEN, 2014.
- (82) Saeys, M.; Reyniers, M.; Thybaut, J.; Neurock, M.; Marin, G. B. *J. Phys. Chem. B* **2005**, *109*, 2064–2073.
- (83) Saeys, M.; Reyniers, M.; Thybaut, J.; Neurock, M.; Marin, G. B. *J. Catal.* **2005**, *236*, 129–138.
- (84) Horiuti, I.; Polanyi, M. *Trans. Faraday Soc.* **1934**, *30*, 1164–1172.
- (85) Morin, C.; Simon, D.; Sautet, P. *Surf. Sci.* **2006**, *600*, 1339–1350.
- (86) Ma, H. Y.; Wang, G. C. *J. Catal.* **2011**, *281*, 63–75.
- (87) Sabbe, M. K.; Canduela-Rodriguez, G.; Reyniers, M. F.; Marin, G. B. *J. Catal.* **2015**, *330*, 406–422.

CHAPTER III – COMPUTATIONAL AND EXPERIMENTAL METHODOLOGY

This chapter aims at introducing all the methods that we used during *ab initio* calculations and the catalytic experiments. We start by a brief introduction of the method we used for all the calculation in this thesis (periodic density functional theory (DFT)). Then, we present different hypothesis and parameters chosen for DFT calculations and the code employed. In addition, we explain how we can achieve the calculation of thermodynamic calculations and also a benchmarking test for the vibrational frequency calculations. In the second part, regarding catalytic experiments on dehydrogenation of methyl-cyclohexane into toluene, we focus on presenting the experimental set-up and protocol, followed by the reaction conditions employed in the catalytic tests and then the method of post-treatment of the experimental results.

1. *Ab initio* molecular modeling

We aim at solving the Schrödinger equation. The basic assumptions employed are presented Appendix-III. In the following, we focus on the method chosen here, namely Density Functional Theory.

1.1 Density functional theory (DFT)

The methods based on the density functional theory (DFT) are very convenient and efficient for quantum calculations of large chemical systems, as a very good compromise between the calculation time and the required accuracy.

This part will concentrate on how density functional theory (DFT) of ab initio method can help to solve the Schrödinger equation¹ by working with the electron density of the system as the basic variable. In the case of DFT, we do not work on possible forms of the wave function, like in the Hartree-Fock method,² using Slater determinant³ to build the wave function. DFT is about to use an approximation on the Hamiltonian part.

1.1.1 The Hohenberg-Kohn theorems

The density functional theory is mainly based on two theorems established by Hohenberg et Kohn⁴. The first theorem states that for an N -electrons system, the external potential $v(\mathbf{r})$ that defines the whole nuclear frame for a molecule completely fixes the Hamiltonian; thus N and $v(\mathbf{r})$ determine all properties for the ground state (Non-degenerate ground states). And this external potential $v(\mathbf{r})$ is determined by the electron density $\rho(\mathbf{r})$ and we have $\rho(\mathbf{r})$ expressed by:

$$\rho(\mathbf{r}) = N \int \dots \int |\Psi(r, r_2, \dots, r_N)|^2 dr_2 \dots dr_N \quad \text{Equation (III-1)}$$

Since ρ determines the number of electrons, it follows that $\rho(\mathbf{r})$ also determines the ground-state electronic wave function Ψ and all other electronic properties of the system. Then we have:

$$E[\rho] = V_{ne}[\rho] + T_e[\rho] + V_{ee}[\rho] = \int \rho(r)v(r)dr + F_{HK}[\rho] \quad \text{Equation (III-2)}$$

Where $T_e[\rho]$ is the kinetic energy of the electrons, $V_{ne}[\rho]$ the nuclei-electron attraction and $V_{ee}[\rho]$ the electron-electron repulsion and $v(r)$ the external potential. The Hohenberg-Kohn functional $F_{HK}[\rho]$ is a universal functional of ρ , i.e. system independent, as it does not depend on the nuclei coordinates or the nuclear charges,

$$F_{HK}[\rho] = T_e[\rho] + V_{ee}[\rho] \quad \text{Equation (III-3)}$$

We may write

$$V_{ee}[\rho] = J[\rho] + \text{exchange-correlation energy} \quad \text{Equation (III-4)}$$

Where $J[\rho]$ is the classical repulsion. The second term (non-classical term) is a very elusive, very important quantity; it is the major part of the “exchange-correlation energy”. However, there exists no exact form of $F_{HK}[\rho]$ and one has to use approximations.

The second Hohenberg-Kohn theorem provides the energy variational principle.⁵ According to the variation principle the energy of an assumed trial density ρ_{trial} is always a higher value than the exact ground state energy E_0 that can only be obtained if the exact ground state density is inserted in Equation (III-5).

$$E_0 \leq E[\rho_{trial}] = F_{HK}[\rho_{trial}] + V_{ee}[\rho_{trial}] \quad \text{Equation (III-5)}$$

It means that it's possible to use the variational principle to determine the energy of a molecular structure.

1.1.2 The Kohn-Sham equations

The idea developed by Kohn and Sham⁶ consists of considering a *fictitious* system formed by an uniform non-interacting electron gas and having the same electron density as the real gas. The exact wave function of this *fictitious* system can be described by a Slater determinant and Kohn and Sham proposed to express the density $\rho(r)$ by the following equation:

$$\rho(r) = \sum_{i=1}^{N_{elec}} |\varphi_i(r)|^2 \quad \text{Equation (III-6)}$$

Where φ_i stands for the space part of the spin-orbital χ_i .

From this approach, Kohn and Sham proved that the electronic energy, E , from the ground state of a *real* system can be expressed by this equation:

$$E[\rho(r)] = \sum_{i=1}^{N_{elec}} \int \varphi_i(r) \left(-\frac{\nabla^2}{2}\right) \varphi_i(r) dr + \frac{1}{2} \iint \frac{\rho(r_1)\rho(r_2)}{|r_1 - r_2|} dr_1 dr_2 - \sum_{I=1}^{N_{nuclei}} \int \frac{Z_I}{|R_I - r|} \rho(r) dr + E_{XC}[\rho(r)] \quad \text{Equation (III-7)}$$

Where r_1 and r_2 represent the coordinates of two interacting electrons. In equation (III-7), the first term on right represent the kinetic energy of the electrons in the *fictitious* system. The second term relates to the Coulombian energy of the repulsion between a pair of electrons. The third term stands for the energy due to the nucleus-electrons attractions. $E_{XC}[\rho(r)]$ is called the exchange-correlation energy and collects all the non-classic electronic interactions, which contains:

$$E_{XC}[\rho(r)] = [T(\rho) - T_s(\rho)] + [E_{ee} - J(\rho)] \quad \text{Equation (III-8)}$$

Where $T(\rho)$ is the exact kinetic energy of the real system, $T_s(\rho)$ is the kinetic energy of the fictitious system. E_{ee} is the total energy related to the electronic repulsions and $J(\rho)$ represents the classical Colombian energy of the electron-electron repulsion.

If we apply the variational principle to the functions φ_i (spin-orbitals space part), we will have the Kohn-Sham equation that is similar to the principal Hartree-Fock equations:

$$\left[-\frac{\nabla_1^2}{2} + \int \frac{\rho(r_2)}{|r_1 - r_2|} dr_2 - \sum_{I=1}^{N_{\text{noyaux}}} \frac{Z_I}{|R_I - r_1|} + V_{XC}(r_1) \right] \varphi_i(r_1) = \varepsilon_i \varphi_i \quad \text{Equation (III-9)}$$

V_{XC} is called the exchange-correlation potential functional and defined by:

$$V_{XC} = \frac{\delta E_{XC}[\rho(r)]}{\delta \rho(r)} \quad \text{Equation (III-10)}$$

The Kohn-Sham equations are resolved by using an approach of the self-consistent field (SCF). The test function is used in the Equation (III-10) from which a new orbitals function is obtained and then re-used again in the Kohn-Sham equations. This iterative process is done till an energy convergence is reached. The new φ_i orbitals are used to build a Slater determinant. They are developed over a basis sets where the coefficients are obtained by a similar way to Hartree-Fock theory.² The density functional theory (DFT) method is an exact theory, but the functional allowing to obtain E_{XC} is unknown. The DFT methods varies thus by the chosen approximations to get an acceptable estimation of E_{XC} .

1.1.3 Exchange-correlation functionals

Several types of exchange-correlation functional (E_{XC}) have been proposed in the literature.^{7,8} There are three main families of functionals.

The first one is called *local-density approximation* (LDA). It applies the uniform-electron-gas results to infinitesimal portions of the non-uniform-electron distribution for the system of an atom or molecule or solid. The LDA is applicable to systems with slowly-varying densities but cannot be formally justified for highly inhomogeneous systems such as atoms and molecules. Thus a second functional generation was developed and based principally on the idea to take into account not only the electronic density $\rho(r)$, but also the gradient $\Delta\rho(r)$, which is called the *generalized gradient approximation* (GGA). Finally, the third functional generation is the hybrid functionals.

- *Local-density approximation (LDA)*

Here we introduce the equation for LDA,

$$E_{XC}^{LDA}(\rho) = \int \rho(r) \varepsilon_{xc}(\rho) dr \quad \text{Equation (III-11)}$$

If the electron density for the electrons with different spins, i.e. α -spin and β -spin is not identical, the LDA approach is replaced by the *Local spin density approximation* (LSDA). In this case, the total electron density can be written as the sum of the electron densities with α -spin (ρ_α) and β -spin (ρ_β):

$$E_{XC}^{LSDA}(\rho) = \int \rho(r) \varepsilon_{xc}(\rho_\alpha, \rho_\beta) dr \quad \text{Equation (III-12)}$$

However, the LDA and LSDA are identical for closed-shell systems. Although the exchange-correlation functional of the LSDA is based on a strong approximation, it is of major importance for DFT, since it is the only functional where the form of the exchange-correlation energy is exactly known. Unfortunately, due to the rapidly varying electron densities in molecules, the LSDA approach cannot be employed for many chemical problems like for thermochemical data, electron correlation is overestimated and electron exchange is underestimated. That is why LSDA overestimates bonding energies. Somehow, often with the compensations of errors, LDA, LSDA can still offer an average performance which is accurate enough for some calculations.

- Generalized gradient approximation (GGA)

A way to improve on the LDA or LSDA is to allow the exchange-correlation energy per particle to depend not only the density at the point \mathbf{r} , but also on the density gradients. Then we have:

$$E_{XC}^{GGA}(\rho) = \int \rho(r) \varepsilon_{xc}(\rho_\alpha, \rho_\beta, \nabla \rho_\alpha, \nabla \rho_\beta) dr \quad \text{Equation (III-13)}$$

A large diversity of GGA functionals have been developed. In this thesis, we use the exchange-correlation functional GGA-PBE, developed by Perdew, Burke and Ernzerhof in 1996 for our calculations.^{9,10}

However, all GGA functionals lack in describing long-range electronic correlation effects, responsible for Van der Waals forces (in particular dispersion), playing an important role for

many chemical problems (e.g. orientation of molecules on surfaces). Therefore, finding DFT functionals including dispersion forces have become an active field of research over the last years.

However, in GGA functionals, the van der Waals (vdW) dispersion forces is not properly accounted for, which will cause a significant impact when doing the calculations of molecular adsorption on surface. These vdW dispersion forces, however can be integrated into the classic PBE functional according to several ways. One of them is called Opt-PBE,¹¹ a non-local functional that incorporate a non-local description of the correlation functional, such as vdW-DF method.¹² Another approach consists in adding a correction term to the GGA one, this is for example done in the PBE-dDsC functional.^{13,14} This functional adds a vdW term E_{disp} in the GGA functional, by using the atom pair correction parameters to calculate the vdW interactions.

$$E_{DFT-D} = E_{KS-DFT} + E_{disp} \quad \text{Equation (III-14)}$$

The dispersion term depends on dispersion coefficients (calculated from atomic ionization potentials and static dipole polarizabilities), the distance between atomic pairs and the sum of atomic van der Waals radii. In PBE-dDsC, the atom pair specific parameters (dispersion coefficients and short range damping strength) are determined from the electron density.

In this work, we applied both the functional PBE as implemented in VASP 5.3.5 and the PBE-dDsC functional as implemented in VASP 5.4.1.¹⁵ A comparison between the results of these two methods and will be presented in Chapter IV, *section 5*.

1.2 Molecular modeling

This part of methodology is inspired by ref.^{16,1,17–20}.

1.2.1 Plane waves and periodic boundary conditions

A crystal consists in three-dimensional periodic array of atoms. The three-dimensional integration scheme allows for great freedom in choosing a suitable basis for representing the KS orbitals. We will thus perform periodic boundary calculations. It is necessary to have a basis set which is capable of reasonably spanning the orbital function space when cut to the minimum. The basis set allows to a fast-converging series when more and more functions are allowed.¹⁶

A suitable approach for periodic calculations is the expansion of the basis set by plane waves. Since the crystal is a periodic entity and via the Bloch Theorem²¹ which is the general solution for the stationary Schrödinger equation for a periodic potential $V(r+L)=V(r)$ the eigenfunction can be written in the form:

$$\psi_i(r) = e^{ikr} u_{ik}(r) \quad \text{Equation (III-16)}$$

where $u_{ik}(r)$ is a periodic function that has the period of the crystal lattice with $u_{ik}(r)=u_{ik}(r+\vec{R})$ and \vec{R} is a translational vector of the lattice. The Bloch theorem changes the problem of computing an infinite number of electronic wave functions to calculate a finite number of wave functions at an infinite number of k -points in the first Brillouin zone (to each k -vector a k -point in the reciprocal lattice is attributed starting from the Γ -point, which is the origin of the reciprocal lattice²²). The Born-von-Karman approximation says that a wave function must be periodic if a super cell is build up by a primitive cell.

$$\psi(r + N_i R_i) = \psi(r) \quad \text{Equation (III-17)}$$

N_i being an integer and R_i are primitive vectors of the lattice. Combining both theorems allows to write the wave functions as a sum of plane waves :

$$\psi_{n,k}(r) = c_1 e^{iG_1 r} + c_2 e^{iG_2 r} + c_3 e^{iG_3 r} + \dots = \sum_G c_G e^{i(k+G)r} \quad \text{Equation (III-18)}$$

where G is a reciprocal lattice vector, C_G are the coefficients, \mathbf{k} is a vector in the reciprocal lattice and \mathbf{r} is a position vector. In principle there is an infinite number of plane waves but in practice only those reciprocal lattice vectors are kept in the expansion that fulfill the following condition :

$$\frac{|k + G|^2}{2} < E_{cut} \quad \text{Equation (III-19)}$$

while the remaining coefficients are set to zero. Hence, the cut-off energy, E_{cut} determines the energy and the number of plane waves that are kept in the expansion. From this, it is obvious that the higher the cut-off energy, the more plane waves are included in the expansion and thus the better the description of the electronic system. However, a higher number of plane waves is computationally more expensive.

1.2.2 Pseudo-potentials and PAW method

The fact that core electrons have a low kinetic energy, i.e. a short wave length, means that they have to be treated with a higher spatial resolution. Pseudo-potentials²³ serve to replace the atomic all-electron potential in such a way, that the electronic core states are no longer treated

explicitly. They are treated as frozen cores. In quantum mechanics, all wave functions describing electronic states need to be orthogonal to each other. Hence, the valence electron wave function has to be orthogonal to the core electron wave function which is difficult to describe numerically, due to the high oscillation of the wave function near the core. Thus, it is more justifiable to replace the real wave function by an ionic component describing the cores by a nodeless, smoother wave function (frozen core approximation) which describe the electrons properties in the bonding region and nearly zero probability for the valence electrons in the core region (i.e. no oscillation of the wave function, see Figure III-1). Hence, the wave function of the pseudo-potentials has the same scattering properties of the all electron wave function outside the scattering region (defined by a cut-off radius r_c) and a smoother behavior inside the core region.

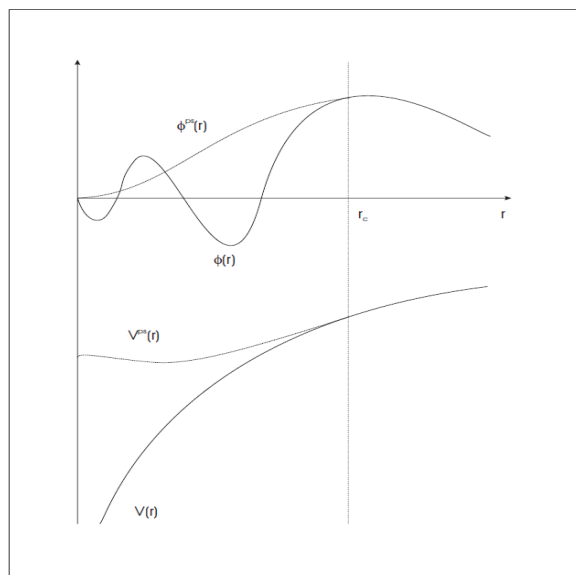


Figure III- 1 diagram illustrating the replacement of an all-electrons wave function $\phi(r)$ (with oscillation near the core) and a core potential $V(r)$ by a pseudo-wave function $\phi^{PS}(r)$ (no oscillation near the core) and a pseudo-potential $V^{PS}(r)$, r_c , the cut-off radius ²⁴

The method used for this approach is called pseudo-potentials of the projector augmented wave (PAW)²⁵ method. The main idea is to replace the real valence electron wave function φ_V^{AE} into three terms:

$$\varphi_V^{AE} = \varphi_V^{PS} - \sum_i c_i \psi_i^{PS} + \sum_i c_i \psi_i^{AE} \quad \text{Equation (III-20)}$$

where φ_V^{PS} is a valence electron pseudo-wave function which reproduces the behavior of the all electron wave function (in the augmentation region) expected in the core region, ψ_i^{AE} is exact in the augmentation region (incorporating the node structure of the exact wave function) and smoothly decays to zero in the outside and a net part ψ_i^{PS} which is also smooth. The latter two are local functions defined in the augmentation spheres where i comprises the quantum numbers n , l and m .

1.2.3 Geometry optimization

Once the electronic energy of the fundamental state is calculated at the desired level, geometry relaxation can be performed, aiming at minimizing forces on each atom. All residual forces applied on the cores are calculated by the Hellman-Feynman theorem.^{26,27} Then, a conjugate gradient algorithm is performed until the convergence criterion is fulfilled.

The force due to the movement of the atom A in the direction of α is conventionally the derivative of energy compared to this movement¹⁹ :

$$F_{A,\alpha} = -\frac{\partial E}{\partial \alpha_A} \quad \text{Equation (III-21)}$$

Where $\partial\alpha$ represents an infinitesimal movement. It is calculated with the Hellmann-Feynman theorem which stand for the derivative of a steady state energy with respect to a parameter P, equal to the mean value of the partial derivative of the Hamiltonian on this steady state. So we have here:

$$F_{A,\alpha} = -\frac{\partial E}{\partial \alpha_A} = -\left\langle \psi(\vec{r}_i, \vec{R}_I) \left| \frac{\partial H}{\partial \alpha_A} \right| \psi(\vec{r}_i, \vec{R}_I) \right\rangle \quad \text{Equation (III-22)}$$

The step to move the atoms on function of forces in order to minimize the energy has been done in the present work by two different methods. The Quasi-Newton algorithm²⁸ proposes a geometric convergence depending only on forces acting in the system. With the conjugate gradient algorithm,²⁹ the convergence is provided both by the electron energy and the forces. The first method is used in my thesis when doing the geometry optimization for the transition state, aiming to obtain a better description of minimum energy, while the second one used generally for all the discussed optimized structures of local minima such as intermediates.

In the present work, all calculations were performed using the ab initio plane-wave pseudopotential method as implemented in VASP Package (5.3.5 and 5.4.1).^{30,31} The PBE^{9,10} and PBE-dDsC^{13,14} functionals were applied. The projected augmented wave (PAW) method^{25,32} was used to describe the core-electron interactions and the electron wave functions are developed on a set of plane waves with a cut-off energy of 400 eV. The electronic convergence criterion is 10^{-6} eV and the convergence criterion on forces for nuclei is 0.01 eV/Å for geometry optimizations. The Pt₁₃/γ-Al₂O₃ (100) (Figure III-2) system considered in the present study consists of a

tri-periodic cell, the size of which is $16.7 \times 16.8 \times 25.8 \text{ \AA}^3$, occupied by 7.2 \AA thick γ -alumina slabs (normal to the z axis) separated by a 18.6 \AA vacuum layer. During geometry optimization, only the two uppermost alumina layers, the platinum cluster and the adsorbed molecule were allowed to relax. The properties of free gas phase molecules were calculated thanks to $25 \times 25 \times 25 \text{ \AA}^3$ cells for all C_7 molecules, and a $20 \times 20 \times 20 \text{ \AA}^3$ cell for H_2 in order to provide a enough large cell to prevent lateral interactions. The calculations was performed on a $1 \times 1 \times 1$ k-point grid. For the Pt(111) system, the surface was modeled by periodic five-layer slabs and (3×3) (1/9 ML) super cell, only the three uppermost platinum layers were allowed to relax along with the adsorbed molecule. The nearest distance of the Pt atoms was 2.82 \AA on Pt(111) and the height of the super cell is 29.2 \AA . The calculations was performed on a $5 \times 5 \times 1$ k-point grid. The cut-off energy, electronic and forces convergence criterions are the same as for the calculations of cluster system.

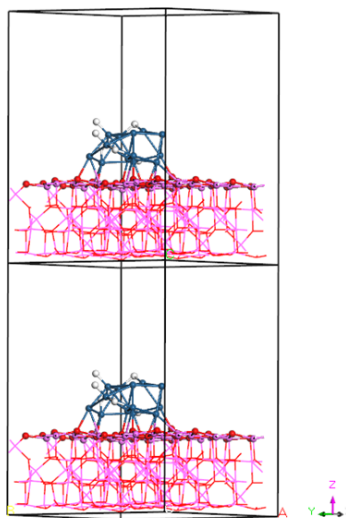


Figure III- 2 The periodic $Pt_{13}/\gamma-Al_2O_3$ (100) system considered in present work

1.2.4 *Ab initio* Molecular Dynamics

Ab initio molecular dynamics allows to simulate the atoms' evolution of a system over time. This method varies from the conjugate gradient method for the evolution of atom positions that molecular dynamic doesn't look for minimizing the system energy from a certain geometry, but to leave it evolve under the influence of residual forces. This permits the system to exceed the lowest energy barriers and thus to explore different potential wells. To do that, the residual forces are calculated by the Hellmann-Feynman theorem²⁶ and then the Newton movement equations are integrated by the Verlet algorithm.³³

The trajectories and speeds of each atoms are also defined. Several types of molecular dynamics are described in the literature and basically distinguished by their speed control and thus the temperature during the calculations. The choice we made for our work is a type “velocity scaled”, which means that at each step of the dynamics, the temperature is calculated from the atom speeds and a same multiplicative factor is applied for each speed in order to obtain the required temperature. The parameters adjusted are the dynamic step and also the temperature. The increase of the temperature can improve the migration of atoms and the space of explored configurations. However, the step should stay below the lowest period of interatomic vibration. Otherwise, a bad description of the interaction will cause an uncorrected evolution of the system.

In our calculations, velocity scaled molecular dynamics (MD) was performed to explore the configurations of the cluster, in relation with its intrinsic fluctuality, dependent on the adsorbed molecules. We set a time step of 5 fs and regulated the hydrogen mass as 10 g/mol instead of 1. Three distinct temperatures of 500K, 800K and 1200K have been employed in order to improve the migration of atoms and the number of explored configurations. Same relaxed atoms as for the

geometry optimization are concerned for the molecular dynamics. In addition, the molecular dynamics with all platinum frozen has also been tested for the temperature of 1200K. For selected low energy configurations identified along MD, a subsequent “quenching” step of geometry optimization at 0K is applied after each MD in order to calculate the energy of the quenched system in a similar manner as the original system, for the sake of comparison.

1.2.5 Nudged Elastic Band Method

The Nudged Elastic Band (NEB) method³⁴⁻³⁶ is one popular method used to find saddle points and minimum energy paths (MEP) between two stable intermediates (known reactants and products) being local minima on the potential energy surface (Figure III-3). The method works by optimizing a number of intermediate images along the reaction path. Each image finds the lowest energy possible while maintaining equal spacing to neighboring images. On the NEB, this constrained optimization is done by adding spring forces along the band between images and by projecting out the component of the force due to the potential perpendicular to the band and any point on the path is an energetic minimum in all directions perpendicular to the path. The geometric structure belonging the first order saddle-point is called transition state. The difference between the energy of the initial state and the transition state is the corresponding electronic activation energy of a given reaction. To start a NEB calculation, typically a linear interpolation between the initial and final geometries is needed, whereas for more complex reactions, e.g. rotation motions, an interpolation in internal coordinates might be a more suitable approach.³⁵

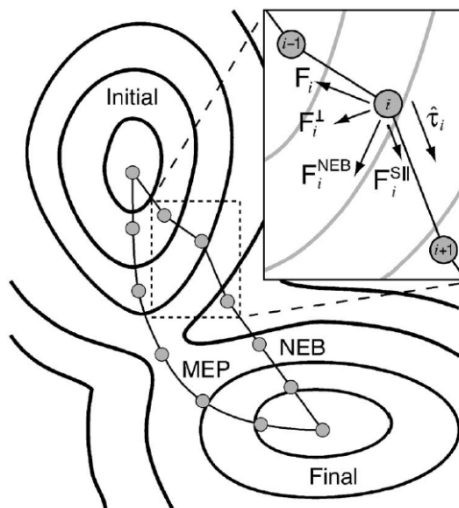


Figure III- 3 Schematic representation of the potential energy surface of an arbitrary reaction. The minimum energy path (MEP) and the nudged elastic band path (NEB) are shown as well as the NEB forces acting on image i ^{20,35}

Thus, the images nominated by $R_0, R_1, R_2, \dots, R_N$, where R_0 is the reactant and R_N is the final product, $N-1$ intermediates along the guessed reaction path have to be optimized ($N=9$ normally during our investigations). So, the forces function is noted as F , can be expressed as :

$$F(R_1, \dots, R_N) = \sum_{i=1}^{N-1} E(R_i) + \sum_{i=1}^N \frac{k}{2} (R_i - R_{i-1})^2 \quad \text{Equation (III-22)}$$

Where k is the spring constant, a force projection is introduced, referring to as "nudging". Since the corner-cutting results from the component of the spring force perpendicular to the path and the reason for the down-sliding comes from the parallel component from the interaction between the atoms in the system, the structures along the NEB path are relaxed to the MEP by a force projection scheme. Here, potential forces are perpendicular to the band and the spring forces act parallel to the band. Hence, this leads to a NEB force on image i containing two components:

$$F_i^{NEB} = F_i^\perp + F_i^{\parallel} \quad \text{Equation (III-23)}$$

with :

$$F_i^\perp = -\nabla(R_i) + \nabla(R_i)\hat{\tau}_i\hat{\tau}_i \quad \text{Equation (III-24)}$$

being the force component due to the potential perpendicular to the band and :

$$F_i^{\parallel} = k(|R_{i+1} - R_i| - |R_i - R_{i-1}|)\hat{\tau}_i \quad \text{Equation (III-25)}$$

as the spring force parallel to the band.

Note,
$$\hat{\tau}_i = \frac{R_{i+1} - R_{i-1}}{|R_{i+1} - R_{i-1}|} \quad \text{Equation (III-26)}$$

is the unit vector at an image i estimated from two adjacent images, R_{i+1} and R_{i-1} , along the path.

The most common strategies for finding a saddle point between the initial and final states are first to roughly optimize the NEB path, followed by performing a quasi-Newton structure optimization on the image with the highest energy. Another approach, which is similar to the NEB method and called climbing-image NEB (CI-NEB³⁷) can be used to more efficiently determine the saddle point. In the CI-NEB method, the images with the highest energy, is not subjected to a spring force coming from adjacent images and thus climbs to the saddle point.

In this thesis work, we combined these two methods. To start with, an interpolation scheme involving both Cartesian and internal coordinates is used (Opt'n-Path developed by Paul Fleurat-Lessard).³⁸ we performed firstly a NEB path between the initial and final states, as implemented in the VASP Transition State Theory (VTST) module,³⁹ then picked up the points near the “suspect” saddle point among the results and performed a climbing-image NEB path this time. The supposed transition state is then relaxed using a quasi-Newtonian algorithm²⁸ ($E_{\text{cutoff}} = 400$ eV) until convergence criteria are reached (electrons: 10^{-6} eV; nuclei: $0.01 \text{ eV} \cdot \text{\AA}^{-1}$).

1.3 Thermodynamic calculations

In order to evaluate free energies, equilibrium and rate constants, we apply *ab initio* thermodynamic calculations derived from the vibrational frequency calculations, the latter being performed with VASP.

1.3.1 Expression of enthalpic and entropic terms according to statistical thermodynamics

The thermodynamic potential for transformation at constant pressure and temperature, as in the case of the reactions taking place under the reaction conditions, is the Gibbs free energy G . It is expressed as a function of the enthalpy H and entropy S of the system:

$$G = H - T \times S \quad \text{Equation (III-27)}$$

We consider in practice the intensive molar quantities (rated X_m in the following). They all depend explicitly on the temperature. The molar enthalpy of a system is expressed as follows:

$$H_m = U_{elec,m} + U_{vib,m} + U_{trans,m} + U_{rot,m} + PV_m \quad \text{Equation (III-28)}$$

Where $U_{elec,m}$, $U_{vib,m}$, $U_{trans,m}$, $U_{rot,m}$, V_m are respectively the electronic energy, vibrational energy, translational energy and the molar volume. The molar volume term PV_m can be considered for an ideal gas system and for condensed phase systems, the term will be assimilate H_m and U_m in this case. The first term electronic energy is obtained by the result of DFT calculations, other energy terms can be calculated using the results from statistical thermodynamics.

Vibrational energy is obtained by knowing all of the vibrational frequencies of the system using the formula:

$$U_{vib,m}(T) = N_A \left[\sum_i \frac{1}{2} h \nu_i + \sum_i \frac{h \nu_i \times e^{-\frac{h \nu_i}{k_B T}}}{1 - e^{-\frac{h \nu_i}{k_B T}}} \right] \quad \text{Equation (III-29)}$$

where h is Planck's constant, k_B is the Boltzmann constant and T the absolute temperature. The first term of $U_{vib,m}$ corresponding to the vibrational energy of the system at 0K and is called "Zero Point Energy".

Relational and translational components of the internal energy have an analytical expression in the case of ideal gas:

$$U_{trans,m}(T) = U_{rot,m}(T) = \frac{3}{2} N_A k_B T$$

For a linear molecule: $U_{rot,m}(T) = N_A k_B T$ Equation (III-30)

Different from the case of a molecule adsorbed on a surface, the translational and rotational energies can only be defined in the same manner when it comes to an ideal gas. The surface diffusion phenomena, which is difficult for molecular modeling, can take place, for example. As a first approximation, it is assumed in the following that the translation and rotation modes are converted into vibration modes, and thus the associated enthalpy (as well as those of the entropy) are included in the vibrational energy.

Similarly, the molar entropy energy of system can be written as follows:

$$S_m = S_{vib,m} + S_{trans,m} + S_{rot,m} \quad \text{Equation (III-31)}$$

Where $S_{vib,m}$, $S_{trans,m}$ and $S_{rot,m}$ are respectively the molar vibrational, translational and rotational entropy. From the vibrational frequencies we can calculate the vibrational entropy:

$$S_{vib,m}(T) = N_A k_B \left[\sum_i \frac{\frac{h\nu_i}{k_B T} \times e^{-\frac{h\nu_i}{k_B T}}}{1 - e^{-\frac{h\nu_i}{k_B T}}} - \sum_i \ln(1 - e^{-\frac{h\nu_i}{k_B T}}) \right] \quad \text{Equation (III-32)}$$

For rotational and translational components in the case of an ideal gas, the following formula are used:

$$S_{trans,m}(T) = \frac{5}{2} N_A k_B + N_A k_B \ln \left[\frac{(2\pi M k_B T)^{\frac{3}{2}} V}{N_A h^3} \right] \quad \text{Equation (III-33)}$$

where P is the partial pressure of the gas, M is molar mass (formula Sackur-Tetrode)⁴⁰⁻⁴², and

$$S_{rot,m}(T) = N_A k_B \left[\frac{\sqrt{\pi}}{\sigma} \left(\frac{8\pi^2 k_B}{h^2} \right)^{\frac{3}{2}} \sqrt{A_e \times B_e \times C_e} \right] \quad \text{Equation (III-34)}$$

where A_e , B_e and C_e are the rotational constants of the molecule, and σ is the symmetry number.

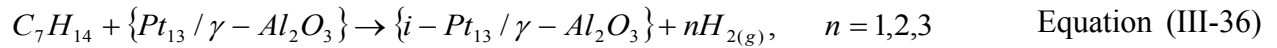
Again, for an adsorbed molecule, it is considered that rotation and translation modes are converted into the vibration modes by only using the vibrational component to describe the molar entropy of a system.

So far, for an adsorbed molecule phase, thus we have :

$$H = U_{vib} + U_{elec}, \quad S = S_{vib}$$

$$G = U_{vib} + U_{elec} - T \times S_{vib} \quad \text{Equation (III-35)}$$

So, in our case, the dehydrogenation reaction of $MCH_{(g)}$ leading to an adsorbed intermediate i and to the release of dihydrogen in gas phase (Equation (III-36)) is characterized by the dehydrogenation Gibbs free energy $\Delta_r G_{dehyd, MCH_{(g)}}(i)$ defined by Equation (III-37):



$$\Delta_r G_{dehyd, MCH_{(g)}}(i) = G_i + nG_{H_{2(g)}} - G_{MCH_{(g)}} - G_{Pt_{13} / \gamma - Al_2O_3}, \quad n = 1,2,3 \quad \text{Equation (III-37)}$$

Notably, the electronic reaction energy variation and reaction enthalpy for the same dehydrogenation reaction, are defined similarly as $\Delta_r E_{dehyd, MCH_{(g)}}(i)$ and $\Delta_r H_{dehyd, MCH_{(g)}}(i)$ respectively.

Thus, for two neighboring intermediates along reaction path, the dehydrogenation reaction Gibbs free energy from i to j $\Delta_r G_{i \rightarrow j}$ will be given by Equation (III-38) :

$$\Delta_r G_{i \rightarrow j} = \Delta_r G_{dehyd, MCH_{(g)}}(j) - \Delta_r G_{dehyd, MCH_{(g)}}(i) \quad \text{Equation (III-38)}$$

Similarly, the activation Gibbs free energy $\Delta_r G_{i \rightarrow TS_i}^\ddagger$ from reactant i to the corresponding transition state (TS_i) will be calculated by Equation III-(39) :

$$\Delta_r G_{i \rightarrow TS_i}^\ddagger = \Delta_r G_{dehyd, MCH_{(g)}}(TS_i) - \Delta_r G_{dehyd, MCH_{(g)}}(i) \quad \text{Equation (III-39)}$$

With the help of the vibrational frequencies described in the following paragraph, the partition function calculations are performed in order to deduce enthalpy, entropy and Gibbs free energies

of each system and these thermodynamic data are evaluated as a function of the temperature varying from 0 K to 1000 K, at standard condition of 1 bar pressure.

1.3.2 Vibrational frequencies calculations

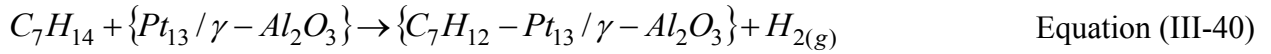
Harmonic vibrational frequency calculations were determined, with a displacement of ± 0.02 Å around the equilibrium atomic positions. All vibrational analysis has been done primarily at the PBE level. If after doing the geometry optimization at the PBE-dDsC level, the structure does not change, we considered that the PBE-dDsC have barely no influence on vibrational frequencies of each structure (for the sake of limited calculation time). So we mainly modified the electronic energies and kept the same vibrational contribution (in enthalpy, entropy and zero point energy terms). Some exceptions are observed however, in particular for the radical intermediate methylcyclohexyl adsorbed on the cluster, which will be presented later in the results. So in this case, the vibrational frequencies have been recalculated at PBE-dDsC level for the new methylcyclohexyl configuration.

These calculations allow us to determine reaction enthalpies, entropies and Gibbs free energies. These harmonic vibrational frequency calculations are also performed to evaluate the reliability of the identified transition states (according to the previously described method), whereas one and only one imaginary frequency appears in the frequency calculation corresponding to the reaction coordinate, since it belongs to a first order saddle point. However, in some cases, some low vibrational imaginary frequencies might arise, relating to the soft modes.⁴³ We assessed that this apparition of low imaginary frequencies is related to the chosen criterion for the geometry optimization convergence. Piccini et al.^{44,45} explained that since soft

vibrations can couple with the surface modes, the vibrational structure of the whole crystal framework changes consistently with the presence of the adsorbate. This means that the crystal adapts its structure to accommodate the molecule weakening the strength of some bonded interactions, which gives rise to a highly entropic adsorbed state. This vibration of the crystal framework forms the structure adaption was also observed when we visualized the soft modes of our cluster system.

In order to eliminate these soft modes in form of imaginary frequencies, we firstly attempted different parameters combination “packages” in terms of cut-off energy (400, 500, 600 eV), precision flag in VASP (normal, accurate, high), electronic convergence criterion (10^{-5} , 10^{-6} , 10^{-8} eV) and forces convergence criterion (0.01, 0.02 eV/Å) to optimize the methyl-cyclohexene adsorbed system for a benchmarking test (reaction presented in Equation III-(40)), since that this is one of the crucial reaction intermediate considered in our mechanism later. These tests were done to probe if there is a potential connection between the extinction of these parasite imaginary frequencies and the calculation parameters. Among all the parameters choices applied on the methyl-cyclohexene adsorbed system, it turns out only five parameter “packages” managed to eliminate these imaginary frequencies: (1) cut-off energy = 400 eV; normal precision; electronic convergence criterion = 10^{-5} eV; forces convergence criterion = 0.02 eV/Å; (2) cut-off energy = 400 eV; normal precision; electronic convergence criterion = 10^{-5} eV; forces convergence criterion = 0.01 eV/Å; (3) cut-off energy = 500 eV; normal precision; electronic convergence criterion = 10^{-5} eV; forces convergence criterion = 0.01 eV/Å; (4) cut-off energy = 400 eV; normal precision; electronic convergence criterion = 10^{-8} eV; forces convergence criterion = 0.005 eV/Å; (5) cut-off energy = 400 eV; accurate precision; electronic convergence criterion = 10^{-8} eV; forces convergence criterion = 0.005 eV/Å. Sometimes, with more severe

optimization parameters (ex. high cut-off energy and precision, 600 eV), the extinction of parasite imaginary frequencies are not guaranteed. However, the cut-off energy = 400 eV at normal precision are constantly efficient. In addition, high electronic and forces convergence criterions are also recommended by our tests for the extinction of these parasite imaginary frequencies (tests (4) and (5)). Nevertheless, these high criterions demand relatively long calculation time.



On the other hand, the contribution of these small parasite imaginary frequencies, which are converted from negative eigenvalue to positive by DFT at the end of calculation, can be tremendous and uncertain to the vibrational entropy term if no proper countermeasures are adopted. This can be seen by the expression of vibrational entropy term in Equation (III-41),

$$\text{When } \nu_i \rightarrow 0, \text{ we have } \frac{\frac{h\nu_i}{k_B T} \times e^{-\frac{h\nu_i}{k_B T}}}{1 - e^{-\frac{h\nu_i}{k_B T}}} \rightarrow 1 \text{ and } \ln(1 - e^{-\frac{h\nu_i}{k_B T}}) \rightarrow -\infty, \text{ so } S_{vib,i} \rightarrow +\infty.$$

$$S_{vib,i} = N_A k_B \left[\frac{\frac{h\nu_i}{k_B T} \times e^{-\frac{h\nu_i}{k_B T}}}{1 - e^{-\frac{h\nu_i}{k_B T}}} - \ln(1 - e^{-\frac{h\nu_i}{k_B T}}) \right] \quad \text{Equation (III-41)}$$

An analysis of the vibrational frequencies was thus done to evaluate the entropy deviation induced by the soft modes and imaginary frequencies obtained by different calculation parameters for methyl-cyclohexene system at reforming temperature $T = 800$ K. The last five vibrational frequencies coming out from the DFT calculations are listed in Table III-1, which includes soft modes and imaginary frequencies (underlined value) that are converted from

negative eigenvalue to positive by DFT at the end of calculation. Here in Table III-1, three parameter “packages” (with same electronic convergence criterion = 10^{-5} eV and forces convergence criterion = 0.02 eV/Å, for the sake of calculation time) were chosen to make a comparison: (a) cut-off energy = 400 eV; normal precision; (b) cut-off energy = 400 eV; High precision; (c) cut-off energy = 500 eV; normal precision. These three cases were representative among all because the case (a) have no parasite imaginary frequencies, while the cases (b) and (c) reveals the most (\pm) deviation on total vibrational entropy at 800 K compared to (a) during our analysis, due to the apparition of parasites imaginary frequencies. The vibrational entropy corresponding to each frequency is calculated by using Equation (III-41). It indicates thereby from Table III-1 that the apparition of these soft modes or imaginary frequencies contributes $-20 \sim +3$ kJ/mol to the vibrational entropies term TS_{vib} at 800 K.

Table III- 1 Frequency analysis for the contributions of last five soft modes and imaginary frequencies to the vibrational entropies at T=800 K calculated on PBE level (The underlined values correspond to imaginary frequencies)

	(a) $E_{\text{cut-off}}=400$ eV, normal precision		(b) $E_{\text{cut-off}}=400$ eV, high precision		(c) $E_{\text{cut-off}}=500$ eV, normal precision	
	Relevant frequencies, ν_i (cm ⁻¹)	$TS_{vib,i}$ (kJ/mol) at 800 K	Relevant frequencies, ν_i (cm ⁻¹)	$TS_{vib,i}$ (kJ/mol) at 800 K	Relevant frequencies, ν_i (cm ⁻¹)	$TS_{vib,i}$ (kJ/mol) at 800 K
Last five vibrational frequencies	38.98	30.4	29.91	32.6	35.78	31.1
	35.97	31.1	29.21	32.8	26.16	33.7
	29.21	32.8	17.88	36.9	12.75	39.7
	28.31	33.1	<u>14.69</u>	<u>38.5</u>	<u>83.24</u>	<u>24.1</u>
	11.43	40.6	<u>39.56</u>	<u>30.3</u>	<u>86.22</u>	<u>23.8</u>
$\Sigma \nu_i$ and $\Sigma TS_{vib,i}$	143.9	168	131.3	171	244.2	152
Deviation $\Delta \Sigma$ compared to case (a)	0	0	-12.7	+3	+100.3	-16

In addition, a recommended method for treating residual imaginary frequencies has been proposed by Sabbe et al.⁴⁶, which is to replace the frequencies lower than a given frequency cutoff by a common value. In line with this previous work, we replaced all frequencies lower than 50 cm^{-1} and all spurious imaginary frequencies (if any) by 50 cm^{-1} before thermodynamic calculations. For transition states, the imaginary frequency corresponding to the reaction coordinate and to a first order saddle point has to be eliminated before the Gibbs free energy calculation. The reaction enthalpy and Gibbs free energy for the dehydrogenation of methyl-cyclohexane (taken in gas phase) to adsorbed methyl-cyclohexene and one molecule H_2 released in gas phase has been calculated here in Figure III-4.

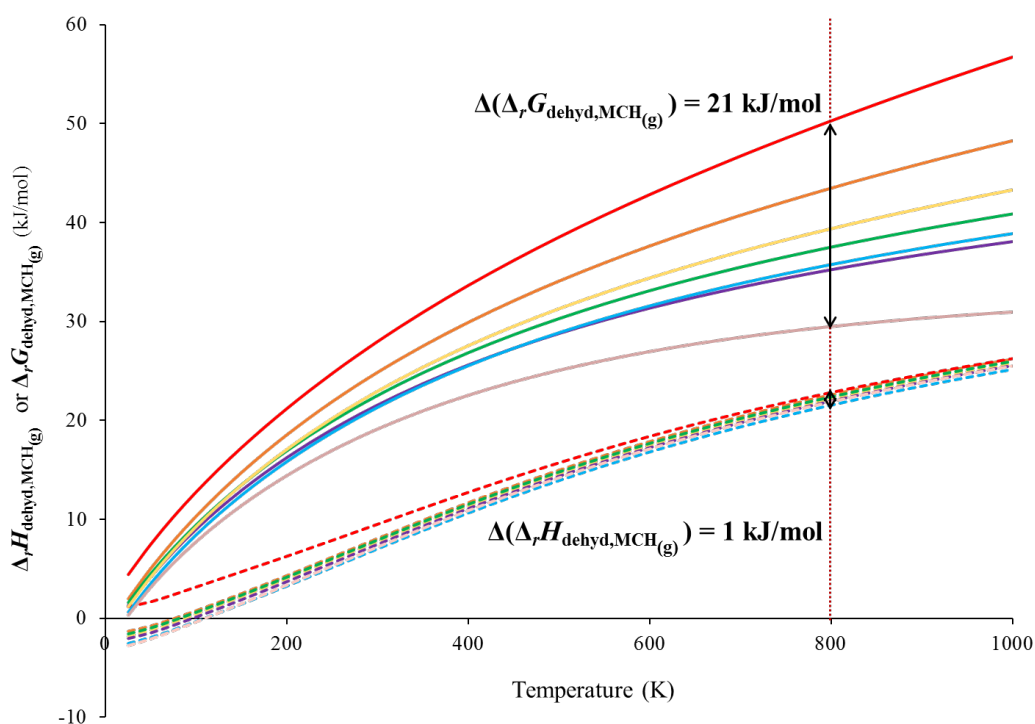


Figure III- 4 Deviation of dehydrogenation Gibbs energy $\Delta_r G_{\text{dehyd},\text{MCH}(g)}$ and Enthalpy energy $\Delta_r H_{\text{dehyd},\text{MCH}(g)}$ for the dehydrogenation of methyl-cyclohexane to adsorbed methyl-cyclohexene, using different parameters for the DFT calculations parameters. Curve style legend: Line (reaction Gibbs free energy); Dot line (reaction enthalpy). Curve color legend: $E_{\text{cutoff}} = 500\text{ eV}$, normal precision (red); $E_{\text{cutoff}} = 400\text{ eV}$, normal precision (orange); $E_{\text{cutoff}} = 500\text{ eV}$, accurate precision (yellow); $E_{\text{cutoff}} = 400\text{ eV}$, accurate precision (green); $E_{\text{cutoff}} = 500\text{ eV}$, high precision (blue); $E_{\text{cutoff}} = 600\text{ eV}$, normal precision (purple); $E_{\text{cutoff}} = 400\text{ eV}$, high precision (pink).

We investigated the effect of the energy cutoff (400, 500, 600 eV) and the precision (normal, accurate, high) of the calculation, at same electronic convergence criterion = 10^{-5} eV and forces convergence criterion = 0.02 eV/Å. It can be noticed in Figure III-4 that the parameter choices (energy cutoff and precision) used for the calculation strongly impacts the Gibbs free energy values, even though after replacing all frequencies lower than 50 cm^{-1} and all spurious imaginary frequencies (if any) by 50 cm^{-1} . It can be seen that the deviation on the reaction enthalpy is very small, taking the reforming temperature 800 K for a comparison, the deviation is close to 1 kJ/mol, which can be neglected on the final result. However, the deviation on the Gibbs free energy is higher (21 kJ/mol at 800 K). This makes this kind of calculation very sensitive to the chosen parameters in the reforming conditions. This important deviation on the Gibbs free energy is thus due to the vibrational entropic terms, since enthalpies varied very little in our case.

Since the “standard” calculation (cut off energy of 400 eV, normal precision) leads to Gibbs energy values in the center of this fluctuation interval with a reasonable computational time and without any spurious imaginary frequency, we chose it as the best compromise for further calculations and with a slightly higher electronic convergence criterion = 10^{-6} eV and forces convergence criterion = 0.01 eV/Å.

2. Catalytic experiment

This second part of the chapter aims at presenting the catalytic tests based on the methyl-cyclohexane dehydrogenation reaction in our work. In the literature, different catalyst tests have been done under different reaction conditions, with variable platinum contents in catalyst.⁴⁷⁻⁵² As it can be observed in Table III-2, a large range of reaction conditions is used on purpose to provide specific experimental data for dedicated kinetic studies. In our work, the adapted reaction conditions and catalyst will be also chosen to provide these experimental data, in order to enable the later confrontation with the kinetic model parameterized by the *ab initio* calculations. So in this chapter, the protocols of catalyst preparation will be presented first, followed by the catalyst characterizations. The employed experimental conditions and protocols for the tests will then be described in detail. At last, the test results will be interpreted in comparison with the available literature, depending on the reaction conditions employed, such as temperature, reaction space time, hydrogen partial pressure and methyl-cyclohexane partial pressure.

Table III- 2 Summary of the methyl-cyclohexane dehydrogenation reaction conditions used for alumina supported platinum catalysts in the literatures⁴⁷⁻⁵²

First author	wt% Pt	Pressure (bar)	Temperature (°C)	H ₂ /HC (mol/mol)	WHSV (g _{MCH} ·h ⁻¹ ·g _{cata} ⁻¹)	Space time (g _{cata} ·s·g _{MCH} ⁻¹)
Alhumaidan ⁴⁷	1.0	0-9	340 – 450	0 – 9	2.9 – 11.5	313 – 1241
Rochefort ⁴⁸	0.06 – 0.82	1.01	300	5	580 – 2300	1.6 – 6.2
Sinfelt ⁴⁹	0.3	1.4 – 6.3	315 – 372	2 – 20	50 – 100	36 – 72
Van Trimpont ⁵⁰	0.5 (0.67-Cl; sulfided)	4.5 – 20	309 – 410	9 – 100	8 – 200	18 – 450
Usman ⁵¹	1.0	1 – 9	340 – 380	0 – 8.4	3 – 12	300 - 1200
Maria ⁵²	Sulfided	6 – 16	289 – 309	2.5 – 10	14 – 60	60 – 257

2.1 Methodology and experimental techniques

2.1.1 Catalyst preparation and characterization

The catalytic reforming catalysts are prepared by depositing platinum (0.3 wt%) on a γ -alumina support (beads shape). Due to the use of chlorinated platinum precursor, 0.12 wt% chlorine remains on the catalyst, which can be considered as a nearly non-chlorinated catalyst during our catalytic tests, in order to compare with the *ab initio* calculation model chosen. Indeed, industrial reforming catalysts are far more chlorinated (about 1% wt) resulting from a specific chlorination treatment. The employed catalysts were synthesized and then characterized in the Catalysis and Separation Division, by Carine Guégan. The protocols of catalyst synthesis and characterization are now presented :

Preparation and acidification of alumina support :

The support (boehmite type) is firstly calcined for 2 h at 520 °C (Heating rate: 5 °C/min), under a dry air flow rate of 1 L.h⁻¹.g⁻¹ of support, in order to transform the boehmite into γ -alumina. Pre-calcination of the support can remove hydroxyl groups from the alumina. This results in the presence of highly reactive sites where the metal will preferentially attach. To avoid a heterogeneous distribution, the alumina is therefore rehydrated progressively by adding water drop by drop. This step also makes it possible to avoid excessive exothermicity and bursting of the beads during the introduction of the support into the fluidized bed in the presence of a large quantity of water. The support is then placed in the fluidized bed, the alumina is contacted with a sufficient amount of hydrochloric acid (HCl) at 35% concentration. The hydrochloric acid (HCl) is injected with a syringe during 45 minutes. After a total acidification time of 2 h, then the liquid is withdrawn from the alumina support.

Impregnation of Pt :

The impregnation of the platinum is carried out by ion exchange in a solution using an adsorption competitor (Cl^-), in order to allow a quick migration of the platinum into the catalyst grain. To do this, the hexachloroplatinic acid (H_2PtCl_6) + hydrochloric acid (HCl) is then added (in the form of $[\text{PtCl}_6]^{2-}$ in an acid phase). The H_2PtCl_6 solution is prepared by dissolving the contents of a flask of 25 g of hexachloroplatinic acid (concentration of 38-40% by weight of Pt) in 300 g of water. The solution ($\text{H}_2\text{PtCl}_6 + \text{HCl}$) is then injected into the addition pot which contains the alumina support with a syringe during 45 minutes (same method as the acidification). The quantity of H_2PtCl_6 injected is calculated by aiming at 0.35 wt% Pt that will be impregnated at last instead of 0.3 wt%. This quantity of metal precursor introduced is slightly greater than the target quantity and empirically determined. The quantity of HCl injected is calculated as reference of 0.5 wt% Cl of the support. An adsorption equilibrium then takes place rapidly between the Cl^- and PtCl_6^{2-} ions at the surface of the support. The fluidization lasts a total of 4 h and then the liquid is withdrawn.

Drying and calcination :

The catalyst is dried overnight in an oven at 120 °C and then is calcined for 2 h at 520 °C, (heating rate: 5 ° C/min.), with a dry air flow rate of 1 L.h⁻¹.g⁻¹ of the catalyst.

Dechlorination :

The catalyst obtained after the drying and calcination is a catalyst contains 1.35 wt% Cl (chlorine, analyzed by X-ray fluorescence), which is not our desired Cl content. Therefore, our employed catalyst for the catalytic reaction tests requires a chlorine elimination to reach a non or

low-chlorinated state. A step of dechlorination has to be done in this case. The dechlorination consists in principle in injecting a quantity of water at high temperature in a given time.

In a quartz reactor, the catalyst is put inside to be dechlorinated, an inert buffer made by quartz and carborundum (SiC) are charged (≈ 200 g for a reactor of diameter ≈ 60 mm et ≈ 500 g for the diameter ≈ 80 mm) to prevent the catalysts from blowing away by water and air during the dechlorination process. The reactor is placed in a vertical tubular furnace and processed under a stream of dry air of $1 \text{ L.h}^{-1}\text{g}_{\text{cata}}^{-1}$. The heating rate of the furnace is set at $5 \text{ }^\circ\text{C}/\text{min}$ from room temperature to $520 \text{ }^\circ\text{C}$. At this temperature of $520 \text{ }^\circ\text{C}$, 8000 ppm of water are then injected into the gas pendant 80 h. At last, the catalyst is cooled in dry air ($11 \text{ L.h}^{-1}\text{g}_{\text{cata}}^{-1}$) and discharged at room temperature. Thus, the catalyst is about to be determined by X-ray fluorescence for the new chlorine content and also the platinum content.

X-ray fluorescence:

The elemental mass loadings are determined by X-ray fluorescence (XRF). The analysis of the wavelength dispersive X-ray fluorescence spectrum allows to get the information on identification of the nature of the simple elements by the energetic distribution of the characteristic rays on the spectrum and at same time, the intensity of each characteristic radiation is directly related to the amount of each element in the material.⁵³ Therefore, the chlorine (Cl) content (wt%) analyzed by XRF is 0.121 and the platinum (Pt) content (wt%) is 0.295 for the catalyst synthesized. Accuracy is respectively ± 0.006 and 0.007% .

Electron microprobe :

The metal and chlorine distributions inside the catalyst beads are determined by electron microprobe. The electron microprobe is an analytic technique to characterize the composition of chemical components within a material by analyzed the characteristic wavelength of the emitted X-ray to the sample elements when they are bombarded by a focused incident electron beam (or electron probe), without destroying the sample.⁵⁴ The electron microprobe produces two-dimensional images of elemental distributions that gives us a quantitative analysis in order to determine the mass concentration of the sample elements.⁵⁴ Figure III-5 presents the microprobe scanning results for the catalyst by calculated the average value of five scanning results. It can be noticed from the figure that the three elements aluminum, platinum and chlorine are all homogeneously distributed. The three elements content is generally constant as an evolution of scanning distance. The global concentration determined by the electron microprobe analysis is 0.289 wt%, which is agreed with the FX results.

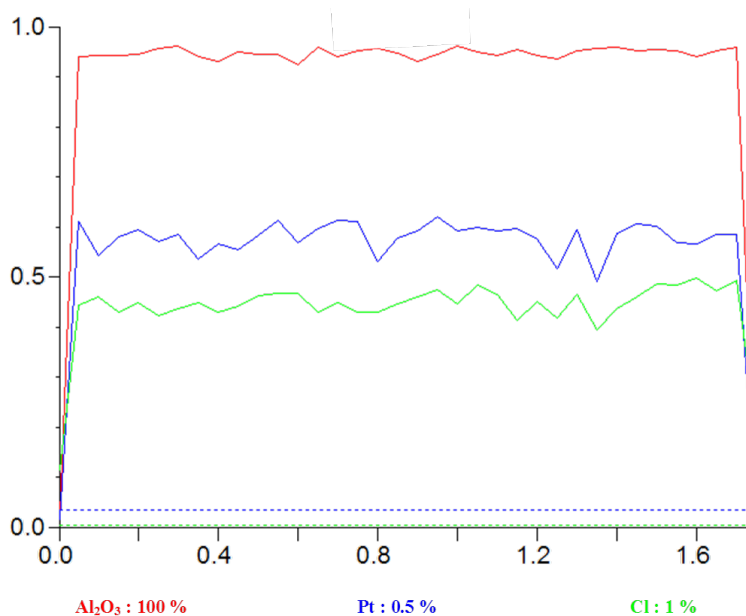
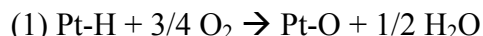


Figure III- 5 Electron microprobe scanning results for 0.3%Pt-0.12%Cl/ γ -Al₂O₃ (average microprobe calculated from five individual microprobe scanning results)

H₂-O₂ titration :

The H₂-O₂ titration is a common technique used to quantify the platinum dispersion. The pretreatment protocol includes a decrease in temperature between the calcination (550°C under dry air) and the reduction, and a rise in temperature under hydrogen for the reduction (550 °C). Once the catalyst is reduced, the first titration of O₂ occurs. The catalyst is treated in contact with the oxygen pulses; the hydrogen atom on the platinum atom is thus oxidized into water and progressively replaced by adsorbed molecular oxygen. The reaction of this titration step can be written as:



The remaining oxygen flow rate is detected and the detection ends when the inlet oxygen flow rate is equal to the outlet oxygen flow rate. Then the catalyst goes through a second reduction at room temperature this time. The reaction of this reduction step can be expressed as :



Then, second titration starts after this reduction step undergoing exactly the same reaction as the first titration. The metal dispersion can be thus calculated by the first titration :

$$\text{Disp (\%)} = \frac{V_1}{\frac{22400 \cdot T_a}{273} \cdot \frac{3}{4} \cdot \frac{\text{wt\% Pt}}{100 \cdot M_{Pt}}}$$

With V_1 = chemisorbed volume at the first titration (mL/g) expressed at conditions T_a = reference temperature (25°C) and P = atmospheric pressure (101325 Pa); M_{Pt} = molar mass of platinum (195.08 g/mol) ; wt\% Pt = Pt content obtained by XRF and corrected by the loss of mass at 550 °C.

By using this $\text{H}_2\text{-O}_2$ titration analysis, the dispersion of platinum in our catalyst is determined at 90 %.

Transmission Electron Microscopy :

The transmission electron microscopy (TEM) technique aims at visualizing the homogeneity of metallic nano-metric particles dispersion in the catalyst, by sending an electron beam transmitting through the sample. The grinded catalyst sample is diluted in ethanol and stirred continuously in an ultrasonic bath. Then the obtained suspension is set on a copper grid with holey-carbon-film support where the alcohol is evaporated. TEM experiments are performed on Jeol JEM 2100F microscope at 200 kV. The pictures obtained for our catalyst are shown in Figure III-6. It can be seen that the catalyst sample represents a homogeneous metallic phase dispersion (white spots in Figure III-6). Meanwhile, the particle sizes in the catalyst are also presented in the Table III-3 by showing the size range and average size. The average size for the sample is 0.85 nm and the size range is around 0.35-1.46 nm. This result is in good agreement with the high dispersion level calculated above by $\text{H}_2\text{-O}_2$ titration.

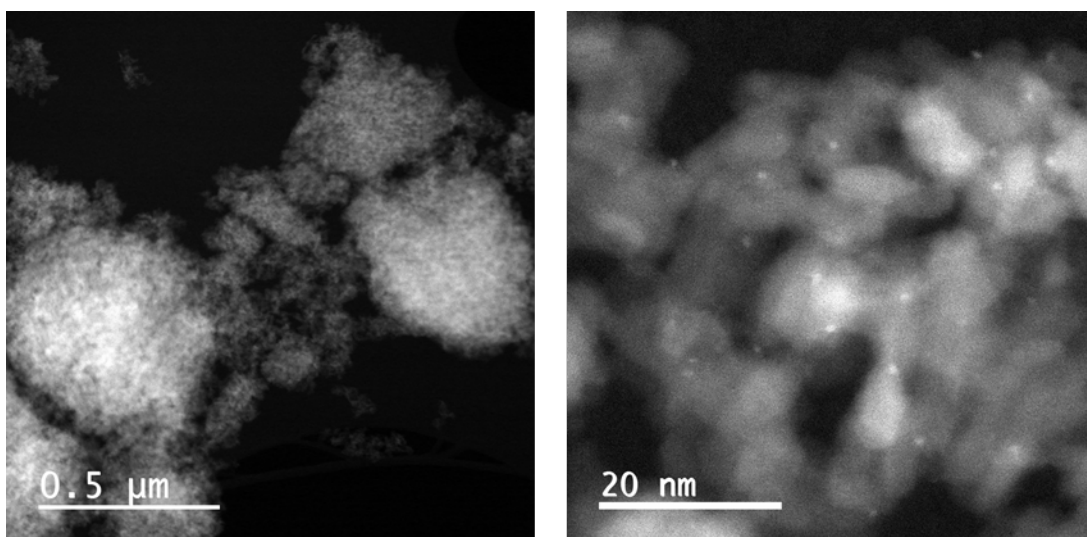


Figure III- 6 Transmission electron microscopy (TEM) results for the catalyst sample of 0.3%Pt-0.12%Cl/ $\gamma\text{-Al}_2\text{O}_3$ at two different magnifications

Table III- 3 Maximum, minimum and average particle sizes obtained by TEM for the catalyst sample of 0.3%Pt-0.12%Cl/ γ -Al₂O₃

	Size (nm)
Average	0.85
Min	0.35
Max	1.46

So far, the platinum dispersion of the catalyst is determined to be about 90%. However, it is crucial to control the catalyst granulometry to avoid internal transport gradients between the catalyst body surface and the catalyst body center, in order to get reliable results. So, for this purpose, the beads have been grinded and sieved to 200 – 355 μ m before catalytic tests, a choice that we made after comparing the test results of different granulometries (See in Appendix-III). The catalyst weight for each test is 0.56 g.

2.1.2 Catalytic test set-up

The simplified reaction set-up scheme is presented in Figure III-7, which consists of 3 parts : inlet zone (feedstock tank, pump and different gas flow lines), reaction zone (reactor and reactor oven) and outlet zone (high/low pressure separator, sampler, chromatogram analyzer and gas counter).

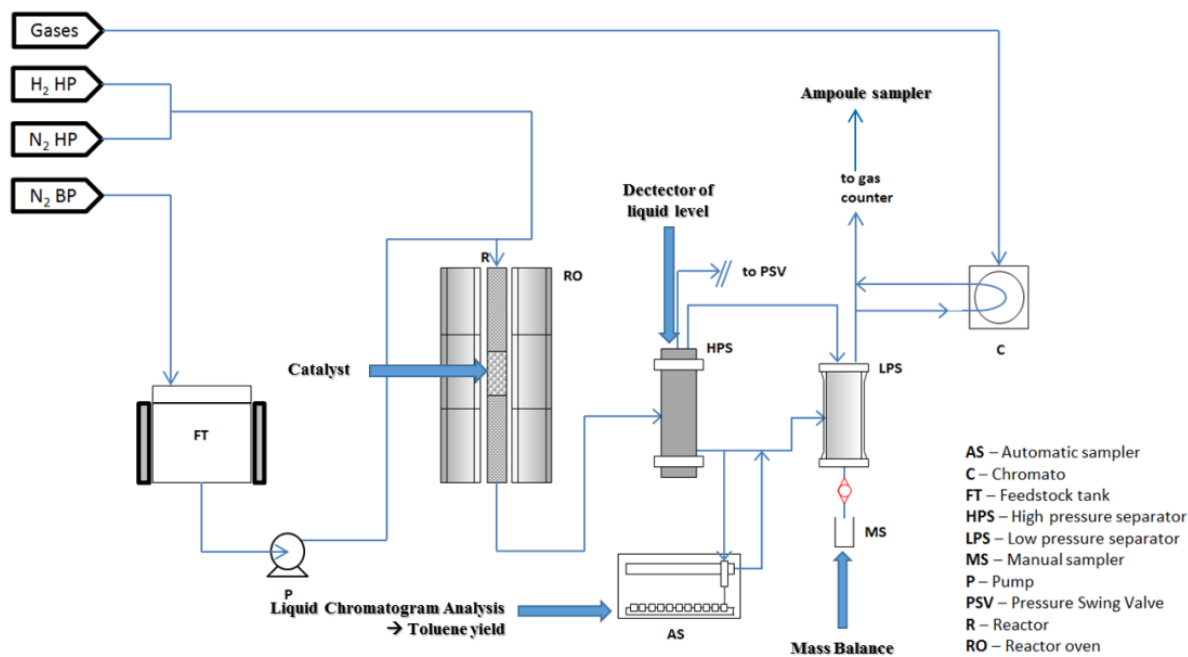


Figure III- 7 Simplified reaction set-up scheme of the catalytic test set-up⁵⁵

Inlet zone

The adjustable and controllable parameters for the reaction conditions are the reaction temperature, the inlet gas flow rate for H₂ gas, the inlet methyl-cyclohexane charge flow rate and the total pressure during the reaction. The reaction temperature is set up by a heating system connected with the reaction oven (RO) that surrounds the reactor and is surveyed by three thermocouples extending into the reactor (R). The H₂ gas is directly injected into the reactor from the gas flow line and one can measure its flow rate from the gas flow controller. The methyl-cyclohexane liquid charge (Sigma-Aldrich, 99% reagent grade, 0.77 density, 2.5 L/bottle) is stored in the feedstock tank (FT) of 3 liters, and is pressurized by a line of low nitrogen pressure. The liquid charge is pumped from the feedstock tank to the reactor inlet at reaction pressure by

the pump (P). This liquid charge flow is regulated by the pump and is measured by a manually burette upstream of the reactor.

Reaction zone

The catalytic tests for the methyl-cyclohexane dehydrogenation reaction are carried out in a vertical fixed bed reactor with an internal diameter of 19 mm and a length of 585 mm. However, the reaction area measures only 470 mm. The catalyst (0.56 g) is loaded in the middle of the reactor, where the catalytic stuffing zone measures about 32.5 mm. The reactor oven (RO) is made up of three hot shells. Each shell measures 150 mm height and the middle shell mainly heats the catalytic zone of reactor, as described in Figure III-8. There are three thermocouples T_{2c} , T_{2b} and T_{2a} , extending into the reactor at T2 shell level and reaching different levels in the catalytic zone : top, middle and bottom levels, respectively. The distance between T_{2c} and T_{2a} is about 50 mm. The two extreme thermocouples T_{2c} and T_{2a} are positioned outside of the catalytic zone, in order to measure the temperatures of the influent entering/exiting the catalytic zone, while the T_{2b} measures the exact reaction temperature in the catalytic bed. During the tests, these three thermocouples send back the temperature from the three levels on catalytic zone instantaneously and allow us to survey and adjust the reaction temperatures timely. The catalytic zone is filled up with a total volume of 10 cm^3 of the following mixture: 1 cm^3 of catalyst (corresponding to 0.56 g) and 9 cm^3 of silicon carbide (SiC) equivalent of 13.68 g, to reach a dilution ratio of 1/10. This mixture is loaded in the catalytic zone by dividing the load into three identical portions, in order to guarantee a good homogeneity on the distribution of particles within the catalytic layers in this isothermal zone. The total layer length of the catalytic zone in

the reactor is about 32.5 mm, located in the middle of the reactor. The rest of the reactor is filled up with inert silicon carbide (SiC). Quartz wool covers the bottom of the reactor. Between each layer, the reactor should be tapped delicately to insure that the catalytic zone remains immobile in the middle of the reactor during the test, where the three thermocouples are accurately placed and report the reactor temperature before, during and after the charge admission into the catalytic zone.

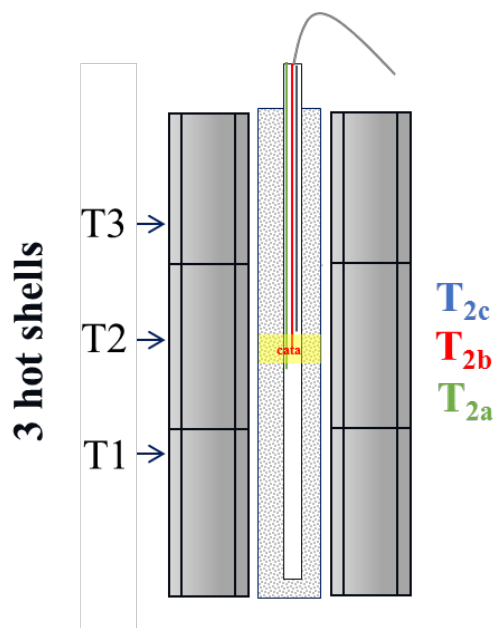


Figure III- 8 Reactor zone for catalytic reaction (fixed bed reactor). The yellow zone corresponds to the catalytic bed.

Outlet zone

At the outlet of the reactor, the reaction products in gaseous phase at high reaction pressure are blown into the first high pressure separator (HPS), in order to cool down and to condense the “heavy” compounds into liquid phase and separate them from H₂. At the output of

the high pressure separator (HPS), an automatic pressure swing valve (PSV) can be found to control the pressure in the reactor. Once the desired liquid level (4 % of the HPS total volume in this work) is set up, this level in the separator is full-time controlled and adjusted by the help of a plug-in detector in the separator. The automatic pressure swing valve (PSV) is connected with this detector in order to be turned on/off depending on the liquid level. That allows us to have a continuous product feed flow from the high pressure separator (HPS) to the low pressure separator (LPS), instead of being accumulated in the high pressure separator (HPS). Before the liquid flow goes into the low pressure separator (LPS), we force a part of the product feed to pass into an automatic sampler (AS), which can be programmed to recover the product liquid feed hourly and can analyze 80 samples at maximum for each test.

Then the samples are analyzed by a gas chromatograph (GC) analyzer equipped with a flame ionization detector (FID) in order to determine the product yield in the liquid portion. The liquid sample is vaporized into gas at the moment of being injected into the gas chromatograph (GC). In gas chromatograph (GC), the sample comes through in a carried gas stream as a mobile phase (helium), interacted with the liquid stationary phase inside a capillary column. The different compounds in the sample move in the column with different rates depending on their properties. As the sample exits the end of column, they are detected and identified electronically by the flame ionization detector (FID). The flame ionization detector (FID) combusts the organic compounds in the sample into ions by a hydrogen flame and the generation of these ions is proportional to the concentration of the organic compounds in the sample. The concentration is described by the response factors related to the number of the carbon atoms in the molecule. The rest of the product getting out of the high pressure separator (HPS), without being analyzed by gas chromatograph (GC), are contained in the low pressure separator (LPS). This is also where

we can weigh the product mass to set the mass balance of the reaction. At the end, the gas flow released from the low pressure separator (LPS) goes through the gas counter to measure the flow rate. An ampoule sampler is used to analyze and determine the quantity of product in the gaseous phase escaped from the separator. This part of product is thus considered into the calculation of product yield and to correct the final mass balance of the reaction. The system of the ampoule sampler to trap the product in the output gas is presented in Figure III-9.

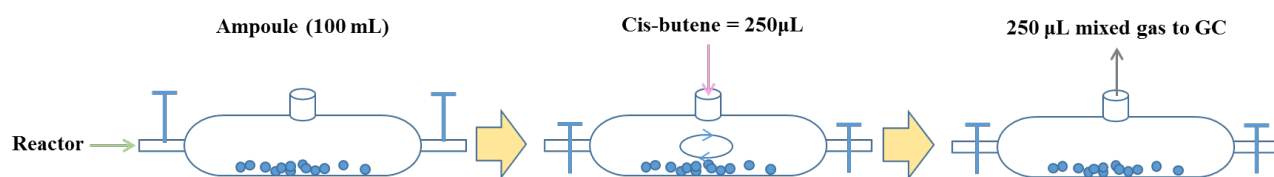


Figure III- 9 Ampoule sampler system to quantify the product on gaseous phase

The output gas flow from the low pressure separator (LPS) is firstly flowing through a 100 mL ampoule that contains glass balls, which role is stirring the mixed gas and also calibrating the gaseous volume in the ampoule to 100 mL. After about 15 minutes, we close the two valves of the ampoule and then inject 250 μL of pure cis-2-butene as reference gas. With the help of the glass balls inside, we mix the gas and then retrieve 250 μL mixed gas and analyze it by gas chromatograph (GC). By this way, we identify and quantify the different gaseous components outlet of the reaction zone. The detail quantifications and calculations will be presented in next section.

2.1.3 Reaction conditions

The operating conditions are different from those generally applied in the industrial reforming processes^{56–58}. The dehydrogenation reaction of alkyl cyclohexanes into aromatics is a highly endothermic reaction and reported to have a reaction heat of about 215 kJ/mol for all carbon numbers.⁵⁹ At the same time, these reactions present also a very high equilibrium constants which have an order of magnitude of 10^6 .⁵⁹ The reaction is very favored with high temperatures and can reach a very high conversion at reaction equilibrium. Moreover, the reaction rate of dehydrogenation of alkyl cyclohexanes is very fast compared to other reforming reactions : about 6 times faster than that of isomerization of paraffins and naphthenes and 25 times faster than those of dehydrocyclisation of paraffins and hydrocracking.⁵⁹ Another important reaction that should be considered is the coke formation, which is the slowest process in catalytic reforming (1000 times slower than the dehydrogenation reaction⁵⁹). However, this reaction is sensitive to the hydrogen partial pressure and the hydrogen to hydrocarbon ratio.^{59,60} The coking rate increases by decreasing the hydrogen to hydrocarbon ratio at constant total pressure.⁶⁰

It is thus important to employ the optimal operating conditions to ensure the catalyst stability from metal sintering, to achieve a large conversion range and also to guarantee no thermal effects or diffusional limitations. The high temperature may favor the conversion but in our study, we would like to achieve conversion levels in a relative large range, in order to study the reaction kinetics. So, lower temperatures compared to the industrial catalytic reforming temperatures were employed. On the other hand, the lower temperature can eliminate the other reforming reactions as hydrocracking and hydrogenolysis. In order to avoid catalyst deactivation by coke formation, the total partial pressure was maintained at 13 bar and the hydrogen to hydrocarbon ratio was set at 15 for most catalytic tests, excepted for those which are aim at studying the partial pressure

impact. For those purposes and by previous catalytic tests done at IFPEN,⁵⁵ the choice of reaction conditions for the methyl-cyclohexane dehydrogenation reaction is presented in Table III-4.

Table III- 4 Reaction conditions for the methyl-cyclohexane dehydrogenation catalytic test over Pt/ γ -Al₂O₃ catalyst

	TEST-1	TEST-2	TEST-3	TEST-4	TEST-5	TEST-6	TEST-7	TEST-8	TEST-9	TEST-10	TEST-11	TEST-12
WHSV* (g _{MCH} h ⁻¹ g _{cata} ⁻¹)	40	70	100	130	150	20	40	40	40	40	40	40
Space time (g _{cata} ·s·g _{MCH} ⁻¹)	90	51	36	28	24	180	90	90	90	90	90	90
Total Pressure (bar)	13	13	13	13	13	13	19.8	5.8	4.8	2.8	12.7	12.5
P(H ₂) (bar)	12.2	12.2	12.2	12.2	12.2	12.2	19.0	5.0	4.0	2.0	12.2	12.2
P(MCH) (bar)	0.8	0.8	0.8	0.8	0.8	0.8	0.8	0.8	0.8	0.8	0.5	0.3
H ₂ /HC* (mol/mol)	15	15	15	15	15	15	24	6	5	2.5	24	41
H ₂ inlet volumetric flow rate (L/h)	77	135	193	251	290	39	120	32	25	13	124	206
MCH inlet volumetric flow rate (ml/h)	29	51	72	94	108	15	29	29	29	29	29	29
Temperature (°C)	320→340→ 360→380→ 360	360	360	360	360	360	360	360	360	360	360	360

* : WHSV = weight hourly space velocity
MCH = methyl-cyclohexane
H₂/HC = hydrogen to hydrocarbon ratio

The tests are parameterized according to four investigation purposes. Test-1 is a complete and model test with 4 different temperatures from 320 to 380°C and one repeated temperature (360°C) at the end to confirm that the catalyst is not deactivated. The pressure and the weight hourly space velocity (WHSV) are chosen to achieve different conversion ranges for each temperature while minimizing coking or sintering the catalyst. The catalyst is considered as non-deactivated if the conversion at the repeated temperature 360 °C at the end of the test is found identical to the one at the same temperature 360 °C before. For the other tests, are varied each time one operating condition to make comparison with the others at one temperature of 360°C, which was found to give access to the wider conversion range by changing the reaction conditions. Test-1 to Test-5 aim at varying the weight hourly space velocity (WHSV) parameter

in order to unravel the conversion and reaction rate as a function of space time, by using Equations (III-42) and (III-43):

$$\text{WHSV} \left(\frac{\text{g}_{\text{MCH}}}{\text{h} \cdot \text{g}_{\text{cata}}} \right) = \frac{\text{Mass flow rate of MCH}}{\text{Catalyst mass}} = \frac{F_{\text{m,MCH}}}{m_{\text{cata}}} \quad \text{Equation (III-42)}$$

$$\text{Space time} \left(\frac{\text{h} \cdot \text{g}_{\text{cata}}}{\text{g}_{\text{MCH}}} \right) = \frac{1}{\text{WHSV}} = \frac{m_{\text{cata}}}{F_{\text{m,MCH}}} \quad \text{Equation (III-43)}$$

Test-7 to Test-10 aim at quantifying the impact of hydrogen partial pressure as compared to Test-1, keeping the methyl-cyclohexane partial pressure constant; while Test-1, 11 and 12 focus on the impact of methyl-cyclohexane partial pressure at constant hydrogen partial pressure. Van Trimont et al.⁵⁰ already performed a similar approach in order to estimate the partial reaction orders for each reactant, but for different reaction conditions and different catalysts. They used a sulfur-pretreated (100 ppm of sulfur) Pt/Al₂O₃ catalyst containing 0.59 wt% of platinum and the hydrogen partial pressure (P_{H₂}) varied from 5 to 20 bar at constant methyl-cyclohexane partial pressure (P_{MCH}) of 0.5 bar. The temperature employed was set at 350 °C and the weight hourly space velocity was around 30 (g_{MCH}·h⁻¹·g_{cata}⁻¹). The detailed comparison of these results will be presented later.

Notably, due to limitations of the set-up (both in terms of flows and minimal mass of catalyst), the WHSV was limited to 150 g_{MCH}·h⁻¹·g_{cata}⁻¹, corresponding to a minimal space time of 24 s·g_{cata}·g_{MCH}⁻¹. Indeed, if we increase the charge flow rate, the hydrogen flow rate has to be increased as well with regard to keep the H₂/HC ratio constant. The maximum hydrogen flow rate

for our laboratory set up is 300 L/h. Test-5 reaches this limit. Moreover, the minimal methylcyclohexane flow rate is 29 mL/h to ensure a stable flow rate.

2.2 Experimental protocol of catalytic tests

2.2.1 Catalyst activation

Before contacting the charge with the catalyst, the latter was activated in two *in situ* steps : drying and reduction. The drying process is undertaken by heating the catalyst to 150 °C at the heating rate of 5°C/min under a N₂ gas flow rate of 10 L/h, during 1 h. Then the temperature increases from 150 °C to 500 °C by same heating rate for around 1.2 h to thus undergo the reduction process performed at 500 °C for 5 h, under a H₂ gas flow rate of 30 L/h. These activation steps should be redone as long as the catalyst is unloaded and a new one is reloaded into the reactor during the test sequences.

2.2.2 Thermal profile inside the reactor

The catalytic tests are supposed to be undertaken under an isothermal condition. Nevertheless, the dehydrogenation reaction is very endothermic and when the reactant feed flow reaches the catalytic zone (Figure III-8) into the reactor, it passes firstly by the thermocouple T_{2c}, the one on the top. The whole catalytic zone measures 32.5 mm for the feed to flow through and when the feed flow arrives at T_{2a}, the endothermic reaction completes and the product forms. That explains the fact that the temperature from T_{2c} to T_{2a} decreases, the latter being at the lowest temperature compared to the other two thermocouples.

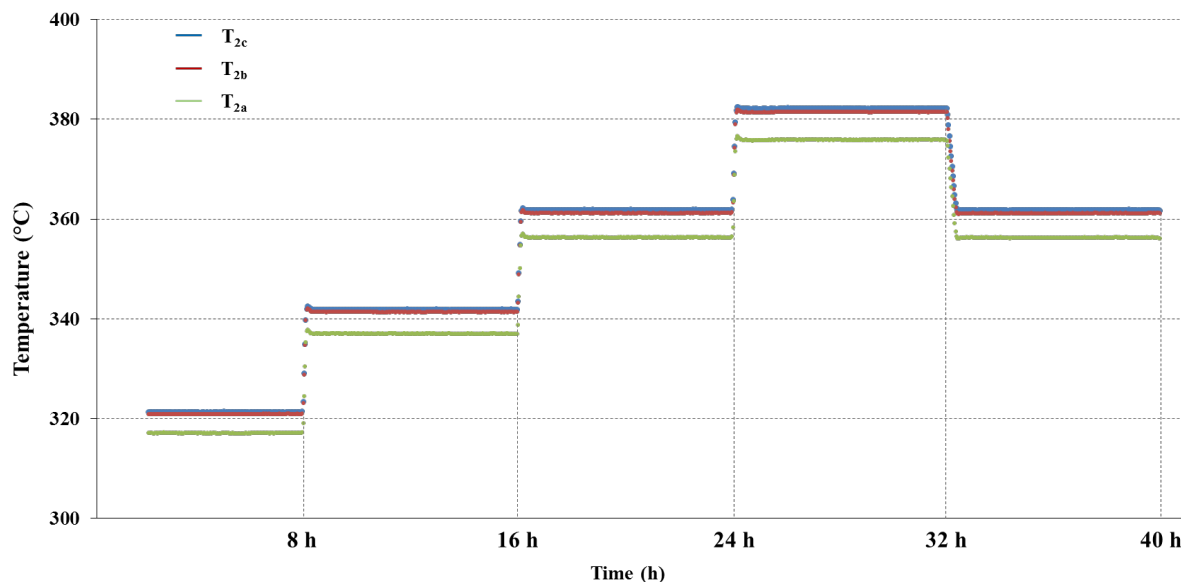


Figure III- 10 Thermal profile detected by three thermocouples during Test-1

The maximum deviation observed in Figure III-10 (T_{2a}) for the average measured temperature with respect to the recorded temperature is however about 3-4 °C, lower than in a previous study (10 °C).⁵⁵ We can thus conclude that the isothermicity is reasonable during the reaction. Figure III-10 corresponds to a complete and model Test-1 performed in our work. For each temperature studied, the reaction is left to execute during 8 h, in order to guarantee the reaction equilibrium before shifting to the next temperature. The automatic sampler (AS) (Figure III-7) collects hourly the product feed at the output of reactor, which makes 8 conversion points for each temperature.

2.2.3 Reactant conversion and mass balance calculations

Product yield in liquid phase

The automatic sampler allows us to analyze the liquid products collected hourly from the outlet of the reactor and to calculate the product yield obtained in the liquid effluent. From the chromatography spectrum, the only observed components are toluene and methyl-cyclohexane (more than 99% in total). Toluene only was detected as the product of the reaction, also in the gas effluent analyzed by gas chromatogram, which suggests that there are no obvious nor relevant side reactions happening beside the dehydrogenation reaction. Therefore, only methyl-cyclohexane and toluene were considered for further calculations. Note that this result also justifies why in the *ab initio* kinetic modeling we neglect the desorption of partially dehydrogenated molecules.

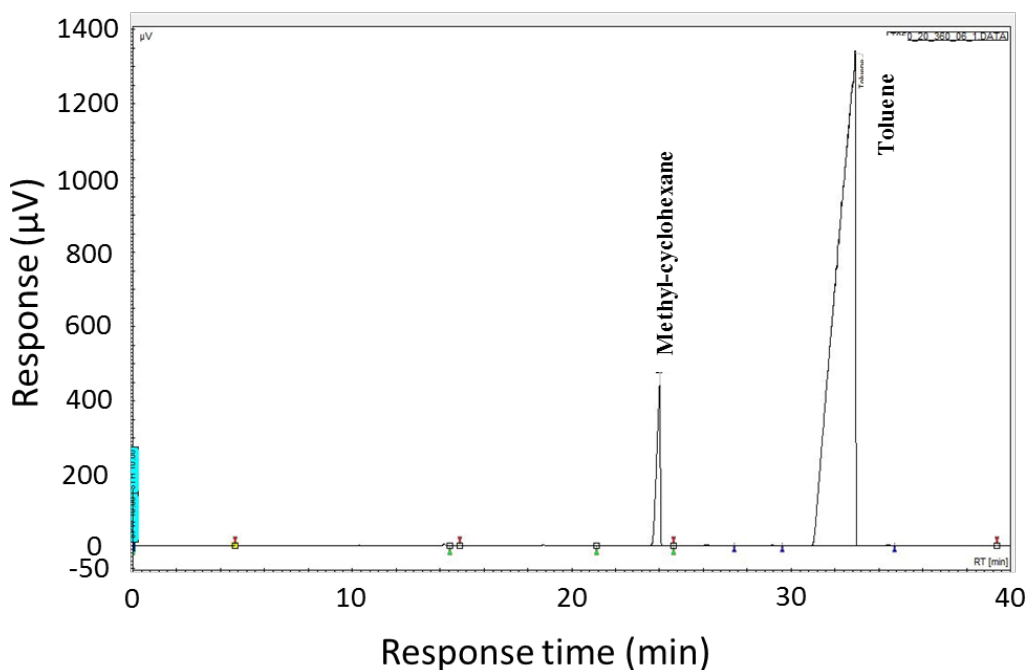


Figure III- 11 Liquid effluent chromatograph for Test - 8

An example of an obtained liquid effluent chromatogram is showed in Figure III-11. As the Flame Ionization Detector (FID) measures an ion flux, it is directly proportional to the number of carbon atoms in the molecule. The areas obtained from chromatograms were converted into mass fractions by using response factors (RF) calculated thanks to Equations (III-44) to (III-46) :

$$RF_{Tol} = \frac{aM_{Tol}}{n_{carbon} \times M_{carbon}} = 1.01$$

Equation (III-44)

$$RF_{MCH} = \frac{aM_{MCH}}{n_{carbon} \times M_{carbon}} = 1.08$$

Equation (III-45)

Where a is a correction factor that is given for correcting the molecular mass in the response factor expression of the gas chromatograph, the value of a equals 0.923; M_i is the molecular mass for each molecule i ; n_{carbon} is the number of carbon atoms of the molecules (7 in both cases). The toluene yield in weight in liquid phase $y_{Tol(l)}$ is then calculated by Equation (III-46).

$$y_{Tol(l)} = \frac{RF_{Tol}A_{Tol}}{RF_{Tol}A_{Tol} + RF_{MCH}A_{MCH}}$$

Equation (III-46)

A_i represents the peak area surface of each component in the chromatograph. These areas are normalized by the response factor RF_i .

Product yield in gaseous phase

The quantity of each component, methyl-cyclohexane and toluene in gaseous phase is determined by ampoule sampler system already explained in Figure III-9. Especially for high flow rate (Test-3 to Test-5) and high reaction temperatures ($T = 360, 380\text{ }^{\circ}\text{C}$), the charge and product feed parts became non-negligible in the outlet gaseous flow. Firstly we determined the quantity of each component in the 100 mL ampoule by using the reference of 250 μL cis-butene gas and also the analysis of the chromatograph on the 250 μL gas sample shown in the Figure III-12 as example.

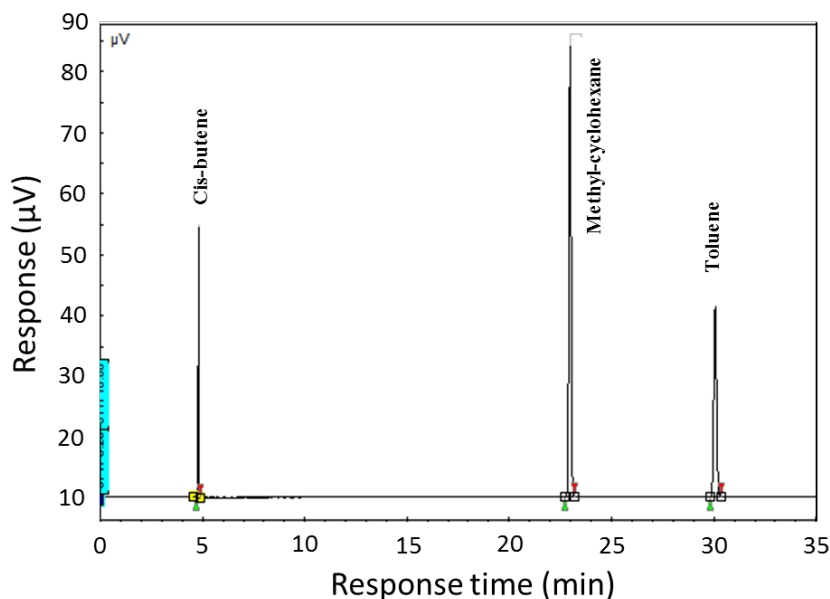


Figure III- 12 Gaseous effluent chromatograph for Test-7

From the pick areas A_i , we can calculate the amount of methyl-cyclohexane and toluene in the 100 mL of sample from Equations (III-47)-(III-49).

$$n_{0,MCH(g)} = n_{0,butene(g)} \times \frac{A_{MCH} RF'_{MCH}}{A_{butene} RF'_{butene}}$$

Equation (III-47)

$$n_{0,Tol(g)} = n_{0,butene(g)} \times \frac{A_{Tol} RF'_{Tol}}{A_{butene} RF'_{butene}}$$

Equation (III-48)

$$RF'_i = \frac{I}{n_{carbon}}$$

Equation (III-49)

$n_{0,i}$ represents the number of mole of each component i found in the sample volume $V_0 = 100$ mL, RF' is the new response factor employed, which is simply related to the number of carbon atoms counted in the molecule. Assuming that the amount of each component in our outlet gas feed volume $V_{measured}$ is proportional to that in ampoule volume V_0 , we thus have:

$$n_{MCH(g)} = n_{0,MCH(g)} \times \frac{V_{measured}}{V_0}$$

Equation (III-50)

$$n_{Tol(g)} = n_{0,Tol(g)} \times \frac{V_{measured}}{V_0}$$

Equation (III-51)

$$n_{H_2} = \frac{V_{measured}}{V_m} - n_{MCH(g)} - n_{Tol(g)}$$

Equation (III-52)

With V_m the molar volume of an ideal gas at 1 atmosphere of pressure and at room temperature (25 °C) equals 24.4 L/mol. So the toluene yield in outlet $Y_{Tol}\%$ by considering both the liquid and gaseous phases can be calculated according to Equation (III-53).

$$Y_{Tol}\% = \frac{m_{Tol(g)} + m_{Tol(l)}}{m_{Inlet}} \times 100\%$$

Equation (III-53)

With $m_{Tol(g)}$ the mass of toluene in gaseous phase, $m_{Tol(l)}$ the mass of toluene in liquid phase from the manual sampler (MS in Figure III-7), which can be obtained by the toluene yield in Equation (III-53). m_{Inlet} the inlet mass of methyl-cyclohexane liquid feed flow introduced into the set-up, which can be calculated from the inlet methyl-cyclohexane (MCH) volumetric rate flow (Table III-4) and density.

Mass balance

It is crucial to establish the mass balance between the inlet and the outlet, for the sake of the reliability of the calculated conversion. This mass balance could be affected by several factors, such as facility leaks, secondary reactions, manipulation uncertainties, etc. The mass balance can be established by comparing the total mass at the inlet and that at the outlet. The calculation is summarized in Table III-5.

Table III- 5 Mass balance between inlet and outlet for each catalytic test

	INLET	OUTLET
$m_{MCH(l)}$	$m_{MCH(l)} = F_{l,MCH} \cdot d_{MCH} \cdot t_{measured}$ $F_{l,MCH}$: MCH volumetric rate flow (ml/h) $d_{MCH} = 0.77$ (g/cm ³) $t_{measured}$: mass inlet during certain time (h)	$m'_{MCH(l)} = m_{(l)} \cdot (1 - y_{Tol(l)})$ $m_{(l)}$: mass collected by manual sampler (MS) $y_{Tol(l)}$: Toluene yield in liquid phase
$m_{MCH(g)}$	--	$m_{MCH(g)}$ determined by ampoule sampling
$m_{Tol(l)}$	--	$m_{Tol(l)} = m_{(l)} \cdot y_{Tol(l)}$
$m_{Tol(g)}$	--	$m_{Tol(g)}$ determined by ampoule sampling
m_{H_2}	$m_{H_2} = F_{g,H_2} \cdot M_{H_2} \cdot t_{measured} / V_{m,H_2}$ F_{g,H_2} : H ₂ gas volumetric rate flow (L/h) $M_{H_2} = 2$ (g/mol) $V_{m,H_2} = 24.1$ (L/mol)	m'_{H_2} determined by ampoule sampling
Total mass	$m_{Inlet} = m_{MCH(l)} + m_{H_2}$	$m_{Outlet} = m'_{MCH(l)} + m_{Tol(l)} + m'_{H_2} + m_{MCH(g)} + m_{Tol(g)}$
Balance %	$X\% = (m_{Outlet} - m_{Inlet}) / m_{Inlet} \cdot 100\%$ Loss : X% < 0 Gain : X% > 0	

The tolerance on the loss or gain on this mass balance is around 5 % - 10 % maximum, because of the uncertainty on the calculation by the unavoidable manipulation errors or facility defects. As we can observe in Table III-6, most of our tests have respected this tolerance. However, the loss or gain on the mass balance could indeed have some impacts on the toluene conversions and eventually underestimate the product yield. To correct this dependence caused by mass balance on our conversion, we adopted a normalization method on our conversion calculations.

Table III- 6 Mass balance calculated for each catalytic test along with their reaction conditions

	TEST-1	TEST-2	TEST-3	TEST-4	TEST-5	TEST-6	TEST-7	TEST-8	TEST-9	TEST-10	TEST-11	TEST-12
WHSV (g _{MCH} h ⁻¹ g _{cata} ⁻¹)	40	70	100	130	150	20	40	40	40	40	40	40
Space time (g _{cata} ·s·g _{MCH} ⁻¹)	90	51	36	28	24	180	90	90	90	90	90	90
Total Pressure (bar)	13	13	13	13	13	13	19.8	5.8	4.8	2.8	12.7	12.5
P(H₂) (bar)	12.2	12.2	12.2	12.2	12.2	12.2	19	5	4.0	2.0	12.2	12.2
P(MCH) (bar)	0.8	0.8	0.8	0.8	0.8	0.8	0.8	0.8	0.8	0.8	0.5	0.3
H₂/HC	15	15	15	15	15	15	24	6	5	2.5	24	41
Mass balance X%	320 : -6.7% 360 : - 10.7% 380 : -2.6%	--	-7.0%	-6.4%	-12.6%	--	- 5.9%	0.0%	- 3.6%	- 13.7%	- 5.6%	1.6 %

The normalization can be done on either outlet mass or inlet mass, by simply applying the ratio between total inlet mass and total outlet mass ($\frac{m_{Inlet}}{m_{Outlet}}$). Here it is given an example on normalized outlet mass appeared in Equation (III-53), specifically calculated for the normalized total liquid mass in outlet $m'_{Outlet(l)}$ and the gaseous toluene mass in outlet $m'_{Tol(g)}$:

$$m'_{Outlet(l)} = m_{Outlet(l)} \times \frac{m_{Inlet}}{m_{Outlet}}$$

Equation (III-54)

$$m'_{Tol(g)} = m_{Tol(g)} \times \frac{m_{Inlet}}{m_{Outlet}}$$

Equation (III-55)

Hence, the new normalized toluene yield in weight redefined from Equation (III-53) can be expressed as :

$$Y'_{Tol}\% = \frac{m'_{Tol(g)} + Y_{Tol(l)} \times m'_{Outlet(l)}}{m_{Inlet}} \times 100\%$$

Equation (III-56)

2.2.4 Reaction kinetics calculations

Arrhenius plot

Once the conversion is determined, the apparent activation energy can be obtained by assuming the reaction behaves as an irreversible first order reaction to the reactant (methylcyclohexane). Thus, the reaction rate can be written by power-law rate equation :

$$r = kP_{MCH} = -\frac{dP_{MCH}}{dt} \Leftrightarrow \ln\left(\frac{P_{MCH}}{P_{0,MCH}}\right) = -kt$$

$$\Leftrightarrow k = \frac{1}{t} \ln\left(\frac{1}{1-X_{MCH \rightarrow Tol}}\right)$$

Equation (III-57)

Where r is the overall reaction rate, k is the apparent reaction rate constant, t is the space time and $X_{MCH \rightarrow Tol}$ is the equivalent toluene yield in concentration (mol/mol), which can be deduced from Y_{Tol} by Equation (III-58).

$$Y_{Tol} = \frac{m_{Tol}}{m_{Inlet}} = \frac{n_{Tol}M_{Tol}}{n_{MCH,0}M_{MCH}}$$

$$\Rightarrow X_{MCH \rightarrow Tol} = \frac{n_{MCH,0} - n_{MCH}}{n_{MCH,0}} = \frac{n_{Tol}}{n_{MCH,0}} = \frac{Y_{Tol}M_{MCH}}{M_{Tol}}$$

Equation (III-58)

Meanwhile, according to the Arrhenius equation :

$$k = Ae^{\frac{E_a}{RT}} \Leftrightarrow \ln k = \ln A - \frac{E_a}{RT}$$

Equation (III-59)

Combing Equation (III-57) and Equation (III-59), we obtain Equation (III-60) which describes the relation between the reaction temperatures T and reaction constant k , provided that the space time is kept constant :

$$\ln \left[\ln \left(\frac{1}{1-X_{MCH \rightarrow Tol}} \right) \right] = -\frac{E_a}{RT} + const.$$

Equation (III-60)

For a temperature remaining within a small interval, we assume that the slope of this linear relation of $\ln \left[\ln \left(\frac{1}{1-X_{MCH \rightarrow Tol}} \right) \right]$ as a function of $\frac{1}{T}$ (called Arrhenius plot) is nearly constant, and we can deduce the apparent activation energy of the reaction for the targeted temperature.

Eyring plot

Henry Eyring developed the transition state theory in 1935 and Equation (III-61) gives the corresponding Eyring equation⁶¹ in the case of an order 1 elementary step.

$$k = \frac{k_B T}{h} e^{-\frac{\Delta_r G^\ddagger}{RT}} = \frac{k_B T}{h} e^{-\frac{\Delta_r H^\ddagger}{RT}} e^{-\frac{\Delta_r S^\ddagger}{R}}$$

Equation (III-61)

where k is the reaction rate constant, k_B is the Boltzmann constant, h is the Planck constant. This equation defines the relationship between the activation Gibbs free energy $\Delta_r G^\ddagger$, the activation enthalpy $\Delta_r H^\ddagger$, the activation entropy $\Delta_r S^\ddagger$ and the reaction rate constant.

Once more, if we combine Equation (III-57) and Equation (III-61), we will then have :

$$\ln\left(\frac{k}{T}\right) = \ln\left[\frac{\ln\left(\frac{1}{1-X_{MCH \rightarrow Tol}}\right)}{T}\right] = -\frac{\Delta_r H^\ddagger}{R} \cdot \frac{1}{T} + const.$$

Equation (III-62)

$$\text{With } const. = \ln\left(\frac{k_B}{h}\right) + \frac{\Delta_r S^\ddagger}{R}.$$

For a temperature remaining within a small interval, we assume that the slope of this

linear relation of $\ln\left[\frac{\ln\left(\frac{1}{1-X_{MCH \rightarrow Tol}}\right)}{T}\right]$ as a function of $\frac{1}{T}$ is constant, and we can thus calculate the

apparent activation enthalpy of the reaction for the targeted temperature. Simultaneously, the Eyring plot allows also an access to the pre-factor term depending on the activation entropy.

Experimental reaction rate

During the experiments, the methyl-cyclohexane conversions to toluene were obtained by Equation (III-56) and (III-58), for each experimental space time. Normally, if the studied conversion plotting curve is continuous as a function of space time, one can calculate the reaction rate at one specified experimental point by simply deriving the slope of the curve on this point. However, the curve is discontinuous in our case, due to a limited sampling of conversion with respect to space time. So, in this case, we use the points before and after to estimate the slope of the middle point, as presented in Figure III-13.

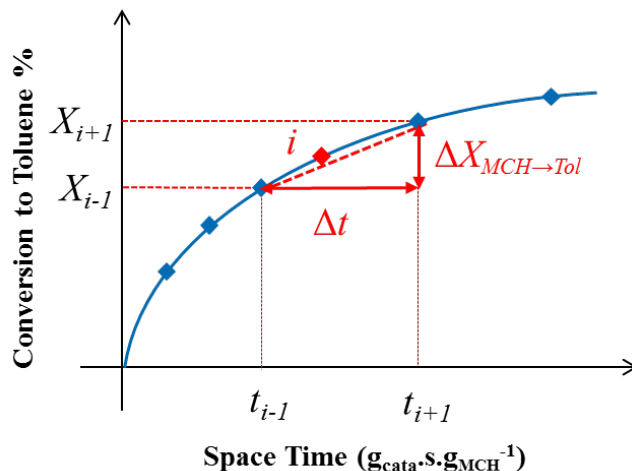


Figure III- 13 Scheme depicting the determination of experimental reaction rate of point i (red point) on the conversion plot scheme as a function of space time

So, for a flow system at steady-state conditions, the reaction rate of the point i at a given space time (or conversion) can be calculated by using the experimental data of t_{i-1} , X_{i-1} , t_{i+1} and X_{i+1} . Then, we have :

$$r_i = \frac{\Delta X_{MCH \rightarrow Tol}}{M_{MCH} \Delta t} \quad \text{Equation (III-63)}$$

Where $\Delta X_{MCH \rightarrow Tol}$ is the variation of the molar conversion of methyl-cyclohexane to toluene ($= X_{i+1} - X_{i-1}$) at a given space time for a space time variation, Δt ($= t_{i+1} - t_{i-1}$). M_{MCH} stands for the molar mass of methyl-cyclohexane.

References

- (1) Parr, R. G.; Yang, W. T. *Density-Functional Theory of Atoms and Molecules*; Oxford Science Publications, 1989.
- (2) Szabo, A.; Ostlund, N. S. *Modern Quantum Chemistry: Introduction to Advanced Electronic Structure Theory. Chapter 3. The Hartree-Fock Approximation*; Dover Publications, 1989.
- (3) Slater, J. C. *Phys. Rev.* **1929**, *34*, 1293–1323.
- (4) Hohenberg, P.; Kohn, W. *Phys. Rev. Lett* **1964**, *136*, B864.
- (5) Trefethen, L. N.; Bau, III, D. *Numerical Linear Algebra*; SIAM., 1997.
- (6) Kohn, W.; Sham, L. J. *Phys. Rev. Lett* **1965**, *140*, A1133.
- (7) Cramer, C. J. *Essentials of computational chemistry. Theories and models*, 2nd; Wiley&Sons Ltd, 2003.
- (8) Jensen, F. *Introduction to computational chemistry*; Wiley&Sons Ltd, 2003.
- (9) Perdew, J. P.; Kieron, B.; Ernzerhof, M. *Phys. Rev. Lett* **1996**, *77*, 3865–3868.
- (10) Grimme, S. *J. Comput Chem.* **2006**, *27*, 1787–1799.
- (11) Klimes, J.; Bowler, D. R.; Michaelides, A. *J. Phys. Condens. Matter.* **2010**, *22*, .022201.
- (12) Klimes, J.; Michaelides, A. *J. Chem. Phys.* **2012**, *137*, 120901.
- (13) Steinmann, S. N.; Corminboeuf, C. *J. Chem. Phys.* **2011**, *134*, .044117.
- (14) Steinmann, S. N.; Corminboeuf, C. *J. Chem. Theory Comput.* **2011**, *7*, 3567–3577.
- (15) Bucko, T.; Lebegue, S.; Hafner, J.; Angyan, J. G. *Phys. Rev. B: Condens. Matter Mater. Phys.* **2013**, *87*, 64110.
- (16) Seminario, J. M.; Politzer, P. *Modern Density Functional Theory : A Tool for Chemistry*; Elsevier Science, 1995.
- (17) Scacchi, G.; Bouchy, M.; Foucaut, J. F.; Zahraa, O.; Fournet, R. *Cinétique et catalyse, 2e édition*; Lavoisier, 2011.
- (18) Larmier, K. Thesis : Approche moléculaire de la réactivité des alcools sur catalyseurs acido-basiques, Université de Pierre et Marie Curie, 2014.
- (19) Morin, C. Thesis : Étude quantique de l'activité des surfaces de métaux de transition pour la transformation des molécules aromatiques par catalyse hétérogène; Laboratoire de Chimie, ENS de Lyon, 2004.
- (20) Silaghi, M. C. Thesis : Ab initio Molecular Modelling of the Dealumination and Desilication Mechanisms of Relevant Zeolite Frameworks, ENS de Lyon & IFPEN, 2014.
- (21) Bloch, F. *Z. Physik* **1929**, *52*, 555–600.
- (22) Kittel, C. *Introduction to Solid State Physics*; John Wiley & Sons, Inc, 1996.
- (23) Vanderbilt, D. *Phys Rev B* **1985**, *32*, 8412–8415.
- (24) Payne, M. C.; Teter, M. P.; Allen, D. C.; Arias, T. A.; Joannopoulos, J. D. *Rev. Mod. Phys* **1992**, *64*, 1045–1097.
- (25) Blöchl, P. E. *Phys. Rev. B* **1994**, *50*, 17953–17979.
- (26) Feynman, R. P. *Phys. Rev.* **1939**, *56*, 340–343.
- (27) Atkinks, P. W.; Friedman, R. S. *Molecular quantum mechanics, 3rd ed*; Oxford University

Press, 1997.

(28) Pulay, P. *Chem. Phys. Lett* **1980**, 73, 393.

(29) Press, W. H.; Flannery, B. P.; Teukolsky, S. A.; Vetterling, W. T. *Numerical Recipes*; Cambridge University Press, 1986.

(30) Kresse, G., Furthmüller, J. *Comput. Mater. Sci.* **1996**, 6, 15–50.

(31) Kresse, G.; Furthmüller, J. *Phys. Rev. B: Condens. Matter Mater. Phys.* **1996**, 54, 11169–11186.

(32) Kresse, G.; Joubert, J. *Phys. Rev. B: Condens. Matter Mater. Phys.* **1999**, 59, 1758–1775.

(33) Verlet, L. *Phys. Rev.* **2010**, 159, 98–103.

(34) Henkelman, G.; Jónsson, H. *J. Chem. Phys.* **2000**, 113, 9978–9985.

(35) Sheppard, D.; Terrell, R.; Henkelman, G. *J. Chem. Phys.* **2008**, 128.

(36) Mills, G.; Jacobsen, W. *Classical and quantum dynamics in condensed phase simulations. Chapter : Nudged elastic band method for finding minimum energy paths of transitions*; World Scientific Publishing, 1998.

(37) Henkelman, G.; Uberuaga, B. P.; Jónsson, H. *J. Chem. Phys.* **2000**, 113, 9901–9904.

(38) Fleurat-Lessard, P. Opt'n Path.: <http://perso.ens-lyon.fr/paul.fleurat-lessard/index.html>.

(39) Hafner Research Group, University of Vienna. Transition State Tools for VASP. <http://theory.cm.utexas.edu/vtsttools/>.

(40) Sackur, O. *Ann. Phys. (Berlin)* **1913**, 40, 67–86.

(41) Tetrode, H. *Ann. Phys. (Berlin)* **1912**, 38, 434–442.

(42) Tetrode, H. *Ann. Phys. (Berlin)* **1912**, 39, 255–256.

(43) Lin, C. Y.; George, M. W.; Gill, P. M. W. *Aust. J. Chem.* **2004**, 57, 365–370.

(44) Piccini, G.; Alessio, M.; Sauer, J.; Zhi, Y.; Liu, Y.; Kolvenbach, R.; Jentys, A.; Lercher, J. A. *J. Phys. Chem. C* **2015**, 119, 6128–6137.

(45) Piccini, G. M.; Sauer, J. *J. Chem. Theo. Comput.* **2013**, 9, 5038–5045.

(46) Canduela-Rodriguez, G.; Sabbe, M. K.; Reyniers, M. F.; Joly, J. F.; Marin, G. B. *Phys. Chem. Chem. Phys.* **2014**, 16, 23754–23768.

(47) Alhumaidan, F.; Cresswell, D.; Garforth, A. *Ind. Eng. Chem. Res.* **2011**, 50, 2509–2522.

(48) Rochefort, A. *J. Catal.* **1992**, 138, 482–490.

(49) Sinfelt, H. J.; Hurwitz, H.; Shulman, R. A. *J. Phys. Chem.* **1960**, 64, 1559–1562.

(50) Van Trimpont, P. A.; Marin, G. B.; Froment, G. F. *Ind. Eng. Chem. Fundam.* **1986**, 25, 544–553.

(51) Usman, M.; Cresswell, D.; Garforth, A. *Ind. Eng. Chem. Res.* **2012**, 51, 158–170.

(52) Maria, G.; Marin, A.; Wyss, C.; Muller, S.; Newson, E. *Chem. Eng. Sci.* **1996**, 51, 2891–2896.

(53) Van Grieken, R. E., Markowicz, A. A. *Handbook of X-Ray Spectrometry (2nd ed.)*, Marcel Dekker Inc, 2002.

(54) Jansen, W.; Slaughter, M. *Am. Mineral* **1982**, 67, 521–533.

(55) Salgueiro Dos Loios, J. *Intership : Developement of a catalytic test on a model reaction for naphtha catalytic reforming, IFPEN*, 2015.

(56) Leprince, P. *3 Procédés de Transformation. Chap.4 Reformage Catalytique, 105-169*;

Technip, 1998.

(57) Gjervan, T.; Prestvik, R.; Holmen A. *Basic Principles in Applied Catalysis. Catalytic Reforming*, 125-158; Springer, 2004.

(58) Rahimpour, M. R.; Jafari, M.; Iranshahi, D. *Appl. Energy* **2013**, *109*, 79–93.

(59) Verstraete, J. Thesis : Kinetische Studie van de Katalytische Reforming van Nafta over een Pt-Sn/Al₂O₃ Katalysator, Universiteit Gent, 1997.

(60) Myers, C. G.; Lang, W. H.; Weisz, P. B. *Ind. Eng. Chem. Res.* **1961**, *53*, 299–302.

(61) Eyring, H. *J. Phys. Chem.* **1935**, *3*, 107–115.

Appendix-III

1. Quantum chemistry

1.1 – The Schrödinger equation

Any problem in the electronic structure of the matter is covered by Schrödinger's equation including time dependency. In most cases studied here, however, one is concerned with atoms and molecules without time-dependent interactions. Hence, in order to obtain the energy of a polyatomic system, one must solve the following simplified Schrödinger equation ¹:

$$\hat{H} \left| \Psi(\vec{r}_1, \vec{r}_2, \dots, \vec{r}_N, \vec{R}_1, \vec{R}_2, \dots, \vec{R}_M) \right\rangle = E \left| \Psi(\vec{r}_1, \vec{r}_2, \dots, \vec{r}_N, \vec{R}_1, \vec{R}_2, \dots, \vec{R}_M) \right\rangle \quad \text{Equation (III-64)}$$

Where E is the electronic energy, Ψ is the wave function, and \hat{H} is the Hamiltonian operator. The product Ψ with its conjugate complex $|\Psi\Psi^*|$ (or often noted as $|\Psi|^2$) is known as probability distribution function of the particle, in the sense to express the probability of finding the system with position coordinates. In the case of a molecular system (with several electrons and nuclei), Ψ is a function of the coordinates of electrons and nucleus of the molecule that we define here by, respectively, \vec{r} and \vec{R} . The different solutions of the Equation (III-65) correspond to different steady states of the molecular system. The state with the lowest energy is called ground state of the system.

For a molecular system, Hamiltonian consists of terms of kinetic energy and potential energy of nucleus and electrons:

$$\hat{H} = \hat{T}_e + \hat{T}_n + \hat{V}_{ee} + \hat{V}_{nn} + \hat{V}_{ne} \quad \text{Equation (III-65)}$$

With

$$\hat{T}_e = -\frac{1}{2} \sum_{i=1}^N \nabla_i^2, \quad \hat{T}_n = -\sum_{A=1}^M \frac{\nabla_A^2}{2M_A},$$

$$\hat{V}_{ee} = \sum_{i=1}^N \sum_{i>j}^N \frac{1}{|r_i - r_j|}, \quad \hat{V}_{nn} = \sum_{A=1}^M \sum_{B>A}^M \frac{Z_A Z_B}{|R_A - R_B|}, \quad \hat{V}_{ne} = -\sum_{i=1}^N \sum_{A=1}^M \frac{Z_A}{|r_i - R_A|} \quad \text{Equation (III-66)}$$

The operator for the electrons kinetic energy \hat{T}_e , for the kinetic energy of the nuclei \hat{T}_n , the one for describing the electrostatic electron-electron interaction \hat{V}_{ee} , the electrostatic nucleus-nucleus interaction \hat{V}_{nn} and the electrostatic nucleus-electron interaction \hat{V}_{ne} . They are all given in atomic units. In the above shown equations M_A and Z_A stand for the mass and charge of a nucleus, respectively.

1.2 – The Born Oppenheimer approximation

As the Schrödinger equation of a many-body system can neither analytically be solved, one has to make approximations. The Born Oppenheimer (B.O)¹⁷ approximation is considered as the first approximation used for simplifying the resolution of Schrödinger equation. The idea in this approach lays in the separation of electron and nucleus motion by using the fact that nucleus, due to their higher mass (several 10^3 times heavier), move much slower than electrons. So we can consider that electrons react instantaneously to any position change of nuclei. This approximation makes the assumption that the kinetic energy and electrostatic repulsion term of the nuclei in the total Hamiltonian can be considered as constant and independent of the time, hence resulting in

an electronic Hamiltonian describing the motion of N electrons in an external field of M fixed point charges:

$$\hat{H}_{elec} = \hat{T}_e + \hat{V}_{ee} + \hat{V}_{ne} \quad \text{Equation (III-67)}$$

Where the solution to this electronic Hamiltonian is the electronic wave function

$$\Psi_{el} = \Psi_{el}(r_1, r_2, \dots, r_i; R_1, R_2, \dots, R_A) \quad \text{Equation (III-68)}$$

It describes the electron motion explicitly and the nuclear coordinates parametrically, i.e. for a given nuclei configuration Ψ_{el} is a different function of the electron coordinates. Hence, the total energy E_{tot} is then the sum of electronic energy E_{elec} and the constant term for the nuclear repulsion E_{nn} . Thus,

$$\hat{H}_{elec} \Psi_{elec} = E_{elec} \Psi_{elec} \quad \text{Equation (III-69)}$$

and

$$E_{tot} = E_{elec} + E_{nn} \quad \text{Equation (III-70)}$$

The BO approximation allows us to build an equation of electronic Hamiltonian which ignores the term kinetic energy of nucleus (T_n).

$$H_{el} = -\frac{1}{2} \sum_i^{el} \nabla_i^2 - \sum_i^{el} \sum_I^n \left(\frac{Z_I}{r_{iI}} \right) + \sum_i^{el} \sum_{j>i}^{el} \left(\frac{1}{r_{i,j}} \right) + \sum_I^n \sum_{J<I}^n \left(\frac{Z_I Z_J}{R_{I,J}} \right) \quad \text{Equation (III-71)}$$

1.3 - Variational principle for the ground state

When a system is in the state Ψ , which may or may not satisfy the Schrödinger equation, the average of many measurements of the energy is given by the formula:¹

$$E[\Psi] = \frac{\langle \Psi | \hat{H} | \Psi \rangle}{\langle \Psi | \Psi \rangle} \quad \text{Equation (III-72)}$$

Where

$$\langle \Psi | \hat{H} | \Psi \rangle = \int \Psi^* \hat{H} \Psi \, dx \quad \text{Equation (III-73)}$$

Since, furthermore, each particular measurement of the energy gives one of the eigenvalues of \hat{H} , we immediately have

$$E[\Psi] \geq E_0 \quad \text{Equation (III-74)}$$

The energy calculated from a given Ψ is beyond to the true ground-state energy E_0 . Full minimization of the functional $E[\Psi_0] = E_0$; that is,

$$E_0 = \min_{\Psi} E[\Psi] \quad \text{Equation (III-75)}$$

For a system of N electrons and given nuclear potential $v(\mathbf{r})$, we use

$$\delta \left[\langle \Psi | \hat{H} | \Psi \rangle - E \langle \Psi | \Psi \rangle \right] = 0 \quad \text{Equation (III-76)}$$

to define a procedure for giving from N and $v(\mathbf{r})$ to the ground-state wave function Ψ . Note that in this statement there is no mention of the kinetic-energy or electron-repulsion parts of \hat{H} , because these are universal so that they are determined by N . We say that E is a functional of N and $v(\mathbf{r})$.

2. Granulometry study for the employed catalyst

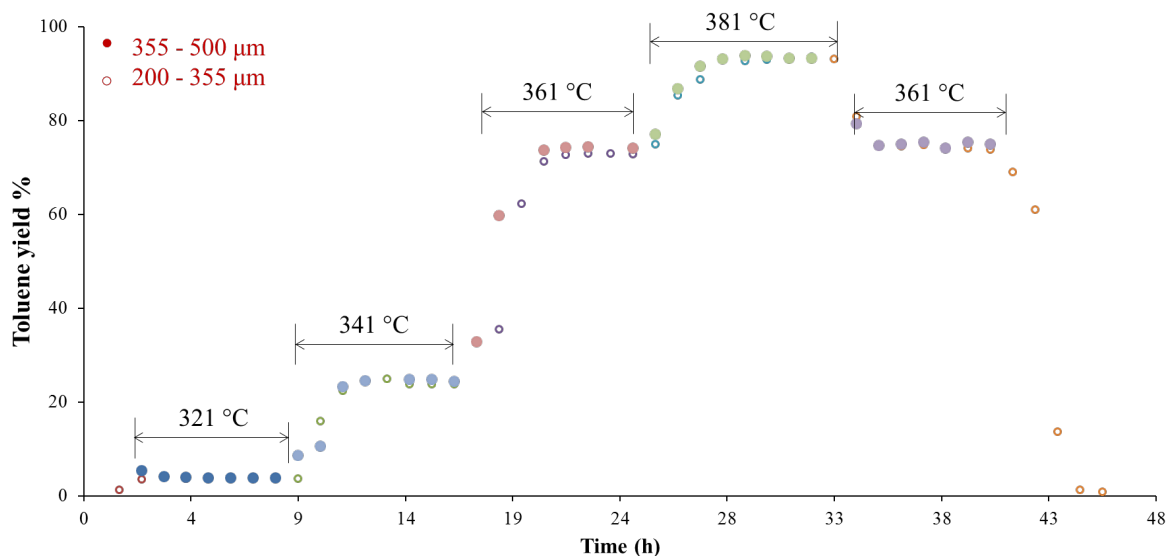


Figure III- 14 Comparison of toluene yields on different granulometries (200-355 μm vs 355-500 μm)

The comparison of toluene yields is made on two different granulometries : 200 – 355 μm and 355 – 500 μm. No great conversion difference is observed in Figure III-14 at all four temperatures. For the sake of reducing the diffusion limitation of the catalyst, the 355 – 500 μm is chosen.

CHAPTER IV - KINETICS OF METHYLCYCLOHEXANE DEHYDROGENATION ON ULTRA-DISPERSED Pt/Al₂O₃ CATALYSTS: ELEMENTARY STEPS FROM AB INITIO CALCULATIONS

Introduction

This chapter is devoted to the DFT calculations of the free energy profiles of the dehydrogenation steps of methyl-cyclohexane into toluene on Pt₁₃/γ-alumina systems. We will proceed as follows: We will first start by recalling the atomistic model used in *section 1.* Due to the complexity of the reaction network, we will first identify one representative pathway involving 4-methylcyclohexene based on a preliminary analysis of the stability of C₇H₁₂ intermediates (*section 2.*) at PBE level. The adsorbed configuration of 4-methylcyclohexene will be then refined as a function of Pt sites and by molecular dynamics in *section 3.* Such a study will be generalized to other intermediates involved along the dehydrogenation pathway relating to 4-methylcyclohexene (*section 4.*). A comparison with the Pt(111) surface will be also given in *section 3.* and *4.* To analyze the effect of dispersion corrections, a systematic comparison of the structure and energetics of these intermediates will be then analyzed with the PBE and PBE-dDsC functionals in *section 5.* The complete Gibbs free energy profiles will then be established at PBE and PBE-dDsC levels in *sections 6.* and *7.*, whereas a direct comparison of this profile with the case of the (111) surface will be provided in the final sections (*section 8.* and *9.*).

1. Atomistic model of the catalyst

As we mentioned in the introduction, a previously established Pt₁₃/γ-Al₂O₃ model of catalyst will be used to undertake a kinetic investigation. We focus here on the dehydrated and dechlorinated (100) γ-alumina surface as determined in previous DFT works^{1,2} using the bulk model of γ-alumina as solved by Krokidis et al.³ Indeed, in catalytic reforming conditions, this alumina facet is shown to be mostly dehydrated and dechlorinated.⁴ On this facet, a rather strong interaction exists between the metal cluster and the alumina support,⁵⁻⁷ which stabilizes a Pt₁₃ cluster with a bi-planar (BP) structure interacting with the γ-alumina surface through 7 platinum atoms (S1 to S7 in Figure IV-1).⁶ The morphology and electronic properties of the platinum cluster were shown to be very sensitive to the hydrogen pressure such as applied in the reforming conditions.⁶ By increasing the hydrogen coverage on the surface of these nano-particles, a reconstruction takes place, from the BP structure at low hydrogen coverage (θ_H) to a cuboctahedron (CUB) at H/Pt ratio higher than 1.5. This structural reconstruction is associated with a large change of the electronic properties of the platinum sites, from a metallic to a partially oxidized state. This phenomenon has been confirmed experimentally by X-ray absorption near-edge structure (XANES) and extended X-ray-absorption fine-structure (EXAFS) measurements on γ-Al₂O₃ supported Pt nano-particles.^{8,9} The hydrogen coverage at 25°C was found to increase from 1.9 to 2.5 H/Pt with an increase of pressure from 1 to 21 bars, revealed by XANES.⁹ The EXAFS revealed a structure change from 2D to 3D, evidenced by increasing Pt-Pt coordination numbers and decreasing Pt-O coordination numbers.¹⁰

By applying the results obtained in the DFT calculation of Mager-Maury et al.⁶, under catalytic reforming conditions (temperature of 800 K and a hydrogen partial pressure close to 10 bar), an interval of 6 to 18 hydrogen atoms per cluster is found to be the most stable situation.

Considering the bulkiness of the methyl-cyclohexane reactant and toluene product, the accessibility of both molecules is strongly hindered for H/Pt ratio greater than 1 (e.g. H coverage above 13). In addition, we also noticed that DFT calculations might slightly overestimate the H coverage when compared to XANES experiments,^{8,9} so we decided to undertake our study with 6 hydrogen atoms covering the Pt₁₃ cluster, as shown in Figure IV-1.

For 6 H atoms, the BP morphology of the platinum particle is only slightly modified with respect to the bare cluster, thus this allows us to define the layer interacting with the alumina surface as the atoms holding the letter “S”, and the layer contacting with vacuum space by using the letter “V” (see Figure IV-1). Likewise, we define all the hydrogen atoms by using letter “H”. We will start our mechanistic investigations by considering all those different adsorption sites, with migration of hydrogen atoms on the metal particles when needed (for example, to access the V6 site).

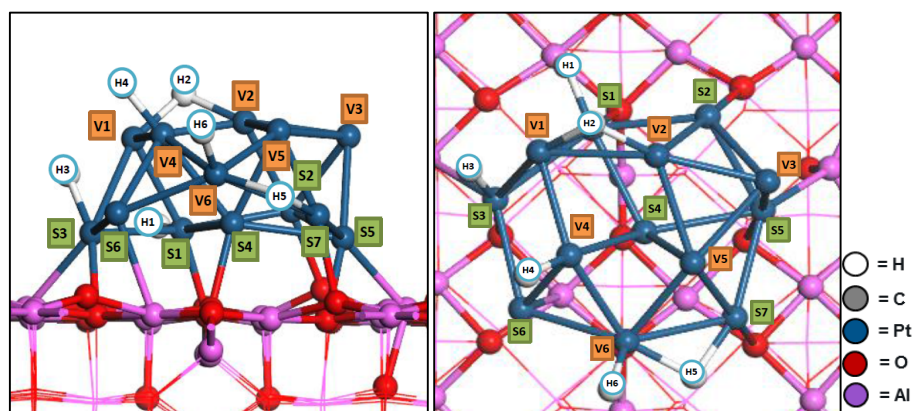


Figure IV- 1 Molecular structure of the starting model of Pt₁₃/γ-Al₂O₃ (100) with 6 adsorbed hydrogen atoms. The labels of each Pt site and H atom is reported as explained in the main text. Left: side view ; Right: top view.

2. Preliminary investigation on the stability of C₇H₁₂ intermediates

The proposed mechanism for the dehydrogenation of methyl-cyclohexane (MCH) into toluene (Tol) involves firstly two key intermediates invoked in numerous studies:¹¹⁻²⁰ methyl-cyclohexene (MCHe) and methyl-cyclohexadiene (MCHde). Nevertheless, if one analyzes the complete reaction network by considering all possible elementary steps, there is a large number of other possible surface intermediates (Figure IV-2). In particular, assuming subsequent mono-dehydrogenation steps, we can readily imagine the various radical intermediates formed after the C-H bond breaking from the initial molecule, before the formation of one new double-bond.

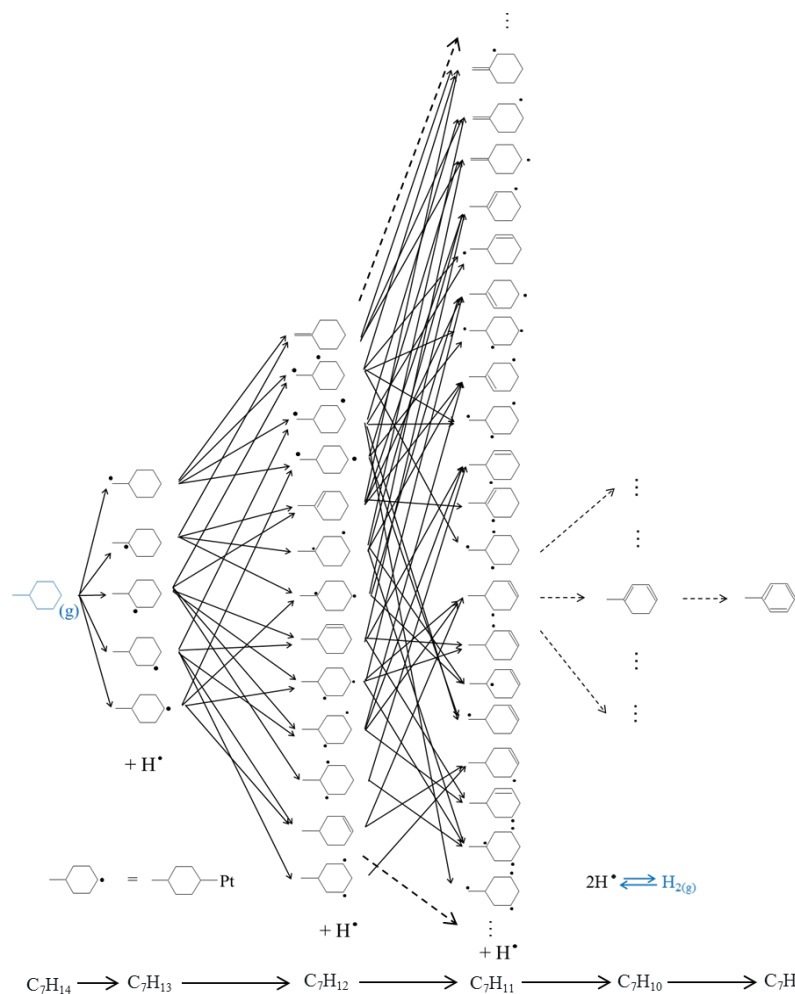


Figure IV- 2 Simplified and non-exhaustive reaction network of dehydrogenation of methyl-cyclohexane to toluene by sequential C-H bond cleavage at each step. (black dot means radical component formed on the metal surface)

In addition, for each intermediate, several adsorption configurations on the platinum cluster may exist. Performing an exhaustive investigation becomes very rapidly unrealistic. So, in order to analyze a complete reaction pathway, our strategy is to focus on some relevant intermediates formed with respect to the literature.

2.1 Respective stability of C₇H₁₂ radical and non-radical intermediates

Firstly, we study the dehydrogenation of methyl-cyclohexane (C₇H₁₄) into methyl-cyclohexene (C₇H₁₂) or related compounds on Pt₁₃H₆/γ-Al₂O₃ (100), the H₂ molecule being released in gas phase, as we would like to keep the hydrogen coverage constant. We start by a systematic exploration of the stability of the various possible C₇H₁₂ intermediates adsorbed on Pt₁₃H₆/γ-Al₂O₃ (100) involving thus numerous isomers for methyl-cyclohexene (MCH_e) and also radical intermediates as reported in Table IV-1 and Figure IV-3 for the two sites V3 and V5, which are chosen due to their availability for the molecule from a steric point of view (non-occupied by H atoms). The corresponding dehydrogenation electronic energies of methyl-cyclohexane_(g) into these different intermediate isomers (and dihydrogen in gas phase) have been evaluated and compared in Table IV-1. The dehydrogenation electronic energy of methyl-cyclohexane can be calculated in the same way of the free energy notion mentioned in Chapter III: Methodology, *section 1.3.1* with Equation (III-36) and (III-37), then we have :

$$\Delta_r E_{dehyd, MCH_{(g)}} = E\{C_7H_{12} - Pt_{13}H_6 / \gamma - Al_2O_3\} + E(H_{2(g)}) - E(C_7H_{14}) - E\{Pt_{13}H_6 / \gamma - Al_2O_3\}$$

Equation (IV-1)

Table IV- 1 Dehydrogenation energy of $MCH_{(g)}$ into C_7H_{12} intermediates on $Pt_{13}/\gamma-Al_2O_3$ (PBE level). The corresponding adsorption modes are illustrated in Figure IV-3.

	C_7H_{12}	Adsorption mode	Adsorption site(s)	$\Delta_r E_{dehyd, MCH(g)}$ (kJ/mol)
(a)		π	V3	32
(b)		π	V3	44
(c)		π	V3	32
(d)		π	V3	36
(e)		di- σ	V3V5	78
(f)		di- σ	V3V5	77
(g)		di- σ	V3V5	80

Note: The two black dots means two σ bonds connected with the Pt(V3) and Pt(V5) sites.

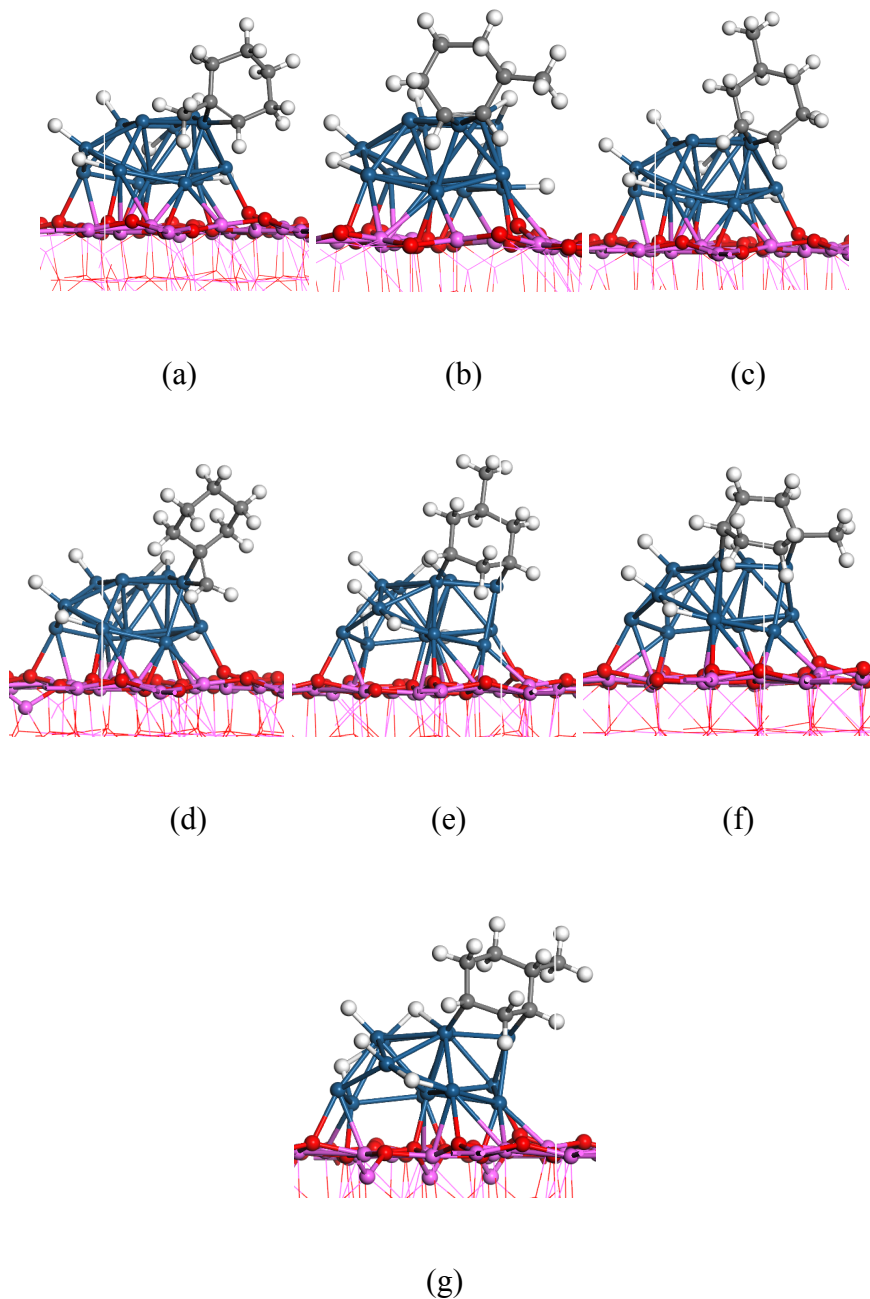


Figure IV- 3 Various dissociative adsorption modes during dehydrogenation of MCH to C_7H_{12} intermediates on the Pt cluster : (a) 1-Methyl-cyclohexene, (b) 3-Methyl-cyclohexene, (c) 4-Methyl-cyclohexene, (d) Methylene cyclohexene (e) C_3,C_5 -radical, (f) C_1,C_4 -radical, (g) C_2,C_4 -radical. Corresponding energies are given at the PBE level in Table IV-1.

Here the calculated energies are not yet corrected by the thermodynamic contributions and correspond to the electronic energies at 0 K only. The dehydrogenation energies are positive,

which reflects the energy cost to form the partially unsaturated species from the saturated MCH molecule, despite the adsorption of the former on the surface. Considering the relative dehydrogenation energies, it appears that all radical intermediates are far more unstable than the intermediates exhibiting a π bond. Among the latter, the 1 and 4-methyl-cyclohexene (lines (a) and (c) respectively in Table IV-1) are slightly more stable than the other ones. The peculiar stability of 4-methyl-cyclohexene (4-MCHe) can likely be explained by the fact that the methyl group in this configuration causes less steric hindrance between the whole molecule and the cluster. According to this first analysis, 4-MCHe-Pt₁₃H₆/ γ -Al₂O₃ will be chosen as a key relevant intermediate of methyl-cyclohexane dehydrogenation to be considered along the reaction network (see next sections).

2.2 Analysis of the adsorption modes of 4-methyl-cyclohexene with respect to ethylene, comparison with Pt(111)

We also found that the dissociative-adsorption di- σ mode is less favorable than π mode for all olefinic intermediates. Raybaud et al.²¹ reported for the dissociative-adsorption of ethane on Pt₁₃H₆/ γ -Al₂O₃ (100) that the di- σ mode for ethylene was preferred when the two hydrogen atoms removed from ethane are maintained on the cluster. A complementary study has been performed to identify the most stable adsorption modes related to the effect of hydrogen coverage (θ_H), as the cluster is richer in hydrogen ($\theta_H = 8$) in Raybaud et al., and the intrinsic nature of the molecules (Appendix-IV-1), so as to understand the discrepancy between the preferred adsorption modes of ethylene and MCHe. From these calculations, this can be assigned both to an effect of hydrogen coverage and nature of the adsorbed molecule.

The different adsorption modes of alkenes on the Pt(111) surface are reported in the literature from experimental methods. It is found for the case of ethylene, for temperature below 52 K, that the π mode is the most stable; when temperature is over 52 K and up to 220 K, di- σ bonded ethylene become dominant on the Pt (111) surface.²²⁻²⁴ While it is also reported that at the temperature 50 K, base pressure 3×10^{-11} Torr, a conversion occurs freely between the di- σ and π bonded ethylene, and the two surface species co-exist.²⁵ It is also pointed that the π mode is the precursor and primary intermediate for undergoing the ethylene hydrogenation reaction.²⁶ In our work, these two different adsorption modes of 4-methyl-cyclohexene were examined on Pt (111) surface, same as on the cluster. Table IV-2 presents their stabilities.

Table IV- 2 Dehydrogenation energy of relevant C₇H₁₂ adsorbed on Pt (111) surface at the PBE level

	C ₇ H ₁₂	Configuration	$\Delta_r E_{dehyd, MCH(g)}$ (kJ/mol)
(a)		di- σ	70
(b)		π	86
(c)		di- σ	102

As a matter of fact, the same conclusion can be drawn that the di- σ mode is more favorable at low coverage condition (here $\theta_H = 0$ ML). Otherwise, as for the supported cluster, the radical intermediate (c) in Table IV-2 is much less stable than the olefinic intermediates (a) and (b) by at least 16-32 kJ/mol. For this reason, we did not calculate all the possible radical intermediates, which exhibit di- σ dissociative-adsorption modes. The result is similar to the DFT study of Sabbe et al.²⁷ of cyclohexene on Pt(111). They found that the benzene hydrogenation reaction favored the path via 1,3-cyclohexadiene and cyclohexene, compared to the path via the

1,2,3,5- or 1,2,4,5-tetrahydrobenzene radicals, as also reported experimentally by Bera et al.²⁸. In contrast, the study of Saeys et al.^{29,30} reported a path via 1,3,5-trihydrobenzene and 1,2,3,5-tetrahydrobenzene as predominant. Campbell et al.¹⁹ found that the experimentally observed pathway for cyclohexane dehydrogenation on Pt(111) proceeds via adsorbed cyclohexene, again consistent with an ortho pathway as Sabbe et al. proposed.

3. Adsorption of 4-methylcyclohexene on Pt₁₃H₆/γ-Al₂O₃ (100): static and molecular dynamics investigation

3.1 Stability of the adsorbed intermediate on Pt₁₃H₆/γ-Al₂O₃ as a function of the adsorption site

In the previous paragraph, we calculated the dehydrogenation energy of methylcyclohexane(g) to 4-methyl-cyclohexene on the V3 platinum site. It is however important to check the sensitivity to the sites for this dissociative adsorption process. Meanwhile, the different possible adsorption conformations of 4-methyl-cyclohexene should also be carefully investigated as a function of the molecule orientation with respect to the cluster. Thus, a systematic geometry optimization investigation was performed, considering 20 adsorption sites and combination of sites and 57 conformations. The feature of the most stable conformations for each site are gathered in Table IV-3.

Table IV- 3 Calculated feature (dehydrogenation energy, distances) for different 4-MCHe adsorption modes at different adsorption sites at the PBE level

Adsorption Site(s)	Most stable adsorption mode	Number of adsorption conformations calculated	$\Delta_r E_{\text{dehyd,MCH(g)}}$ (kJ/mol)	$d_{\text{C3-C4}}(\text{\AA})$	$d_{\text{C3-M}}(\text{\AA})$	$d_{\text{C4-M}}(\text{\AA})$
V1	π	6	51	1.41	2.23	2.22
V2	π	6	84	1.42	2.17	2.22
V3	π	6	32	1.42	2.17	2.17
V4	π	1	71	1.43	2.18	2.14
V5	π	5	55	1.41	2.24	2.24
V6*	π	2	99	1.43	2.17	2.17
S2	π	3	63	1.43	2.12	2.13
S6	π	2	88	1.43	2.13	2.11
S7	π	2	130	1.40	2.27	2.33
V1-V2	di- σ	2	97	1.50	2.10	2.10
V2-V3	di- σ	2	72	1.48	2.14	2.13
V2-V5	di- σ	2	110	1.44	2.26	2.27
V3-V5	di- σ	2	74	1.46	2.12	2.17
V5-V6**	di- σ	2	73	1.50	2.13	2.10
V1-V4	di- σ	2	62	1.48	2.20	2.13
V4-V6	di- σ	2	127	1.50	2.12	2.12
V4-V5	di- σ	3	136	1.46	2.21	2.25
V2-V4	di- σ	2	129	1.50	2.17	2.15
V3-S2	di- σ	3	72	1.49	2.10	2.10
V2-S2	di- σ	2	69	1.48	2.10	2.10

*: The conformation involves the displacement of atom H6 from a top position on V6 to a bridge position between V4 and S6

** : The conformation involves the displacement of atom H6 from a top position on V6 to a bridge position between V6 and S6 (Figure IV-1)

It is shown that the most stable adsorption mode for 4-methyl-cyclohexene is always the π mode on site V3 (32 kJ/mol), which exhibits a minimum dehydrogenation energy. That is probably due to the fact that the V3 site has less hydrogen atoms surrounded and causes a lower steric hindrance for the adsorption of molecule. As already discussed in the previous paragraph, it is also observed that the π mode is generally more favored than di- σ mode for a given site. For example, $\Delta_r E_{\text{dehyd,MCH}}$ is equal to 32 and 55 kJ/mol at V3 and V5 for the π mode, respectively. Compared to the di- σ mode on both sites, $\Delta_r E_{\text{dehyd,MCH}}$ increases up to 74 kJ/mol.

The C3-C4 average distance for the π mode (1.42 Å) is much shorter than for the di- σ mode (1.48 Å). The C3-C4 (double bond) distance for the isolated methyl-cyclohexene molecule in gaseous phase measures 1.34 Å. This implies that the energy cost induced by the deformation of the molecule is likely higher in the di- σ mode. Meanwhile, the carbon-metal average distances for the di- σ mode (2.15 Å) is shorter than for the π mode (2.19 Å), which suggests that the di- σ bonded molecule exhibits higher interaction strength than π -bonded molecule. However, the compensation of these two forces between carbon-carbon bonds and carbon-metal bonds makes the π mode generally more favored than di- σ mode.

3.2 Static conformation analysis for the adsorption of 4-MCHe on the V3 site

It should also be noticed that for a given adsorption site and for the given π mode, several local energy minima of the system are found according to the orientation of the molecule. Considering the most stable adsorption π mode for 4-methyl-cyclohexene on the V3 site, the energy variations for different conformations are presented respectively in Table IV-4 and Figure

IV-4. It should be emphasized that these conformations were obtained by merely rotating the molecule from their initial positions. It can be shown that in this case, the variation remains within an interval of 16 kJ/mol, which means that temperature effect may allow the molecule to explore these various metastable states on this given site.

Table IV- 4 Dehydrogenation energies and bond lengths for the adsorbed 4-MCHe with the π mode on the V3 site for various conformations at the PBE level. The corresponding molecular structures are given at the PBE level in Figure IV-4.

Adsorption Site	Adsorption mode	$\Delta_r E_{\text{dehyd.MCH(g)}}$ (kJ/mol)	$d_{\text{C3-C4}}(\text{\AA})$	$d_{\text{C3-M}}(\text{\AA})$	$d_{\text{C4-M}}(\text{\AA})$
V3-1	π	43	1.42	2.18	2.20
V3-2	π	36	1.41	2.19	2.19
V3-3	π	48	1.43	2.18	2.14
V3-4	π	44	1.41	2.25	2.17
V3-5	π	48	1.41	2.30	2.16
V3-6	π	32	1.42	2.17	2.17

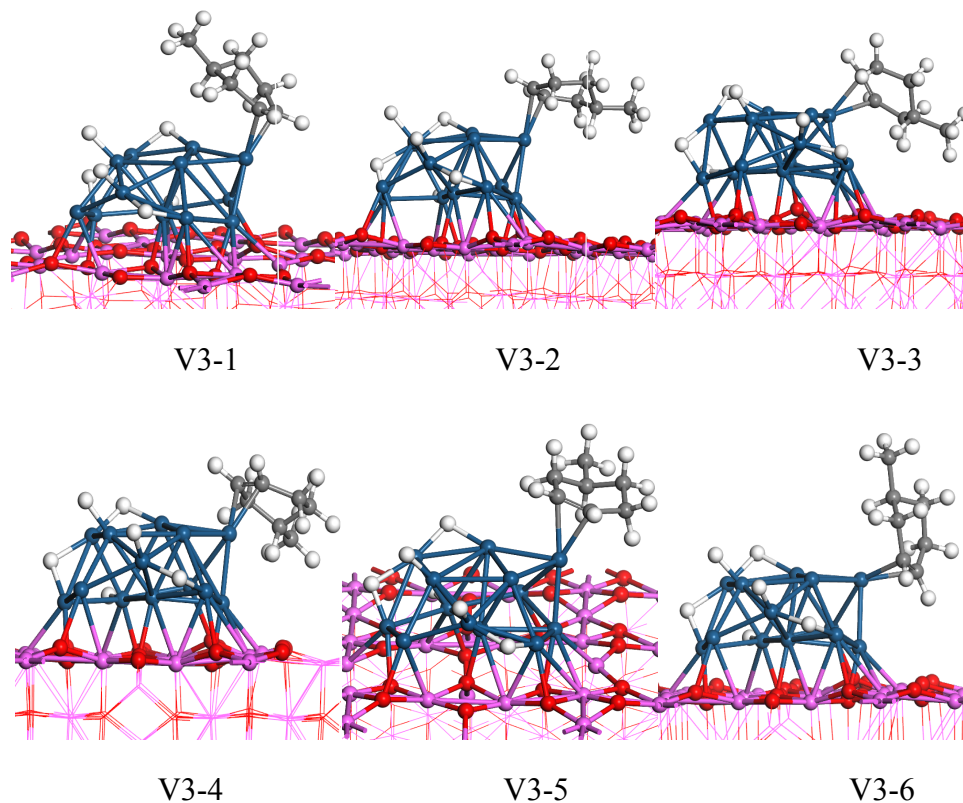


Figure IV- 4 Different conformations for the adsorbed 4-MCH with the π mode on the V3 site (PBE level). The corresponding energy data are given at the PBE level in Table IV-4.

While the molecule rotates around the axis perpendicular to the π -bond, the energy is minimized when the carbon-metal distances are also minimized and well symmetric (2.17 and 2.19 Å, for V3-6 and V3-2 respectively). For the less stable conformation V3-5, the difference between these two distances reaches 0.14 Å. In addition, for the most stable cases (V3-6 and V3-2), the methyl group of the molecule remains the furthest from the cluster and from the support surface, which may thus minimize the steric hindrance.

3.3 Molecular Dynamics conformational analysis of the adsorption of 4-MCHe on the V3 site

To further refine the adsorption geometry on the V3 site, we also used *ab initio* molecular dynamics (AIMD), in order to explore more systematically the various possible conformations of 4-methyl-cyclohexene on Pt₁₃H₆/γ-Al₂O₃ (100) at a given temperature, which enables to overcome the lowest energy barriers and thus to explore different potential minima.

The molecular dynamics approach explained in the Chapter III: Methodology, *section 1.2.4* has been performed at 3 distinct temperatures (500K, 800K and 1200K) for the 4-MCHe–Pt₁₃H₆/γ-Al₂O₃ (100) on the V3 site, starting from the most stable configuration (V3-6 in Figure IV-4). Figure IV-5 reports the profile of potential energy during molecular dynamics at these three temperatures.

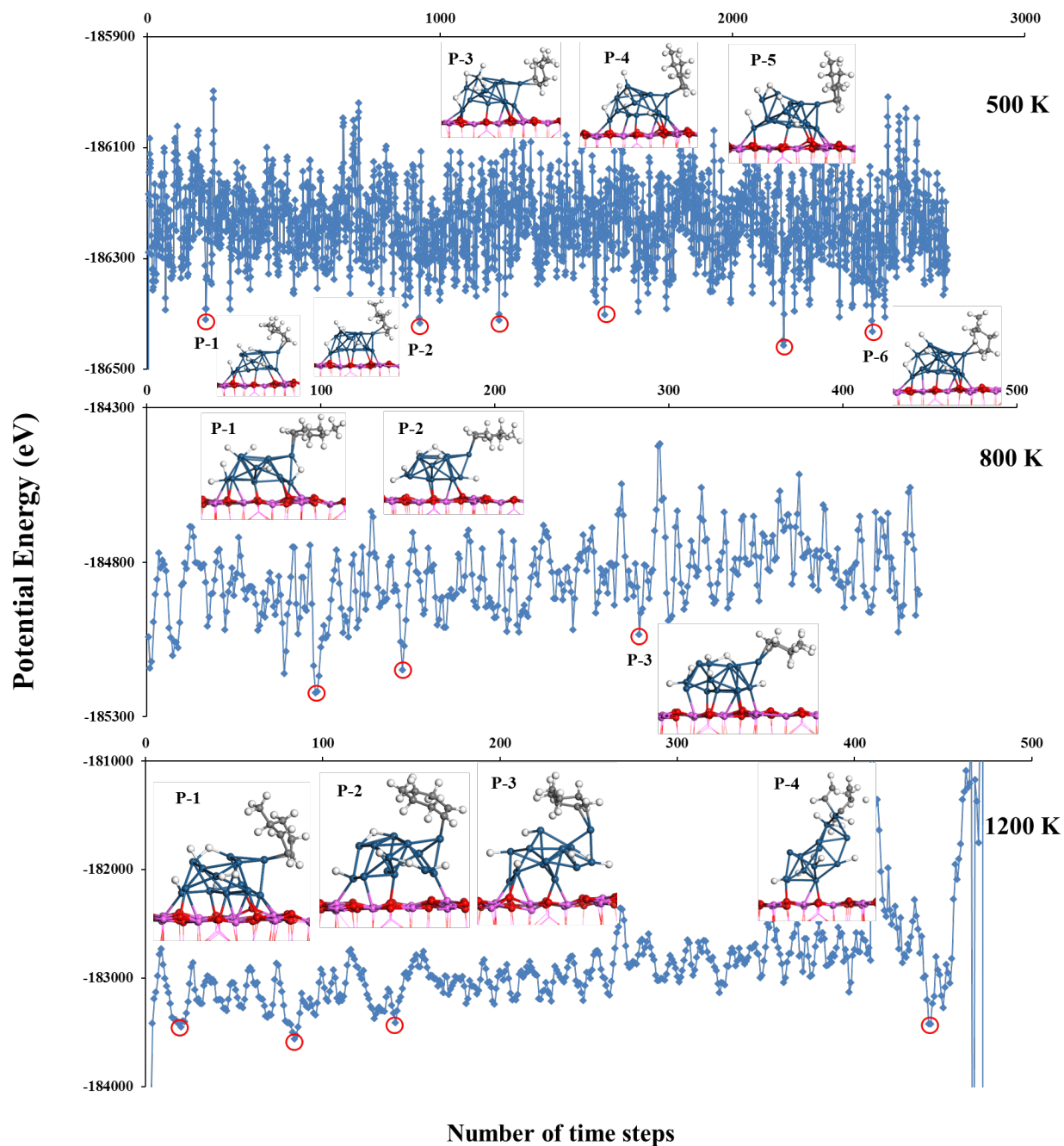


Figure IV- 5 Potential energy as a function of time steps during AIMD for 4-MChE–Pt₁₃H₆/γ-Al₂O₃(100) system on the V3 site : (a) 500 K; (b) 800K; (c) 1200K. (PBE level)
 (the structures correspond to the chosen points that correspond to local minimum on the energy curve shown by circles, labeled by “P-n”)

Depending on temperature, the potential energy fluctuates in a more or less large interval. For T=500 K, energy range is about 400 kJ/mol; for T=800 K, energy range is about 800 kJ/mol and for T=1200 K, energy range exceeds 1200 kJ/mol. Moreover, the system at higher temperature becomes unstable and the system is rapidly destroyed (at $t > 500$ fs). This explains why we extract less points to be quenched on the profile at T=1200 K than at T=500 K.

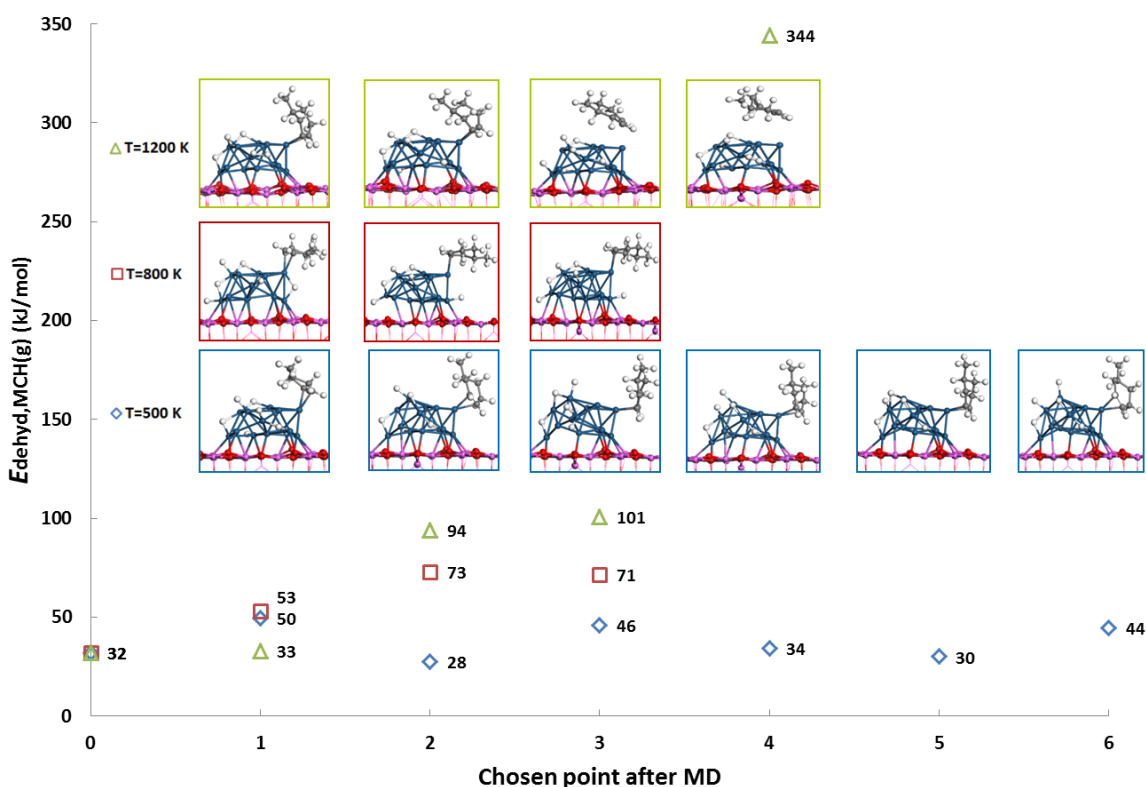


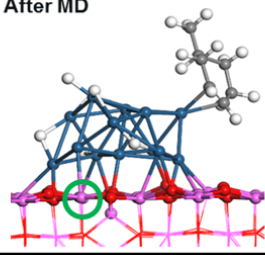
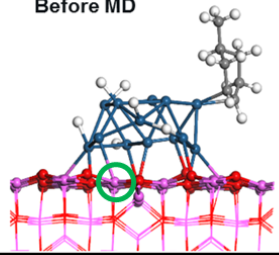
Figure IV- 6 Calculated dehydrogenation electronic energy after quenching the relevant points of AIMD at temperature 500, 800 and 1200 K (P-0 : initial system before MD calculation). The structures correspond to the optimized geometry after quench at the PBE level

Figure IV-6 presents the dehydrogenation electronic energy results for the quenched configurations chosen among the most relevant steps along AIMD after the quench. It shows that

the dehydrogenation energies obtained after quenching the systems from the MD at 500 K reach lower energy values compared to 800 and 1200 K. In particular, two new configurations are found at 500 K and exhibit lower energies than the starting configuration (obtained from the static approach). The configuration (P-2) leads to a dehydrogenation energy of methylcyclohexane(g) to 4-methyl-cyclohexene equal to 28 kJ/mol and will be considered as the most stable system for the further study. The temperatures 800 K and 1200 K are probably too high and induce a progressive destabilization of the molecule (even after quench), which slightly desorbed from the cluster as illustrated by the insets in Figure IV-6.

Therefore, it is concluded that at T= 500 K, the whole AIMD calculations plus quench method enables to reach lower energy configurations. Consequently, for the other intermediates presented later, MD calculations are undertaken at T=500 K systematically. The energy and structural data for this optimized system before and after AIMD are compared in Table IV-5.

Table IV- 5 Most relevant geometrical parameters for the system before and after MD at the PBE level

	After MD	Before MD
		
$E_{\text{dehyd,MCH(g)}} \text{ (kJ/mol)}$	28	32
H6 position	V4	V6
Distance $\text{Pt}_{(V6-S4)}, \text{\AA}$	2.79	2.53
*Distance $\text{Pt}_{(S6)}-\text{Al}_{87}, \text{\AA}$	2.62	2.58
Distance $\text{Pt}(V3)-\text{C}^{\ominus}, \text{\AA}$	2.15; 2.14	2.17; 2.17
Distance $\text{C}=\text{C}, \text{\AA}$	1.43	1.42

* : Atom Al₈₇ stands for the aluminum atom marked by green cycle on the structure images, the one which is linked with the Pt_(S6) before and after MD.

Firstly, it can be noticed that the shape of the metal cluster differs significantly. The distances between Pt(V6-S4) atoms are obviously increased by an order of 0.26 Å and simultaneously the distances between the metal cluster and the support are also changed, as it can be particularly observed that Pt(S6)-Al(87) has been raised because of the increase of Pt(V6-S4) distance. Meanwhile a migration of hydrogen (H6) atom from site V6 to V4 happened. Nevertheless, the molecule remains almost in a similar position becoming slightly closer to the metallic cluster (slightly shorter M-C distances).

On purpose of figuring out the effect of this deformation on the energy, the decomposition of the energy into various components has been performed. The dehydrogenation energy was decomposed to several parts, including the metal cluster deformation, the support deformation, the interaction of the metal cluster with adsorbed molecule, the interaction of the support with the metal cluster. The detailed analysis is reported in Appendix-IV-2. In summary, the separation of the metal cluster and the support is highly endothermic and requires + 980 kJ/mol. MD calculations weakened the interaction (decrease about 131 kJ/mol) between the metal cluster and the support. But these positive energies are mostly compensated by the final recombination energies of the metal cluster and the support. Whereas the deformation energy of the support is modest, the deformation of the metal cluster after MD reveals a gain on electronic energy of 81 kJ/mol. From this analysis, it can be concluded that MD calculations give access to the deformation of the metal cluster in the presence of the adsorbed intermediate, which can stabilize the system and needs to be considered during the simulation of other intermediates.

4. Stability of other intermediates along the dehydrogenation pathway, comparison with Pt(111) surface

Following the previous detailed study of the 4-methyl-cyclohexene key intermediate, we now investigate the other intermediates involved in the simplified reaction network of Figure IV-7. We consider here a mechanism composed of sequential C-H breaking reactions, assuming that the molecule undergoes a mono-dehydrogenation steps and that one hydrogen atom is removed from the molecule to cluster, which can be described by a dissociative adsorption step of atomic hydrogen. This hypothesis induces 6 C-H cleavage steps, which produce 3 radical intermediates: methyl-cyclohexyl, methyl-cyclohexenyl, and methyl-cyclohexadienyl. Since at each step, one extra hydrogen is added to the cluster, we remove every two steps the two extra hydrogen atoms by releasing one H₂ molecule, which can be described as an associative desorption of molecular hydrogen, in order to keep the hydrogen coverage almost constant (6 or 7 hydrogen atoms) along the reaction pathway.

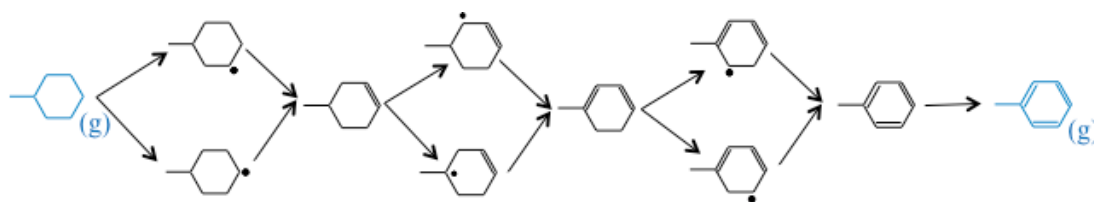


Figure IV- 7 Simplified network for the dehydrogenation of MCH into toluene via 4-methyl-cyclohexene

Based on the previous result on MCHe showing that the metallic cluster may undergo significant geometry relaxation, we add supplementary steps including AIMD simulations (500 K plus quench process) to check the stability of the clusters and find their optimal morphology, as a

function of the adsorbed intermediate. We also explore if a cluster geometry found for another adsorbed intermediate cannot be valid also for the given intermediate, crossing the {morphology, adsorbate} couples. The platinum cluster exhibits an important structural fluctuonality, which deserves the stabilization of the system according to the different intermediate that are formed. This finding reveals the whole complexity of the investigation of the reaction pathway and energy profile, which is very sensitive to the optimized structures.

Table IV- 6 Adsorption modes, sites and dehydrogenation electronic energies for key intermediates adsorbed on Pt₁₃H₆/γ-Al₂O₃ (100) along the dehydrogenation path at the PBE level.

	Species	Adsorption mode	Adsorption site	$\Delta_r E_{\text{dehyd.MCH(g)}} \text{ (kJ/mol)}$	
(a)		Methyl-cyclohexyl radical*	σ (chair-axial)	V3	-40
(b)			σ (chair-equatorial)	V3	-43
(c)		4-Methyl-cyclohexene	π	V3	28
(d)		4-Methyl-cyclohexenyl radical*	$\pi\sigma$ (conjugated)	V3-V5	23
(e)			$\pi\sigma$	V3-V5	23
(f)		1-Methyl-1,3-cyclohexadiene	$\sigma\pi\sigma$	V2-V3-V5	127
(g)			2π	V3-V5	98
(h)		1-Methyl-1,3-cyclohexadienyl radical*	$\pi\pi\sigma$	V2-V3-V5	24
(i)				$\pi\pi\sigma$	V2-V3-V5
(j)		Toluene	bri- $2\pi 2\sigma$	V2-V3-V4-V5	174
(k)			3π	V2-V3-V5	120

*For the radical species, the cluster keeps one more hydrogen atom transferred from the molecule (7 hydrogen atoms in total on the cluster in these cases).

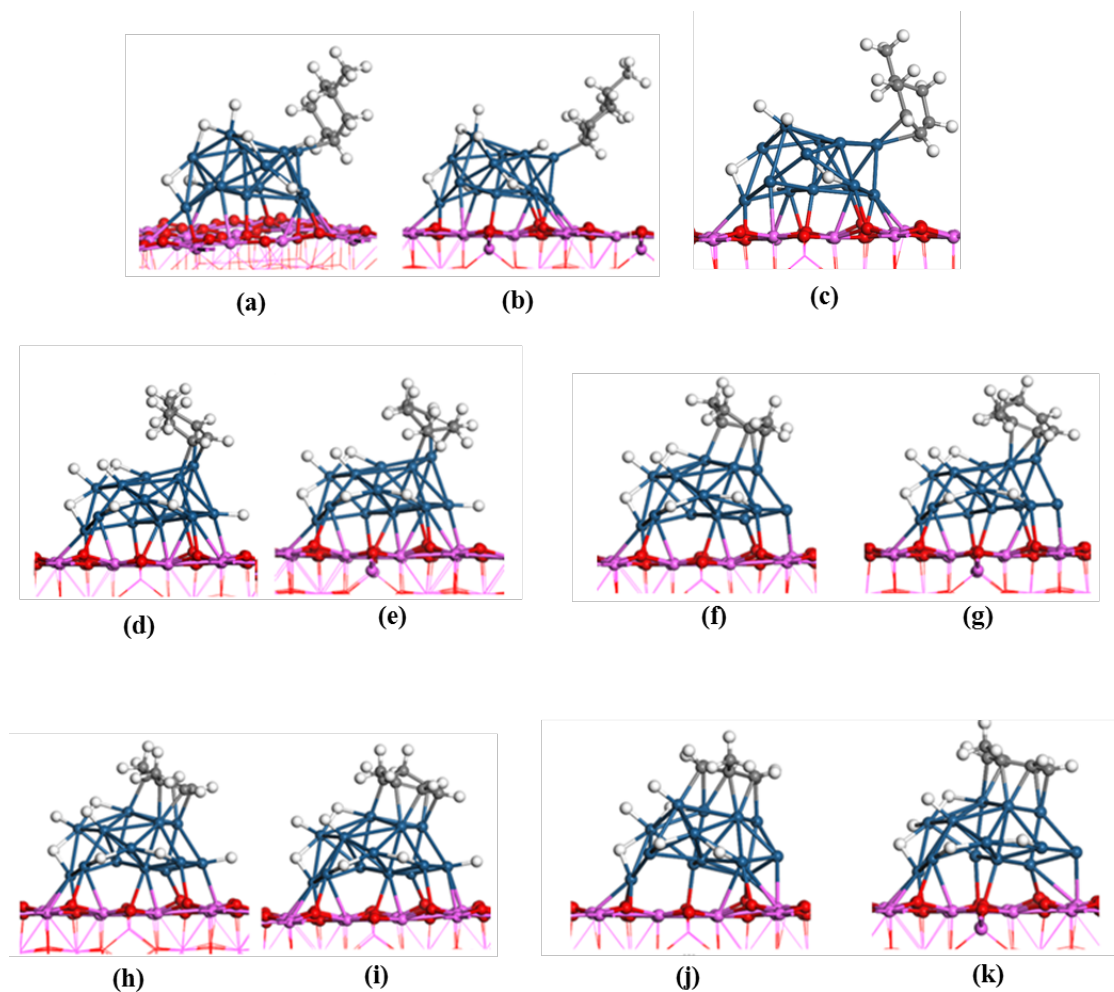


Figure IV- 8 Stable adsorption modes of each intermediate on $Pt_{13}H_6/\gamma-Al_2O_3(100)$ at the PBE level : (a) Methyl-cyclohexyl C3- σ , (b) Methyl-cyclohexyl C4- σ ; (c) Methyl-cyclohexenyl $\pi\sigma$ (conjugated) (d) Methyl-cyclohexenyl $\pi\sigma$; (e) Methyl-cyclohexadiene 1,4-di- σ -2,3- π (f) Methyl-cyclohexadiene 2 π ; (g) Methyl-cyclohexadienyl C5- $\sigma\pi\pi$ (h) Methyl-cyclohexadienyl C6- $\sigma\pi\pi$; (i) Toluene bri-2 π 2 σ (j) Toluene 3 π

Table IV-6 and Figure IV-8 present the features of the most stable geometries calculated for each intermediate at the PBE level. For non radical species, two relevant species are depicted. It must be noticed that the π mode adsorption becomes the predominant adsorption mode for methyl-cyclohexadiene and toluene. Ma et al.³¹ and Morin et al.^{32,33} found for 1,3-cyclohexadiene

and benzene adsorbed on Pt (111) surface, that the most stable adsorption modes are 1,4-di- σ -2,3- π and bri 2 π 2 σ , respectively. This result may again highlight the specific behavior of the cluster. Moreover a reconstruction of the cluster takes place in the course of the dehydrogenation reaction, as we can see from Figure IV-8. These reconstructions come up with several hydrogen migrations on the cluster, and with local structural reconstruction of the cluster itself, which aims at stabilizing the system by adapting its morphology and H locations as a function of the adsorption modes of the molecules. At this point, three cluster morphologies are observed, which implies that these reconstruction steps and hydrogen migration steps along with C-H cleavage steps must be considered for studying the reaction mechanism.

To enrich our understanding, we simultaneously achieved a complementary study of dehydrogenation of methyl-cyclohexane to toluene on Pt (111) surface at the PBE level to compare with the Pt₁₃H₆/ γ -Al₂O₃ (100) surface. The geometry and energy of the most stable intermediates are reported in Table IV-7.

Table IV- 7 Adsorption modes, sites and dehydrogenation electronic energies for key intermediates adsorbed on Pt (111) along the dehydrogenation path at the PBE level.

Species	Adsorption mode	$\Delta_r E_{\text{dehyd,MCH(g)}} \text{ (kJ/mol)}$	$d_{\text{C-C}} \text{ (\AA)}^{**}$	$d_{\text{Pt-C}} \text{ (\AA)}^{***}$
 Methyl-cyclohexyl radical*	σ (Chair-equatorial)	-5	1.53	3.22
 Methyl-cyclohexene	di- σ	69	1.53	3.15
 4-Methyl-cyclohexenyl radical*	$\pi\sigma$	65	1.51	2.67
 1-Methyl-1,3-cyclohexadiene	$\sigma\pi\sigma$	125	1.50	2.38
 1-Methyl-1,3-cyclohexadienyl radical*	$\sigma\sigma\pi\sigma$	108	1.49	2.23
 Toluene	brt- $2\pi2\sigma$	161	1.47	2.04

*For the radical species, the surface keeps one more hydrogen atom transferred from the molecule.

** $d_{\text{C-C}}$: average C-C bond length

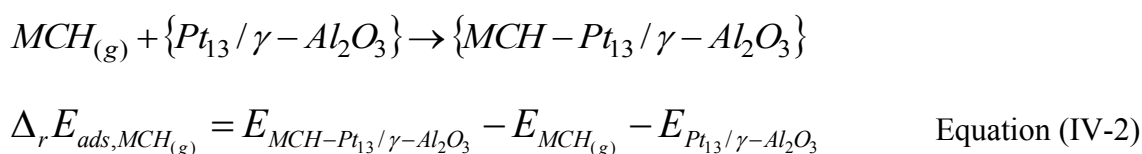
*** $d_{\text{Pt-C}}$: the vertical distance between the C6 ring center and the first metal surface layer.

Table IV-7 shows that adsorption configurations of the relevant intermediates on Pt (111) significantly differ from those obtained on the cluster. The results on the (111) surface agree with published studies.^{32,33,31} The di- σ mode of methyl-cyclohexene is more favorable on the Pt (111) surface. Meanwhile, a conjugated σ - π adsorption mode has been found for both methyl-cyclohexadiene and toluene, compared to the π mode on the cluster. One can explain this phenomenon related to the hydrogen coverage in the case that we investigate here for Pt (111), a $\theta_{\text{H}} = 0$ ML favors inherently the σ mode. The average bond length decreases indicating the formation of a double bond on the molecule. Moreover, the distance between the molecule and

the metal surface decreases in the course of the dehydrogenation, suggesting a stronger and stronger interaction between the molecule and the metal. At last, we find that the dehydrogenation energies for the most stable intermediates on cluster (Table IV-5) are less positive than those on Pt (111) at the PBE level, which suggests that our cluster model stabilizes better the intermediates, referring to the conventional Pt (111) ideal surface at the PBE level.

5. Effect of the functional : PBE vs. PBE-dDsC

The most relevant reaction pathway (with intermediates (b), (c), (d), (g), (h) and (k) in Figure IV-8) was thus chosen to pursue investigations at the PBE-dDsC level between the various possibilities shown in Figure IV-7, by choosing the more stable intermediates in terms of dehydrogenation electronic energy presented by Table IV-6. Meanwhile, the electronic energy were recalculated at the PBE-dDsC level for these intermediates, aiming to take into account the dispersion corrections, as explained in Chapter III: Methodology, *section 1.1.3*. In addition, a new intermediate state has been taken into account for the adsorption of MCH molecule in gas phase on the catalyst system at the at the PBE-dDsC level. This step occurs through a physisorption step, which is a precursor state before the dehydrogenation reaction. The energy of this physisorption step can be calculated by the following reaction :



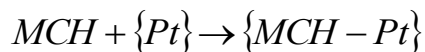
5.1 Effect of the functional on the MCH physisorption step

Table IV- 8 Electronic physisorption energy, $\Delta_r E_{ads,MCH(g)}$ (in kJ/mol), for methyl-cyclohexane calculated with PBE and PBE-dDsC functionals over $Pt_{13}H_6/\gamma-Al_2O_3$ (100) cluster

Functional	(a)	(b)
PBE	21	17
PBE-dDsC	1	-45

Table IV-8 reports the stability of two physisorption modes for methyl-cyclohexane on the cluster: configuration (a) is directly related to the geometry of methyl-cyclohexyl (the first intermediate of the reaction, Figure IV-8 (b)), whereas configuration (b) takes into account the possible interaction with the alumina support with a flat adsorption configuration parallel to the surface of the support. Adsorptions are significantly more favorable with the PBE-dDsC functional (up to 62 kJ/mol). Whereas with the PBE functional, no significant difference between configurations (a) and (b) is observed, the latter is strongly preferred with the PBE-dDsC functional.

A similar work was performed for the MCH physisorption on the Pt (111) surface with two configurations: vertical and parallel (Table IV-9). The gain on stability is once again underlined by applying PBE-dDsC functional and the parallel configuration is again more enhanced than the vertical one. Nevertheless, the decrease of energy on Pt (111) surface for the parallel or vertical configurations (93 and 50 kJ/mol) is much stronger than those on the cluster (62 and 20 kJ/mol). This suggests that the platinum surface has a stronger stabilizing effect on intermolecular interactions than the $\gamma-Al_2O_3$ support.



$$\Delta_r E_{ads, MCH(g)} = E_{MCH-Pt} - E_{MCH(g)} - E_{Pt} \quad \text{Equation (IV-3)}$$

Table IV- 9 Electronic physisorption energy, $\Delta_r E_{ads, MCH(g)}$ (in kJ/mol), for methyl-cyclohexane calculated with PBE and PBE-dDsC functionals on Pt(111)

Functional	(a)	(b)
PBE	-6	-12
PBE-dDsC	-56	-105

5.2 PBE-dDsC impact on adsorption configuration for the dehydrogenated intermediates

Despite that PBE-dDsC functional generally induces only minor structure change for most of the intermediates after re-optimizing the systems obtained at the PBE level, we observed among all one particular intermediate that exhibits a major structural difference: methyl-cyclohexyl adsorbed on the cluster with one more hydrogen atom dissociated from the molecule to the cluster. The molecule cannot maintain its initial configuration and rotated slightly around the equatorial Pt-C bond while performing the geometry optimization with the PBE-dDsC functional (Figure IV-9). This configuration change can be likely explained by the fact that the dispersion forces between the molecule and the support are strong enough to induce such a

rotation. On the Pt (111) surface, the adsorption configurations of all intermediates stay closely consistent between PBE and PBE-dDsC.

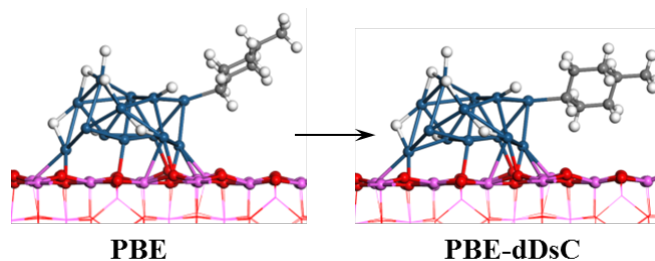


Figure IV- 9 The unmaintained methyl-cyclohexyl configuration optimized with the PBE-dDsC functional

5.3 PBE-dDsC impact on dehydrogenation energies of various intermediates

Table IV- 10 Adsorption modes, sites and dehydrogenation electronic energies for key intermediates adsorbed on Pt₁₃H₆/γ-Al₂O₃ (100) along the dehydrogenation path at the PBE-dDsC level, with energies calculated with the PBE functional in parenthesis.

	Species	Adsorption mode	Adsorption site	$\Delta_r E_{\text{dehyd,MCH(g)}}$ (kJ/mol)
	Methyl-cyclohexyl radical	σ	V3	-87 (-48*)
	4-Methyl-cyclohexene	π	V3	3 (28)
	4-Methyl-cyclohexenyl radical	$\pi\sigma$	V3-V5	-4 (23)
	1-Methyl-1,3-cyclohexadiene	2π	V3-V5	73 (98)
	1-Methyl-1,3-cyclohexadienyl radical	$\pi\pi\sigma$	V2-V3-V5	-1 (24)
	Toluene	3π	V2-V3-V5	104 (120)

*Note : the new configuration of methyl-cyclohexyl radical obtained by PBE-dDsC was recalculated with the PBE functional (energy given in parenthesis) and the configuration remained same as the one with PBE-dDsC.

Table IV-10 shows the dehydrogenation energies of the chosen intermediates for the reaction pathway, at the PBE-dDsC level. Compared to the energies calculated with PBE, we observe that the energy decrease is around 20 kJ/mol for each intermediate, except for the methyl-cyclohexyl radical for which it is reduced of about 40 kJ/mol, the latter decrease being even stronger than for MCH physisorption (Table IV-8). The configurations of physisorbed MCH and methyl-cyclohexyl are quite similar, both parallel with an interaction with the alumina support. Starting from methyl-cyclohexene, the intermediates tend to rotate toward the cluster and move away from alumina till the formation of toluene, which is adsorbed flat on the cluster and shows nearly no contact with alumina for this configuration ((j) in Figure IV-8). The dehydrogenation energies for each intermediate on the Pt (111) surface is also calculated at the PBE-dDsC level (Table IV-11). Once again, on the surface, the gain of stability (50-90 kJ/mol) for intermediates from PBE to PBE-dDsC is much more remarkable than that on the cluster. The platinum metal surface once again induces stronger intermolecular interactions than the γ -Al₂O₃ support. Moreover, this tremendous decrease on the Pt (111) surface results in similar stabilities for intermediates on both surface and cluster systems with the PBE-dDsC functional, which was not the case with the PBE functional. The enhanced stabilities of the intermediates on the supported cluster previously found with the PBE functional is thus not confirmed by the PBE-dDsC level.

Table IV- 11 Adsorption modes, sites and dehydrogenation electronic energies for key intermediates adsorbed on the Pt(111) surface along the dehydrogenation path at the PBE-dDsC level, with energies calculated with the PBE functional in parenthesis.

Species	Adsorption mode	$\Delta_r E_{\text{dehyd, MCH(g)}} \text{ (kJ/mol)}$	
	Methyl-cyclohexyl radical	σ (Chair-equatorial)	-96 (-5)
	Methyl-cyclohexene	di- σ	-2 (69)
	4-Methyl-cyclohexenyl radical	$\pi\sigma$	-13 (65)
	1-Methyl-1,3-cyclohexadiene	$\sigma\pi\sigma$	53 (125)
	1-Methyl-1,3-cyclohexadienyl radical	$\sigma\sigma\pi\sigma$	27 (108)
	Toluene	br π -2 π 2 σ	91 (161)

Considering the important role of dispersion corrections in the energetics of the dehydrogenation reaction, in the following section the whole reaction path will be first analyzed by using PBE-dDsC. At the end of this contribution (*section IV.9.*), we will come back to the comparison between the two energy profiles obtained with PBE and PBE-dDsC functionals.

6. Detailed reaction mechanism and free energy profiles of methyl-cyclohexane dehydrogenation over $\text{Pt}_{13}\text{H}_6/\gamma\text{-Al}_2\text{O}_3$ (100) with the PBE-dDsC functional

In what follows, we will estimate electronic energy, enthalpy, entropy and Gibbs free energy for each intermediate and transition state, with the PBE-dDsC functional. The ultimate

goal is to deduce forward and backward rate constants for each elementary step. For that purpose, we will consider firstly a temperature of 625 K, since this temperature is used in kinetic experiments reported in the literature^{11,12,34} and also later for our catalytic tests. In addition, since the reforming process is generally performed at a higher temperature close to 800K, we will also consider it as a complementary analysis. This may also allow us to check the sensitivity of our model with respect to this reaction condition. Note that in practice, if the geometries and energies were determined at the PBE-dDsC level, the vibrational analysis required for the estimation of enthalpies and entropies was most of the time performed at the PBE level, except when some significant geometry changes were observed between both functionals. Specifically, the five first structures in the reaction path: methyl-cyclohexane physisorption intermediate, first C-H bond cleavage transition state, methyl-cyclohexyl + H adsorption intermediate, second C-H bond cleavage transition state and methyl-cyclohexene + 2H adsorption intermediate.

6.1 General feature on temperature influence

The general view of the electronic energy profile at 0 K and the free energy profiles for two temperatures are illustrated in Figure IV-10, while Table IV-12 reports the corresponding name of the intermediates and elementary steps identified along the reaction pathway.

Table IV- 12 Various intermediates and nature of elementary steps along the dehydrogenation of methyl-cyclohexane over $\text{Pt}_{13}\text{H}_6/\text{Al}_2\text{O}_3 (100)$

ref	Surface intermediates	Elementary step	Transition state	Reaction type
	Methyl-cyclohexane (g)	--	--	calculation reference
(A)	Methyl-cyclohexane	(1) $\text{MCH (g)} \rightarrow \text{A}$	--	methyl-cyclohexane adsorption
(B)	Methyl-cyclohexyl + H	(2) $\text{A} \rightarrow \text{B}$	TS_a	C-H bond cleavage
(C)	Methyl-cyclohexene + 2H	(3) $\text{B} \rightarrow \text{C}$	TS_b	C-H bond cleavage
(D)	Methyl-cyclohexene	(4) $\text{C} \rightarrow \text{D} + \text{H}_2$	--	H_2 desorption
(E)	Methyl-cyclohexenyl + H	(5) $\text{D} \rightarrow \text{E}$	TS_d	C-H bond cleavage
(F)	Methyl-cyclohexenyl + H	(6) $\text{E} \rightarrow \text{F}$	TS_e	H atom migration
(G)	Methyl-cyclohexenyl + H	(7) $\text{F} \rightarrow \text{G}$	TS_f	cluster reconstruction
(H)	Methyl-cyclohexadiene + 2H	(8) $\text{G} \rightarrow \text{H}$	TS_g	C-H bond cleavage
(I)	Methyl-cyclohexadiene	(9) $\text{H} \rightarrow \text{I} + \text{H}_2$	--	H_2 desorption
(J)	Methyl-cyclohexadiene	(10) $\text{I} \rightarrow \text{J}$	TS_i	cluster reconstruction
(K)	Methyl-cyclohexadienyl + H	(11) $\text{J} \rightarrow \text{K}$	TS_j	C-H bond cleavage
(L)	Methyl-cyclohexadienyl + H	(12) $\text{K} \rightarrow \text{L}$	TS_k	H atom migration
(M)	Toluene + 2H	(13) $\text{L} \rightarrow \text{M}$	TS_1	C-H bond cleavage
(N)	Toluene	(14) $\text{M} \rightarrow \text{N} + \text{H}_2$	--	H_2 desorption
	Toluene (gas phase)	(15) $\text{N} \rightarrow \text{Tol (g)}$	--	toluene desorption

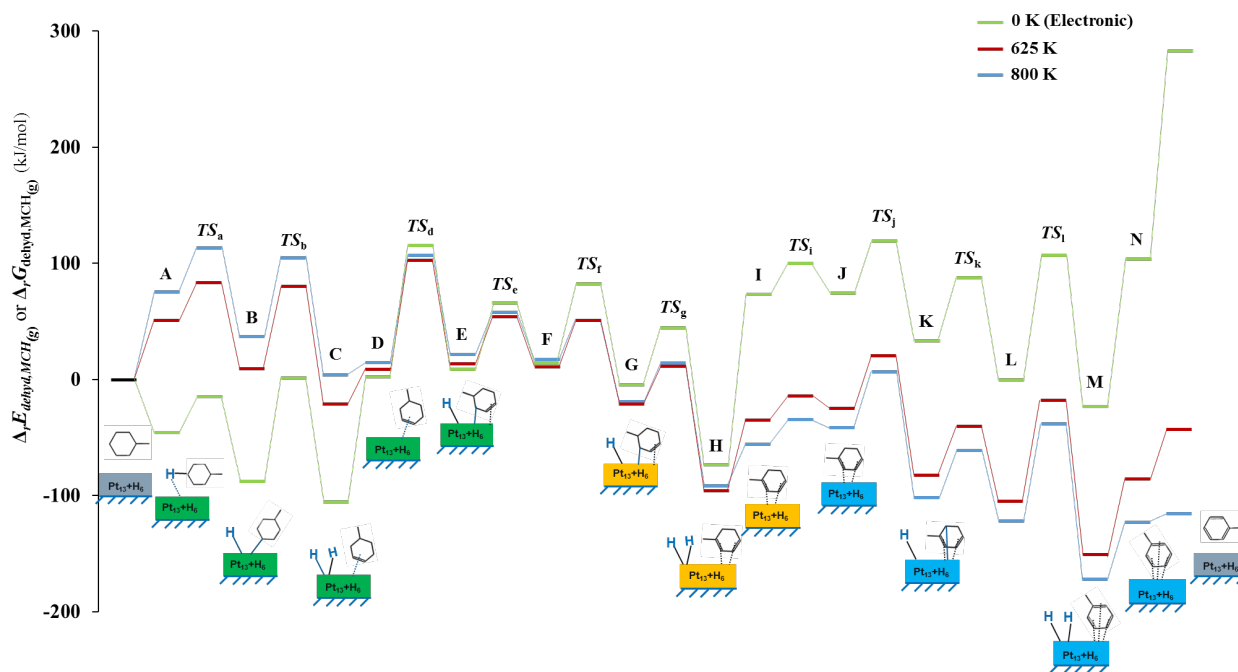


Figure IV- 10 Free energy profile for methyl-cyclohexane dehydrogenation over $\text{Pt}_{13}\text{H}_6/\gamma\text{-Al}_2\text{O}_3$ at 625 K and 800 K along with the corresponding electronic energy profiles at 0 K at the PBE-dDsC level. The various colors for clusters in the schemes correspond to different cluster morphologies induced by major cluster reconstructions.

As already mentioned, there are three different cluster morphologies observed in general, which implies to take into account these reconstruction steps and hydrogen migration steps along with C-H cleavage steps in the reaction mechanism. These three cluster morphologies are illustrated in different colors (green, yellow and blue) in Figure IV-10, along with the original cluster (grey) at the beginning and end of the catalytic cycle (See the thermodynamic data of Figure IV-10 in Appendix-IV-3). Meanwhile, several hydrogen atom migration steps are also created to mitigate the transition for C-H bond cleavage or cluster reconstruction steps. The number of hydrogen atoms on the cluster fluctuates according to $6 \rightarrow 7 \rightarrow 8 \rightarrow 6$ sequences because the H_2 desorption step sequentially occurs after two C-H bond cleavage steps. The transition states are also indicated for relevant elementary steps. A detail analysis on these elementary steps and their transition states will be given later in this section.

In Figure IV-10, comparing now the general trends for the two reaction temperatures 625K and 800K with the electronic energy profile at 0 K, a crossing point at intermediate methylcyclohexenyl+H (F) is observed for the three profiles which reflect an inversion in the relative stabilities of the intermediates formed. Before (F), the increase of temperature destabilizes all intermediates, whereas beyond (F) it stabilizes the profile. This trend is not related to the enthalpy terms (including vibrational, rotational and translational contributions), which variation is very small (3 kJ/mol) for these two temperatures 625 K and 800 K. On the other hand, it is mainly due to the entropy term ($T\Delta S$). Hence, before the formation of intermediate (F), in particular for the first MCH physisorption step, the intermediate dehydrogenation reactions are generally exothermic at 0 K and become more and more endergonic when temperature increases. After the formation of intermediate (F), this thermodynamic trend shifts. As three molecules of H_2 are formed and released in gas phase sequentially, the entropy of the system increases and as a consequence the Gibbs free dehydrogenation energy decreases both at 625 K and 800 K, compared to the opposite profile at 0 K. Notably, for the H_2 desorption steps ($C \rightarrow D$, $H \rightarrow I$, $M \rightarrow N$) and toluene molecule (N) desorption step, the temperature effect is significantly crucial. These steps become less endergonic when the temperature goes from 0 K to 800 K, related to the entropic effects. Especially for the last toluene desorption steps, the Gibbs free energy decrease of this desorption step from 0 K to 800 K is about 170 kJ/mol. This information can be used to explain why the industrial reforming process employs preferentially this temperature at 800 K, not only because the overall reaction is endothermic, but also because toluene desorption becomes much easier above 800 K. A similar analysis can be made for the three H_2 desorption steps, which become less endergonic at high temperature due to the same entropic effects. In other word, the increase of temperature favors the desorption steps but of course disfavors the

MCH adsorption step for entropic reasons. At last, this temperature impact has little effect on the other elementary steps (C-H bond cleavage, cluster reconstruction and H atom migration steps).

In order to make a detailed analysis of the complex reaction mechanism, all the elementary steps will be discussed in what follows according to the 5 different families highlighted in Table IV-12: methyl-cyclohexane adsorption and toluene desorption, C-H bond cleavage, cluster reconstruction, H atom migration, H₂ desorption. Reaction, possibly activation when determined, energies ($\Delta_r E$, $\Delta_r E^\ddagger$), enthalpies ($\Delta_r H$, $\Delta_r H^\ddagger$), entropic terms ($T\Delta_r S$, $T\Delta_r S^\ddagger$) and Gibbs free energies ($\Delta_r G$, $\Delta_r G^\ddagger$) will be commented for each steps at 625 K, using as a reference the reactant of the given step.

6.2 Methyl-cyclohexane adsorption and toluene desorption

The methyl-cyclohexane adsorption occurs through a physisorption step, which is a precursor state before the first C-H bond cleavage. This step is exothermic ($\Delta_r H = -40$ kJ/mol) and endergonic ($\Delta_r G = 51$ kJ/mol). The large difference between enthalpy and free energy is due to the complete loss of rotational and translational entropies for this physisorption step, which corresponds to a decrease of 91 kJ/mol from the gas phase to the adsorbed state. Note that we make the assumption that methyl-cyclohexane is an immobile complex on the catalytic surface. However, this entropy loss is at the origin of the positive Gibbs free energy and causes a high free energy barrier for the system. This barrier depends on the temperature (Figure IV-10): the higher the temperature, the higher the barrier.

Table IV- 13 Thermodynamic data for the methyl-cyclohexane adsorption and toluene desorption elementary steps involved in the methyl-cyclohexane dehydrogenation mechanism on Pt₁₃H₆/γ-Al₂O₃ at the PBE-dDsC level

Elementary step	Reaction energy, enthalpy, entropy term and Gibbs free energy at 625 K (kJ/mol)			
	$\Delta_r E$	$\Delta_r H$	$T\Delta_r S$	$\Delta_r G$
MCH (g) → A	-45	-40	-91	51
N → Tol (g)	179	174	130	44

Note: (i) Before intermediate (A) (during step (1)), there is one extra step, where we consider a preliminary cluster reconstruction from the original structure to the deformed one. This step will not be presented in the following reaction energy profiles and is assumed as merged within a single step (1). An analysis has been done for this step, *Reconstruction A* in *section 6.4*.

(ii) The same occurs for the deformed cluster after the last toluene desorption step, from the deformed cluster of (N) alone to the original cluster alone, a *Reconstruction N_{1,2}* happens at the end of reaction path. The analysis of this step is also reported in the *section 6.4*.

By contrast, the toluene desorption step is endothermic and endergonic with a large gain of entropy due to the release of toluene from the adsorbed state to gas phase. The free energy variation of this step is also strongly temperature dependent (Figure IV-10): the higher the temperature, the lower the Gibbs free energy barrier for toluene desorption. Notably, the 3π adsorption mode of toluene on the cluster makes it rather complicated to study the transition state of the desorption step to gas phase.

As indicated in the note of Table IV-13, one should underline that the energies reported here include also the cluster reconstruction step as illustrated in Figure IV-10. It is however interesting to decouple these two steps from a thermodynamic point of view: this will be done in *section 6.4*.

6.3 C-H bond cleavage

Table IV- 14 Thermodynamic and kinetic data for the C-H bond cleavage elementary steps involved in the methyl-cyclohexane dehydrogenation mechanism over Pt₁₃H₆/γ-Al₂O₃ (100) at the PBE-dDsC level

Elementary Transition step		Reaction energy, enthalpy, entropy term and Gibbs free energy at 625 K (kJ/mol)				Forward Activation energy, enthalpy, entropy term and Gibbs free energy at 625 K (kJ/mol)				Backward Activation energy, enthalpy, entropy term and Gibbs free energy at 625 K (kJ/mol)			
States		$\Delta_r E$	$\Delta_r H$	$T\Delta_r S$	$\Delta_r G$	$\Delta_r E^\ddagger$	$\Delta_r H^\ddagger$	$T\Delta_r S^\ddagger$	$\Delta_r G^\ddagger$	$\Delta_r E^\ddagger$	$\Delta_r H^\ddagger$	$T\Delta_r S^\ddagger$	$\Delta_r G^\ddagger$
A → B	TS_a	-42	-48	-7	-41	31	19	-14	33	73	67	-7	74
B → C	TS_b	-18	-27	3	-31	88	74	4	70	106	101	1	101
D → E	TS_d	6	-6	-12	6	113	98	3	95	107	104	15	89
G → H	TS_g	-70	-78	-4	-74	47	33	0	33	118	111	4	107
J → K	TS_j	-41	-52	6	-58	45	34	-10	44	86	86	-17	103
L → M	TS_l	-23	-30	16	-46	107	94	7	87	130	124	-8	132

The C-H bond cleavage steps are suspected to be the most important ones related to the reactivity and selectivity of the catalysts. The relevant intermediates and transition structures for these steps are shown in Figure IV-11, while their thermodynamic and kinetic feature are reported in Table IV-14. These steps are all exothermic and mostly exergonic except that the third C-H bond cleavage from methyl-cyclohexene to methyl-cyclohexenyl + H (D → E) which is slightly endergonic. This step exhibits very low reaction electronic energy and enthalpy, but the biggest loss in entropy compared to other five C-H cleavage steps. Moreover, when it comes to activation data, the third C-H bond cleavage step (TS_d) gives the higher barrier in the forward direction in terms of electronic energy, enthalpy and free energy. This is probably due to the rotation and translation of the MCHe molecule (D) towards the cluster during the breaking of this

C-H bond (Figure IV-11). The second most energy demanding step in forward reaction (electronic energy, enthalpy and free energy) is the last C-H bond cleavage step (TS_i) on methylcyclohexadienyl + H to form the most stable intermediate toluene + 2H (L \rightarrow M). The difference on free activation energy between these two steps is very small (8 kJ/mol) and their activation free energy is much higher than the other four C-H bond cleavage steps. So far, it is hard to make conclusion on the rate-determining step because these two are very competitive.

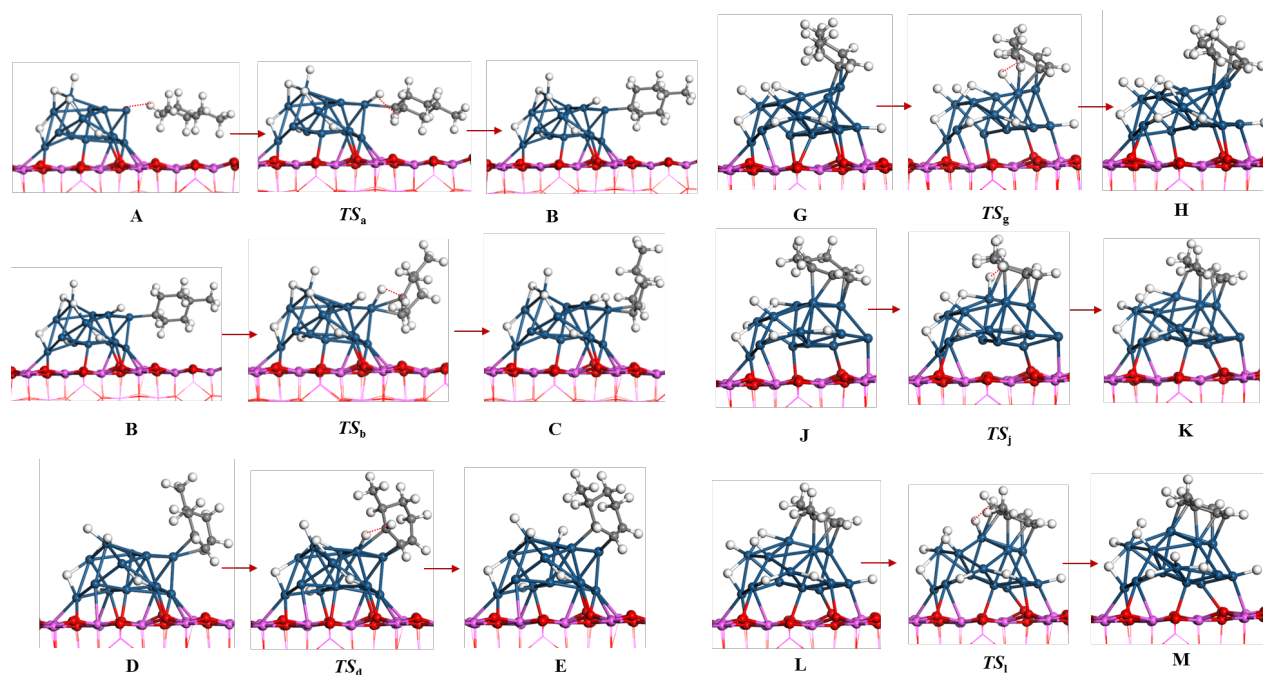


Figure IV- 11 Configurations of all transition states of C-H bond cleavage steps for methyl-cyclohexane dehydrogenation reaction mechanism over $Pt_{13}H_6/\gamma-Al_2O_3(100)$ at the PBE-dDsC level

Moreover, the activation data among these six steps are widespread over large enthalpy and free energy intervals (19-98 kJ/mol for enthalpies and 33-95 kJ/mol for free energies) which allows us to check if a Brønsted–Evans–Polanyi (BEP) linear relationship^{35–37} exists here. This

relation aims to rationalize possible correlations between the reaction activation energy ($\Delta_r E^\ddagger$) and the reaction energy ($\Delta_r E$) within a given nature of elementary steps. This method was already employed to reduce computational burden of complex system for the bond breakings of C-O, C-H and C-C of different reaction type, by using these linear relationships.^{31,38-41} It is described by the following equation :

$$\Delta_r E^\ddagger = \alpha \Delta_r E + \beta \quad \text{Equation (IV-4)}$$

We explored if the Brønsted–Evans–Polanyi (BEP) linear relationship holds for the six C-H cleavage steps (forward reactions, reported in Table IV-15 and Figure IV-12). As shown in Table IV-15, the electronic activation energy and enthalpy exhibit a relatively better linear correlation with similar coefficients α and β , compared to Gibbs free energy. The Gibbs free energy does not follow such a relationship, which is related to entropy effects. For a cluster system with a high fluctuonality character (as we will see below), the enthalpy and entropy can hardly be expected to vary linearly when it is not simply related to the dissociation of a bond (C-H) but also depending on the cluster morphology. This linear relationship is also investigated on the Pt (111) surface, presented in the same Table IV-12. A very good linearity is found for E, H and G. This BEP comparison between the two systems once again emphasizes that the cluster system cannot be described simply as the Pt (111) surface because of its peculiar fluctuonality, inducing some complexity. If we now look at Figure IV-12, the BEP linear relationship that we obtained for the reaction free energies and activation free energies seems to enable to have a better linear behavior without two exceptional points, the points corresponding to first C-H bond cleavage step and the last one. It suggests that our calculations may perhaps underestimate the first C-H bond cleavage activation free energy and overestimate the last one. These two steps

involved intermediates fully interacting with the support, or fully interacting with the platinum surface, which may be at the origin of various impacts of the PBE-dDsC functional.

Table IV- 15 Brønsted–Evans–Polanyi (BEP) linear relations for C-H bond cleavage steps on Pt₁₃H₆/γ-Al₂O₃ (100) cluster and Pt (111) surface on electronic energy ($\Delta_r E$), enthalpy ($\Delta_r H$) and Gibbs free energy ($\Delta_r G$)

	Pt ₁₃ H ₆ /γ-Al ₂ O ₃ (100)			Pt (111)		
	$\Delta_r E$	$\Delta_r H$	$\Delta_r G$	$\Delta_r E$	$\Delta_r H$	$\Delta_r G$
α	1.10	1.13	0.75	1.20	1.33	1.31
β (kJ/mol)	106	104	91	81	83	84
R^2	0.66	0.67	0.56	0.90	0.95	0.81

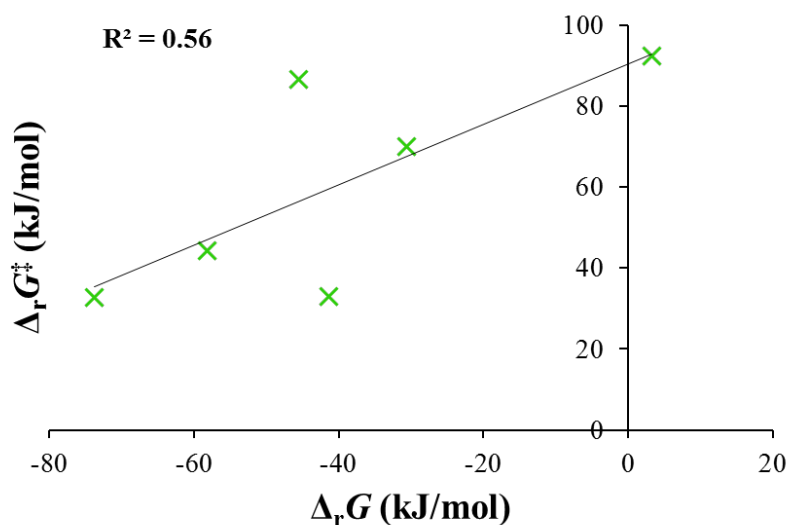


Figure IV- 12 Brønsted–Evans–Polanyi (BEP) linear relationships for Gibbs free energy profile for C-H bond cleavage steps in methyl-cyclohexane dehydrogenation reaction over Pt₁₃H₆/γ-Al₂O₃ (100) at the PBE-dDsC level

If we look at the backward reaction, activation enthalpies and free energies exhibit much smaller variation intervals from one step to another than those for forward reactions (around 30 kJ/mol of gap). Particularly, the backward activation enthalpies are all higher than the forward ones, which makes the corresponding transition states rather “early”. As for free energy, by the

influence of entropies, most of them are “early” states except for the third C-H cleavage ($D \rightarrow E$) which shows an “intermediate” transition states (the activation Gibbs free energies in both directions are barely the same). Furthermore, theoretically, these “early” states are supposed to be structurally similar to initial states because they are energetically closer to initial states. But in our case, due to the complexity of the system and reaction elementary step, the structural resemblance of the transition state falls in between the reactant and product structures, where it reflects the partial similarities of both, presented in Figure IV-11 (See the other BEP figures in Appendix-IV-5).

Figure IV-11 illustrates the structures of these six transition states, with similar features: at the transition state, a three centers configuration involves one carbon atom, one hydrogen atom and one platinum site (Figure IV-13). Such a configuration was found already on Pt (111) surface during the dehydrogenation/hydrogenation reaction of alkenes on the metal surface.^{31,42} At last, if we compare our activation energy of these C-H bond cleavages with the work of Van Trimpont et al.¹² at a temperature of 643 K, the activation enthalpies ($\Delta_r H^\ddagger$) for the fourth ($G \rightarrow H$) and last C-H bond cleavage ($L \rightarrow M$) were found to be 68 and 91 kJ/mol, respectively by performing a Hougen-Waston kinetic model. From our side, at $T = 625$ K, for the same steps, activation enthalpies of 33 and 94 kJ/mol are found, respectively, where an agreement can be achieved on the value of later one.

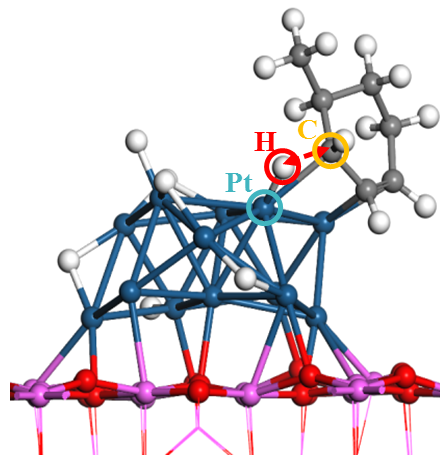


Figure IV- 13 Three centers configuration on the transition state TS_d (the third C-H bond cleavage TS)

At this stage, it should be also underlined that during the transition states search for C-H bond cleavage involving methyl-cyclohexenyl (G), methyl-cyclohexadiene (J), and methyl-cyclohexadienyl (L), several metastable precursor states (E, F, J and K) have been found so that the NEB approach can be successfully achieved to locate a relevant saddle point. This is often due to steric hindrances induced by the methyl group and/or hydrogen atoms on the cluster that implies either cluster reconstruction or H migration. Thus, in the two following sections, we analyze the elementary steps involved in cluster reconstruction and H migration, which are often pre-required step for the C-H bond cleavages.

6.4 Cluster reconstruction

As we pointed out before and in a previous theoretical study,⁶ the reaction environment induces a morphology change of the Pt₁₃ cluster. In the present case, we find that four main cluster reconstructions occur and lead to three morphologies distinct from the initial structure

along the dehydrogenation path (including adsorption A and desorption N steps). These deformed clusters obtained by molecular dynamics stabilize the adsorbed intermediates in the course of dehydrogenation reaction, which reflects the fluctuonality of the supported cluster contrasting with the ideal Pt(111) surface.

Table IV- 16 Thermodynamic and kinetic data for the cluster reconstruction steps at the PBE-dDsC level

Elementary step	Transition States	Reaction energy, enthalpy, entropy term and Gibbs free energy at 625 K (kJ/mol)				Forward Activation energy, enthalpy, entropy term and Gibbs free energy at 625 K (kJ/mol)				Backward Activation energy, enthalpy, entropy term and Gibbs free energy at 625 K (kJ/mol)			
		$\Delta_r E$	$\Delta_r H$	$T\Delta_r S$	$\Delta_r G$	$\Delta_r E^\ddagger$	$\Delta_r H^\ddagger$	$T\Delta_r S^\ddagger$	$\Delta_r G^\ddagger$	$\Delta_r E^\ddagger$	$\Delta_r H^\ddagger$	$T\Delta_r S^\ddagger$	$\Delta_r G^\ddagger$
Recons. A		35	32	7	25	--				--			
F → G	TS_f	-18	-17	15	-32	68	61	22	40	86	78	6	72
I → J	TS_i	1	1	-10	11	27	20	0	20	25	19	9	10
Recons. N ₁		-41	-40	-16	-25	--				--			
Recons. N ₂		52	56	-13	70	--				--			

It should be first noticed that the initial cluster (with only 6 H atoms adsorbed on it) does not remain as the most stable when the reactant, methyl-cyclohexyl, methyl-cyclohexene and toluene are adsorbed on it. So at the very beginning of the reaction, the cluster slightly reconstructs before methyl-cyclohexyl is formed (green cluster in Figure IV-10). In that case, a preliminary reconstruction step may occur between the grey cluster and the green cluster (Figure IV-10), as soon as the methyl-cyclohexane is physisorbed on the cluster. If we assume that methyl-cyclohexane is adsorbed on the initial non reconstructed cluster (grey), the corresponding electronic energy variation $\Delta_r E$ (reconstruction A in Figure IV-14) is +35 kJ/mol while the free energy variation $\Delta_r G$ is about +25 kJ/mol in Table IV-16. If we assume that the reconstruction

step occurs before methyl-cyclohexane adsorption (cluster reconstruction from grey to green without adsorbed molecule), the electronic energy cost is very similar: $\Delta_r E = +37$ kJ/mol, which means that the methylcyclohexane physisorption does not impact strongly the cluster reconstruction. At the same time, the adsorption energies of methyl-cyclohexane ($\Delta_r E = -82$ before the reconstruction vs -80 kJ/mol after the reconstruction) does not depend strongly whether the cluster is reconstructed or not. So, the reconstruction might occur either before or after methylcyclohexane physisorption.

Regarding the last step, the toluene molecule is proved to be more stable on the deformed cluster (blue cluster in Figure IV-10) than on the initial cluster found by AIMD. However, once toluene is desorbed from the blue cluster, there is actually a supplementary step to restore the morphology of the initial cluster (grey cluster in Figure IV-10). From a thermodynamic point of view (Table IV-16, Figure IV-14), the toluene desorption exhibits an electronic energy $\Delta_r E$ of $+220$ kJ/mol, corresponding to $\Delta_r G$ of 89 kJ/mol, while the subsequent cluster reconstruction into the initial one involves $\Delta_r E = -41$ kJ/mol and $\Delta_r G = -25$ kJ/mol presented in Table IV-16 as Recons. N₁. If one assumes that the reconstruction occurs first in presence of adsorbed toluene and then the desorption occurs, the energy variation sequences are $\Delta_r E = +52$ kJ/mol ($\Delta_r G = +70$ kJ/mol, presented in Table-16, Figure IV-14 as Recons. N₂) and $\Delta_r E = +127$ kJ/mol ($\Delta_r G = -5$ kJ/mol). Contrary to the methyl-cyclohexane adsorption step, the energy variations involved depend strongly on the order of the steps. According to this thermodynamic analysis, we suspect that the toluene desorption may occur preferentially after the cluster reconstruction.

As shown in Table IV-16, the F \rightarrow G reconstruction (with methyl-cyclohexenyl) is exothermic and exergonic,. Conversely, the I \rightarrow J reconstruction (with methyl-cyclohexadiene) is endothermic and endergonic. The forward activation Gibbs free energies for the two

reconstruction steps during the reaction ($F \rightarrow G$ and $I \rightarrow J$) are significantly smaller (40 and 20 kJ/mol at 625 K) than the highest ones calculated for the C-H bond cleavages. It can also be noticed that in the course of the $I \rightarrow J$ reconstruction several H atom migrations occur simultaneously. It should also be remarked that these cluster reconstruction steps remain moderate when compared to the morphological reconstructions invoked by the hydrogen coverage and temperature changes mentioned in the introduction, discovered by the previous study of Mager-Maury et al.⁶ That could explain the fact that the Gibbs free activation energies of these steps are smaller than those of the C-H cleavage steps.

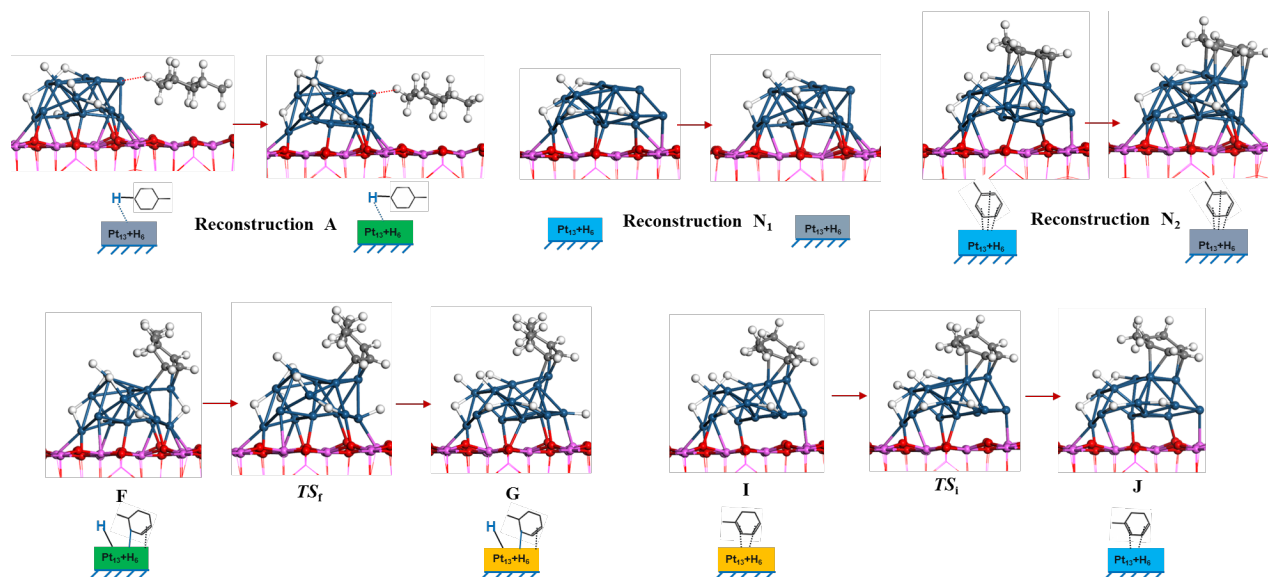


Figure IV- 14 Geometries (side views) of the reactant, transition state and product for the cluster reconstruction steps at the PBE-dDsC level

6.5 H atom migration

Table IV- 17 Thermodynamic and kinetic data for H atom migration steps at the PBE-dDsC level

Elementary step	Transition States	Reaction energy, enthalpy, entropy term and Gibbs free energy at 625 K (kJ/mol)				Activation energy, enthalpy, entropy term and Gibbs free energy (forward) at 625 K (kJ/mol)				Activation energy, enthalpy, entropy term and Gibbs free energy (backward) at 625 K (kJ/mol)			
		$\Delta_r E$	$\Delta_r H$	$T\Delta_r S$	$\Delta_r G$	$\Delta_r E^\ddagger$	$\Delta_r H^\ddagger$	$T\Delta_r S^\ddagger$	$\Delta_r G^\ddagger$	$\Delta_r E^\ddagger$	$\Delta_r H^\ddagger$	$T\Delta_r S^\ddagger$	$\Delta_r G^\ddagger$
E \rightarrow F	TS_e	5	6	8	-2	57	53	12	41	52	47	4	43
K \rightarrow L	TS_k	-34	-30	-8	-23	55	48	6	42	89	78	13	65

These steps (Figure IV-15) were investigated either to stabilize the intermediates formed on the cluster (K \rightarrow L), or to release one occupied Pt site required for the next step (E \rightarrow F). In this latter case, this reveals that increasing the hydrogen coverage can hinder the dehydrogenation reaction. By the fact that we chose a non-zero but rather low initial hydrogen coverage as a modeling point, the reaction pathway may be affected if higher hydrogen coverage would be varied. For these reasons, these two elementary steps have quite different reaction energies (Table IV-17): E \rightarrow F is endothermic while K \rightarrow L is exothermic. They are both exergonic. However, despite these slight differences, forward activation enthalpies and activation free energies are rather similar. The Gibbs free activation energies at 41-42 kJ/mol are generally smaller than those of C-H bond cleavages but equal or higher than those of cluster reconstructions.

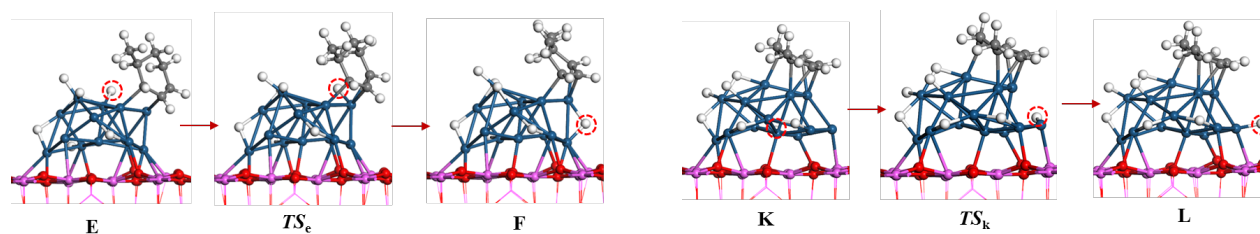


Figure IV- 15 Transition states for H migration steps at the PBE-dDsC level

6.6 H₂ desorption

Table IV- 18 Thermodynamic data of H₂ desorption steps at the PBE-dDsC level

Elementary step	Reaction energy, enthalpy, entropy term and Gibbs free energy at 625 K (kJ/mol)			
	$\Delta_r E$	$\Delta_r H$	$T\Delta_r S$	$\Delta_r G$
C \rightarrow D + H ₂	108	103	74	29
H \rightarrow I + H ₂	147	141	81	60
M \rightarrow N + H ₂	127	124	59	65

In order to keep the hydrogen coverage constant ($\theta_H = 6$ hydrogen atoms) on the cluster, we remove the two extra hydrogen atoms (from the system exhibiting 8 adsorbed hydrogen atoms) after their dissociation from each intermediate, releasing H₂ in the gas phase. These three H₂ molecule desorption steps are all endothermic and endergonic (Table IV-18), despite a gain of rotational and translational entropy (as already mentioned for toluene desorption step). The reaction Gibbs free energy of these steps varies consequentially depending on the reaction temperature: the higher the temperature, the lower the barrier. The search of the transition state for the first H₂ desorption has been made and is presented in Appendix-IV-5. In summary, the energy of transition state is very close to the final state. It also means if one look at the backward reaction of this desorption step, the adsorption of H₂ molecule onto the cluster, this adsorption step is not activated. It was also already reported on the Pt surface, the adsorption step of hydrogen reveals no activation energy.^{43,44} As a result, the activation free energies for the H₂ molecule desorption steps are considered identical to their reaction free energy in forward steps and non-activated ($\Delta_r G^\ddagger = 0$) for backward steps.

7. Effect of the functional on the Gibbs free energy profile over $\text{Pt}_{13}\text{H}_6/\gamma\text{-Al}_2\text{O}_3$

(100): PBE vs PBE-dDsC

In order to take into account the dispersion forces into account, the whole reaction pathway has been calculated so far by performing PBE-dDsC functional. However, it may be interesting to highlight the cases (if any) where the PBE-dDsC functional is critical to be applied with respect to PBE.

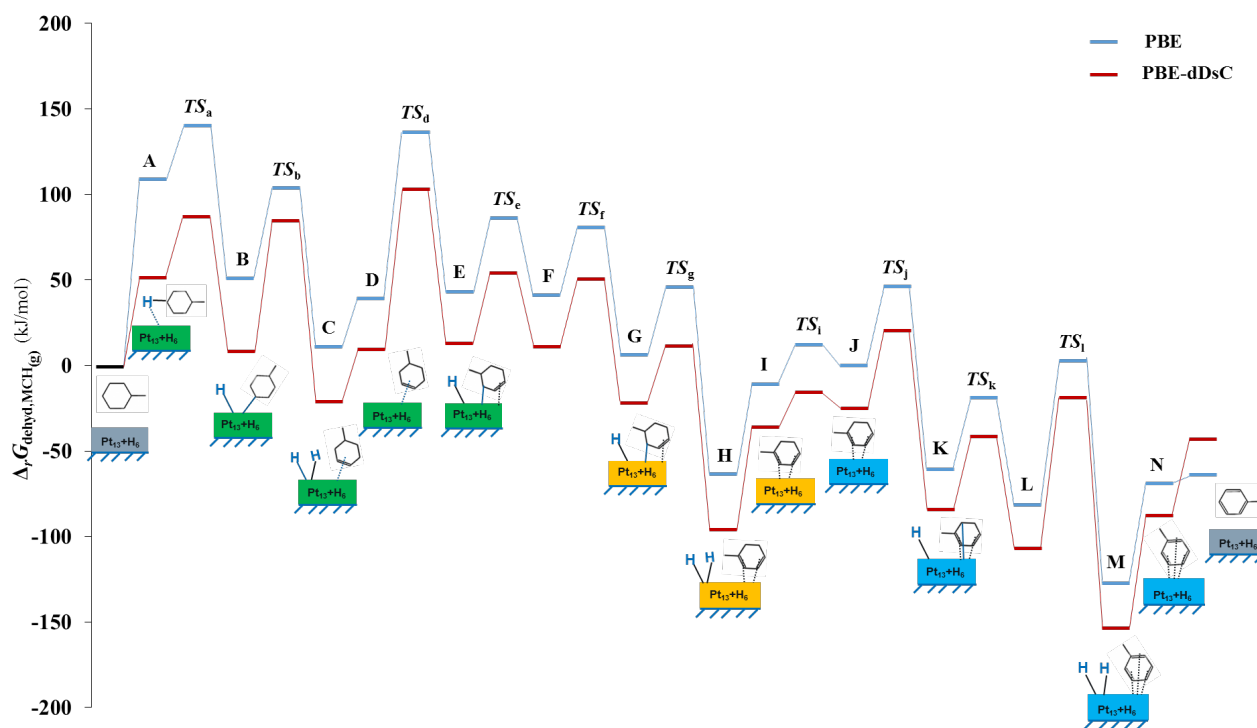


Figure IV- 16 Gibbs free energy profiles for methyl-cyclohexane dehydrogenation reaction mechanism over $\text{Pt}_{13}\text{H}_6/\gamma\text{-Al}_2\text{O}_3$ calculated with the PBE (blue line) and the PBE-dDsC (red line) functionals at 625 K

The Gibbs free energy profiles at 625 K calculated with PBE-dDsC and PBE are presented in Figure IV-16. Apart from the first methyl-cyclohexane adsorption step and the last

toluene desorption step, the PBE-dDsC free energy profile is stabilized by around 30 kJ/mol with respect to the PBE profile at a temperature of 625 K. For all the intermediates and transition states except for the $A \rightarrow B \rightarrow C$ steps, the structures almost do not depend on the functional. Figure IV-16 highlights that the dispersion forces have significantly impacted the adsorption configuration of methyl-cyclohexane (A) and methyl-cyclohexyl (B), as we have already discussed in *section IV.5.*, these new configurations with PBE-dDsC functional are much more stable.

In this case, with these two specific configurations for (A) and (B), we explored a new reaction pathway for the first five states as presented in Figure IV-17. As a consequence, the new vibrational frequencies have thus been calculated at the PBE level for obtaining the correct Gibbs free energies.

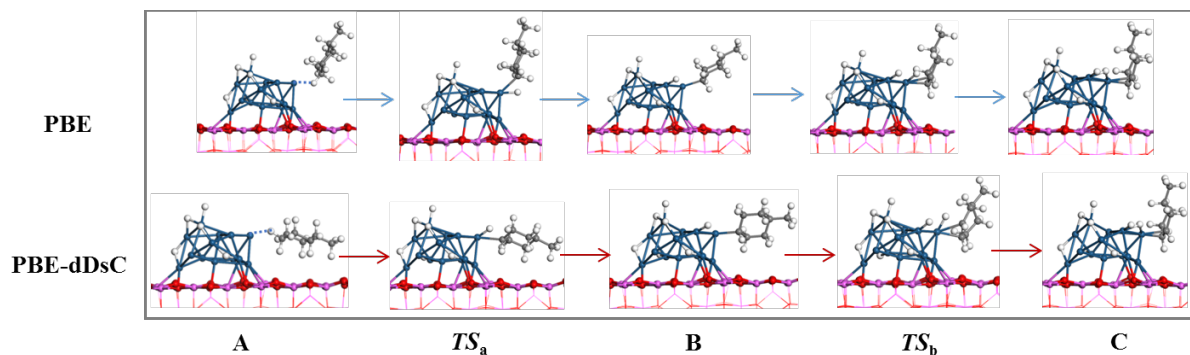


Figure IV- 17 First five reaction intermediates and transition states discovered by PBE-dDsC functional during the geometry optimization calculation compared with those implied in reaction pathway with the PBE functional

The free energy of TS_a is increased by about 50 kJ/mol with PBE compared to the PBE-dDsC functional, a difference likely due to the interaction term between the molecule and the

support. Moreover, the activation free energy for $B \rightarrow TS_b$ appears to be higher with PBE-dDsC ($\Delta_r G_{B \rightarrow TS_b}^\ddagger = 70$ kJ/mol) than with PBE ($\Delta_r G_{B \rightarrow TS_b}^\ddagger = 52$ kJ/mol). This can be explained by the fact that TS_b corresponds a C-H bond cleavage from intermediate B to C involving a relatively large rotation of the adsorbed molecule within PBE-dDsC (which is not required with PBE).

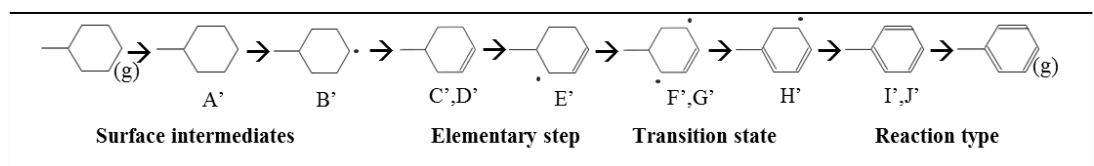
Hence, the highest free energy transition state is TS_d with PBE-dDSC, whereas it is TS_a with PBE. However, the most energy demanding step (third C-H bond cleavage on methylcyclohexene $D \rightarrow E$ with TS_d as the transition state) is the same for PBE and PBE-dDsC, with a free activation energy $\Delta_r G_{D \rightarrow TS_d}^\ddagger = 95$ kJ/mol with PBE-dDsC vs. 103 kJ/mol with PBE. The Gibbs free energy of the very last intermediate in Figure IV-16 corresponds to the global Gibbs reaction free energy (gas phase methyl-cyclohexane dehydrogenation to toluene). This reaction free energy in gas phase increases (by 21 kJ/mol) when the dispersion forces are considered (PBE-dDsC versus PBE).

To conclude, the choice of the exchange correlation functional affects both the free energy profile and part of the reaction mechanism. The most demanding step is still the same but overall, the choice of the functional may affect the results of further kinetic modeling.

8. Detailed reaction mechanism and free energy profile of methyl-cyclohexane dehydrogenation over the Pt(111) surface

8.1 Reaction mechanisms of methyl-cyclohexane dehydrogenation over the Pt(111) surface at the PBE-dDsC level

Table IV- 19 Various intermediates and nature of elementary steps along the dehydrogenation of methyl-cyclohexane over the Pt(111) surface



	Surface intermediates	Elementary step	Transition state	Reaction type
ref	Methyl-cyclohexane (gas)	--	--	calculation reference
(A')	Methyl-cyclohexane	(1) MCH (g) \rightarrow A'	--	methyl-cyclohexane adsorption
(B')	Methyl-cyclohexyl + H	(2) A' \rightarrow B'	TS _{a'}	C-H bond cleavage
(C')	Methyl-cyclohexene + 2H	(3) B' \rightarrow C'	TS _{b'}	C-H bond cleavage
(D')	Methyl-cyclohexene	(4) C' \rightarrow D' + H ₂	--	H ₂ desorption
(E')	Methyl-cyclohexenyl + H	(5) D' \rightarrow E'	TS _{d'}	C-H bond cleavage
(F')	Methyl-cyclohexadiene + 2H	(6) E' \rightarrow F'	TS _{e'}	C-H bond cleavage
(G')	Methyl-cyclohexadiene	(7) F' \rightarrow G' + H ₂	--	H ₂ desorption
(H')	Methyl-cyclohexadienyl + H	(8) G' \rightarrow H'	TS _{g'}	C-H bond cleavage
(I')	Toluene + 2H	(9) H' \rightarrow I'	TS _{h'}	C-H bond cleavage
(J')	Toluene	(10) I' \rightarrow J' + H ₂	--	H ₂ desorption
	Toluene (gas phase)	(11) J' \rightarrow Tol (g)	--	toluene desorption

In order to enrich the discussion of the results obtained on the supported cluster, we report here a parallel study on the ideal Pt(111) surface. Thus, we investigate a similar sequential C-H bond cleavage reaction mechanism of methyl-cyclohexane over this ideal surface. One key

difference is the absence of strong reconstruction phenomenon. Moreover, results for the hydrogenation reaction of benzene and dehydrogenation reaction of cyclohexane previously reported in the literature^{30,33,18,27} on such a surface model also provide references for this part of work, in terms of molecular structures and adsorption energies. The various intermediates involved in the reaction mechanism of methyl-cyclohexane dehydrogenation over Pt(111) are presented in Table IV-19. Compared to the mechanism taking place over Pt₁₃H₆/γ-Al₂O₃ (100), the reaction mechanism simply implies the C-H bond cleavage and the molecule adsorption/desorption steps.

In particular, for the hydrogenation of benzene another reaction pathway («ortho» Path³³) has been proposed in the literature. Instead of forming the methyl-cyclohexene molecule adsorbed on Pt (111), the two carbon atoms which form di-σ bonds with platinum atoms should be on the meta position and then go through an ipso adsorption configuration (Table IV-20). These intermediate configurations have been also investigated in our case. However, they are found to be relatively less stable in terms of electronic energies when compared to the intermediates D', E' and F' at the PBE level (Table IV-20). In addition, the ipso adsorption configuration cannot be stabilized during the geometry optimization and turned to pass directly to the configuration of C₇H₁₀ + 2H. For that reason Table IV-20 does not report any electronic energy for the ipso intermediate (C₇H₁₁ +H) at the PBE level. This significant discrepancy with the case of benzene hydrogenation is certainly due to the steric hindrance of the methyl- group on the carbon atom bearing one radical and thus the ipso intermediate is not as “flat” as in absence of methyl group.

Table IV- 20 Calculated electronic energies for intermediates in reaction «ortho» pathway and proposed pathway over Pt(111) at the PBE level

« ortho » intermediates	$\Delta_r E_{dehyd,MCH}$ (kJ/mol)	Proposed intermediates	$\Delta_r E_{dehyd,MCH}$ (kJ/mol)
 (Di- σ -meta)	102	 (D')	69
 (Ipsos)	--	 (E')	65
 (F')	51	 (F')	56

8.2 General feature on temperature influence and detailed reaction pathway over Pt(111) at the PBE-dDsC level

In the following, the energy and free energy (at 625 and 800 K) profiles over Pt(111) for the proposed reaction pathway have been investigated at the PBE-dDsC level, as shown in Figure IV-18, including transition states (See Appendix-IV-7 for the thermodynamic data corresponding to Figure IV-18).

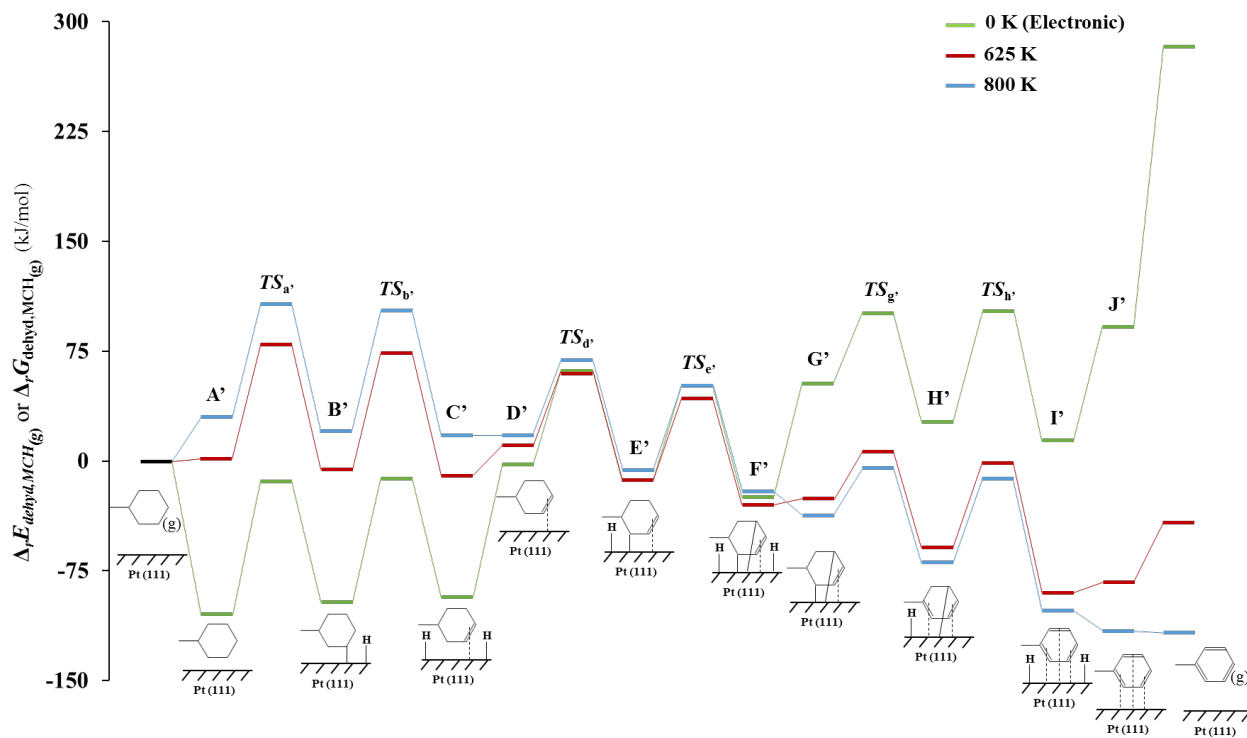


Figure IV- 18 Free energy profile for methyl-cyclohexane dehydrogenation reaction mechanism over the Pt(111) surface at 625 K and 800 K along with the corresponding electronic energy profiles at 0 K at the PBE-dDsC level.

The enthalpy of intermediates does not vary very much when the temperature goes from 625 to 800 K (around 5 kJ/mol increase on enthalpy), similar to that on the cluster. Once again, the free energies are more strongly affected by the temperature change, which is linked to the sensibility of entropy term depending on the temperature, especially for the MCH adsorption step ($\text{MCH}_{(\text{g})} \rightarrow \text{A}'$), the toluene desorption step ($\text{J}' \rightarrow \text{Tol}_{(\text{g})}$) and the H_2 desorption steps ($\text{C}' \rightarrow \text{D}'$, $\text{F}' \rightarrow \text{I}'$ and $\text{I}' \rightarrow \text{J}'$). At 0 K, the first physisorption step of methyl-cyclohexane molecule is exothermic, while increasing the temperature, the free energy of this step increases because of the increase of entropy loss ($T\Delta_r S < 0$). On the contrary for the molecule desorption steps, these steps present a gain of entropy ($T\Delta_r S > 0$). In particular, the H_2 and toluene desorption free energies at 625 K are still endergonic but become totally exergonic when the temperature goes to 800 K. The

toluene desorption involves a significantly huge drop in the profile from 0 K to 800 K because of this entropy effect. Last but not least, the same shift on free energy also occurs after the second H₂ desorption, similar to what we observed on the cluster in Figure IV-10. This phenomenon depends on the temperature but not on the type of catalyst surface or reaction mechanism. It can be used to explain the fact that at high temperature, the molecule adsorption step can be difficult to achieve but once the molecule adsorbs on the surface, the reaction can be more easily performed at high temperature to give the product. Note that we did not investigate here the effect of hydrogen coverage on the Pt (111) surface, which may also affect the free energy profiles.

Table IV-21 reports the thermodynamic and kinetic data for all the elementary steps at 625 K calculated at the PBE-dDsC level. The temperature is chosen at 625 K in order to make a comparison with the investigation performed on the cluster.

Table IV- 21 Thermodynamics and kinetic data for all elementary steps involved in methyl-cyclohexane dehydrogenation over Pt (111) at 625 K calculated with the PBE-dDsC functional

Elementary step	Transition States	Reaction energy, enthalpy, entropy term and Gibbs free energy at 625 K (kJ/mol)				Activation energy, enthalpy, entropy term and Gibbs free energy (forward) at 625 K (kJ/mol)				Activation energy, enthalpy, entropy term and Gibbs free energy (backward) at 625 K (kJ/mol)			
		$\Delta_r E$	$\Delta_r H$	$T\Delta_r S$	$\Delta_r G$	$\Delta_r E^\ddagger$	$\Delta_r H^\ddagger$	$T\Delta_r S^\ddagger$	$\Delta_r G^\ddagger$	$\Delta_r E^\ddagger$	$\Delta_r H^\ddagger$	$T\Delta_r S^\ddagger$	$\Delta_r G^\ddagger$
MCH (g) \rightarrow A'	--	-105	-104	-105	1	--	--	--	--	--	--	--	--
A' \rightarrow B'	TS_a	9	-3	4	-7	91	80	1	78	82	83	-2	85
B' \rightarrow C'	TS_b	3	-7	-3	-4	84	72	-7	79	81	79	-4	83
C' \rightarrow D' + H ₂	--	91	96	75	21	--	--	--	--	--	--	--	--
D' \rightarrow E'	TS_d	-11	-24	0	-24	63	45	-5	50	74	69	-5	74
E' \rightarrow F'	TS_e	-12	-26	-9	-16	64	49	-7	57	76	75	2	73
F' \rightarrow G' + H ₂	--	78	81	77	4	--	--	--	--	--	--	--	--
G' \rightarrow H'	TS_g	-26	-39	-6	-34	47	31	-1	32	74	70	4	66
H' \rightarrow I'	TS_h	-12	-24	7	-31	76	58	1	57	88	82	-6	88
I' \rightarrow J' + H ₂	--	77	82	75	7	--	--	--	--	--	--	--	--
J' \rightarrow Tol (g)	--	192	187	147	40	--	--	--	--	--	--	--	--

The structure of intermediates and transition states involved in C-H bond breaking steps are shown in Figure IV-19.

The methyl-cyclohexane molecule adsorption reaction is an slightly endergonic step with nearly zero reaction free energy at 625 K.

The C-H bond cleavage steps are all exothermic and exergonic. The ranges on these activation enthalpies and activation free energies are both about 50 kJ/mol. Nevertheless, BEP linear relationship on these C-H bond cleavage steps (Table IV-15 and Appendix-IV-4) were found both for enthalpy and free energy, better than on the cluster. This time, the most demanding step in terms of free activation energy is the second C-H bond cleavage step (B' \rightarrow C')

via TS_b), in competition with the first one ($A' \rightarrow B'$ via TS_a), which is not in an agreement with what we have found on the cluster model (third C-H bond cleavage was limiting whereas on Pt(111) it requires relatively low free activation energy).

The H_2 desorption steps are all endothermic and endergonic at the temperature of 625 K, as well as the desorption step of toluene at the last of reaction. The reaction free energy of these steps are also temperature-dependent because of the gain of entropy. The hydrogen atoms obtained by dissociation of the H_2 molecule are co-adsorbed temporally on Pt (111) in a three-fold hollow site, which has been already proved to be the most stable adsorption mode on this metal face⁴⁵. The activation energy of hydrogen desorption has been estimated experimentally at about 40 kJ/mol⁴⁶. From a previous theoretical DFT work, the hydrogen desorption electronic activation energy was determined as 53 kJ/mol at high hydrogen coverage (7/6 of a ML) in a small unit cell⁴⁷. The values we calculate (Table 18) are generally higher than these two previously mentioned values, which can likely be assigned to the presence of the hydrocarbon intermediates co-adsorbed with the 2 hydrogen atoms at the surface.

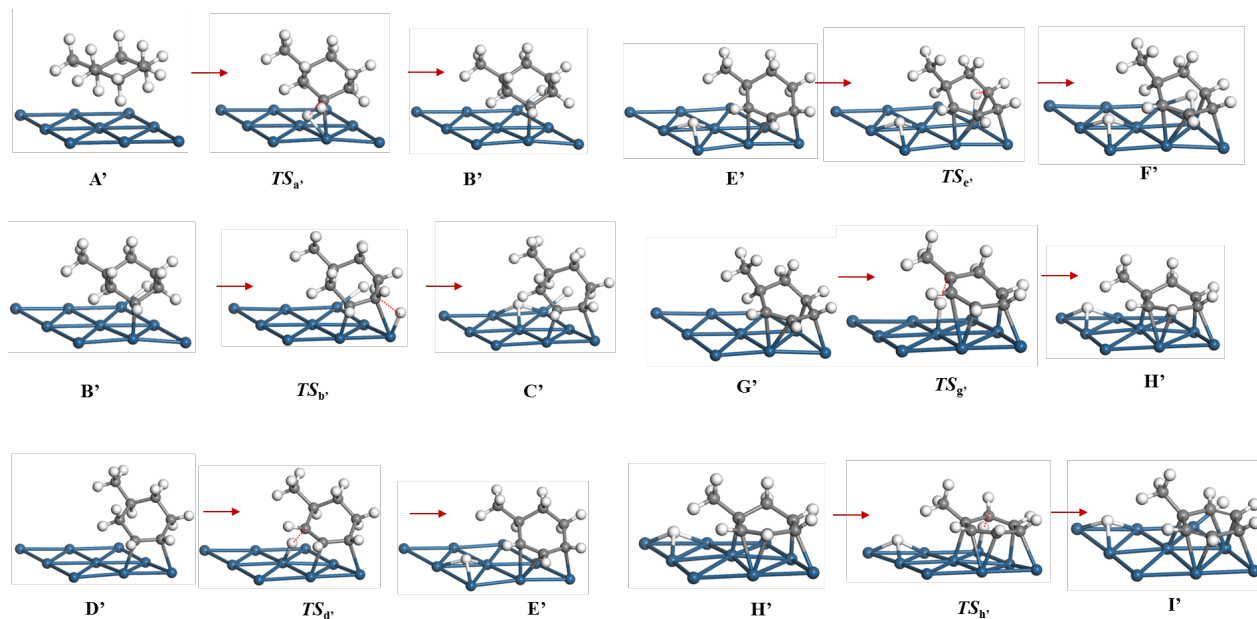


Figure IV- 19 Configurations of all transition states of C-H bond cleavage steps for methyl-cyclohexane dehydrogenation over Pt(111) calculated with the PBE-dDsC functional

8.3 Comparison of Gibbs free energy profiles on Pt(111) with PBE-dDsC and PBE functionals

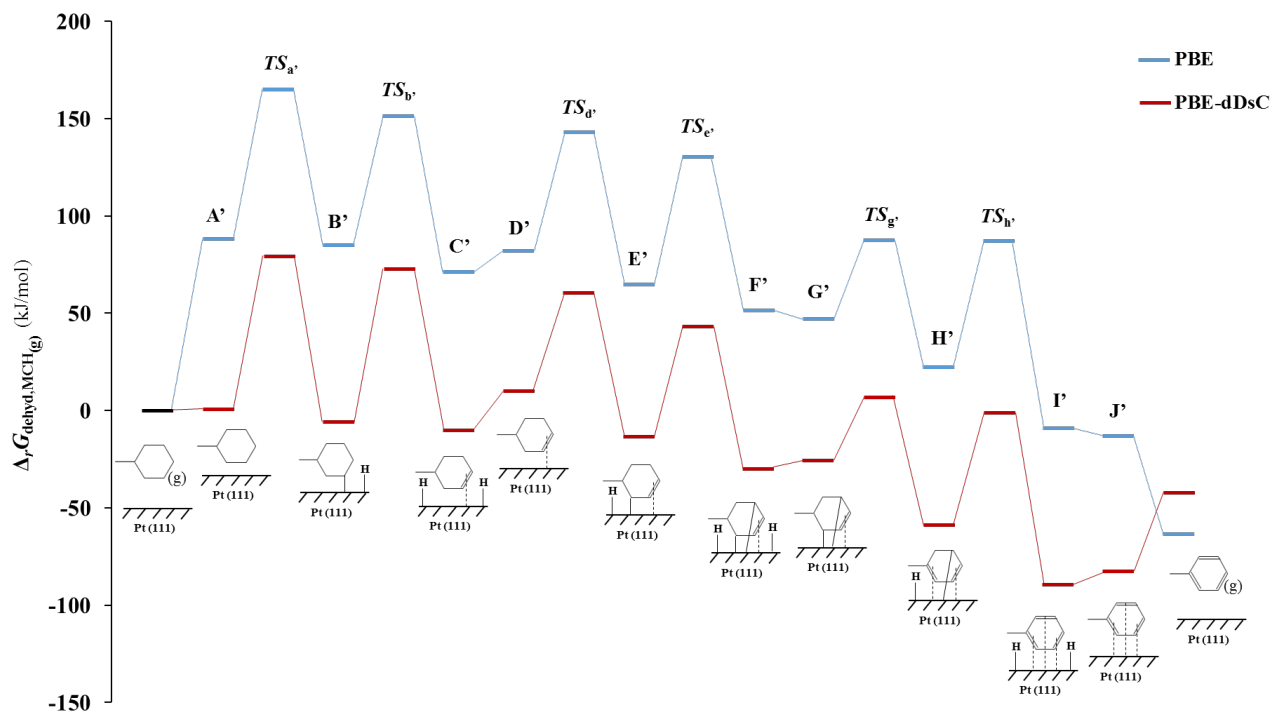


Figure IV- 20 Free energy profiles for methyl-cyclohexane dehydrogenation reaction mechanisms over Pt (111) calculated with the PBE (blue line) and PBE-dDsC (red line) functionals at 625 K

Figure IV-20 illustrates the comparison of free energy profiles for the reaction mechanisms over Pt(111) surface at the PBE and PBE-dDsC levels, at 625 K. The whole free energy profile (except for toluene in gas phase) is shifted by around 80 kJ/mol, which hints that the metal surface is more affected by the inclusion of dispersion forces with the adsorbed intermediates as compared to the cluster (around 30 kJ/mol of free energy decrease from PBE to PBE-dDsC). Meanwhile, for the methyl-cyclohexane physisorption step, which we have already discussed in *section 5.*, the reaction free energy decreases radically when the van der Waals forces are introduced into the system (decrease of 93 kJ/mol for the reaction free energy). With

PBE, the second and last H₂ desorption, toluene desorption steps are exergonic ($\Delta_r G_{F' \rightarrow G'} = -5$ kJ/mol, $\Delta_r G_{I' \rightarrow J'} = -4$ kJ/mol and $\Delta_r G_{J' \rightarrow Tol(g)} = -50$ kJ/mol on PBE), while with PBE-dDsC, these steps become endergonic. The most demanding step with PBE is the $MCH_{(g)} \rightarrow TS_a$, with $\Delta_r G_{MCH_{(g)} \rightarrow TS_a}^\ddagger = 165$ kJ/mol due to the high energy barrier for the first molecule adsorption step. However, this step with PBE-dDsC exhibits a total free energy of 79 kJ/mol, which is identical to the second C-H bond cleavage in terms of free activation energy ($\Delta_r G_{B' \rightarrow C'}^\ddagger = 79$ kJ/mol with PBE-dDsC vs $\Delta_r G_{B' \rightarrow C'}^\ddagger = 66$ kJ/mol with PBE).

9. Comparison of Gibbs free energy profiles on Pt (111) and on Pt₁₃H₆/γ-Al₂O₃ (100) with the PBE-dDsC functional

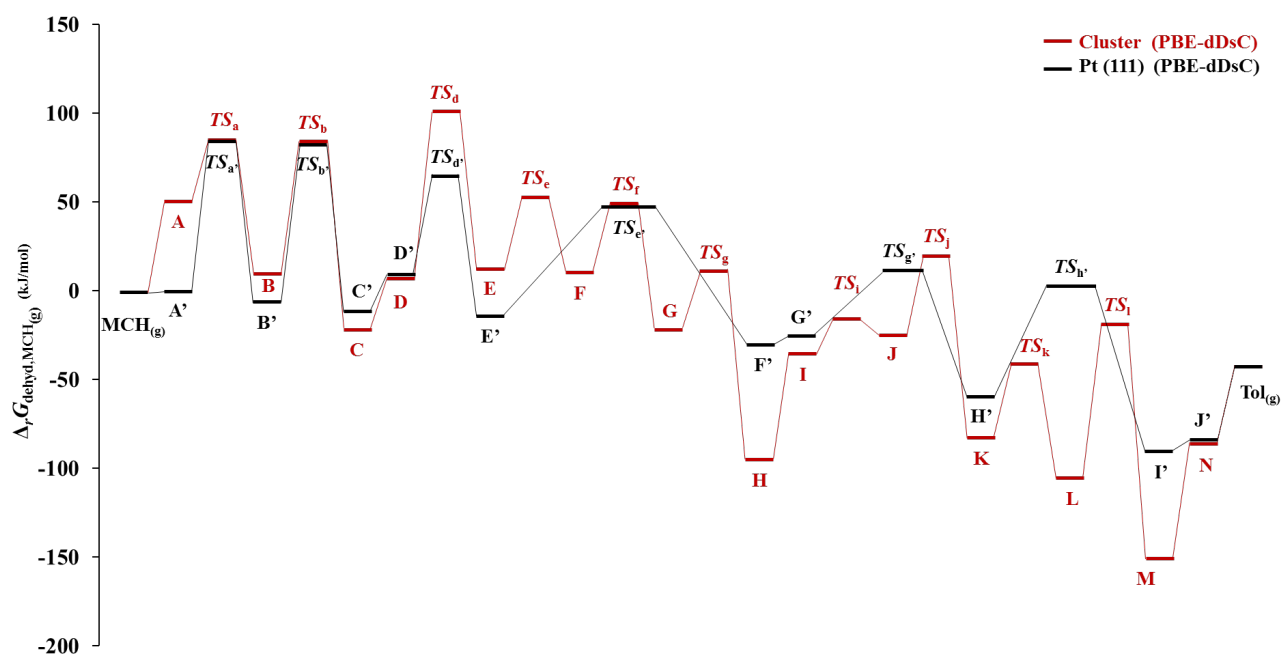


Figure IV- 21 Comparison of free energy profiles for methyl-cyclohexane dehydrogenation reaction mechanism on Pt₁₃H₆/γ-Al₂O₃ and Pt (111) at 625 K calculated with the PBE-dDsC functional

The Gibbs free energy profiles for both the cluster and Pt(111), calculated with the PBE-dDsC functional at 625 K, are presented in Figure IV-21. One remarkable point is that the contribution of dispersion forces stabilizes significantly the reaction on Pt(111). With PBE the cluster stabilizes all the intermediates and transition states compared to the (111) surface (Appendix-IV-8) but this stabilization is eliminated at the PBE-dDsC level. In a general manner, it is hard to conclude about the system which will catalyze the reaction most efficiently, from the free energy diagrams only. The profiles are very close at the beginning of the reaction but the cluster still stabilizes more strongly the intermediates (and most transition states) starting from H (methyl-cyclohexadiene). This could be in favor of the supported cluster but the very strong stabilization of adsorbed toluene could also be a drawback, rendering the desorption of the product limiting in certain conditions. Kinetic modeling is required to conclude on the respective reactivities of the two catalytic systems.

So far, the importance of applying the PBE-dDsC functional is thus emphasized both on the cluster and the surface. For next step to integrate our *ab initio* results into kinetic models, the parameters obtained by PBE-dDsC will be used.

Conclusions and perspectives

This chapter aimed at the investigation of the reactivity of metallic nano-aggregates, composed of platinum supported on γ -alumina, as models of catalytic reforming catalysts. We addressed so far the simulation of the dehydrogenation reaction of methyl-cyclohexane into toluene over Pt_{13} clusters supported on $\gamma\text{-Al}_2\text{O}_3$, by periodic Density Functional Theory (DFT) calculations at the PBE-dDsC and PBE levels. Our present modeling results obtained on the $\text{Pt}_{13}\text{H}_6/\gamma\text{-Al}_2\text{O}_3$ (100) and Pt (111) systems are based on the assumption that the reaction pathway consists of important intermediates such as methyl-cyclohexyl radical, methyl-cyclohexene, methyl-cyclohexenyl radical, methyl-cyclohexadiene and methyl-cyclohexadienyl radical, formed subsequently by dissociation of C-H bonds on the cluster or the surface. On $\text{Pt}_{13}\text{H}_6/\gamma\text{-Al}_2\text{O}_3$ (100), the fluctuonality of the cluster induces also several steps of cluster reconstruction and hydrogen atom migration. A combination of ab initio molecular dynamics, transition states search and vibrational properties determination allowed to make the following conclusions :

(1) Accurate estimation of Gibbs free energies including vibrational contributions for condensed phases and adsorbed molecules was undertaken and showed a high sensitivity towards calculation parameters. Taking into account these contributions is however of paramount importance for the future quantification of rate constants.

(2) The importance of dispersion interactions was emphasized, as estimated with PBE-dDsC (with respect to PBE), both for $\text{Pt}_{13}\text{H}_6/\gamma\text{-Al}_2\text{O}_3$ (100) and Pt(111) systems. The dispersion corrections have significantly decreased the free energy profiles, especially prominent for the first molecule physisorption step of methyl-cyclohexane. These dispersion forces are stronger on the Pt(111) surface than on $\text{Pt}_{13}\text{H}_6/\gamma\text{-Al}_2\text{O}_3$ (100), with a free energy lowering of 80 kJ/mol on Pt(111) against 30 kJ/mol on $\text{Pt}_{13}\text{H}_6/\gamma\text{-Al}_2\text{O}_3$ (100).

(3) Depending on the geometries obtained by DFT calculations for each intermediate, the cluster exhibits an obvious fluctuation along the reaction path, which tends to stabilize the whole system.

(4) The temperature effect is related to entropy, which mostly affects the molecule (methyl-cyclohexane, H₂ and toluene) adsorption/desorption steps on both systems.

(5) The highest energy barrier found so far on Pt₁₃H₆/γ-Al₂O₃ (100) corresponds to the third C-H cleavage step of methyl-cyclohexene into methyl-cyclohexenyl + H with a free activation energy of 95 kJ/mol at the PBE-dDsC level. However, the free activation energies for several steps are competitive (ex. The last C-H cleavage step of methyl-cyclohexadienyl +H to toluene + 2H with an free activation energy of 87 kJ/mol at the PBE-dDsC level), it is thus difficult to draw at this stage an unambiguous conclusion about the nature of the rate limiting step. Furthermore, on the Pt(111) surface, the second C-H cleavage step of methyl-cyclohexyl +H to methyl-cyclohexene + 2 H is found to be the most demanding step with a free activation energy of 79 kJ/mol, which is very close to that of first C-H cleavage step with an free activation energy of 78 kJ/mol at the PBE-dDsC level.

(6) BEP linear relationship for these C-H cleavage steps was determined for both systems and have a better linear behavior on the surface than on the cluster. It is probably because of the complexity of the cluster system, with morphology change from one C-H bond breaking step to another.

(7) The cluster reconstruction steps and hydrogen atom migration steps are generally less activated than the C-H cleavage steps.

The following step of the study will be dedicated to establishing a kinetic model from the present mechanism, where the calculation of rate constants related to each activation energy and corresponding to each elementary step will be proceeded from the present *ab initio* calculations. The kinetic rate constants determined by *ab initio* will be incorporated in a Langmuir-Hinshelwood (LH) kinetic model, based on the stepwise dehydrogenation mechanism: rate equations will be integrated and lead to a quantification of the expected rate of formation of the product, sensitive steps and reaction apparent activation energy and enthalpy. Such a modeling approach, from elementary steps studied *ab initio* to the calculation of macroscopic data, allow us to compare with the conventional kinetic fitting modeling approaches which have already been reported in the literature.^{12,15} As the objectives of the next chapter, we will undertake catalytic tests to compare with the *ab initio* kinetic modeling.

References

- (1) Digne, M.; Sautet, P.; Raybaud, P.; Euzen, P.; Toulhoat, H. *J. Catal.* **2002**, *211*, 1–5.
- (2) Digne, M. *J. Catal.* **2004**, *226*, 54–68.
- (3) Krokidis, X.; Raybaud, P.; Gobichon, A. E.; Rebours, B.; Euzen, P.; Toulhoat, H. *J. Phys. Chem. B* **2001**, *105*, 5121–5130.
- (4) Digne, M.; Raybaud, P.; Sautet, P.; Guillaume, D.; Toulhoat, H. *J. Am. Chem. Soc.* **2008**, *130*, 11030–11039.
- (5) Hu, C. H.; Chizallet, C.; Mager-Maury, C.; Corral-Valero, M.; Sautet, P.; Toulhoat, H.; Raybaud, P. *J. Catal.* **2010**, *274*, 99–110.
- (6) Mager-Maury, C.; Bonnard, G.; Chizallet, C.; Sautet, P.; Raybaud, P. *ChemCatChem* **2011**, *3*, 200–207.
- (7) Mager-Maury, C.; Chizallet, C.; Sautet, P.; Raybaud, P. *ACS Catal.* **2012**, *2*, 1346–1357.
- (8) Gorczyca, A.; Moizan, V.; Chizallet, C.; Proux, O.; Del Net, W.; Lahera, E.; Hazemann, J. L.; Raybaud, P.; Joly, Y. *Angew. Chem. Int. Ed.* **2014**, *53*, 12426–12429.
- (9) Mistry, H.; Behafarid, F.; Bare, S. R.; Roldan Cuenya, B. *ChemCatChem* **2014**, *6*, 348–352.
- (10) Gorczyca, A. Thesis : Caractérisation de catalyseurs métalliques supportés par spectroscopie XANES, apports du calcul quantique dans l'interprétation des spectres expérimentaux. research thesis, Université Joseph Fournier de Grenoble & IFPEN, 2014.
- (11) Sinfelt, H. J.; Hurwitz, H.; Shulman, R. A. *J. Phys. Chem.* **1960**, *64*, 1559–1562.
- (12) Van Trimpont, P. A.; Marin, G. B.; Froment, G. F. *Ind. Eng. Chem. Fundam.* **1986**, *25*, 544–553.
- (13) Van Trimpont, P. A.; Marin, G. B.; Froment, G. F. *Ind. Eng. Chem. Res.* **1988**, *27*, 51–57.
- (14) Alhumaidan, F.; Cresswell, D.; Garforth, A. *Ind. Eng. Chem. Res.* **2011**, *50*, 2509–2522.
- (15) Usman, M.; Cresswell, D.; Garforth, A. *Ind. Eng. Chem. Res.* **2012**, *51*, 158–170.
- (16) Van Trimpont, P. A. Mari, G. B. Froment, G. F. *Appl. Catal.* **1985**, *17*, 161–173.
- (17) Hem, F. C.; Diaz, A. L.; Bussell, M. E.; Hugenschmidt, M. B.; Domagala, M. E.; Campbell, C. T. *J. Phys. Chem. B* **1992**, *96*, 5965–5974.
- (18) Wang, B.; Froment, G. F. *Catal. Lett.* **2017**, *147*, 663–673.
- (19) Lytken, O.; Lew, W.; Campbell, C. T. *Chem. Soc. Rev.* **2008**, *37*, 2172–2179.
- (20) Verstraete, J. Thesis : Kinetische Studie van de Katalytische Reforming van Nafta over een Pt-Sn/Al₂O₃ Katalysator, Universiteit Gent, 1997.
- (21) Raybaud, P.; Chizallet, C.; Mager-Maury, C.; Digne, M.; Toulhoat, H.; Sautet, P. *J. Catal.* **2013**, *308*, 328–340.
- (22) Steininger, H.; Ibach, H.; Lehwald, S. *Surf. Sci.* **1982**, *117*, 685–698.
- (23) Cassuto, A.; Jupille, J. *Surf. Sci.* **1991**, *249*, 8–14.
- (24) Cassuto, A.; Kiss, J.; White, J. M. *Surf. Sci.* **1991**, *255*, 289–294.
- (25) Okada, T.; Kim, Y.; Sainoo, Y.; Komeda, T.; Trenary, M.; Kawai, M. *J. Phys. Chem. Lett.* **2011**, *2*, 2263–2266.
- (26) Cremer, P. S.; Su, X.; Shen, Y. R.; Somorjai, G. A. *J. Am. Chem. Soc.* **1996**, *118*, 2942–2949.

- (27) Sabbe, M. K.; Canduela-Rodriguez, G.; Reyniers, M. F.; Marin, G. B. *J. Catal.* **2015**, *330*, 406–422.
- (28) Bera, T.; Thybaut, J. W.; Marin, G. B. *Ind. Eng. Chem. Res.* **2011**, *50*, 12933–12945.
- (29) Saeys, M.; Reyniers, M.; Thybaut, J.; Neurock, M.; Marin, G. B. *J. Catal.* **2005**, *236*, 129–138.
- (30) Saeys, M.; Reyniers, M.; Thybaut, J.; Neurock, M.; Marin, G. B. *J. Phys. Chem. B* **2005**, *109*, 2064–2073.
- (31) Ma, H. Y.; Wang, G. C. *J. Catal.* **2011**, *281*, 63–75.
- (32) Morin, C.; Simon, D.; Sautet, P. *J. Phys. Chem. B* **2004**, *108*, 5653–5665.
- (33) Morin, C.; Simon, D.; Sautet, P. *Surf. Sci.* **2006**, *600*, 1339–1350.
- (34) Sinfelt, J. H. *J. Mol. Catal. A* **2000**, *163*, 123–128.
- (35) Bell, R. P. *Proc. R. Soc. London* **1936**, *154*, 414–429.
- (36) Evans, M. G.; Polanyi, M. *Trans. Faraday Soc.* **1937**, *33*, 448–452.
- (37) Evans, M. G.; Polanyi, M. *Trans. Faraday Soc.* **1938**, *34*, 11–24.
- (38) Bligaard, T.; Nørskov, J. K.; Dahl, S.; Matthiesen, J.; Christensen, C. H.; Sehested, J. *J. Catal.* **2004**, *224*, 206–217.
- (39) Chen, Y.; Vlachos, D. G. *J. Phys. Chem. C* **2010**, *114*, 4973–4982.
- (40) Zaffran, J.; Michel, C.; Auneau, F.; Delbecq, F.; Sautet, P. *ACS Catal.* **2014**, *4*, 464–468.
- (41) Wang, S. G.; Vorotnikov, V.; Sutton, J. E.; Vlachos, D. G. *ACS Catal.* **2014**, *4*, 604–612.
- (42) Delbecq, F.; Loffreda, D.; Sautet, P. *J. Phys. Chem. Lett.* **2010**, *1*, 323–326.
- (43) Olsen, R. A.; Kroes, G. J.; Baerends, E. J. *J. Chem. Phys.* **1999**, *111*, 11155.
- (44) Arboleda, N. B.; Kasai, H.; Diño, W. A.; Nakanishi, H. *Japanese J. App. Phys.* **2007**, *46*, 4233.
- (45) Baro, A. M.; Ibach, H.; Bruchmann, H. D. *Surf. Sci.* **1979**, *88*, 384–398.
- (46) Christmann, K.; Ertl, G.; Pignet, T. *Surf. Sci.* **1976**, *54*, 365–392.
- (47) Skulason, E.; Karlberg, G. S.; Rossmeisl, J.; Bligaard, T.; Greeley, J.; Jonsson, H.; Nørskov, J. K. *Phys. Chem. Chem. Phys.* **2007**, *9*, 3241–3250.

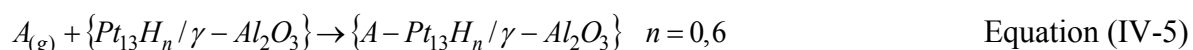
Appendix-IV

1. Comparison on different adsorption modes of MCHe and ethylene, and effect of hydrogen coverage

Raybaud et al.²¹ reported that for ethylene on Pt₁₃H₆/γ-Al₂O₃(100) the di-σ mode was preferred. Two intricate effects are suspected to be the cause of the different behavior observed with the 4-Methyl-cyclohexene:

- 1) the effect of hydrogen coverage on the metal surface and the substituent effect (the 2 hydrogen atoms were maintained on the cluster in the case of the study of Raybaud et al.).
- 2) the intrinsic nature of the molecules.

For that purpose, ethylene and 4-methyl-cyclohexene have been adsorbed on Pt₁₃H₆/γ-Al₂O₃(100) and Pt₁₃/γ-Al₂O₃(100) (Equation IV-5 with A = MCHe, ethylene).



The adsorption energy of these two molecules on the metal face has been calculated as $E_{ads,A}$:

Adsorption energy :

$$E_{ads,A(g)} = E\{A - Pt_{13}H_n / \gamma - Al_2O_3\} - E\{Pt_{13}H_n / \gamma - Al_2O_3\} - E(A_{(g)}) \quad n = 0, 6 \quad \text{Equation (IV-6)}$$

Table IV- 22 Adsorption energy for ethylene and 4-methyl-cyclohexene on the Pt₁₃H₆/γ-Al₂O₃(100) and Pt₁₃/γ-Al₂O₃(100) surface at the PBE level

Pt ₁₃ H _n /γ-Al ₂ O ₃ (100)	<i>E</i> _{ads,Ethylene} (kJ/mol)		<i>E</i> _{ads,4-MCHe} (kJ/mol)	
	di-σ	π	di-σ	π
n = 6	-107	-122	-68	-111
n = 0	-166	-140	-130	-127

Note: for the adsorption, the di-σ is on the site V3-V5 and the π mode is on V3.

The calculated adsorption energies of these two molecules in both di-σ and π modes are reported in Table 21. It can be observed that for both molecules ethylene and 4-MCHe, with 6 co-adsorbed hydrogen atoms, the π mode is well favored. For n=0, the di-σ mode turns out to be more stable for ethylene, while for 4-MCHe the two modes remain energetically competitive. This result proves that the hydrogen coverage impacts the adsorption energies and modes of the two molecules. When there is less hydrogen atom on the metal surface, the molecule seems to prefer to sit on two metal sites. However, it should be underlined that for 4-MCHe, the di-σ mode is intrinsically significantly less favored in general compared to ethylene (39 kJ/mol for the difference on electronic energy for n =6 and 36 kJ/mol for n =0). The two adsorption energies are very close, while for ethylene, the difference of energy for these two adsorption modes at both hydrogen coverage is more pronounced. At the same time, this means that ethylene is more sensible for the hydrogen coverage on the metal surface than 4-MCHe. The former result by Raybaud et al. shows that the di-σ mode can also be possible even at higher H coverage which may reveal also an impact of the position of hydrogen atoms on the adsorption mode. Figure 22 shows the most stable geometry of each system calculated.

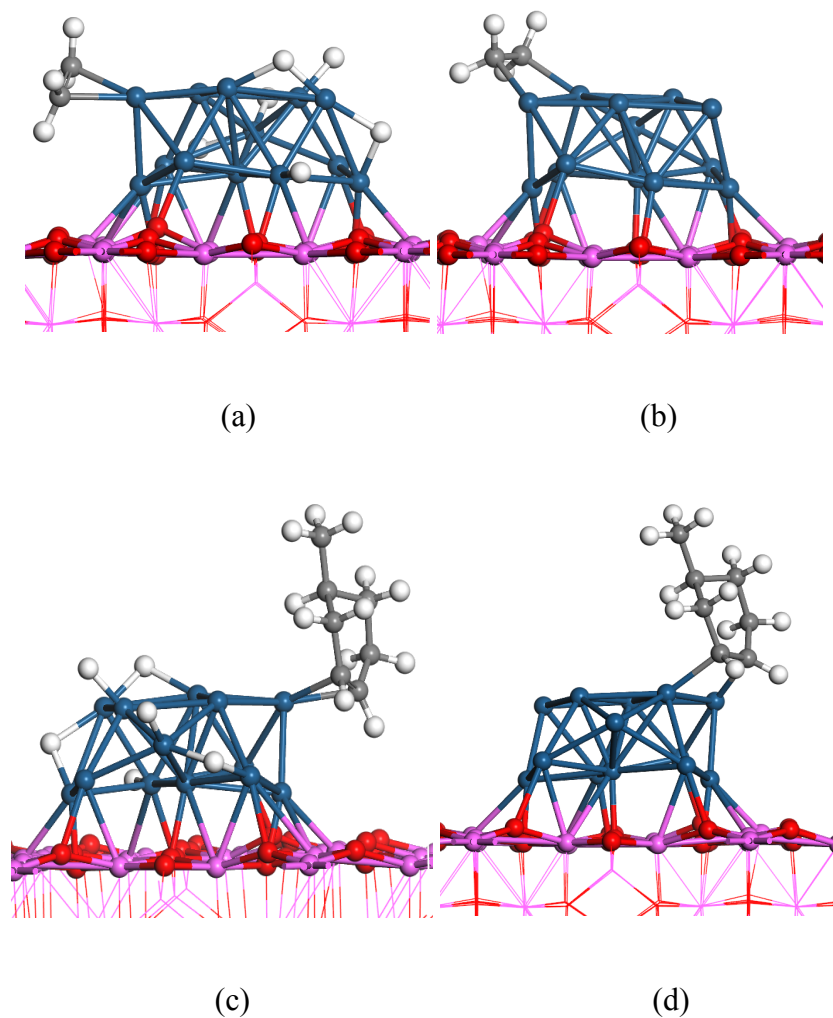


Figure IV- 22 Most stable adsorption geometry for ethylene and 4-methyl-cyclohexene on the Pt₁₃H₆/γ-Al₂O₃(100) and Pt₁₃/γ-Al₂O₃(100) surfaces : (a) ethylene π on Pt₁₃H₆/γ-Al₂O₃(100) ; (b) ethylene di-σ on Pt₁₃/γ-Al₂O₃(100) ; (c) 4-MCHe π on Pt₁₃H₆/γ-Al₂O₃(100) ; (d) 4-MCHe di-σ on Pt₁₃/γ-Al₂O₃(100)

2. Decomposition of the dehydrogenation energy for adsorbed 4-methyl-cyclohexene before and after MD

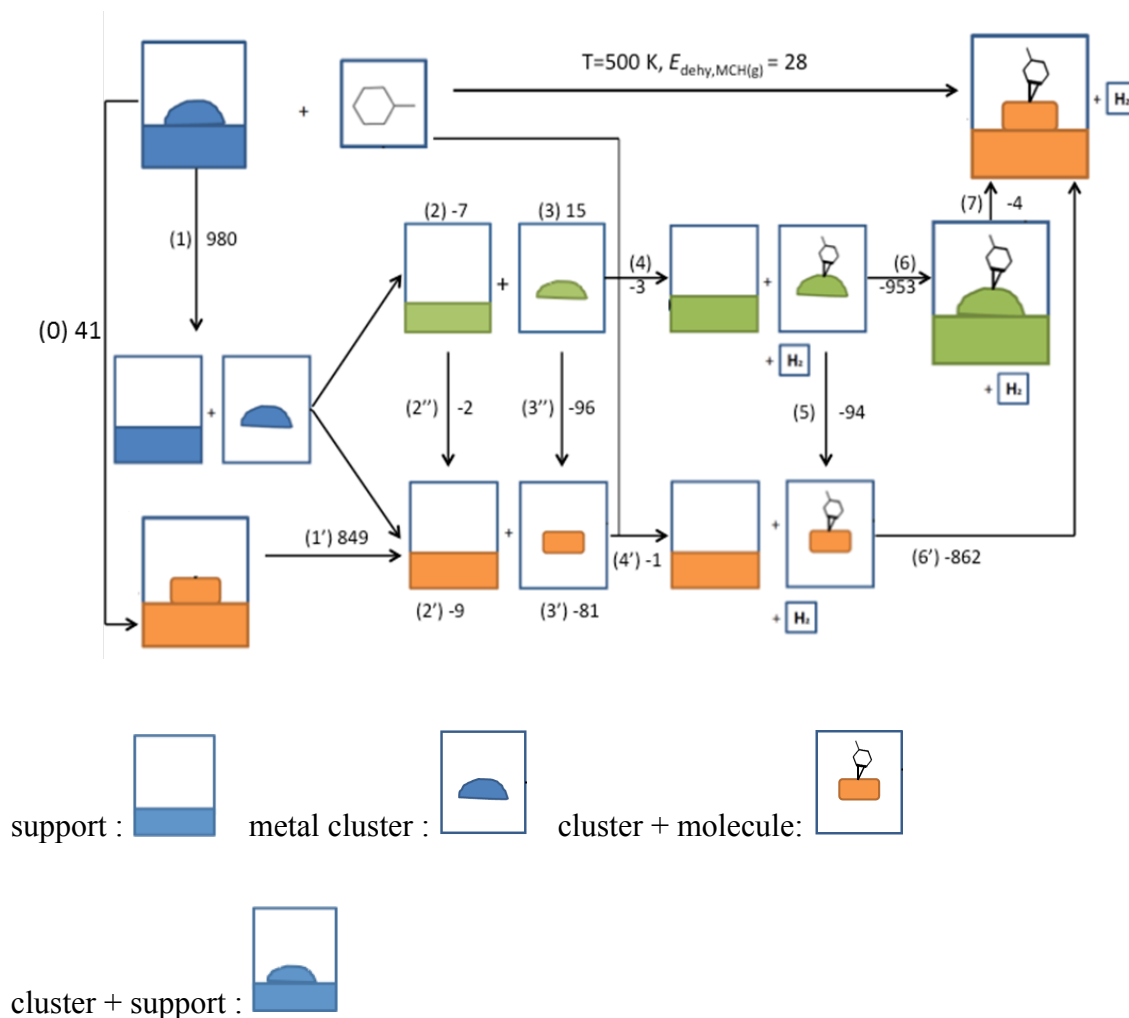


Figure IV- 23 Decomposition of the dehydrogenation energy (in kJ/mol) for adsorbed 4-methyl-cyclohexene before and after MD (Color legend: blue : reference system ; green : system before MD; orange : system after MD calculations.)

The energy of each decomposition step during the dehydrogenation reaction is marked on each arrow on Figure IV-23. Step (0) is the transformation from the reference catalytic system to the deformed catalyst (induced by MCH after MD), which corresponds to +40 kJ/mol, confirming that the reference catalyst model is the most stable one. For step (1), the energy to

separate the metal cluster and the support is highly endothermic and requires +980 kJ/mol. If we compare this value to the one for step (1'), it is found that the MD calculations weakened the interaction (+849 kJ/mol) between the metal cluster and the support. These endothermic energies are mostly compensated by the final recombination energies at step (6) and (6'). Steps (2'') and (3'') correspond to the deformation energy of the support and the cluster (in gas phase). Whereas the deformation energy of the support is modest, the cluster after MD tends to be more stable (negative deformation energy of -81 kJ/mol). After that, the dehydrogenation of $\text{MCH}_{(g)}$ to 4-MCHe is presented by step (4) and (4'), respectively on the cluster before and after MD: both exhibit modest energy change. However, as for step (3''), step (5) is exothermic by -94 kJ/mol: the difference of stability of the metal cluster is still the dominant reason to explain that deformed system is more stable. But once the system is recombined, the difference on the stability stays very small, presented by step (7) = -4 kJ/mol. So by now, it can be concluded that the MD calculations stabilize mainly the metallic cluster in the presence of the molecule and seem to reduce the interaction between the metal and the support.

3. Detailed thermodynamics for reaction path on Pt₁₃H₆/γ-Al₂O₃ (100) cluster at different temperatures at the PBE-dDsC level

SURFACE INTERMEDIATES	T = 0 K			T = 625 K			T = 800 K			
	$\Delta E_{\text{rel},\text{MCH}}^{\text{g}}$ (KJ/mol)	$\Delta H_{\text{rel},\text{MCH}}^{\text{g}}$ (KJ/mol)	$T\Delta S_{\text{rel},\text{MCH}}^{\text{g}}$ (KJ/mol)	$\Delta G_{\text{rel},\text{MCH}}^{\text{g}}$ (KJ/mol)	$\Delta H_{\text{rel},\text{MCH}}^{\text{g}}$ (KJ/mol)	$T\Delta S_{\text{rel},\text{MCH}}^{\text{g}}$ (KJ/mol)	$\Delta G_{\text{rel},\text{MCH}}^{\text{g}}$ (KJ/mol)	$\Delta H_{\text{rel},\text{MCH}}^{\text{g}}$ (KJ/mol)	$T\Delta S_{\text{rel},\text{MCH}}^{\text{g}}$ (KJ/mol)	$\Delta G_{\text{rel},\text{MCH}}^{\text{g}}$ (KJ/mol)
(A) Methyl-cyclohexane <i>TS_a</i>	-45	-40	-91	51	-37	-113	76	-37	-113	76
(B) Methyl-cyclohexyl + H <i>TS_b</i>	-14	-21	-105	83	-18	-131	112	-18	-131	112
(C) Methyl-cyclohexene + 2H	-87	-88	-97	9	-84	-120	36	-84	-120	36
(D) Methyl-cyclohexene <i>TS_d</i>	1	-15	-94	79	-11	-116	105	-11	-116	105
(E) Methyl-cyclohexenyl + H <i>TS_e</i>	-105	-116	-94	-21	-111	-115	4	-111	-115	4
(F) Methyl-cyclohexenyl + H <i>TS_f</i>	3	-13	-20	7	-9	-21	12	-9	-21	12
(G) Methyl-cyclohexenyl + H <i>TS_g</i>	116	85	-17	102	89	-17	106	89	-17	106
(H) Methyl-cyclohexadiene + 2H	9	-19	-32	13	-14	-35	21	-14	-35	21
(I) Methyl-cyclohexadiene <i>TS_i</i>	66	33	-20	54	38	-21	59	38	-21	59
(J) Methyl-cyclohexadiene <i>TS_j</i>	14	-13	-24	11	-8	-24	17	-8	-24	17
(K) Methyl-cyclohexadiene <i>TS_k</i>	82	48	-2	50	53	2	50	53	2	50
(L) Methyl-cyclohexadiene <i>TS_l</i>	-4	-30	-9	-21	-24	-5	-20	-24	-5	-20
(M) Methyl-cyclohexadienyl + H <i>TS_m</i>	44	3	-9	12	8	-5	13	8	-5	13
(N) Methyl-cyclohexadienyl + H <i>TS_n</i>	-74	-108	-13	-95	-102	-9	-92	-102	-9	-92
(O) Methyl-cyclohexadiene <i>TS_o</i>	73	33	68	-35	39	94	-55	39	94	-55
(P) Methyl-cyclohexadiene <i>TS_p</i>	100	53	68	-15	57	92	-35	57	92	-35
(Q) Methyl-cyclohexadiene <i>TS_q</i>	74	34	58	-25	39	81	-42	39	81	-42
(R) Methyl-cyclohexadienyl + H <i>TS_r</i>	119	68	48	20	73	67	6	73	67	6
(S) Methyl-cyclohexadienyl + H <i>TS_s</i>	33	-18	65	-83	-11	91	-102	-11	91	-102
(T) Methyl-cyclohexadienyl + H <i>TS_t</i>	88	30	71	-41	36	97	-61	36	97	-61
(U) Toluene + 2H <i>TS_u</i>	-1	-48	57	-106	-42	81	-122	-42	81	-122
(V) Toluene	107	46	65	-19	52	90	-38	52	90	-38
(W) Toluene (gas phase)	-23	-78	73	-151	-71	102	-172	-71	102	-172
(X) Toluene	104	45	131	-86	51	175	-124	51	175	-124
(Y) Toluene (gas phase)	283	219	262	-42	222	338	-116	222	338	-116

Figure IV- 24 Thermodynamics table for reaction path on Pt₁₃H₆/γ-Al₂O₃ (100) cluster at different temperatures at the PBE-dDsC level

4. BEP linear relationship study of sequential C-H bond cleavage for methyl-cyclohexane dehydrogenation over $\text{Pt}_{13}\text{H}_6/\gamma\text{-Al}_2\text{O}_3$ (100) cluster and Pt(111) surface at 625 K at the PBE-dDsC level

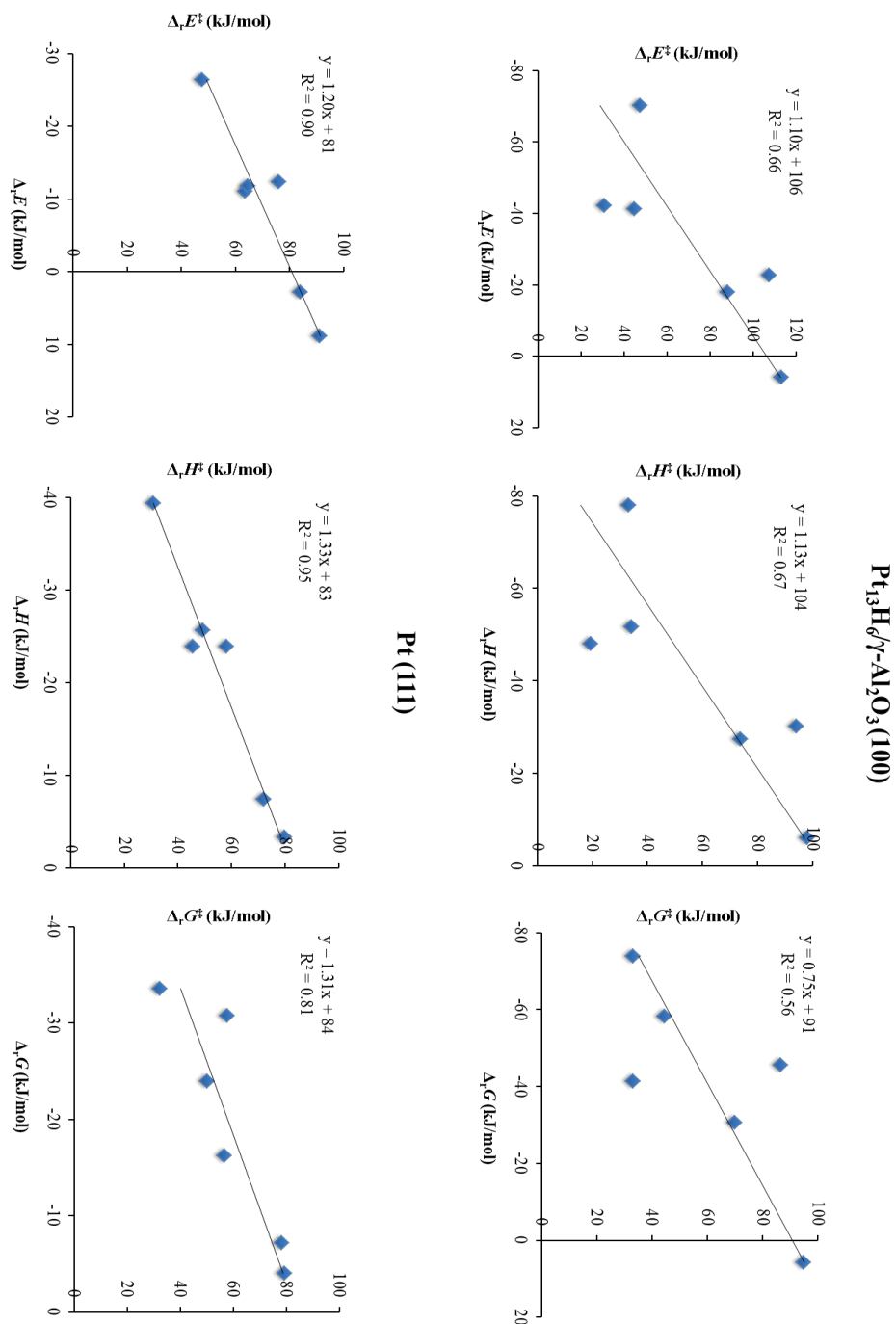


Figure IV- 25 BEP linear relationship of sequential C-H bond cleavage for methyl-cyclohexane dehydrogenation over $\text{Pt}_{13}\text{H}_6/\gamma\text{-Al}_2\text{O}_3$ (100) cluster and Pt (111) surface at 625 K at the PBE level

5. NEB investigation of the first H_2 desorption step

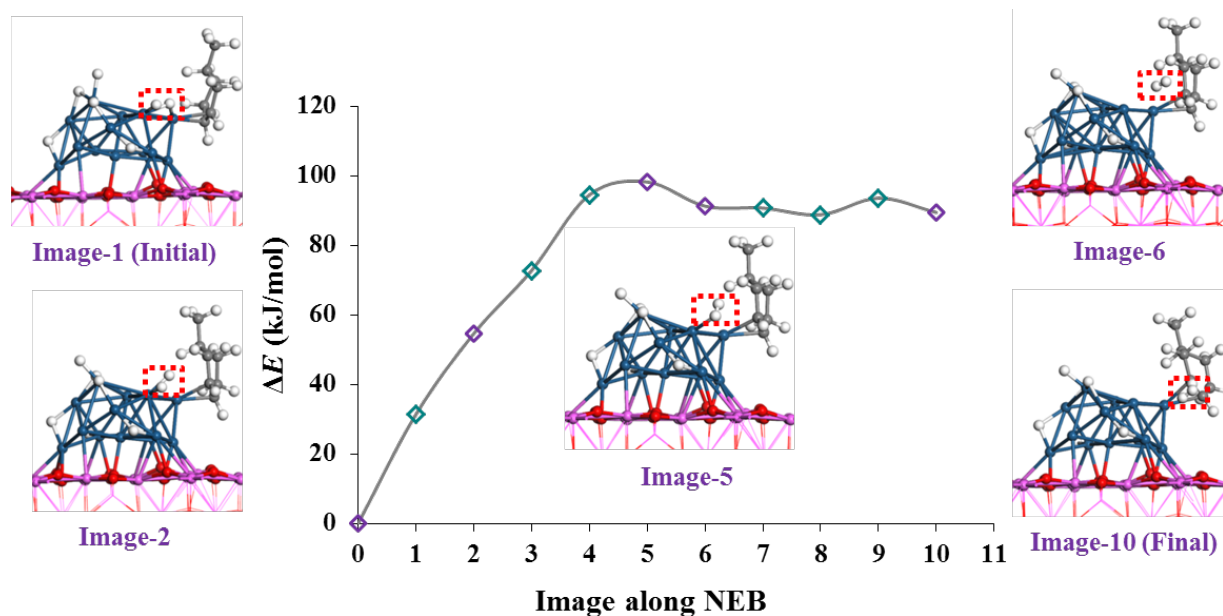


Figure IV- 26 Snapshots and electronic energies images along the NEB performed to simulate the H_2 molecule desorption step $\text{C} \rightarrow \text{D} + \text{H}_2$

To unravel the transition states and activation energies of the H_2 desorption steps, we explored the intermediate states from an initial state with two extra hydrogen atoms on cluster (C) to a final state with a molecule of H_2 formed but remaining close to the cluster, which is an preliminary intermediate just before D. The calculated electronic energies of each image during the NEB (non-converged structure after 70 steps SCF) are reported in Figure IV-24. This activation step starts with one of the two hydrogen atoms (H_a) moving from a bridge position to a top position, sharing the same platinum atom with the second hydrogen atom (H_b). Then $\text{H}_a - \text{Pt}$ bond breaks and the $\text{H}_a - \text{H}_b$ forms (H_2), while H_b is still on top position of platinum atom. Then the $\text{H}_b - \text{Pt}$ bond breaks as well and the new-formed H_2 is desorbed.

6. Detailed thermodynamics study for reaction path on Pt₁₃H₆/γ-Al₂O₃ (100) cluster at the

PBE level

SURFACE INTERMEDIATES	T = 0 K		T = 625 K			T = 800 K		
	$\Delta E_{\text{rel}}^{\text{rel}}(\text{g})$ (KJ/mol)	$\Delta H_{\text{rel}}^{\text{rel}}(\text{g})$ (KJ/mol)	$\Delta H_{\text{rel}}^{\text{rel}}(\text{g})$ (KJ/mol)	$T\Delta S_{\text{rel}}^{\text{rel}}(\text{g})$ (KJ/mol)	$\Delta G_{\text{rel}}^{\text{rel}}(\text{g})$ (KJ/mol)	$\Delta H_{\text{rel}}^{\text{rel}}(\text{g})$ (KJ/mol)	$T\Delta S_{\text{rel}}^{\text{rel}}(\text{g})$ (KJ/mol)	$\Delta G_{\text{rel}}^{\text{rel}}(\text{g})$ (KJ/mol)
(A) Methyl-cyclohexane <i>TS_a</i>	21	25	-83	108	29	-102	131	
(B) Methyl-cyclohexyl + H <i>TS_b</i>	52	44	-95	140	47	-119	166	
	-43	-44	-94	50	-40	-116	76	
(C) Methyl-cyclohexene + 2H <i>TS_c</i>	29	14	-89	103	18	-109	127	
	-71	-81	-92	11	-76	-112	36	
(D) Methyl-cyclohexene <i>TS_d</i>	28	12	-20	32	16	-21	37	
	149	118	-17	135	122	-17	139	
(E) Methyl-cyclohexenyl + H <i>TS_e</i>	38	10	-32	42	16	-35	51	
	97	65	-20	85	69	-21	90	
(F) Methyl-cyclohexenyl + H <i>TS_f</i>	44	17	-24	41	22	-24	47	
	111	78	-2	80	82	2	80	
(G) Methyl-cyclohexenyl + H <i>TS_g</i>	23	-3	-9	6	3	-5	8	
	77	36	-9	45	42	-5	46	
(H) Methyl-cyclohexadiene + 2H <i>TS_h</i>	-42	-76	-13	-63	-70	-9	-60	
	98	58	68	-10	64	94	-30	
(I) Methyl-cyclohexadiene <i>TS_i</i>	127	80	68	12	84	92	-7	
(J) Methyl-cyclohexadiene <i>TS_j</i>	99	59	58	0	64	81	-17	
	145	94	48	46	99	67	32	
(K) Methyl-cyclohexadienyl + H <i>TS_k</i>	56	6	65	-59	12	91	-78	
	110	53	71	-18	58	97	-39	
(L) Methyl-cyclohexadienyl + H <i>TS_l</i>	24	-24	57	-81	-17	81	-98	
	129	68	65	3	74	90	-16	
(M) Toluene + 2H	2	-53	73	-126	-45	102	-147	
(N) Toluene	122	63	131	-68	69	175	-106	
Toluene (gas phase)	262	198	262	-63	201	338	-137	

Figure IV- 27 Thermodynamics table for reaction path on Pt₁₃H₆/γ-Al₂O₃ (100) cluster at different temperatures at the PBE level

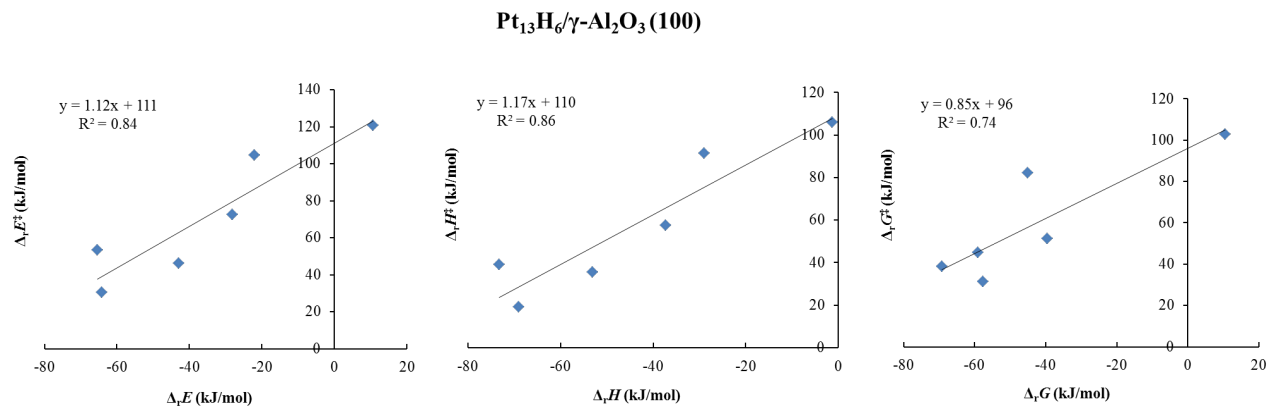


Figure IV- 28 BEP linear relationship of sequential C-H bond cleavage for methyl-cyclohexane dehydrogenation over Pt₁₃H₆/γ-Al₂O₃ (100) cluster at 625 K at the PBE level

As in Figure IV-28, it can be observed that at the PBE level, the BEP linear relationships (electronic energy, enthalpy and free energy) have better behaviors than those with PBE-dDsC (Figure IV-25). This comparison can emphasize again the effect of dispersion forces added to the cluster system.

7. Detailed thermodynamic data for reaction path on Pt(111) surface at different temperatures at the PBE-dDsC level

SURFACE INTERMEDIATES	T = 0 K				T = 625 K				T = 800 K					
	$\Delta E_{\text{rel}}^{\text{rel}} \Delta_{\text{CH}}^{\text{rel}} (\text{kJ/mol})$	$\Delta H_{\text{rel}}^{\text{rel}} \Delta_{\text{CH}}^{\text{rel}} (\text{kJ/mol})$	$T \Delta S_{\text{rel}}^{\text{rel}} \Delta_{\text{CH}}^{\text{rel}} (\text{kJ/mol})$	$\Delta G_{\text{rel}}^{\text{rel}} \Delta_{\text{CH}}^{\text{rel}} (\text{kJ/mol})$	$\Delta H_{\text{rel}}^{\text{rel}} \Delta_{\text{CH}}^{\text{rel}} (\text{kJ/mol})$	$T \Delta S_{\text{rel}}^{\text{rel}} \Delta_{\text{CH}}^{\text{rel}} (\text{kJ/mol})$	$\Delta G_{\text{rel}}^{\text{rel}} \Delta_{\text{CH}}^{\text{rel}} (\text{kJ/mol})$	$\Delta H_{\text{rel}}^{\text{rel}} \Delta_{\text{CH}}^{\text{rel}} (\text{kJ/mol})$	$T \Delta S_{\text{rel}}^{\text{rel}} \Delta_{\text{CH}}^{\text{rel}} (\text{kJ/mol})$	$\Delta G_{\text{rel}}^{\text{rel}} \Delta_{\text{CH}}^{\text{rel}} (\text{kJ/mol})$	$\Delta H_{\text{rel}}^{\text{rel}} \Delta_{\text{CH}}^{\text{rel}} (\text{kJ/mol})$	$T \Delta S_{\text{rel}}^{\text{rel}} \Delta_{\text{CH}}^{\text{rel}} (\text{kJ/mol})$	$\Delta G_{\text{rel}}^{\text{rel}} \Delta_{\text{CH}}^{\text{rel}} (\text{kJ/mol})$	
(A) Methyl-cyclohexane <i>TS_a</i> ^a	-105	-104	-105	1	-100	-130	30	-105	-104	-105	1	-100	-130	30
(B) Methyl-cyclohexyl + H <i>TS_b</i> ^b	-14	-24	-103	79	-21	-129	108	-14	-24	-103	79	-21	-129	108
(C) Methyl-cyclohexene + 2H <i>TS_c</i> ^c	-96	-107	-101	-6	-102	-124	22	-96	-107	-101	-6	-102	-124	22
(D) Methyl-cyclohexene + 2H <i>TS_d</i> ^d	-12	-35	-108	73	-31	-134	103	-12	-35	-108	73	-31	-134	103
(E) Methyl-cyclohexene + 2H <i>TS_e</i> ^e	-93	-114	-104	-10	-108	-126	18	-93	-114	-104	-10	-108	-126	18
(F) Methyl-cyclohexene + 2H <i>TS_f</i> ^f	-2	-19	-29	11	-14	-32	18	-2	-19	-29	11	-14	-32	18
(G) Methyl-cyclohexadiene + 2H <i>TS_g</i> ^g	61	27	-34	61	31	-38	69	61	27	-34	61	31	-38	69
(H) Methyl-cyclohexadiene + 2H <i>TS_h</i> ^h	-13	-42	-29	-13	-37	-31	-6	-13	-42	-29	-13	-37	-31	-6
(I) Methyl-cyclohexadiene + 2H <i>TS_i</i> ⁱ	51	7	-36	43	12	-40	53	51	7	-36	43	12	-40	53
(J) Methyl-cyclohexadiene + 2H <i>TS_j</i> ^j	-25	-68	-38	-30	-61	-41	-20	-25	-68	-38	-30	-61	-41	-20
(K) Methyl-cyclohexadiene + 2H <i>TS_k</i> ^k	53	13	39	-25	19	55	-37	53	13	39	-25	19	55	-37
(L) Methyl-cyclohexadiene + 2H <i>TS_l</i> ^l	100	44	37	7	49	54	-4	100	44	37	7	49	54	-4
(M) Methyl-cyclohexadiene + 2H <i>TS_m</i> ^m	27	-26	33	-59	-19	50	-69	27	-26	33	-59	-19	50	-69
(N) Toluene + 2H	102	32	33	-1	39	51	-12	102	32	33	-1	39	51	-12
(O) Toluene	14	-50	40	-90	-42	60	-102	14	-50	40	-90	-42	60	-102
(P) Toluene (gas phase)	91	32	114	-83	38	154	-115	91	32	114	-83	38	154	-115
(Q) Toluene (gas phase)	283	219	262	-42	222	338	-116	283	219	262	-42	222	338	-116

Figure IV- 29 Thermodynamics data for intermediates and transition states regarding methylcyclohexane dehydrogenation on Pt (111) surface at different temperatures at the PBE-dDsC level

8. Comparison of free energy profiles between the cluster and Pt(111) at the PBE level

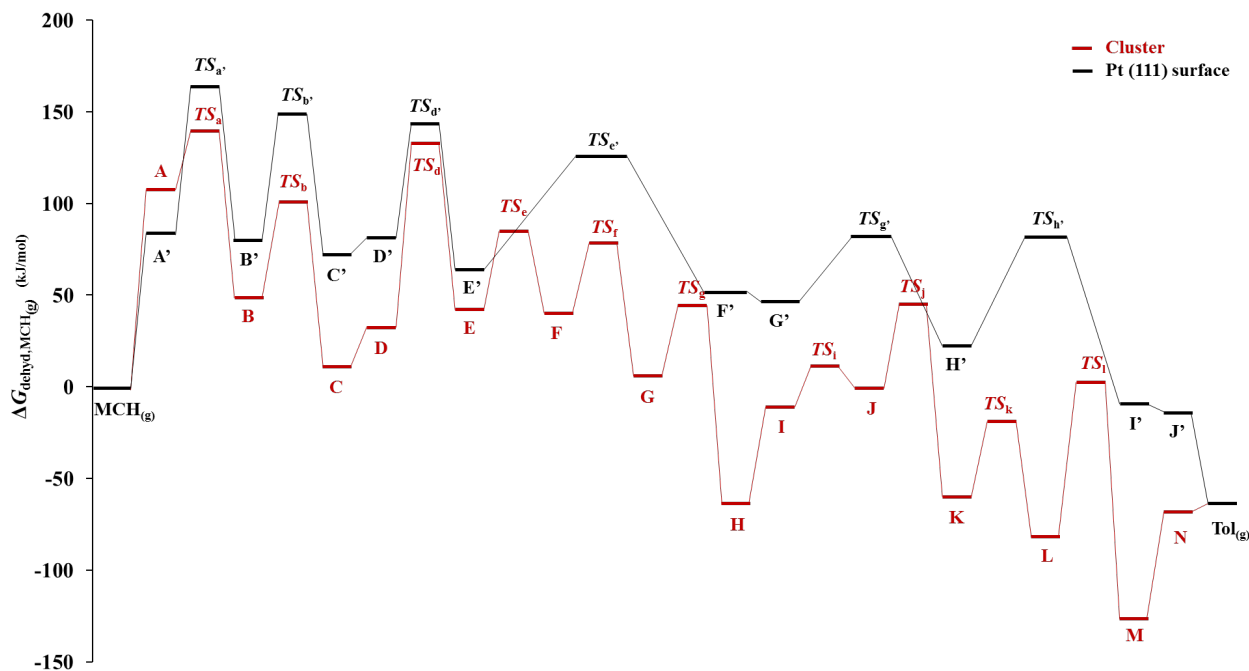


Figure IV- 30 Comparison of free energy profiles for methyl-cyclohexane dehydrogenation reaction mechanism on $\text{Pt}_{13}\text{H}_6/\gamma\text{-Al}_2\text{O}_3$ and Pt (111) at 625 K calculated with the PBE functional

The Gibbs free energy profiles calculated with the PBE functional at 625 K on the $\text{Pt}_{13}\text{H}_6/\gamma\text{-Al}_2\text{O}_3$ (100) cluster and on Pt(111) are compared in Figure IV-30. First of all, it can be noticed that all the intermediates (except A and A') and transition states are more stable on the cluster than on the surface, which may be assigned to the fluxionality of the cluster, which morphology adapts to stabilize at most each intermediate. This would suggest a better reactivity of our $\text{Pt}_{13}\text{H}_6/\gamma\text{-Al}_2\text{O}_3$ (100) cluster discovered with the PBE functional. For both systems, the most demanding step is the dissociative adsorption of the reactant ($\text{MCH}_{(\text{g})} \rightarrow \text{A} / \text{A}' \rightarrow \text{B}/\text{B}'$) at the PBE level: $\Delta_r G_{\text{MCH}_{(\text{g})} \rightarrow \text{TS}_a}^\ddagger = 140$ kJ/mol on cluster and $\Delta_r G_{\text{MCH}_{(\text{g})} \rightarrow \text{TS}_a}^\ddagger = 165$ kJ/mol on Pt (111) surface. For all the other C-H bond cleavage steps, the two systems exhibit different barriers and

most free energy demanding steps. On the cluster, the most demanding step (if we exclude $\text{MCH}_{(g)} \rightarrow \text{A} \rightarrow \text{B}$) is the third C-H bond cleavage step of methyl-cyclohexene ($\text{D} \rightarrow \text{E}$ by TS_d) and on the Pt(111) surface, it becomes the second one (dehydrogenation of methyl-cyclohexyl, $\text{B}' \rightarrow \text{C}'$ by TS_b'). There are also a difference on the energy term between these two systems concerning the three H_2 desorption steps and the toluene desorption step. Those steps are found to be endergonic on the cluster while they turn to be slightly exergonic on the (111) surface. The thermochemistry of these steps is directly connected to the reaction conditions (hydrogen coverage and temperature) as already studied by Mager-Maury et al.⁶. So the endergonicity of these steps may depend on our initial choice of hydrogen coverage. Especially, our cluster system has a higher hydrogen coverage compared to the Pt (111) surface (zero initial hydrogen coverage). On the one hand, the same number of initial hydrogen atom on the cluster ($\theta_{\text{H}} = 6$) cannot be easily adopted for the surface system in reforming conditions.⁶ On the other hand, we have already tried some investigation on zero-hydrogen-coverage cluster system to compare with the non-hydrogenated Pt(111), but the cluster structure turned to be completely deformed, even dislocated, by performing a Molecular Dynamic study at 500 K, which rendered the strict comparison impossible. Moreover, it should also take into account once again the impact of dispersion forces while calculating the energy for those steps.

CHAPTER V – REACTION KINETICS FOR THE DEHYDROGENATION OF METHYLCYCLOHEXANE INTO TOLUENE ON A Pt/Al₂O₃ CATALYST

The first part of this chapter is devoted to the experimental investigation of the kinetics of the reaction, to obtain reliable and reference data to be compared with *ab initio* based kinetic modeling, which comes in second part of the chapter. In this second kinetic modeling part, a preliminary Power-law kinetic study widely applied in many works, will be depicted firstly. Then here follows an extended Langmuir Hinshelwood (LH) kinetic study by using the DFT mechanistic model parameterized by *ab initio* reaction constants, acquired in Chapter IV, in order to unravel the reaction kinetics by considering the various possible rate-determining steps. All the kinetic models will be compared with our experiments, in terms of reaction rates values, reaction rates dependence upon hydrogen partial pressure, methyl-cyclohexane partial pressure, and conversion. The apparent reaction activation enthalpy will also be the object of a comparison between experiments and models. The surface species coverage will also be analysed in some cases.

1. Catalytic experiment

The experiments are performed in the conditions reported in Chapter III: Computational and Experimental Methodology, *section 2.*

1.1 Temperature effect

Four reaction temperatures (320, 340, 360 and 380°C) were investigated by Test-1. Meanwhile the variable temperature range is also crucial for establishing the Arrhenius and Eyring plots.

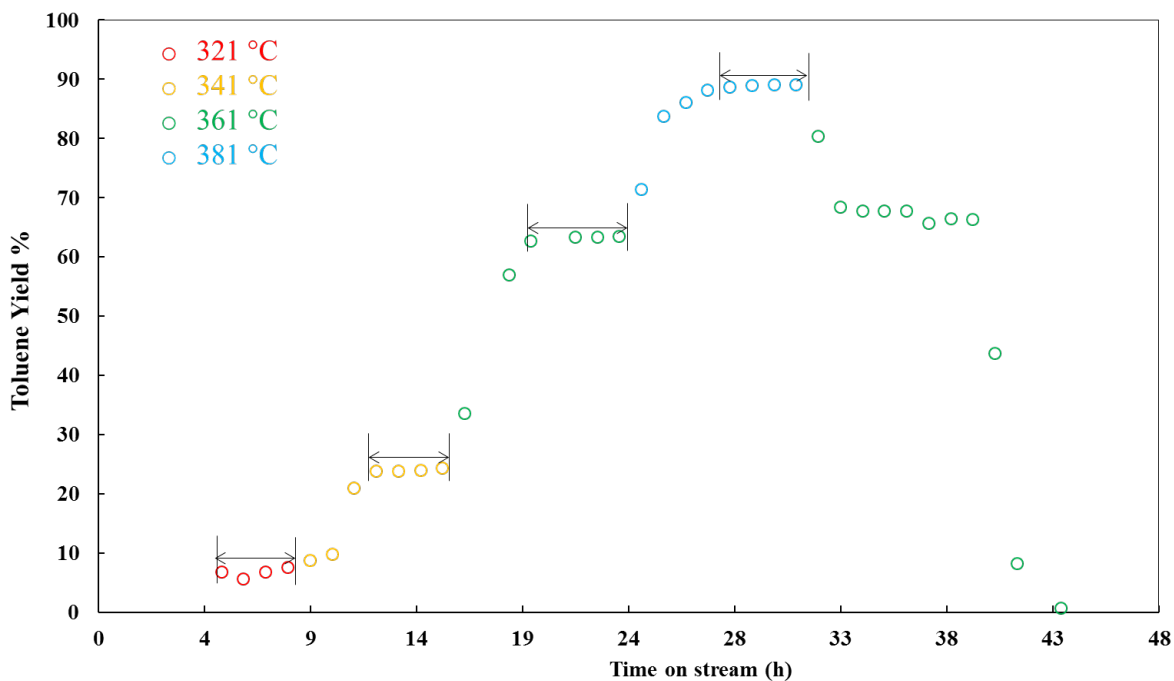


Figure V- 1 Toluene yield in weight in the liquid outlet feed analyzed by gas chromatograph as a function of time for Test-1. The color code indicates the temperatures recorded by thermocouple T_{2b} ; The arrow interval marks the conversion points at steady state that are used to calculate the yield average value.

Figure V-1 depicts the toluene yield in weight hourly in the liquid phase. As explained previously, the four temperatures in Test-1 were maintained 8 hours, the points on the figure are separated by one hour. Between each temperature increase step of 20 °C, the heating rate as mentioned is 5 °C/min and fast enough. Thus, it can be considered that no conversion point in Figure V-1 happens during the heating step. The non-steady state conversion points at the beginning of each temperature are due to the mixture of product of the current temperature and residual product of the previous temperature in the set-up tube before the next sampling. It can be firstly observed that at the end of 8 hours for each temperature, steady state is reached. The product yield increases by increasing the temperature, in line with the strong endothermicity of the reaction. At 380°C, the conversion reaches almost 90%. The return point at 360 °C confirms that the catalyst is not deactivated. The toluene yields measured for each temperature are the average values on all the final points at the steady state (with the intervals marked by the arrows in Figure V-1). These average values are then used for the Arrhenius and Eyring plots (Figures V-2).

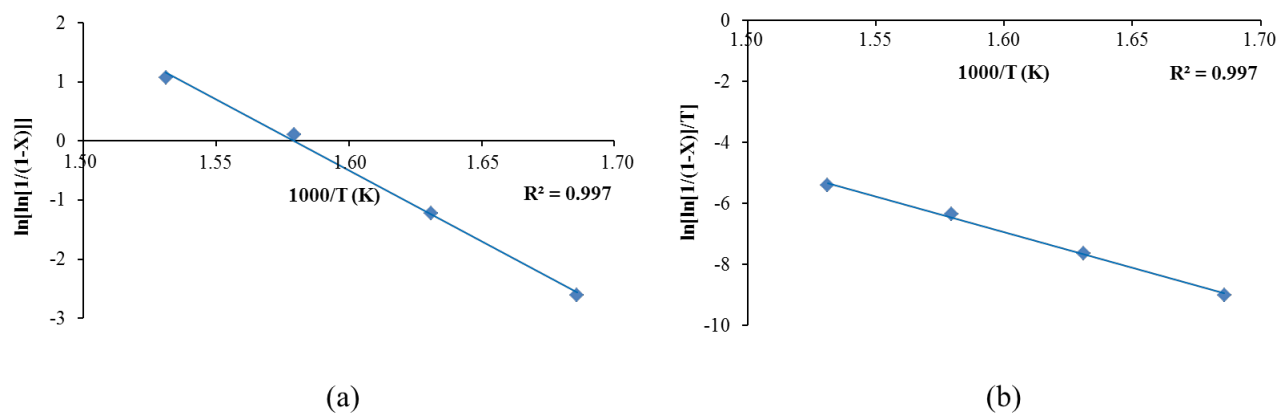


Figure V- 2 (a) Arrhenius plot (Equation III-60) (b) Eyring plot (Equation III-62) deduced from Test 1 at $P(H_2) = 12.2$ bar, $P(MCH) = 0.8$ bar and space time of $90 \text{ g}_{\text{cata}} \cdot \text{s} \cdot \text{g}_{\text{MCH}}^{-1}$.

Very satisfactory linear relationships are obtained (both with $R^2=0.997$, nearly 1). From the two slopes and by using the Equation (III-60) and (III-62) in Chapter III : Computational and Experimental Methodology, *section 2.2.4*, we deduce that the apparent activation energy E_a is equal to 200 kJ/mol, and the apparent activation enthalpy $\Delta_r H^\ddagger$ is equal to 195 kJ/mol with an apparent activation entropy of 0.056 kJ/(mol.K), calculated from Eyring plot by determining the constant in Equation (III-62), which can be expressed as $const. = \ln\left(\frac{k_B}{h}\right) + \frac{\Delta_r S^\ddagger}{R}$.

These apparent activation enthalpies will be compared with the values determined by using the ab initio kinetic models described in the next chapter. At this stage, it is however interesting to recall the values obtained in the literature corresponding to the conditions reported in Table 1. Sinfelt et al.¹ found experimentally an activation energy of 138 kJ/mol for 0.3 wt% platinum-on-alumina catalyst, at reaction temperatures enclosed between 315 and 372 °C with the methyl-cyclohexane partial pressures 0.36 bar and hydrogen pressure 1.1 bar. Maria et al.² found an activation energy of 220 kJ/mol for sulfided platinum on alumina reforming catalyst at reaction temperatures of 282-309 °C, with a hydrogen to methyl-cyclohexane ratio of 2.5-10, total pressure 7 atm and the space time of (1) 61; (2) 82; (3) 123; (4) 246 ($g_{cata.s}/g_{MCH}$). Alhumaidan et al.³ used 1.0 wt% Pt/ γ -Al₂O₃ catalyst and reported an activation energy of about 55 kJ/mol at a total pressure of 1 bar, a H₂/MCH ratio of 9 and at the temperature range from 340 to 450 °C. However, the space time they investigated was (1) 312; (2) 625; (3) 1250 ($g_{cata.s}/g_{MCH}$). Usman et al.⁴ performed similar experiments to Alhumaidan et al.³ on 1.0 wt% Pt/ γ -Al₂O₃ catalyst at temperature range of 340 – 380 °C, found at last the apparent activation energy of 39 kJ/mol. Van Trimont et al.⁵ reported in their work for sulfided catalyst containing 0.59 wt% platinum and 0.67 wt% chlorine, an apparent activation energy of 133 kJ/mol by the Power-law model and 180 kJ/mol found by the dual-site Langmuir-Hinshelwood-Hougen-

Waston (LHHW) model, at the temperature range of 310 – 410 °C, hydrogen partial pressure range of 4.5-20 bar and the methyl-cyclohexane pressure range of 0.15-1.5 bar. The reaction space time range they investigated was around 18-440 ($\text{g}_{\text{cata}}\cdot\text{s}/\text{g}_{\text{MCH}}$).

As an intermediate conclusion, our experimental activation energy is close to the ones found by Sinfelt et al., Van Trimont et al., Maria et al. but differs significantly from those by Alhumadian et al. and Usman et al. which reports rather low apparent activation energy with respect to other studies. It is difficult to explain such a large discrepancy between values reported in the literature, although the operating conditions are differing from one study to another. This justifies all the more the interest of undertaking an ab initio study of this reaction to better solve the kinetic parameters.

1.2 WHSV effect

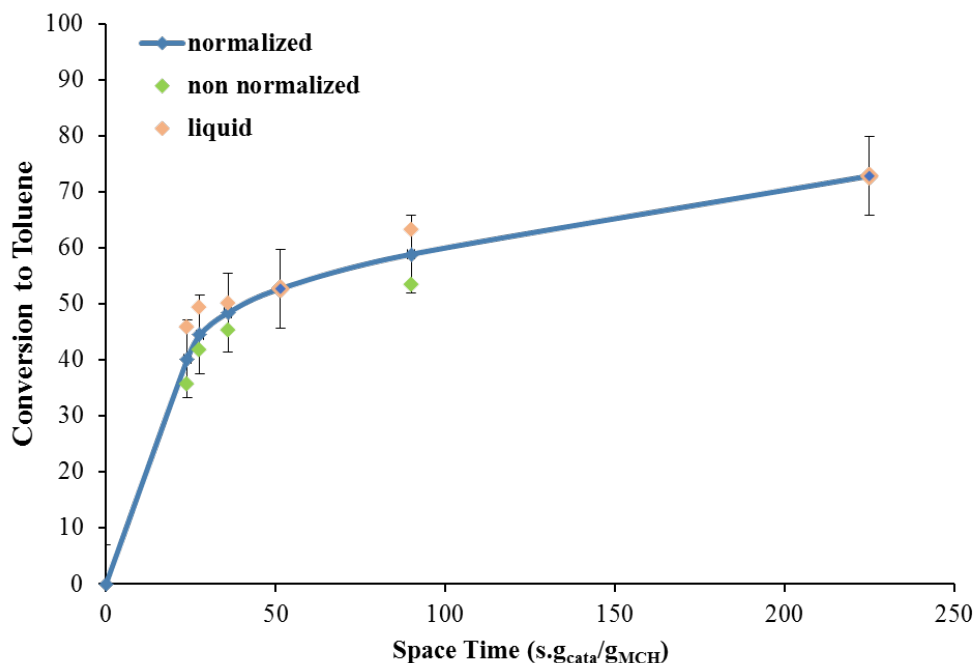


Figure V-3 Methyl-cyclohexane conversion to toluene as a function of space time at 360 °C and $H_2/HC = 15$, with $P(H_2) = 12.2$ bar and $P(MCH) = 0.8$ bar. Both normalized and non-normalized conversions contain the liquid and gaseous phases. The non-normalized conversion is calculated by Equation (III-53) and normalized conversion is calculated by Equation (III-56) in Chapter : Computational and Experimental Methodology, section 2.2.

From Test-1 to Test-6 in the Table III-4 in Chapter III, section 2.1.3, methyl-cyclohexane conversions into toluene were obtained at various weight hourly space velocities (WHSV). By applying Equation (III-43) we deduced the space time from WHSV. Figure V-3 plots the results obtained from three methods to calculate the toluene yield described in Chapter III, section 2.2.3 : the toluene yield in liquid phase, the non-normalized toluene yield containing the liquid and gaseous phase and the normalized toluene yield containing the liquid and gaseous phase. The error bars on each point represent about $\pm 7\%$ conversion. Within this margin of errors, all methods lead to rather similar conversion levels. Some systematic deviations can however be

commented: compared to the normalized toluene yield containing the gaseous phase, the one calculated only in liquid phase is overestimated while the non-normalized one containing the gaseous phase is underestimated. This means that the toluene yield in gaseous phase is lower than that in liquid phase and without the normalization, the non-normalized conversions are thus underestimated by compensating the gaseous phase part with the yield in liquid phase, if this impact depending on mass balance is not eliminated. The conversion increases rapidly till space time reaches $40 \text{ g}_{\text{cata}}\cdot\text{s}/\text{g}_{\text{MCH}}$. It increases more slowly for space time greater than $50 \text{ g}_{\text{cata}}\cdot\text{s}/\text{g}_{\text{MCH}}$. Notably, the reaction kinetics at the very beginning ($t < 25 \text{ g}_{\text{cata}}\cdot\text{s}/\text{g}_{\text{MCH}}$) are not studied because of the constraints of limit operating reaction conditions due to the set-up. Nevertheless, we still managed to fit a simple Power-law type reaction rate fitting model by using these data as described later in this chapter, *section 2.1*. In the following, normalized values of methylcyclohexane conversion to toluene will be reported.

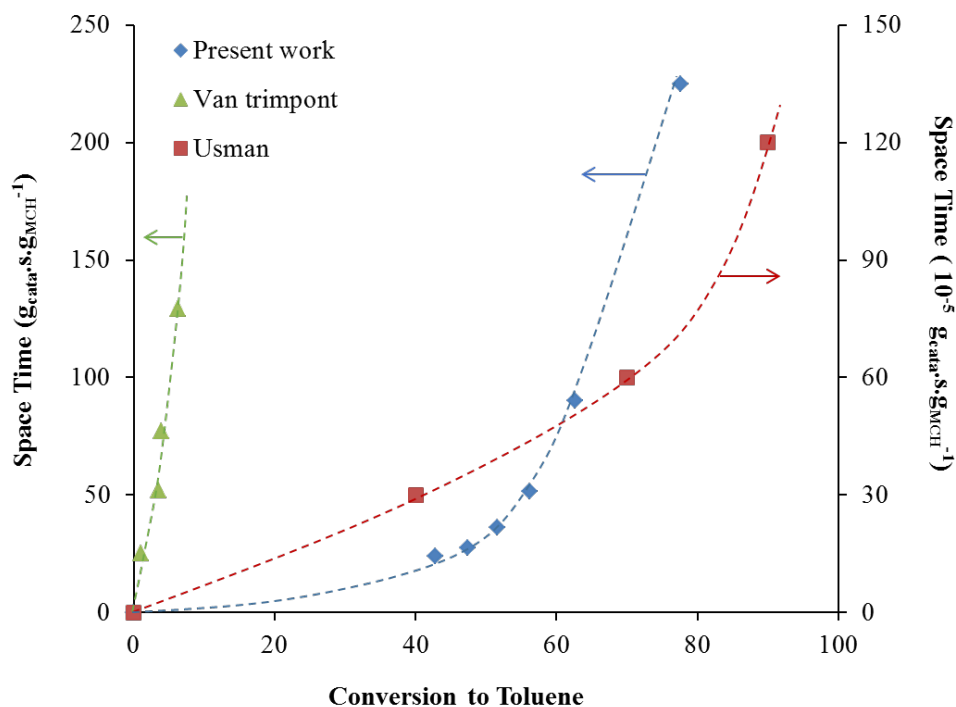


Figure V- 4 Methyl-cyclohexane conversion to toluene by the evolution of space time

The methyl-cyclohexane conversions to toluene as a function of the reaction space time obtained from Tests 1 to 6 are thus compared with the literature,^{5,4} in Figure V-4. First of all, it can be noticed that a high reactant conversion is reached in a much smaller (by a factor of 10⁵) space time in the study of Usman et al.,⁴ whereas conversion levels remain lower in the work of Van Trimpont et al.⁵ That could be probably explained by the different reaction conditions employed in these three works summarized in Table V-1. In particular, Usman et al.⁴ used a higher platinum content in the catalyst and a higher temperature. Moreover, the low hydrogen partial pressure can also lead to higher reaction rates (see next section). If comparing the conversions at steady state, it can be concluded that higher temperature leads to higher conversion to toluene. The work of Van Trimpont et al.⁵ was performed on a sulfided catalyst, which can largely reduce the reactivity of the catalyst. That would explain the conversion

difference between our work and the one of Van Trimpont, despite the similarity on the reaction conditions and a higher platinum content in Van Trimpont’s study.

Table V- 1 Different reaction conditions employed for each curve in Figure V-4

Author	Present work	Usman	V. Trimpont
Wt% Pt	0.3	1.0	0.59
Wt (ppm) Sulfur	--	--	100
P(MCH), bar	0.8	0.6	0.5
P(H ₂), bar	12.2	4.4	15
T (°C)	360	380	350

1.3 MCH and H₂ partial pressures effects

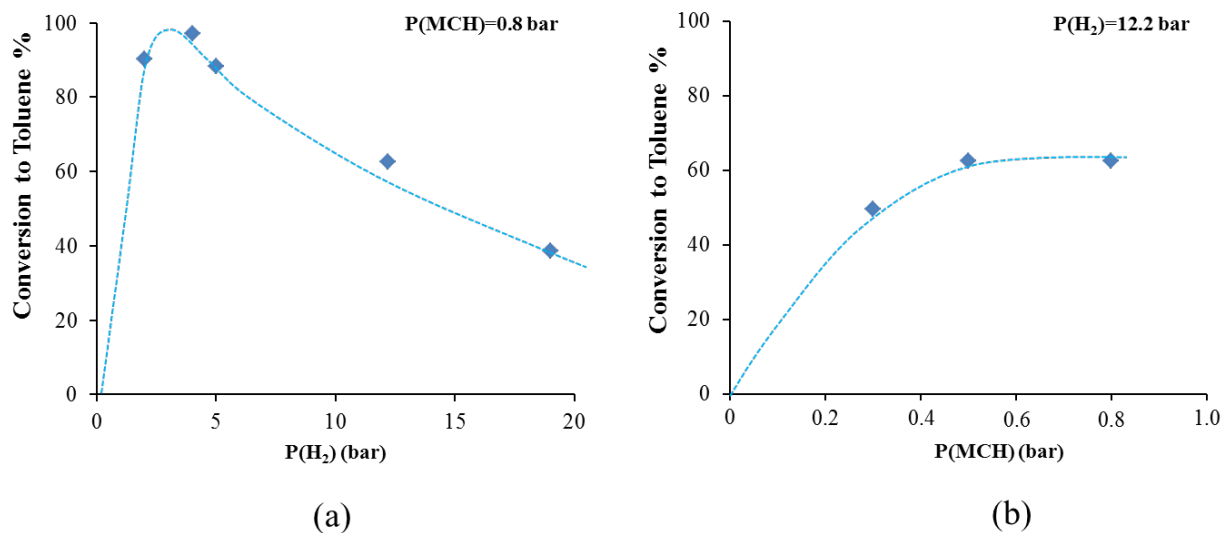


Figure V- 5 Methyl-cyclohexane conversion to toluene as a function of (a) hydrogen partial pressure, at a constant methyl-cyclohexane partial pressure of 0.8 bar; (b) methyl-cyclohexane partial pressure, at a constant hydrogen partial pressure of 12.2 bar. All tests were at temperature $T=360\text{ }^{\circ}\text{C}$ and space time $t=90\text{ g}_{\text{cata}}\cdot\text{s}\cdot\text{g}_{\text{MCH}}^{-1}$

The impact of the partial pressure of methyl-cyclohexane and hydrogen is crucial to be investigated. It was already discussed in the literature^{6,5,7}. So, we addressed those effects thanks to the conditions of Test-7 to Test-10 combined with Test-1. Figure V-5(a) depicts the evolution of the conversion to toluene as a function of the hydrogen partial pressure at a constant methyl-cyclohexane partial pressure of 0.8 bar. Conventionally, the conversion curve should reach a maximum level at one critical hydrogen pressure.^{7,8} A possible explanation is that above this critical hydrogen partial pressure, the conversion decreases by increasing hydrogen pressure because of the reverse reaction and hydrogen “poisoning” of the catalyst.⁸ The low H₂ pressure regime is more difficult to understand. It can be due to deactivation phenomenon induced by coking when H₂ pressure becomes too low. However, a fitting model carried out by Verstraete⁶ by reproducing the kinetic model of Van Trimont⁵ provided us a similar conversion curve regarding hydrogen pressure, without taking the coke formation into account. The origin of this phenomenon will be discussed in detail in *section 2*.

This phenomenon has been observed during our test by Figure V-5(a), even though this maximum curve shape is not very pronounced in our case and the minimal hydrogen pressure we employed ($P(\text{H}_2) = 2$ bar) still provides a relatively high conversion point. The maximum is close to $P(\text{H}_2) = 3$ bar. According to the fitting modelling study carried out by Verstraete⁶ on the kinetic data of Van Trimont, a maximum at around $P(\text{H}_2) = 5$ bar at 350 °C was found, with different reaction conditions mentioned in Table V-1.

In Figure V-5(b), at 360 °C and $P(\text{H}_2) = 12.2$ bar, it is shown how the conversion increases with increasing the methyl-cyclohexane up to $P(\text{MCH}) = 0.5$ bar and reaches a plateau here after. This can be probably explained by the saturation of active sites on the catalyst when the reactant surface concentration becomes too high.

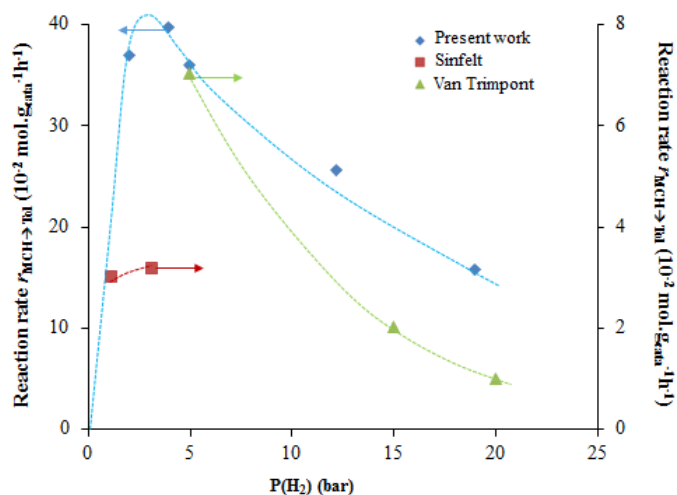
We then calculated initial reaction rates by applying Equation (III-63), using these relatively high conversions illustrated in Figure V-5 to estimate approximately the conversion curve slope at the initial reaction time ($t=0$). Note that with such a method, we likely underestimate somehow the initial reaction rate. Sinfelt¹ and Van Trimont et al.⁵ performed similar studies, on the investigation of the impact of methyl-cyclohexane and hydrogen partial pressure on the reaction rate. Hence, we make a comparison of these studies with ours. The different catalyst types and reaction conditions and studied space time are recalled in Table V-2.

Table V- 2 Different catalysts and reaction conditions employed in this work and in the literature for studying the impact of MCH and H₂ partial pressure on the reaction rate

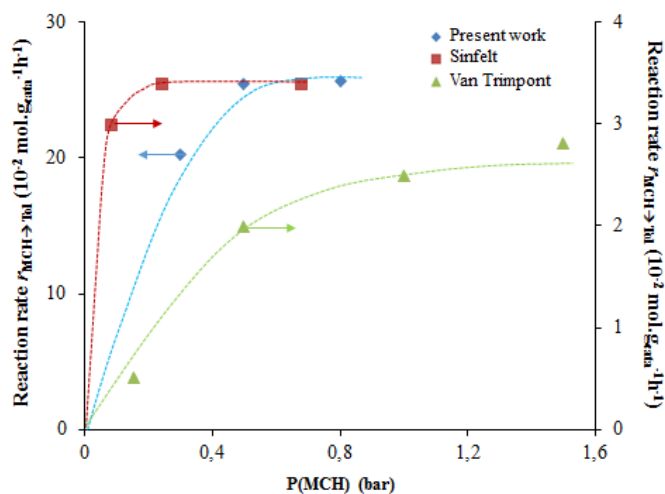
Author	Present work	J.H Sinfelt	V. Trimont
Wt% Pt	0.3	0.3	0.59
Wt (ppm) Sulfur	--	--	100
P _{const.} (MCH) (bar)	0.8	0.4	0.5
P _{const.} (H ₂) (bar)	12.2	1.4	15
T (°C)	360	344	350
WHSV (g _{MCH} ·h ⁻¹ ·g _{cata} ⁻¹)	40	51	28
Space time (g _{cata} ·s·g _{MCH} ⁻¹)	90	71	129

Figure V-6 displays initial reaction rates measured for these three studies. In Figure V-6 (a), we notice that our initial reaction rates are about 5 to 10 times higher than those of Sinfelt and Van Trimont. As previously explained, this is probably because that Van Trimont et al. used catalyst that was presulfided and the reactivity of which was reduced with respect to our catalyst. For Sinfelt, the catalyst seems to be the same as ours but the reaction temperature is lower and especially, the methyl-cyclohexane partial pressure chosen for the study of the effect of the hydrogen partial pressure is twice lower than ours. Moreover, these two previous studies, also less exhaustive in terms of interval of hydrogen partial pressure than ours in Figure V-6(a),

confirm the maximum we observe: Van Trimpont et al. recovered only the decreasing trend in the high hydrogen partial pressure range whereas Sinfelt reported the increasing part at low hydrogen partial pressure. The same difference on reaction rate is also observed in Figure V-6(b), depicting the effect of P(MCH) at constant P(H₂). Nevertheless, we observe similar evolutions of reaction rate as a function of methyl-cyclohexane partial pressure for all three studies.



(a)



(b)

Figure V- 6 Initial reaction rate of methyl-cyclohexane dehydrogenation to toluene as a function of (a) hydrogen partial pressure (b) methyl-cyclohexane partial pressure

1.4 Conclusions and Perspectives

So far, the catalytic tests on methyl-cyclohexane dehydrogenation reaction were achieved in a fixed bed reactor, with the following catalyst : 0.3 wt% platinum and 0.12 wt% chlorine on γ - Al_2O_3 support. The temperature effect has been discussed at four different levels (320, 340, 360, 380 °C) and by applying Arrhenius plot and Eyring plot, we managed to determine the reaction activation energy and activation enthalpy, $E_a = 200$ kJ/mol and $\Delta_r H^\ddagger = 195$ kJ/mol, respectively. These experimental activation energy and enthalpy will be confronted with the values obtained by the kinetic model parameterized by *ab initio* kinetic constants in the next section.

Then, the weight hourly space velocity was set up for a value range from 40 – 150 $\text{g}_{\text{MCH}} \cdot \text{h}^{-1} \cdot \text{g}_{\text{cata}}^{-1}$, in order to deduce the reactant conversion as a function of reaction space time. This evolution permits to describe the reaction kinetics in terms of reaction space time.

The impacts of hydrogen and methyl-cyclohexane partial pressures on conversion and initial reaction rates were unravelled. The comparison with previous works in the literature showed a qualitative agreement in terms of the curve shape. However, regarding reaction rates, the different reaction conditions, especially the pressure ranges and the different type of catalysts (either pre-sulfided or not) made it different quantitatively.

For the next steps of our study, these experimental data will be used firstly to help us to established a power-law type reaction rate fitting model. Secondly, the Langmuir-Hinshelwood (LH) type kinetic model will be built by using the *ab initio* calculation results and finally the discussion will be focused on the confrontation between these experimental results and the LH modelling results, in order to validate our mechanistic investigation on the dehydrogenation of methyl-cyclohexane carried out by DFT calculations.

2. Kinetic modelling investigation

2.1 Power-law kinetic model

2.1.1 Variations of the reaction rate as a function of space time

In order to define the effective reaction rate constant and reaction order more precisely at high conversion as in our case, we proposed a first power-law kinetic model (PL-I) rendering the evolution of the conversion as a function of the reaction space time. The reaction space time is defined as a function of the weight hourly space velocity (WHSV) previously by Equation (III-42) and (III-43) in Chapter III, *section 2.1.3*, which is varied from Test-1 to Test-6 in Table III-4 in that section. A power-law rate reaction is thus rewritten by taking into account the reaction order in MCH, called n , at the corresponding reaction conditions (total pressure of 13 bar, a H₂/HC molar ratio equals 15.3 and temperature at 360 K). However, this new approach does not provide any information about the reaction mechanism but does correlate the effect of the reactant concentration on the experimental reaction rate. We have then:

$$\begin{aligned}
 r &= -\frac{dP_{MCH}}{dt} = kP_{MCH}^n \Leftrightarrow \int_{P_{MCH,0}}^{P_{MCH}} \frac{dP_{MCH}}{P_{MCH}^n} = - \int_0^t k dt \\
 &\Rightarrow P_{MCH} = [P_{MCH,0}^{1-n} - (1-n)kt]^{\frac{1}{1-n}} \\
 &\Rightarrow \frac{P_{MCH,0} - P_{MCH}}{P_{MCH,0}} = X_{MCH \rightarrow Tol} = 1 - \left[1 - \frac{(1-n)kt}{P_{MCH,0}^{1-n}} \right]^{\frac{1}{1-n}}
 \end{aligned}$$

Equation (V-1)

With t the space time ($\text{g}_{\text{cata}} \cdot \text{s} \cdot \text{g}_{\text{MCH}}^{-1}$) and $P_{\text{MCH},0}$ the initial partial pressure of methylcyclohexane (bar). This relation between the conversion and reaction space time allow us to fit the experimental data. The kinetic parameters such as apparent reaction rate constant k ($\text{mol}_{\text{MCH}} \cdot \text{g}_{\text{cata}}^{-1} \cdot \text{h}^{-1} \cdot \text{bar}^{-n}$) and reaction order n are solved by optimizing and minimizing the sum of squared residuals (SSR).

The reaction rate $r(t)$ ($\text{mol}_{\text{MCH}} \cdot \text{g}_{\text{cata}}^{-1} \cdot \text{h}^{-1}$) can then be deduced from this fitting curve by using the expression in Equation (V-2), where M_{MCH} is the molar mass of methylcyclohexane ($98 \text{ g} \cdot \text{mol}^{-1}$):

$$r(t) = \frac{X_{\text{MCH} \rightarrow \text{Tol}}(t + \Delta t) - X_{\text{MCH} \rightarrow \text{Tol}}(t)}{M_{\text{MCH}} \Delta t}$$

Equation (V-2)

Note that for the current fitting, we assume that the H_2 pressure will not significantly change as a function of the space time, due to its high initial value compared to that of methylcyclohexane, so that its contribution to the power law rate expression is merged in the effective rate constant k . Figure V-7 illustrates the Power-law fitting conversions and reaction rates (lines) obtained by Equation (V-1) and (V-2), compared with the experimental results (dots).

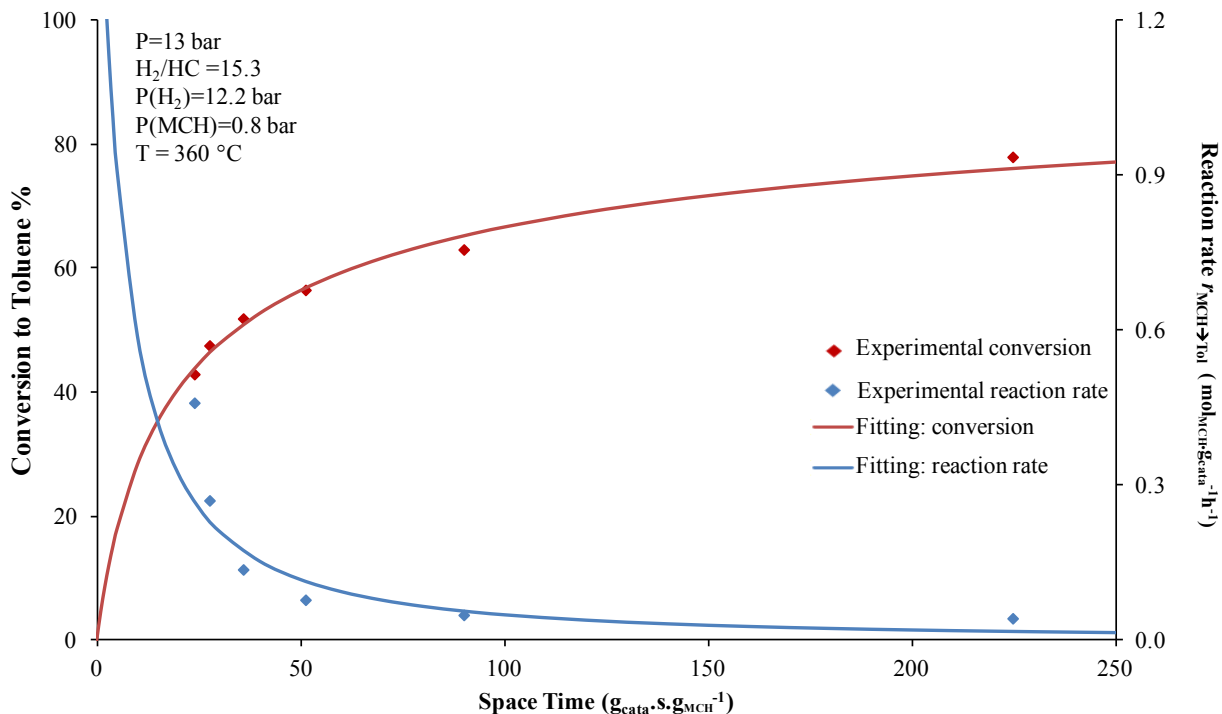


Figure V- 7 Power-law kinetic fitting model (PL-I) for the conversion to toluene and reaction rate as a function of space time fitted by the experimental data.

With fitting parameters reported in Table V-3, the agreement between experiments and the power rate law is satisfactory, except for the very first points of rate values, due to the lack of experimental points at very low contact time, rendering the estimation of the slope rather imprecise from experimental data. Although, the fitting result is quite satisfactory with a SSR of 11.

Table V- 3 Power-law kinetic fitting parameters (PL-I) for conversion as a function of space time (SSR: sum of squared residuals)

Kinetic parameters	Fitting results : PL-I
k	81.8 ($\text{mol}_{\text{MCH}} \cdot \text{g}_{\text{cata}}^{-1} \cdot \text{h}^{-1} \cdot \text{bar}^{-3.3}$)
n	3.3
SSR	11

The fitted rate constant k and reaction order n (for methyl-cyclohexane) are reported in Table V-3. Despite the very satisfying fitting SSR and also a good match with experimental points in Figure V-7, the reaction order for the reactant methyl-cyclohexane is about 3 from the fitting model, which is surprising from a chemical point of view. In the literature, there also exists several studies by using the power-law kinetic fitting model (to provide information and clues for a next step on mechanistic model, before leading to a more formal kinetic model), summarized in Table V-4. The partial reaction order of methyl-cyclohexane is found to be between 0-1, generally. As for the rate constants, the one found in our work seems higher than those in the literature^{5,3,4,6}, by two to three orders of magnitude. Besides the fact that Van Trimont et al. use sulphided catalysts, likely to be less reactive, and Usman et al. work with higher loadings in platinum (1 %) than we do, with suspected impact on the dispersion, this difference may be as consequence of the hydrogen pressure term, which is implicitly included in our rate constant. However, if we use the partial reaction orders of hydrogen in Table V-4 and take into account our employed hydrogen pressure 12.2 bars, we can thus deduce the new rate constants of each study in literature, implicitly including the hydrogen pressure term in the rate constant as ours. We found that the new constants: $0.033 \text{ mol}_{\text{MCH}} \cdot \text{g}_{\text{cata}}^{-1} \cdot \text{h}^{-1} \cdot \text{bar}^{-0.68}$ for Van Trimont et al.; $0.036 \text{ mol}_{\text{MCH}} \cdot \text{g}_{\text{cata}}^{-1} \cdot \text{h}^{-1}$ for Alhumaidan et al.; $0.12 \text{ mol}_{\text{MCH}} \cdot \text{g}_{\text{cata}}^{-1} \cdot \text{h}^{-1} \cdot \text{bar}^{-0.68}$ for Verstraete et al.. Still, it appears to exist an incoherence. Likewise, the rate constant varies

depending on the form of the employed power-law rate equations and also the reaction order, regarding the unit that contains the term bar^{-n} . For this reason, the rate constants found by Usman et al.⁴ is 100 times smaller than that found by Verstraete⁶ and for the new constants, Van Trimpont et al. and Alhumaidan et al. have a good agreement on value but not unit. Moreover, with the same power-law rate equation for the study of Alhumaidan³ and Verstraete⁶, the methylcyclohexane order is different as well as rate constants. All this suggests that a power-law rate model is much too simplified for the present case, and is not sufficient to reflect the real mechanistic complexity. A more precise model for each reaction elementary step has to be established if we are looking forward to finding a logical explanation on the reaction kinetics.

Table V- 4 Summary of the different Power-law kinetic fitting models for the methyl-cyclohexane dehydrogenation reaction in the literature^{4,5,3,6}

First Author	Usman	Van Trimpont	Alhumaidan	Verstraete
Rate equation	$r = k(P_{MCH} - \frac{P_{Tol}P_{H_2}^3}{K})^n$	$r = kP_{MCH}^{n_{MCH}}P_{H_2}^{n_{H_2}}P_{Tol}^{n_{Tol}}$	$r = kP_{MCH}^{n_{MCH}}P_{H_2}^{n_{H_2}}$	$r = kP_{MCH}^{n_{MCH}}P_{H_2}^{n_{H_2}}$
k	0.053 ($\text{mol}_{MCH}\cdot\text{g}_{cata}^{-1}\cdot\text{h}^{-1}\cdot\text{bar}^{-0.5}$)	0.81 ($\text{mol}_{MCH}\cdot\text{g}_{cata}^{-1}\cdot\text{h}^{-1}\cdot\text{bar}^{0.6}$)	0.10 ($\text{mol}_{MCH}\cdot\text{g}_{cata}^{-1}\cdot\text{h}^{-1}\cdot\text{bar}^{0.4}$)	1.34 ($\text{mol}_{MCH}\cdot\text{g}_{cata}^{-1}\cdot\text{h}^{-1}\cdot\text{bar}^{0.3}$)
T (°C)	344	350	344	375
n_{MCH}		0.71	-0.05	0.64
n_{H_2}	0.52	-1.28	-0.41	-0.98
n_{Tol}		0	--	0

* Note: all the employed catalysts in these works are Pt-based catalyst. However, Usman and Alhumaidan used same 1.0 wt% Pt catalyst; while Van Trimpont and Verstraete were on sulphided 0.5 wt% Pt catalyst.

Moreover, this apparent reaction rate constant that we obtained by fitting experimental data describes the reactivity by catalyst mass and the pressure (k is expressed in $\text{mol}_{\text{MCH}} \cdot \text{g}_{\text{cata}}^{-1} \cdot \text{h}^{-1} \cdot \text{bar}^{-n}$), while the rate constant estimated by DFT (s^{-1}) correspond to one catalytic site at standard pressure for mono-molecular transformation of methyl-cyclohexane. So, it is quite hard to compare here directly these two factors. Meanwhile, we cannot simply induce the fitting activation energy from the fitting rate constant without having the value of the pre-factor A , due to the fact that the fitting is done for one temperature condition. Thereby, it emphasizes the difficulty of power-law kinetic model to compare with our DFT results and great interest to build a more formal and compatible mechanistic model at this point.

2.1.2. Impact of MCH and H_2 partial pressures

The same kind of fitting procedures were also done for the influence of hydrogen and methyl-cyclohexane partial pressures on the experimental methyl-cyclohexane conversion to toluene. However, in the literature (Table V-4), the authors often fit the partial pressure of methyl-cyclohexane and hydrogen at the same time. In the present work, in order to simplify this preliminary fitting study and also because of the limited amount of experimental data that could be used for the fitting model, these two parameters P_{MCH} and P_{H_2} were discussed separately (giving rise to the PL-II and PL-III models), by assuming that only one partial pressure governs the reaction at a time while the other remains constant, and thus is merged with the rate constant term. The equations used for these fitting models, written in the following, are established similarly as Equation (V-1) for the first power-law model (PL-I):

$$r = k_a P_{MCH}^{n_a}$$

$$\Rightarrow X_{MCH \rightarrow Tol} = 1 - \left[1 - \frac{(1-n_a)k_a t}{P_{MCH,0}^{1-n_a}} \right]^{\frac{1}{1-n_a}}$$

Equation (V-3)

$$r = k_b P_{H_2}^{n_b}$$

$$\Rightarrow X_{MCH \rightarrow Tol} = 1 - \left[1 - \frac{(1-n_b)k_b t}{P_{H_2,0}^{1-n_b}} \right]^{\frac{1}{1-n_b}}$$

Equation (V-4)

Moreover, the experimental data set used for this fitting is obtained at constant WHSV ($40 \text{ g}_{MCH} \cdot \text{h}^{-1} \cdot \text{g}_{cata}^{-1}$) which corresponds to a constant space time t ($90 \text{ g}_{cata} \cdot \text{s} \cdot \text{g}_{MCH}^{-1}$), with variable initial pressures of methyl-cyclohexane or hydrogen ($P_{MCH,0}$ or $P_{H_2,0}$). For the determination of n_a , the hydrogen partial pressure is kept constant (12.2 bar, Test-1,11,12) and for determination of n_b , the methyl-cyclohexane partial pressure remains constant at 0.8 bar (Test-1,7,8,9,10). Let us recall that experimentally, at $P_{H_2} = 2$ bar and $P_{MCH} = 0.8$ bar (Test-10), maximal conversion is obtained when one considers the effect of $P(H_2)$. However, the power-law model does not achieve to fit the deactivation part at low hydrogen partial pressure. So the fitting is started from the decreasing part (the red point in Figure V-8(b) is not considered in the fitting). The fitting models PL-II for methyl-cyclohexane partial pressure and PL-III for hydrogen partial pressure are thus established, yielding rate constants k_a, k_b ($\text{mol}_{MCH} \cdot \text{g}_{cata}^{-1} \cdot \text{h}^{-1} \cdot \text{bar}^{-n}$) and reaction orders n_a, n_b (Figure V-8 and Table V-5).

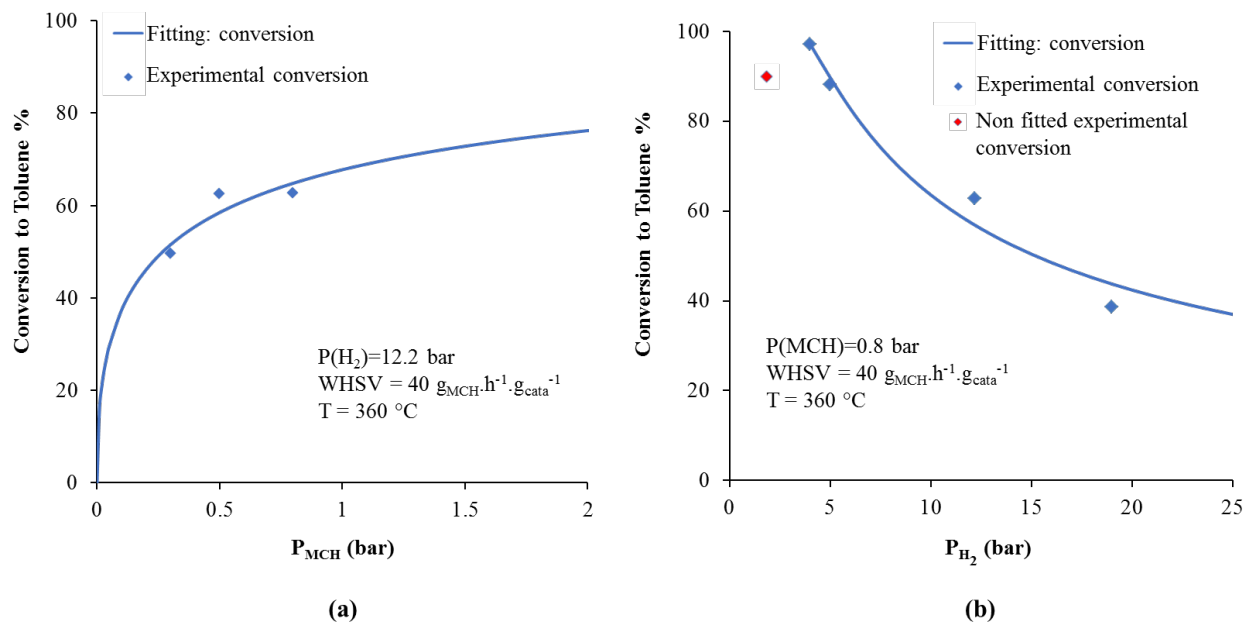


Figure V- 8 Power-law fitting of the conversion, as a function of (a) methyl-cyclohexane partial pressure (PL-II) at constant hydrogen partial pressure of 12.2 bar (b) hydrogen partial pressure (PL-III) at constant methyl-cyclohexane partial pressure of 0.8 bar ; both at a temperature of 360 °C and WHSV of $40 \text{ g}_{MCH}\cdot\text{h}^{-1}\cdot\text{g}_{cata}^{-1}$

Table V- 5 Power-law kinetic fitting parameters for reaction conversion as a function of hydrogen partial pressure (PL-II) and methyl-cyclohexane partial pressure (PL-III)

Kinetic parameters	Fitting results	
	PL-II	PL-III
k	0.60 ($\text{mol}_{MCH}\cdot\text{g}_{cata}^{-1}\cdot\text{h}^{-1}\cdot\text{bar}^{-1.5}$)	1.40 ($\text{mol}_{MCH}\cdot\text{g}_{cata}^{-1}\cdot\text{h}^{-1}\cdot\text{bar}^{-0.3}$)
Reaction order	$n_a = 1.5$	$n_b = 0.3$
SSR	24	61

From the SSR in Table V-5, the fitting results for PL-II and PL-III are worse than that of PL-I (Table V-3), especially regarding the dependence of the conversion with respect to hydrogen partial pressure (PL-III), which emphasizes the complexity of the impact of hydrogen partial pressure on the reaction kinetics.

On the other hand, the reaction orders were found to be 0.3 (close to 0) with respect to hydrogen and 1.5 with respect to methyl-cyclohexane. The MCH reaction order obtained by this last fitting is not compatible with the fitting results of PL-I. Comparing this to the results reported in the literature (Table V-4), the MCH reaction order found by PL-II close to 1 is still higher. The H_2 reaction order determined by PL-III is nearly 0, which seems more coherent with the orders reported in Table 2. Whereas the authors reported this order negatively tends to 0, opposite to the positive order obtained by PL-III. Meanwhile, two extra studies^{1,9} reporting the reaction orders in the literature without applying power-law fitting method are also found. Sinfelt¹ found the reaction to be nearly zero order with respect to methyl-cyclohexane and hydrogen, upon observation of the evolution of the reaction rate as a function of the methyl-cyclohexane and hydrogen partial pressures. As mentioned previously in this chapter, *section 1.3*, this may be explained by the much narrower interval of operating conditions described in the study of Sinfelt. Jossens and Petersen⁹ found the reaction to be positive order in MCH for a very low methyl-cyclohexane concentration (0.03 bar), whereas at higher concentration the order approached zero.

The reaction rate constants are, however, closer to the values reported in the literature than the one found by PL-I. As we determined the H_2 reaction order by PL-III, we can now deduce the intrinsic rate constant contained in the reaction rate determined by PL-I on space time, on the purpose of rendering this rate constant, obtained by the best fitting model among the three, comparable with the values reported in the literature. The component $P_{H_2}^{n_b}$ is thus divided from the k in Table V-3 ($P_{H_2} = 12.2$ bar; $n_b = 0.3$; $k = 81.8 \text{ mol}_{\text{MCH}} \cdot \text{g}_{\text{cata}}^{-1} \cdot \text{h}^{-1} \cdot \text{bar}^{-3.3}$) and the real rate constant k_r determined by PL-I and PL-III equals $38.6 \text{ mol}_{\text{MCH}} \cdot \text{g}_{\text{cata}}^{-1} \cdot \text{h}^{-1} \cdot \text{bar}^{-3.6}$. This is still higher than the values reported in Table V-4.

To conclude, we show in the present section that applying power law rate expressions is possible by that unreliable results are obtained from one fit to the other. This suggests that more detailed atomistic models are required to assess the numerous elementary steps involved in the mechanism as described in the previous Chapter. These conclusions are in agreement with previous works from the literature.^{5,3,4,6}

2.2 Langmuir Hinshelwood mechanistic models

2.2.1. Individual steps and rate constants from DFT

The mechanism considered for the methyl-cyclohexane dehydrogenation reaction and studied by the DFT calculations reported in the previous chapter are much more complex than those considered in the earlier work of Van Trimpont. In particular, it involves 15 elementary steps and includes also the atomic hydrogen migration and cluster reconstruction steps, as we have already explained in the previous chapter. We recall the elementary steps in Table V-6.

Table V- 6 Single site surface reaction mechanisms with generation of molecular hydrogen as obtained by DFT calculations

Surface intermediates	Elementary step	Transition state	Reaction type
(A) Methyl-cyclohexane	(1) $\text{MCH}_{(\text{g})} + \text{L}_0 \rightleftharpoons \text{A}$	--	methyl-cyclohexane adsorption
(B) Methyl-cyclohexyl + H	(2) $\text{A} \rightleftharpoons \text{B}$	TS_a	C-H bond cleavage
(C) Methyl-cyclohexene + 2H	(3) $\text{B} \rightleftharpoons \text{C}$	TS_b	C-H bond cleavage
(D) Methyl-cyclohexene	(4) $\text{C} \rightleftharpoons \text{D} + \text{H}_2$	--	H_2 desorption
(E) Methyl-cyclohexenyl + H	(5) $\text{D} \rightleftharpoons \text{E}$	TS_d	C-H bond cleavage
(F) Methyl-cyclohexenyl + H	(6) $\text{E} \rightleftharpoons \text{F}$	TS_e	H atom migration
(G) Methyl-cyclohexenyl + H	(7) $\text{F} \rightleftharpoons \text{G}$	TS_f	cluster reconstruction
(H) Methyl-cyclohexadiene + 2H	(8) $\text{G} \rightleftharpoons \text{H}$	TS_g	C-H bond cleavage
(I) Methyl-cyclohexadiene	(9) $\text{H} \rightleftharpoons \text{I} + \text{H}_2$	--	H_2 desorption
(J) Methyl-cyclohexadiene	(10) $\text{I} \rightleftharpoons \text{J}$	TS_i	cluster reconstruction
(K) Methyl-cyclohexadienyl + H	(11) $\text{J} \rightleftharpoons \text{K}$	TS_j	C-H bond cleavage
(L) Methyl-cyclohexadienyl + H	(12) $\text{K} \rightleftharpoons \text{L}$	TS_k	H atom migration
(M) Toluene + 2H	(13) $\text{L} \rightleftharpoons \text{M}$	TS_l	C-H bond cleavage
(N) Toluene	(14) $\text{M} \rightleftharpoons \text{N} + \text{H}_2$	--	H_2 desorption
Toluene (gas phase)	(15) $\text{N} \rightleftharpoons \text{Tol (g)} + \text{L}_0$	--	toluene desorption

with L_0 = active site. From A to N are all surface intermediates with active sites intrinsically included.

The enthalpy and Gibbs free energy of the reaction as well as the enthalpy and free energy of activation for each elementary step are calculated from DFT (PBE-dDsC functional, see previous chapter) and are used to determine the reaction rate constant for both forward and backward reactions and equilibrium constant at $T=625$ K (Table V-7), according to the following equations :

Eyring equation :
$$k_r = \frac{k_B T}{h} e^{\frac{-\Delta_r G^\ddagger}{RT}}$$
 Equation (V-5)

Equilibrium constant reaction equation :
$$K_{eq} = e^{\frac{-\Delta_r G}{RT}}$$
 Equation (V-6)

Table V- 7 Thermodynamic and kinetic data calculated by DFT (PBE-dDsC functional) for single site dehydrogenation reaction mechanisms at 625 K

Elementary step	Reaction enthalpy, Gibbs free energy and equilibrium constant (T = 625 K)			Forward activation enthalpy, Gibbs free energy and rate constant (T = 625 K)			Backward activation enthalpy, Gibbs free energy and rate constant (T = 625 K)		
	$\Delta_r H$ (kJ/mol)	$\Delta_r G$ (kJ/mol)	K_{eq}	$\Delta_r H^\ddagger$ (kJ/mol)	$\Delta_r G^\ddagger$ (kJ/mol)	k_{r+} (s ⁻¹)	$\Delta_r H^\ddagger$ (kJ/mol)	$\Delta_r G^\ddagger$ (kJ/mol)	k_{r-} (s ⁻¹)
(1) $MCH_{(g)} + L_0 \rightleftharpoons A$	-40	51	6.01E-05	-40	51	7.83E+08	0	0	1.30E+13
(2) $A \rightleftharpoons B$	-48	-41	2.85E+03	19	33	2.31E+10	67	74	8.13E+06
(3) $B \rightleftharpoons C$	-27	-31	3.63E+02	74	70	1.86E+07	101	101	5.13E+04
(4) $C \rightleftharpoons D + H_2$	103	29	4.05E-03	103	29	5.27E+10	0	0	1.30E+13
(5) $D \rightleftharpoons E$	-6	6	3.33E-01	98	95	1.56E+05	104	89	4.69E+05
(6) $E \rightleftharpoons F$	6	-2	1.54E+00	53	41	5.11E+09	47	43	3.31E+09
(7) $F \rightleftharpoons G$	-17	-32	4.58E+02	61	40	6.21E+09	78	72	1.36E+07
(8) $G \rightleftharpoons H$	-78	-74	1.49E+06	33	33	2.35E+10	111	107	1.58E+04
(9) $H \rightleftharpoons I + H_2$	141	60	1.02E-05	141	60	1.33E+08	0	0	1.30E+13
(10) $I \rightleftharpoons J$	1	11	1.24E-01	20	20	2.60E+11	19	10	2.09E+12
(11) $J \rightleftharpoons K$	-52	-58	7.35E+04	34	44	2.56E+09	86	103	3.48E+04
(12) $K \rightleftharpoons L$	-30	-23	8.04E+01	48	42	3.97E+09	78	65	4.94E+07
(13) $L \rightleftharpoons M$	-30	-46	6.36E+03	94	87	7.62E+05	124	132	1.20E+02
(14) $M \rightleftharpoons N + H_2$	124	65	3.67E-06	124	65	4.78E+07	0	0	1.30E+13
(15) $N \rightleftharpoons Tol_{(g)} + L_0$	174	44	2.30E-04	174	44	3.00E+09	0	0	1.30E+13

2.2.2. Rate limiting steps

From the data reported in Table 6 and looking only at the feature of individual steps, step (5) appears to be a limiting process. In the forward direction, the $D \rightarrow E$ step indeed exhibits the highest activation Gibbs free energy ($95 \text{ kJ}\cdot\text{mol}^{-1}$). It is closely followed by step (13), with $\Delta_r G^\ddagger = 87 \text{ kJ}\cdot\text{mol}^{-1}$. Consequently, in sections 2.3 and 2.4, we will establish two types of kinetic models assuming that either (5) or step (13) is the rate limiting step.

The first family of models (called RDS (I)-(III), see later section 2.3) will use a so-called “extended LH model” (presented in Table V-6) for which each intermediate will be a system embedding the cluster and the adsorbed species. The advantage of this hypothesis is to facilitate the treatment of the H-migration and cluster reconstruction that are considered to generate new intermediates. So, this model does not distinguish the hydrogen atoms from the dehydrogenated MCH molecules but considers all the species adsorbed on the cluster and the reconstructed cluster itself as a global intermediate. Hence, this first family of models will not allow to simulate the coverage of the cluster by the various species instead of the distribution of each global extended intermediate [cluster + adsorbed species]. In particular, competitive adsorption between hydrogen and dehydrogenated MCH molecules will not be considered.

The second family of models (called RDS (IV)-(VI), see later section 2.4) makes the distinction between each adsorbed species and the cluster sites as it is the case in a standard LH model. However, in order to take into account H-migration and clusters reconstructions, these steps will be considered as if they were generating specific intermediate molecular species adsorbed on the cluster. In that case, the competitive adsorption between hydrogen and dehydrogenated MCH molecules will be considered.

2.2.3. TOF-determining intermediates (TDI) and transition states (TDTS)

It is suggested¹⁰ that the method to determine the reaction kinetics with isolated and stable intermediates in one single reaction step may result in overlooking other intermediates that may also play an crucial role in the catalytic reaction and may even induce changes of rate determining step. If we now look at the full Gibbs free energy profiles reported in Figure V-9, we can see that the kinetics may not simply be related to the individual steps (5) and (13). Relying on

the energetic span concept,^{10,11} the rate shall be limited by some elementary step sequences relating TOF-determining intermediates (TDI) and transition states (TDTS). So in this spirit to define the “resting states” (TDI) and “the rate-limiting TS” (TDTS), in order to calculate the apparent activation energy of the catalytic cycle, we herein found three reaction sequences that involves several sequential intermediates or transitions states to form new energy barriers that may affect the assumption of isolated rate-determining step (5) or (13).

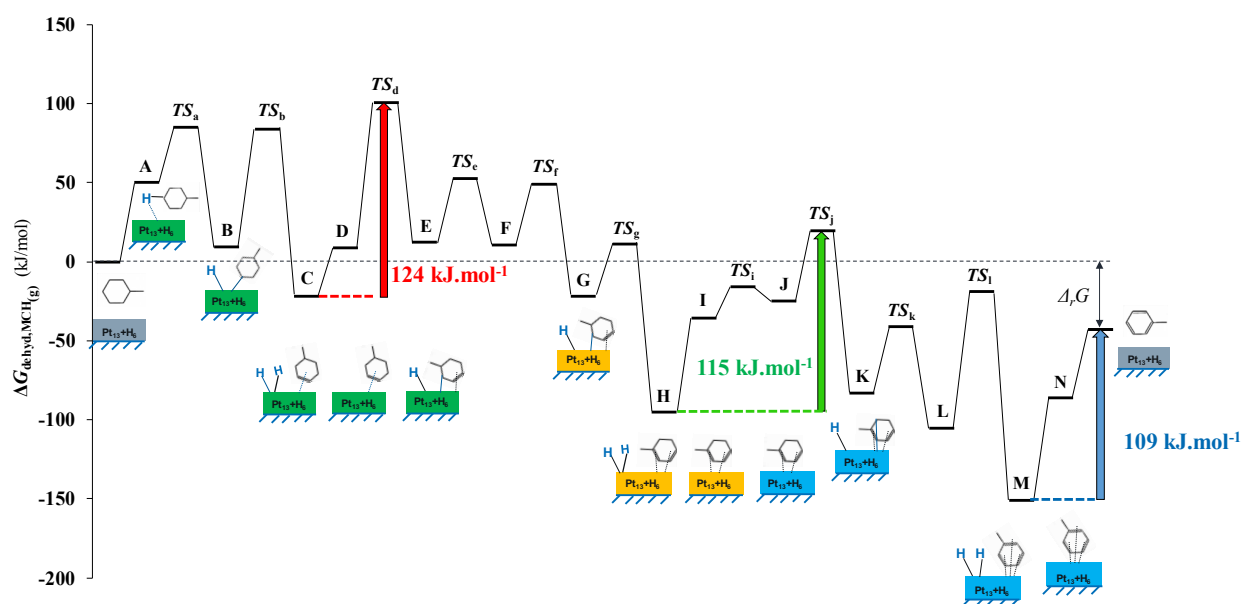


Figure V-9 Free energy profile calculated ab initio with the PBE-dDsC functional at 625 K, with mention of the three reaction sequences appearing to be the most relevant considering TDI and TDTS couples.

From Figure V-9, we can extract three main limiting sequences in the reaction, considering $\{C; TS_d\}$, $\{H; TS_j\}$ and $\{M; Tol_{(g)}+L_0\}$ as possible $\{TDI ; TDTS\}$ couples (the last one is a peculiar case with assimilation of the transition state to the product):

- $C \rightleftharpoons D \rightarrow E$ (via TS_d) with a global activation Gibbs free energy of 124 kJ.mol^{-1}
- $H \rightleftharpoons I \rightleftharpoons J \rightarrow K$ (via TS_j) with a global activation Gibbs free energy of 115 kJ.mol^{-1}

- $M \rightarrow N \rightarrow \text{Tol} + L_0$ with a global activation Gibbs free energy of 109 kJ.mol^{-1}

We can see that with the exception of the first sequence ($C \rightleftharpoons D \rightarrow E$), such considerations do not lead to the same steps to focus on as the previous RDS approach. We tried to develop Langmuir-Hinshelwood models considering those sequences as globally limiting, however we failed in writing rate expressions independent of surface species concentrations due to the merging in single steps of several elementary steps, which prevents to deduce simple expressions for the concentrations of surface species enclosed within the sequence. To find an analytical solution, we then chose to build the models as if the last step of the sequence (in practice more often: the most demanding one of the sequence) was the RDS, with pre-equilibria. This leads to three new models as summarized in Table V-8. The first one (TDTS-(I)) is equivalent to the RDS-(V) model. The two other ones (TDTS-(II) and (III)) are different in nature, as steps (11) and (15) are considered as rate limiting steps. These three models will be integrated into the standard LH mechanistic formalism with the explicit consideration of adsorption competition with adsorbed atomic hydrogen.

Table V- 8 Terminology and main characteristics of the various LH models built.

Name of the model	Approach	Nature of the RDS and {TDI ; TDTS} couple when it applies	Consideration of the backward (reversible) or not (irreversible) for the RDS / limiting sequence	Explicit consideration of adsorption competition with adsorbed atomic hydrogen
RDS-(I)	Single rate determining elementary step	Step (5)	No	No
RDS-(II)		Step (5)	Yes	No
RDS-(III)		Step (13)	Yes	No
RDS-(IV)		Step (5)	No	Yes
RDS-(V)		Step (5)	Yes	Yes
RDS-(VI)		Step (13)	Yes	Yes
TDTS-(I) ⇌ RDS-(V)	Single {TDI ; TDTS} couple	Step (5), {C;TS _d }	Yes	Yes
TDTS-(II)		Step (11), {H;TS _j }	Yes	Yes
TDTS-(III)		Step (15), {M;Tol _(g) +L ₀ }	Yes	Yes

2.3 LH kinetic models based on a single rate determining elementary step without explicit consideration of adsorption competition with adsorbed atomic hydrogen

2.3.1 RDS-(I) model: irreversible rate-determining step (5)

In this first LH kinetic model, we consider the elementary step (5) as rate determining and as being irreversible. The overall reaction rate can be thus expressed as follows :

$$\text{ES (5)} : r = k_5 [D]$$

All other steps are assumed to be at quasi-equilibrium, which leads to the following reaction equilibrium constants :

$$\text{ES (1)} : K_1 = \frac{[A]}{P_{MCH}[L_0]} \Rightarrow [A] = K_1 P_{MCH} [L_0]$$

$$\text{ES (2)} : K_2 = \frac{[B]}{[A]} \Rightarrow [B] = K_2 [A] = K_1 K_2 P_{MCH} [L_0]$$

$$\text{ES (3)} : K_3 = \frac{[C]}{[B]} \Rightarrow [C] = K_3[B] = \prod_{i=1}^3 K_i P_{MCH} [L_0]$$

$$\text{ES (4)} : K_4 = \frac{P_{H_2} [D]}{[C]} \Rightarrow [D] = \frac{K_4 [C]}{P_{H_2}} = \frac{\prod_{i=1}^4 K_i P_{MCH} [L_0]}{P_{H_2}}$$

In order to recover the expression of the surface concentration of all subsequent intermediates to step (6), the equilibrium constant expressions have to be written from the last ES (15):

$$\text{ES (15)} : K_{15} = \frac{P_{Tol} [L_0]}{[N]} \Rightarrow [N] = \frac{P_{Tol} [L_0]}{K_{15}}$$

$$\text{ES (14)} : K_{14} = \frac{P_{H_2} [N]}{[M]} \Rightarrow [M] = \frac{P_{H_2} [N]}{K_{14}} = \frac{P_{H_2} P_{Tol} [L_0]}{K_{14} K_{15}}$$

$$\text{ES (13)} : K_{13} = \frac{[M]}{[L]} \Rightarrow [L] = \frac{[M]}{K_{13}} = \frac{P_{H_2} P_{Tol} [L_0]}{\prod_{i=13}^{15} K_i}$$

$$\text{ES (12)} : K_{12} = \frac{[L]}{[K]} \Rightarrow [K] = \frac{[L]}{K_{12}} = \frac{P_{H_2} P_{Tol} [L_0]}{\prod_{i=12}^{15} K_i}$$

$$\text{ES (11)} : K_{11} = \frac{[K]}{[J]} \Rightarrow [J] = \frac{[K]}{K_{11}} = \frac{P_{H_2} P_{Tol} [L_0]}{\prod_{i=11}^{15} K_i}$$

$$\text{ES (10)} : K_{10} = \frac{[J]}{[I]} \Rightarrow [I] = \frac{[J]}{K_{10}} = \frac{P_{H_2} P_{Tol} [L_0]}{\prod_{i=10}^{15} K_i}$$

$$\text{ES (9): } K_9 = \frac{P_{H_2} [I]}{[H]} \Rightarrow [H] = \frac{P_{H_2} [I]}{K_9} = \frac{P_{H_2}^2 P_{Tol} [L_0]}{\prod_{i=9}^{15} K_i}$$

$$\text{ES (8): } K_8 = \frac{[H]}{[G]} \Rightarrow [G] = \frac{[H]}{K_8} = \frac{P_{H_2}^2 P_{Tol} [L_0]}{\prod_{i=8}^{15} K_i}$$

$$\text{ES (7): } K_7 = \frac{[G]}{[F]} \Rightarrow [F] = \frac{[G]}{K_7} = \frac{P_{H_2}^2 P_{Tol} [L_0]}{\prod_{i=7}^{15} K_i}$$

$$\text{ES (6): } K_6 = \frac{[F]}{[E]} \Rightarrow [E] = \frac{[F]}{K_6} = \frac{P_{H_2}^2 P_{Tol} [L_0]}{\prod_{i=6}^{15} K_i}$$

Then the conservation of the number of sites provides:

$$[L_0] + \sum_{i=A}^N [i] = 1 \quad \text{Equation (V-7)}$$

And :

$$[L_0]^{-1} = 1 + K_A P_{MCH} + \frac{K_D P_{MCH}}{P_{H_2}} + K_C P_{H_2}^2 P_{Tol} + K_B P_{H_2} P_{Tol} + K_E P_{Tol} \quad \text{Equation (V-8)}$$

where:

$$K_A = \sum_{j=1}^3 \prod_{i=1}^j K_i, \quad K_B = \sum_{j=10}^{14} \frac{1}{\prod_{i=j}^{15} K_i}, \quad K_C = \sum_{j=6}^9 \frac{1}{\prod_{i=j}^{15} K_i}, \quad K_D = \prod_{i=1}^4 K_i, \quad K_E = \frac{1}{K_{15}}$$

Equation (V-9) ~ (V-13)

So if we replace the term $[L_0]$ in Equation (V-8) into ES (5) and ES (4), the rate can be written as :

$$r = k_5[D] = \frac{k_5 K_D P_{MCH} [L_0]}{P_{H_2}}$$

$$\Rightarrow r = \frac{k_5 K_D P_{MCH}}{P_{H_2} \left(1 + K_A P_{MCH} + \frac{K_D P_{MCH}}{P_{H_2}} + K_C P_{H_2}^2 P_{Tol} + K_B P_{H_2} P_{Tol} + K_E P_{Tol} \right)}$$

Equation (V-14)

Until now, we derived the overall rate equation from our mechanistic model where all rate constants and equilibrium constants are calculated at the DFT level (Table V-7). Hence, no further assumption on these constants is required to study the evolution of the rate as a function of the partial pressures H_2 , MCH and Tol.

If we first consider the early stage of the reaction ($P_{Tol} = 0$ bar), the initial reaction rate can be expressed as:

$$r_0 = \frac{k_5 K_D P_{MCH}}{P_{H_2} \left(1 + K_A P_{MCH} + \frac{K_D P_{MCH}}{P_{H_2}} \right)}$$

Equation (V-15)

Hence, this initial reaction rate equation presented by Equation (V-15) can be regarded as a simplified mechanistic model where only the first five elementary steps are involved in reaction kinetics. As a matter of fact, it is logical in this condition that the rate-determining step is irreversible and presents a relatively high energy barrier that “blocks” the next elementary steps. The respective influences of hydrogen and methyl-cyclohexane partial pressures on the initial reaction rate (in s^{-1}) is reported in Figure V-10.

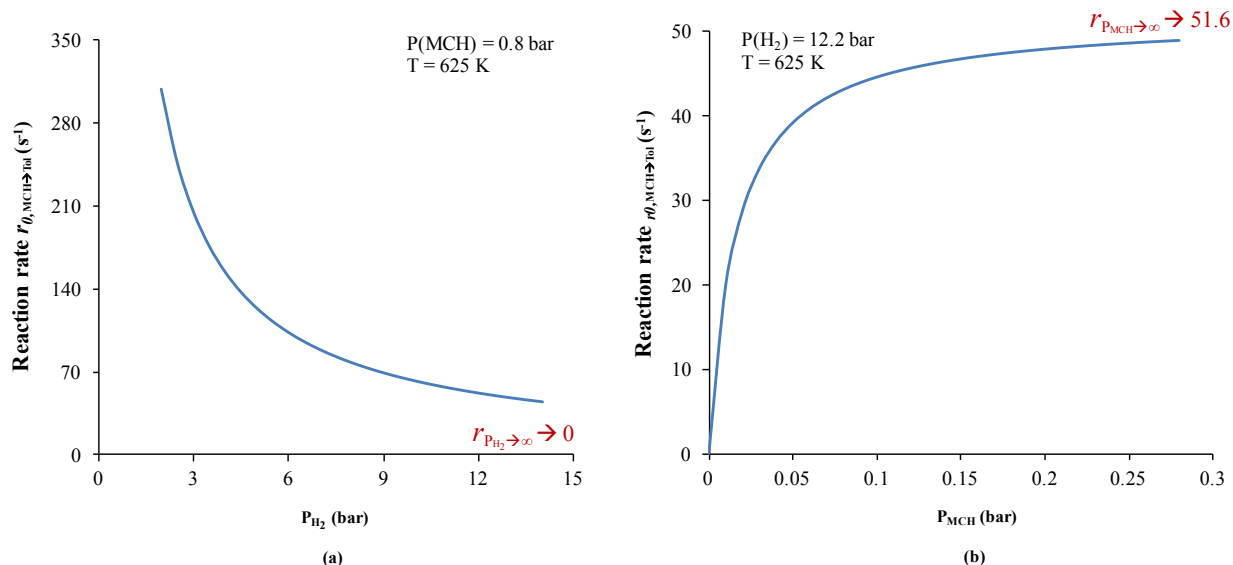


Figure V-10 Initial reaction rates ($P_{\text{Tot}}=0$ bar) calculated by model RDS-(I) (irreversible step (5) as RDS) as a function of (a) H_2 partial pressure at constant methyl-cyclohexane partial pressure of 0.8 bar (b) Methyl-cyclohexane partial pressure at constant H_2 partial pressure of 12.2 bar

These rates correspond to the monomolecular reaction rates on one catalytic site. So they cannot be directly compared to those obtained experimentally ($\text{mol}_{\text{MCH}} \cdot \text{g}_{\text{cata}}^{-1} \cdot \text{h}^{-1}$). It can be observed that the reaction rate decreases and tends to zero when the hydrogen pressure increases, whereas it increases and tends to 51.6 (s^{-1}) by increasing methyl-cyclohexane partial pressure.

In order to make these results and experiments comparable, we introduce the catalyst dispersion and metal content impacts, by assuming that 13 platinum atoms is actually one reaction site with respect to the DFT model. The dispersion for the catalyst used in our experiment is $\text{Pt}_{\text{dispersion}} = 0.90$ and the platinum content is 0.3% ($\text{Pt}_{\text{content}} = 0.003$), as mentioned in Chapter III: Computational and Experimental Methodology, *section 2.1.1*. So the new reaction rate r_0 ($\text{mol}_{\text{MCH}} \cdot \text{g}_{\text{cata}}^{-1} \cdot \text{h}^{-1}$) obtained by model RDS-(I) can be calculated by Equation (V-16) :

$$r_0 (\text{mol}_{\text{MCH}} \cdot \text{g}_{\text{cata}}^{-1} \cdot \text{h}^{-1}) = \frac{r_0 (\text{s}^{-1}) \times \text{Pt}_{\text{content}} \times \text{Pt}_{\text{dispersion}} \times 3600}{13 \times M_{\text{Pt}}} \quad \text{Equation (V-16)}$$

The new reaction rates are thus compared with the experimental results in the Figure V-11. The order of magnitude on both sets of reaction rates (kinetic model versus experiments) is very satisfactory.

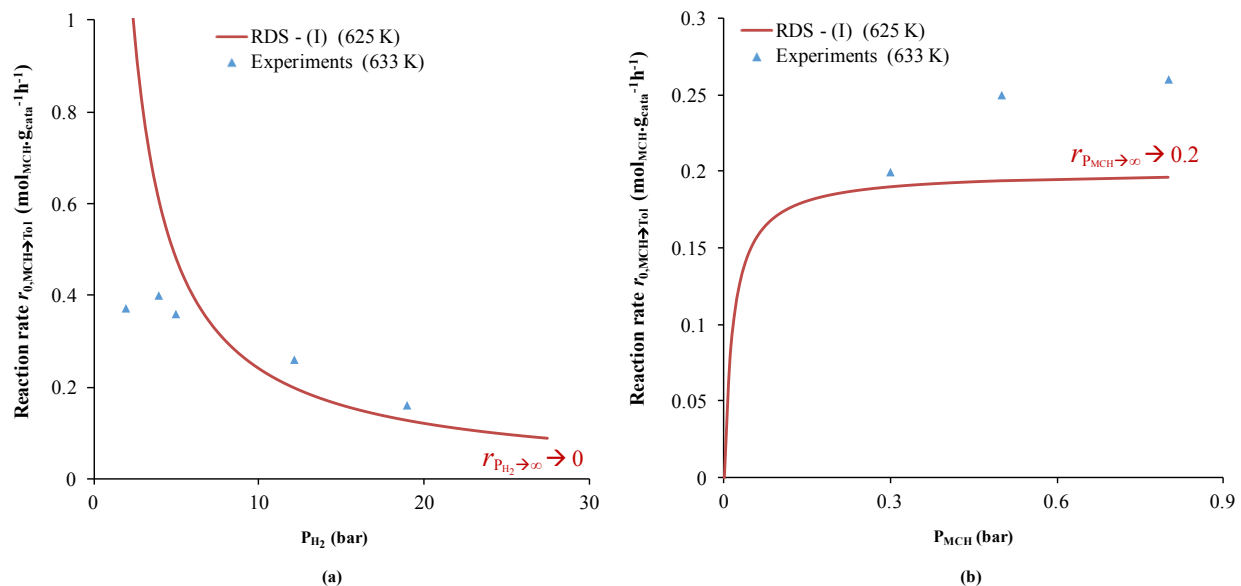


Figure V- 11 Initial reaction rates ($P_{\text{Tol}}=0$) calculated by model RDS-I (irreversible step (5) as RDS) in comparison with experimental results (633 K), as a function of (a) H₂ partial pressure at constant methyl-cyclohexane partial pressure of 0.8 bar (b) Methyl-cyclohexane partial pressure at constant H₂ partial pressure of 12.2 bar at 625 K

However, the maximum observed experimentally as function of the hydrogen partial pressure (also contained in the model of Van Trimpont) is not recovered in our RDS-I) model (Figure V-11 (a)). Even if it is mathematically obvious to understand the distinct behaviours of the two equations (Equation V-16 and Equation II-12 in Chapter II) of initial reaction rate of these two model ($P_{\text{Tol}} = 0$), it is more difficult to understand chemically the origin of this discrepancy. The behaviour of the kinetic modelling rate curve on methyl-cyclohexane pressure seems to be beforehand saturated (at $P_{\text{MCH}} = 0.16$ bar) compared to the experimental results (at

$P_{MCH} = 0.50$ bar) and a difference of $0.05 \text{ mol}_{MCH} \cdot \text{g}_{cata}^{-1} \cdot \text{h}^{-1}$ is reported for the reaction rate at the steady state, in Figure V-11(b).

2.3.2 RDS-(II) model: reversible rate-determining step (5)

If we now consider the elementary step (5) as a reversible rate-determining reaction step, the overall reaction rate becomes:

$$\text{ES (5)} : r = k_5[D] - k_{-5}[E]$$

Using the same method as for RDS-(I) (to obtain Equation (V-14)), the reaction rate equation can be rewritten as :

$$\Rightarrow r = \frac{k_5 K_D K_F P_{MCH} - k_{-5} P_{Tol} P_{H_2}^3}{P_{H_2} K_F \left(1 + K_A P_{MCH} + \frac{K_D P_{MCH}}{P_{H_2}} + K_C P_{H_2}^2 P_{Tol} + K_B P_{H_2} P_{Tol} + K_E P_{Tol} \right)}$$

Equation (V-17)

$$\text{where } K_F = \prod_{i=6}^{15} K_i$$

Once again, if we focus on the initial reaction rate at $P_{Tol} = 0$ bar, the initial overall reaction rate equation remains identical to the one of the RDS-(I) model. However, at non-zero conversion, the toluene partial pressure will increase and affect the reaction rate which may give a different evolution of the rate between these two models. In order to illustrate these evolutions along the reaction course, we will compare the reaction rates as a function of reaction conversion at constant hydrogen partial pressure of 12.2 bar at 625 K. The conversion is fixed by the change of the partial pressures of MCH and Toluene (constraining P_{MCH} and P_{Tol} at 0.8 bar).

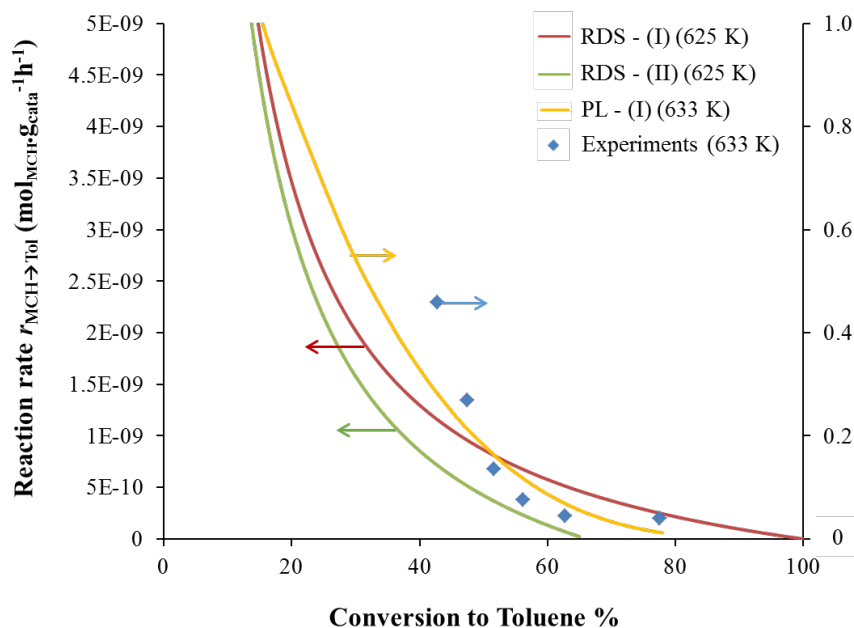


Figure V- 12 Reaction rates as a function of methyl-cyclohexane conversion to toluene for RDS-(I) and RDS-(II) models (irreversible step (5) as RDS), at 625 K and at $P_0(\text{H}_2) = 12.2$ bar and $P_0(\text{MCH}) = 0.8$ bar, as a comparison with PL-(I) model and experimental results

Figure V-12 suggests that the reaction rates during the reaction course for both RDS-(I) and RDS-(II) models cannot be distinguished at low conversion (below 15%). At higher conversion, the RDS-(II) model predicts a slightly lower reaction rate than the RDS-(I) one, which present a ratio of 0.49 at 50% conversion for the reaction rate of reversible and irreversible rate-determining step model. This is easily explained by the fact that the formation of toluene implies that the reverse hydrogenation reactions start to occur and the overall reaction rate is compensated by the effect of backward reaction. One also observes that at reaction equilibrium (where overall reaction rate tends to zero), the methyl-cyclohexane conversion to toluene for RDS-(II) is about 65%, whereas RDS-(I) can almost reach 100% conversion. Regarding the comparison with experiments and Power-Law fitting model PL-(I) (best fitting one as explained

in *section 2.1.1*), whereas the order of magnitude of the initial rates is not correctly rendered by RDS-(I) and (II), the values are strongly underestimated at non-zero conversion.

2.3.3 RDS-(III) model: reversible rate-determining step (13)

As the elementary step (13) exhibits an free energy of activation (87 kJ/mol) which is very close (according to the DFT accuracy) to the one of step (5) (92 kJ/mol), we also built a model with elementary step (13) as a reversible rate-determining step (RDS-(III)). In this case the overall reaction rate is given by:

$$\text{ES (13)} : r = k_{13}[L] - k_{-13}[M]$$

The expressions of equilibrium constants from K_5 is different from RDS-(I) and RDS-(II) models as step (5) is no longer the rate determining step.

$$\text{ES (5)} : K_5 = \frac{[E]}{[D]} \Rightarrow [E] = K_5[D] = \frac{\prod_{i=1}^5 K_i P_{MCH}[L_0]}{P_{H_2}}$$

$$\text{ES (6)} : K_6 = \frac{[F]}{[E]} \Rightarrow [F] = K_6[E] = \frac{\prod_{i=1}^6 K_i P_{MCH}[L_0]}{P_{H_2}}$$

$$\text{ES (7)} : K_7 = \frac{[G]}{[F]} \Rightarrow [G] = K_7[F] = \frac{\prod_{i=1}^7 K_i P_{MCH}[L_0]}{P_{H_2}}$$

$$\text{ES (8)} : K_8 = \frac{[H]}{[G]} \Rightarrow [H] = K_8[G] = \frac{\prod_{i=1}^8 K_i P_{MCH}[L_0]}{P_{H_2}}$$

$$\text{ES (9)} : K_9 = \frac{P_{H_2} [I]}{[H]} \Rightarrow [I] = \frac{K_9 [H]}{P_{H_2}} = \frac{\prod_{i=1}^9 K_i P_{MCH} [L_0]}{P_{H_2}^2}$$

$$\text{ES (10)} : K_{10} = \frac{[J]}{[I]} \Rightarrow [J] = K_{10} [I] = \frac{\prod_{i=1}^{10} K_i P_{MCH} [L_0]}{P_{H_2}^2}$$

$$\text{ES (11)} : K_{11} = \frac{[K]}{[J]} \Rightarrow [K] = K_{11} [J] = \frac{\prod_{i=1}^{11} K_i P_{MCH} [L_0]}{P_{H_2}^2}$$

$$\text{ES (12)} : K_{12} = \frac{[L]}{[K]} \Rightarrow [L] = K_{12} [K] = \frac{\prod_{i=1}^{12} K_i P_{MCH} [L_0]}{P_{H_2}^2}$$

Whereas we still have :

$$\text{ES (15)} : K_{15} = \frac{P_{Tol} [L_0]}{[N]} \Rightarrow [N] = \frac{P_{Tol} [L_0]}{K_{15}}$$

$$\text{ES (14)} : K_{14} = \frac{P_{H_2} [N]}{[M]} \Rightarrow [M] = \frac{P_{H_2} [N]}{K_{14}} = \frac{P_{H_2} P_{Tol} [L_0]}{K_{14} K_{15}}$$

After deducing $[L_0]$ in the same way as we did in model (I), we obtain :

$$L_0^{-1} = 1 + K_A P_{MCH} + \frac{K_J P_{MCH}}{P_{H_2}} + \frac{(K_G + K_I) P_{MCH}}{P_{H_2}^2} + K_H P_{H_2} P_{Tol} + K_E P_{Tol}$$

Equation (V-18)

$$\text{with } K_J = \sum_{i=4}^8 \prod_{j=1}^i K_i, \quad K_H = \frac{1}{K_{14} K_{15}}, \quad K_I = \prod_{i=1}^{12} K_i, \quad K_G = \sum_{j=9}^{11} \prod_{i=1}^j \frac{K_i P_{MCH}}{P_{H_2}^2}$$

So the overall reaction rate expressed by reversible rate-determining step (13) can be written as :

$$r = \frac{k_{13} \frac{K_I}{K_H} P_{MCH} - k_{-13} P_{H_2}^3 P_{Tol}}{\frac{P_{H_2}^2}{K_H} \left[1 + K_A P_{MCH} + \frac{K_J P_{MCH}}{P_{H_2}} + \frac{(K_G + K_I) P_{MCH}}{P_{H_2}^2} + K_H P_{H_2} P_{Tol} + K_E P_{Tol} \right]}$$

Equation (V-19)

The initial reaction rate can thus be written as :

$$r_0 = \frac{k_{13} K_I P_{MCH}}{P_{H_2}^2 \left[1 + K_A P_{MCH} + \frac{K_J P_{MCH}}{P_{H_2}} + \frac{(K_G + K_I) P_{MCH}}{P_{H_2}^2} \right]}$$

Equation (V-20)

The influence of hydrogen partial pressure and methyl-cyclohexane partial pressure on the initial reaction rate for this model is reported in Figure V-13. However, if the increase of the rate with P_{MCH} is well reproduced, once again the maximum of rate by varying the hydrogen partial pressure was not found at $P_{Tol} = 0$ bar. Moreover, the order of magnitude of the initial rates in this RDS-(III) model is worse as compared to RDS-(I) and (II), with respect to experiments (between 3 and 4 orders of magnitude of overestimation by the model).

If we compare our rate expression with the one of van Trimont (Equation (II-4) in Chapter II, *section 4.2.1*), in our mechanistic model, the discrepancy is probably due to the fact that so far we did not consider the competitive adsorption between hydrogen, dehydrogenated MCH molecules and free active sites, whereas this is taken into account by Van Trimont et al.⁵

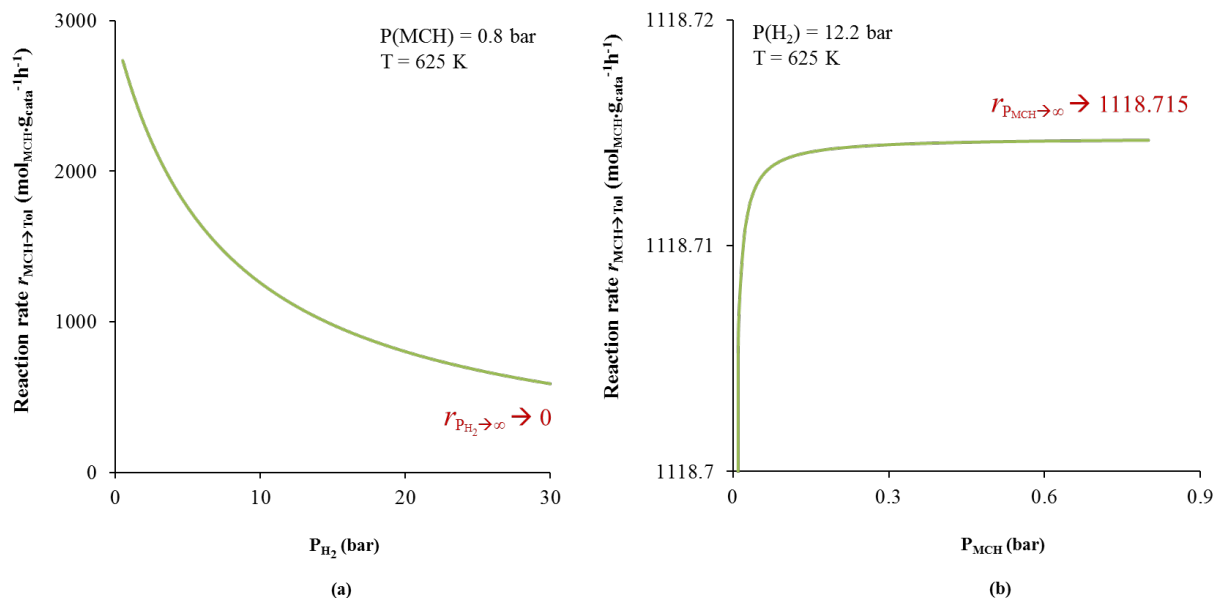


Figure V- 13 Initial reaction rate ($P_{\text{Tol}}=0$) calculated by the RDS-(III) model (reversible step (13) as RDS) as a function of (a) H_2 partial pressure at constant methyl-cyclohexane partial pressure of 0.8 bar (b) Methyl-cyclohexane partial pressure at constant H_2 partial pressure of 12.2 bar

We also investigate the reaction rates as a function of the conversion at constant hydrogen partial pressure of 12.2 bar at 625 K, as we did for the two previous models. RDS-(I), (II) and (III) models are compared in Figure V-14, which reveals that the three models lead to very different rates also at non-zero conversion, in terms of order of magnitude (ratio of 10^8). However, the RDS-(III) model (assuming step (13) as reversible rate-determining) shows a very good agreement with experimental data for non-zero conversion, while the irreversible/reversible rate determining step (5) models failed on these, in spite of the satisfaction of the initial rates. Furthermore, the two reversible rate-determining step models RDS-(II) (step (5)) and RDS-(III) (step (13)) indicate a similar conversion to toluene at the steady state (0.65 conversion).

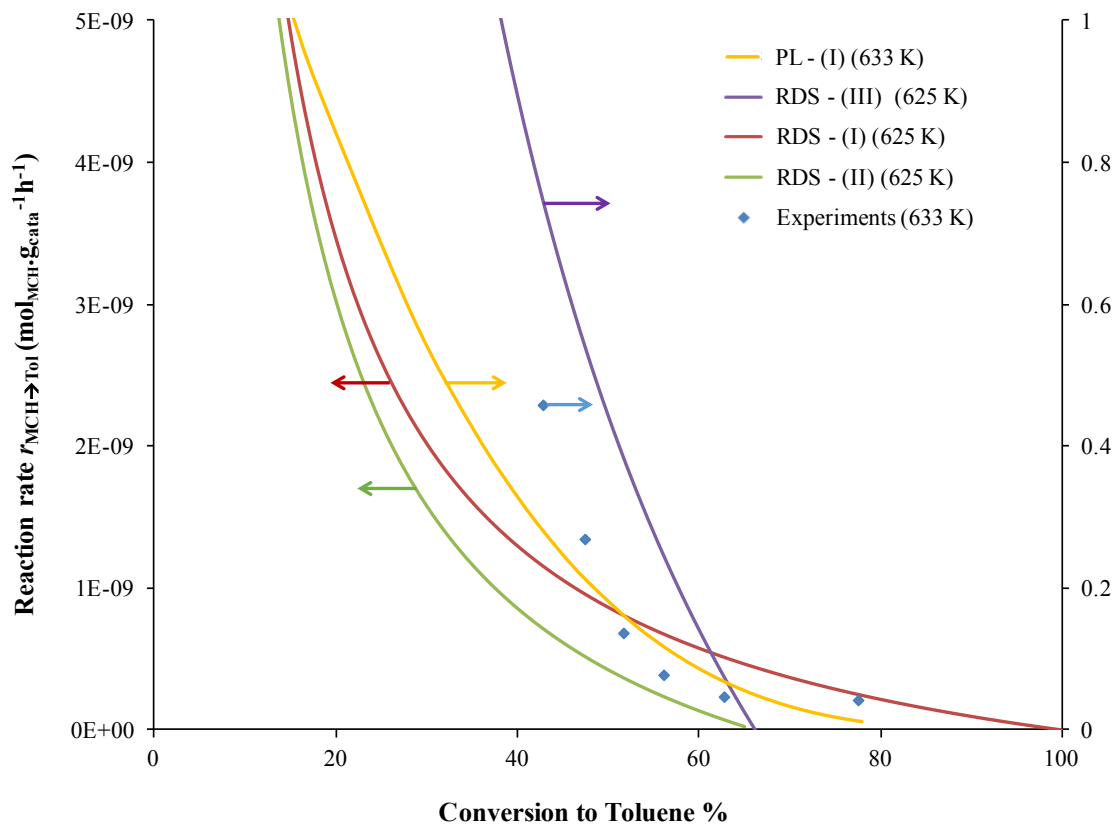


Figure V- 14 Reaction rates as a function of methyl-cyclohexane conversion to toluene for RDS-(I), (II) and (III) models at 625 K, as a comparison with experimental results and PL-(I) model at initial hydrogen pressure of 12.2 bar and initial methyl-cyclohexane pressure of 0.8 bar

So far, we can conclude that these extended LH kinetic models based on a single RDS are not fully satisfying models for all the investigated features (order of magnitude of the rate, at zero and non-zero conversion, as a function of P_{H_2} and P_{MCH}). A tentative conclusion could be that at low conversion, the rate-determining step is rather step (5) as the good order of magnitude are found on for initial reaction rates in models RDS-(I) and (II). However, when reaction goes on and toluene starts to be produced, the rate-determining step is moving towards step (13), considering the better performance of model RDS-(III). However, these models may be too simple to conclude. The next source of possible improvement investigated in the following is the

explicit consideration of the site competition between atomic hydrogen and methyl-cyclohexane dehydrogenation intermediates, which is the object of the *section 2.4*.

2.3.4 Arrhenius plot and Eyring plot for models RDS-(I), (II) and (III)

Table V- 9 Kinetic parameters derived from DFT calculated energy profile (PBE-dDsC functional) for different temperatures

Elementary steps	T = 600K			T = 625 K			T = 650 K			T = 675 K		
	K_{eq}	k_{r+}	k_{r-}	K_{eq}	k_{r+}	k_{r-}	K_{eq}	k_{r+}	k_{r-}	K_{eq}	k_{r+}	k_{r-}
(1) $MCH_{(g)} + L_0 \leftrightarrow A$	8.32E-05	1.04E+09	1.25E+13	6.01E-05	7.83E+08	1.30E+13	4.47E-05	6.05E+08	1.35E+13	3.41E-05	4.79E+08	1.41E+13
(2) $A \leftrightarrow B$	4.19E+03	1.91E+10	4.55E+06	2.85E+03	2.31E+10	8.13E+06	2.00E+03	2.77E+10	1.39E+07	1.44E+03	3.28E+10	2.28E+07
(3) $B \leftrightarrow C$	4.53E+02	9.90E+06	2.18E+04	3.63E+02	1.86E+07	5.13E+04	2.97E+02	3.34E+07	1.13E+05	2.46E+02	5.75E+07	2.34E+05
(4) $C \leftrightarrow D + H_2$	1.09E-03	1.37E+10	1.25E+13	2.54E-03	3.31E+10	1.30E+13	8.65E-03	1.17E+11	1.35E+13	1.75E-02	2.46E+11	1.41E+13
(5) $D \rightarrow E$	5.69E-01	1.11E+05	1.96E+05	5.30E-01	2.49E+05	4.69E+05	3.18E-01	3.35E+05	1.05E+06	3.06E-01	6.81E+05	2.23E+06
(6) $E \leftrightarrow F$	1.47E+00	3.22E+09	2.18E+09	1.54E+00	5.11E+09	3.31E+09	1.61E+00	7.84E+09	4.86E+09	1.68E+00	1.16E+10	6.94E+09
(7) $F \leftrightarrow G$	5.23E+02	3.64E+09	6.96E+06	4.58E+02	6.21E+09	1.36E+07	4.05E+02	1.02E+10	2.51E+07	3.61E+02	1.61E+10	4.45E+07
(8) $G \leftrightarrow H$	2.78E+06	1.73E+10	6.22E+03	1.49E+06	2.35E+10	1.58E+04	8.35E+05	3.11E+10	3.73E+04	4.90E+05	4.05E+10	8.27E+04
(9) $H \leftrightarrow I + H_2$	3.29E-06	4.12E+07	1.25E+13	1.02E-05	1.33E+08	1.30E+13	2.89E-05	3.92E+08	1.35E+13	7.59E-05	1.07E+09	1.41E+13
(10) $I \leftrightarrow J$	1.23E-01	2.12E+11	1.72E+12	1.24E-01	2.60E+11	2.09E+12	1.26E-01	3.13E+11	2.49E+12	1.26E-01	3.72E+11	2.95E+12
(11) $J \leftrightarrow K$	1.11E+05	1.87E+09	1.68E+04	7.35E+04	2.56E+09	3.48E+04	5.01E+04	3.42E+09	6.81E+04	3.53E+04	4.47E+09	1.27E+05
(12) $K \leftrightarrow L$	1.03E+02	2.59E+09	2.53E+07	8.04E+01	3.97E+09	4.94E+07	6.42E+01	5.89E+09	9.17E+07	5.21E+01	8.48E+09	1.63E+08
(13) $L \leftrightarrow M$	8.10E+03	3.45E+05	4.25E+01	6.36E+03	7.62E+05	1.20E+02	5.09E+03	1.59E+06	3.12E+02	4.15E+03	3.14E+06	7.57E+02
(14) $M \leftrightarrow N + H_2$	1.36E-06	1.70E+07	1.25E+13	3.67E-06	4.78E+07	1.30E+13	9.15E-06	1.24E+08	1.35E+13	2.13E-05	3.00E+08	1.41E+13
(15) $N \leftrightarrow Tol_{(g)} + L_0$	5.71E-05	7.14E+08	1.25E+13	2.30E-04	3.00E+09	1.30E+13	8.32E-04	1.13E+10	1.35E+13	2.72E-03	3.83E+10	1.41E+13

DFT calculations provide us thermodynamic and kinetic data that include reaction free energy and activation free energy as a function of the temperature (from 0 to 1000 K). It allows us to parameterize our kinetic model at different temperatures with corresponding reaction rate constants and equilibrium constants as reported in Table V-9. Similarly, as we did for the catalytic test, we study the reaction rates by varying the reaction temperature (600, 625, 650 and 675 K), to derive the apparent kinetic parameters to be compared with experimental temperatures. The initial reaction rates at these four temperatures were calculated by the three Langmuir

Hinshelwood kinetic models RDS-(I), (II) and (III) ($P_{\text{Tol}} = 0$ bar). The predicted Arrhenius plot and Eyring plot are then compared to the experimental ones.

The slope of these two linear relations then gives the apparent activation energy and apparent activation enthalpy. The RDS-(I) and (II) models have the same initial reaction rate so they have the same linear relations for the Eyring plot and Arrhenius plot, shown in Figure V-15. The apparent activation energy calculated by the slope of Arrhenius plot is 202 kJ/mol and the apparent activation enthalpy calculated by the slope of Eyring plot is 196 kJ/mol. These results are in a perfect agreement with what we found experimentally : 200 kJ/mol for the apparent activation energy derived by Arrhenius plot and 195 kJ/mol for the apparent activation enthalpy derived by Eyring plot.

With the RDS-(III) model (Figure V-16), we found an apparent activation energy of 133 kJ/mol and an apparent activation enthalpy of 128 kJ/mol. The difference with experimental results is around 67 kJ/mol for both activation data. This underestimation on reaction apparent activation energy is probably related to the overestimated reaction rates obtained by RDS-(III). Table V-10 give us a summary for these activation energies calculated by our current models and experiments.

Table V- 10 summary of the activation energy and activation enthalpy exploited by Arrhenius and Eyring plot for kinetic models RDS-(I), RDS-(II) and RDS-(III), as a comparison with the experimental values

Model	Experiment	LH kinetic model		
		RDS-(I)	RDS-(II)	RDS-(III)
Activation energy (kJ/mol)	200	202	202	133
Activation enthalpy (kJ/mol)	195	196	196	128

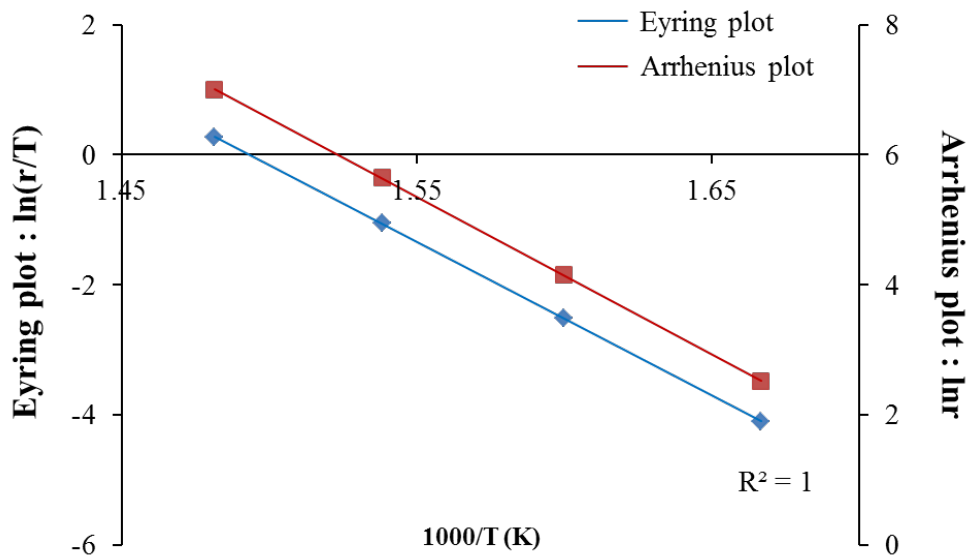


Figure V- 15 Arrhenius plot and Eyring plot for the RDS-(I) and (II) models

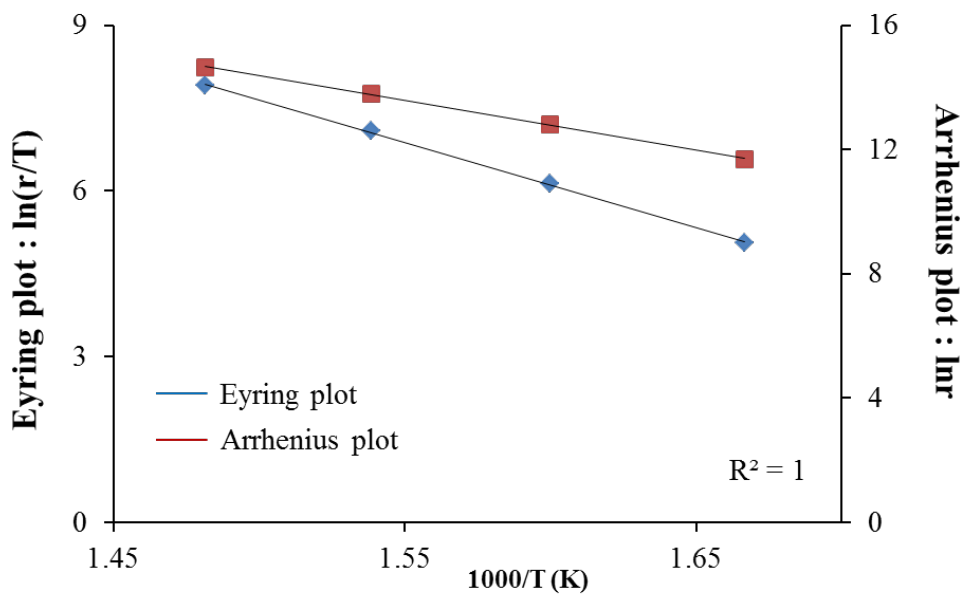


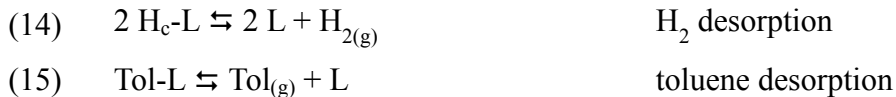
Figure V- 16 Arrhenius plot and Eyring plot for RDS-(III) model

2.4 LH kinetic models based on a single rate determining elementary step including explicit consideration of adsorption competition with adsorbed atomic hydrogen

We rewrote the mechanism following a similar model as the one of Van Trimont et al.⁵, considering adsorbed hydrogen explicitly. However, we have to include the H atom migration and cluster reconstruction steps. We chose to consider these steps as a generation of specific intermediate molecular species adsorbed on the same cluster. Moreover, all the three molecular hydrogen desorption steps are defined successively in our model, from three distinct types of atomic hydrogen, which is different from the model of Van Trimont.⁵ This new reaction scheme including explicit site competition between atomic hydrogen and dehydrogenation intermediates is presented in Table V-11.

Table V- 11 Dual site dehydrogenation mechanisms, including explicit site competition between atomic hydrogen and MCH dehydrogenation intermediates, giving rise to the RDS-(IV), RDS-(V) and RDS-(VI) models

	Elementary step	Reaction type
(1)	$\text{MCH}_{(g)} + \text{L} \rightleftharpoons \text{MCH-L}$	methyl-cyclohexane adsorption
(2)	$\text{MCH-L} + \text{L} \rightleftharpoons \text{A}_1\text{-L} + \text{H}_a\text{-L}$	C-H bond cleavage
(3)	$\text{A}_1\text{-L} + \text{L} \rightleftharpoons \text{MCHe-L} + \text{H}_a\text{-L}$	C-H bond cleavage
(4)	$2 \text{H}_a\text{-L} \rightleftharpoons 2 \text{L} + \text{H}_{2(g)}$	H_2 desorption
(5)	$\text{MCHe-L} + \text{L} \rightleftharpoons \text{A}_2\text{-L} + \text{H}_b\text{-L}$	C-H bond cleavage
(6)	$\text{A}_2\text{-L} \rightleftharpoons \text{A}_{2(d)}\text{-L}$	H atom migration
(7)	$\text{A}_{2(d)}\text{-L} \rightleftharpoons \text{A}_{2(r)}\text{-L}$	cluster reconstruction
(8)	$\text{A}_{2(r)}\text{-L} + \text{L} \rightleftharpoons \text{MCHde-L} + \text{H}_b\text{-L}$	C-H bond cleavage
(9)	$2 \text{H}_b\text{-L} \rightleftharpoons 2 \text{L} + \text{H}_{2(g)}$	H_2 desorption
(10)	$\text{MCHde-L} \rightleftharpoons \text{MCHde}_{(r)}\text{-L}$	cluster reconstruction
(11)	$\text{MCHde}_{(r)}\text{-L} + \text{L} \rightleftharpoons \text{A}_3\text{-L} + \text{H}_c\text{-L}$	C-H bond cleavage
(12)	$\text{A}_3\text{-L} \rightleftharpoons \text{A}_{3(d)}\text{-L}$	H atom migration
(13)	$\text{A}_{3(d)}\text{-L} + \text{L} \rightleftharpoons \text{Tol-L} + \text{H}_c\text{-L}$	C-H bond cleavage



with L = free active site, MCH = Methyl-cyclohexane; A₁ = Methyl-cyclohexyl; MCHe = Methyl-cyclohexene; A₂ = Methyl-cyclohexenyl; MCHde = Methyl-cyclohexadiene; A₃ = Methyl-cyclohexadienyl; Tol = Toluene; H_a, H_b, H_c = three types of atomic hydrogen; subscript (d) = intermediate molecular species from the hydrogen atom migration step; subscript (r) = intermediate molecular species from the cluster reconstruction step; subscript (g) = gas phase.

The free energy and reaction constants for each numbered elementary step remain the same as in Table V-7 and Table V-9. The LHHW rate equations are however re-written by what is following in cases of rate-determining step (5) and (13).

2.4.1 RDS-(IV) model: rate-determining step (5)

As same as for the extended LH kinetic model, we firstly consider the elementary step (5) as rate determining and as being irreversible. The overall reaction rate can be thus expressed as follows :

$$\text{ES (5) : } r = k_5 [MCHe - L] [L] \quad \text{Equation (V-21)}$$

All the steps (1) to (4) are assumed to be at quasi-equilibrium and the steps after (5) are omitted in this simplified case because of the irreversibility of step (5). We will indeed consider initial rates at this stage. At $P_{Tol} = 0$ bar we have $[A_2-L] = [A_{2(d)}-L] = [A_{2(r)}-L] = [MCHde-L] = [MCHde_{(r)}-L] = [A_3-L] = [A_{3(d)}-L] = [Tol-L] = [H_b-L] = [H_c-L] = 0$, so we have :

$$\text{ES (1): } K_1 = \frac{[MCH-L]}{P_{MCH}[L]} \Rightarrow [MCH-L] = K_1 P_{MCH} [L]$$

$$\text{ES (4): } K_4 = \frac{P_{H_2} [L]^2}{[H_a-L]^2} \Rightarrow [H_a-L] = \frac{P_{H_2}^{0.5} [L]}{K_4^{0.5}}$$

$$\text{ES (2): } K_2 = \frac{[A_1-L][H_a-L]}{[MCH-L][L]} \Rightarrow [A_1-L] = \frac{K_2 [MCH-L][L]}{[H_a-L]} = \frac{K_1 K_2 K_4^{0.5} P_{MCH} [L]}{P_{H_2}^{0.5}}$$

$$\text{ES (3): } K_3 = \frac{[MCHe-L][H_a-L]}{[A_1-L][L]} \Rightarrow [MCHe-L] = \frac{K_3 [A_1-L][L]}{[H_a-L]} = \frac{K_1 K_2 K_3 K_4 P_{MCH} [L]}{P_{H_2}}$$

Then the summation of all the coverage of active sites by surface species from above ES (1) to (4) and the vacant sites :

$$[L] + [MCH-L] + [A_1-L] + [MCHe-L] + [H_a-L] = 1$$

$$\Leftrightarrow [L]^{-1} = 1 + K'_A P_{MCH} + K'_B \frac{P_{MCH}}{P_{H_2}^{0.5}} + K'_C \frac{P_{MCH}}{P_{H_2}} + K'_{H_a} P_{H_2}^{0.5} \quad \text{Equation (V-22)}$$

With the new constants defined as :

$$K'_A = K_1, \quad K'_B = K_1 K_2 K_4^{0.5}, \quad K'_C = K_1 K_2 K_3 K_4, \quad K'_{H_a} = K_4^{-0.5} \quad \text{Equation (V-23)}$$

The new constants K'_A and K'_H can be regarded as the adsorption constants for the methylcyclohexane and H_2 (per hydrogen atom and giving H_a atoms, $L + \frac{1}{2} H_2 \leftrightarrow H_a-L$), respectively.

The other constants refer to the combination product of several elementary steps. Equation (V-21), which gives the initial rate, can then be rewritten as :

$$r_0 = \frac{k_5 K'_C P_{MCH}}{P_{H_2} \left(1 + K'_A P_{MCH} + K'_B \frac{P_{MCH}}{P_{H_2}^{0.5}} + K'_C \frac{P_{MCH}}{P_{H_2}} + K'_{H_a} P_{H_2}^{0.5} \right)^2} \quad \text{Equation (V-24)}$$

As this was done previously, the predicted initial rates (already converted in $\text{mol}_{MCH} \cdot \text{g}_{cata}^{-1} \cdot \text{h}^{-1}$) are compared with the experimental ones, as a function of $P(H_2)$ and $P(MCH)$ (Figure 12).

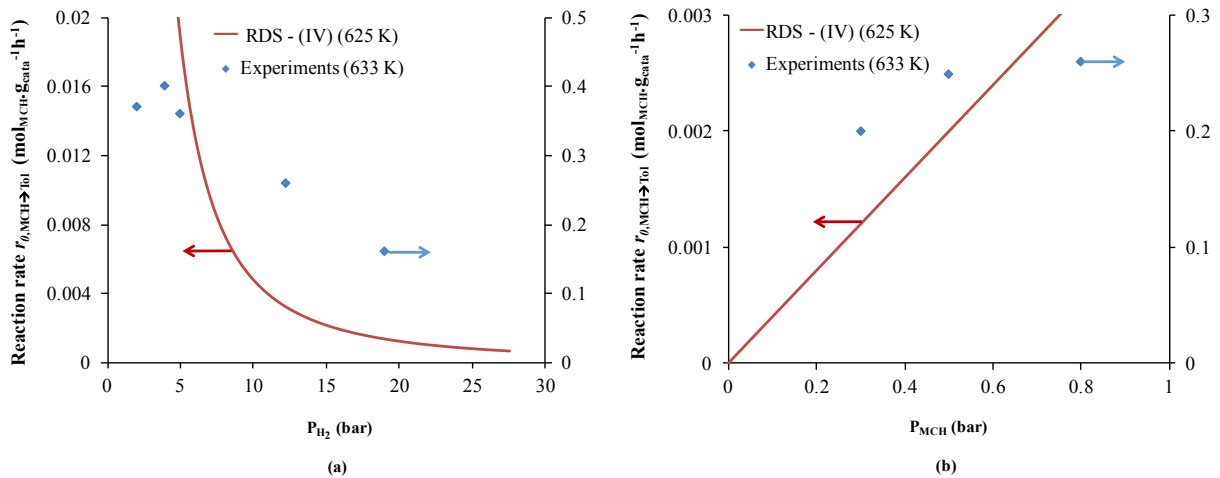


Figure V- 17 Initial reaction rates ($P_{Tot}=0$ bar) calculated by the RDS-(IV) model (irreversible step (5) as RDS) in comparison with experimental results (633 K), as a function of (a) H_2 partial pressure at constant methyl-cyclohexane partial pressure of 0.8 bar (b) Methyl-cyclohexane partial pressure at constant H_2 partial pressure of 12.2 bar at 625 K

The RDS-(IV) model underestimates (by 2 orders of magnitude) the initial reaction rates. However, the same irreversible rate determining step (5) in the RDS-(I) model (see Figure V-11) had a more satisfied order of magnitude to the experiments. The decreasing curve form in Figure V-17(a) is not very satisfying and the expected maximum rate on hydrogen pressure is not yet discovered. The curve seems to tend to $+\infty$ when $P_{H_2} \rightarrow 0$. Nevertheless, by using the Equation

(V-25), it can be demonstrated mathematically that $r_{P_{H_2} \rightarrow 0} \rightarrow \frac{k_5 P_{H_2}}{K_C P_{MCH}} = 0$. This analysis suggests that there is a maximum reaction rate (relatively of huge order of magnitude) at some point of hydrogen pressure between $P_{H_2} = 0$ -1 bar. The position of this maximum is not in agreement with our experimental observations, but its existence suggests that the explicit inclusion of adsorption competition with atomic hydrogen is a relevant approach. In Figure V-17(b), the rate monotonously increases with P_{MCH} instead of reaching a plateau. This is a strong limitation for the validity of the RDS-(IV) model.

2.4.2 RDS-(V) model: reversible rate-determining step (5)

In this next case, the overall reaction rate can be expressed as follows :

$$\text{ES (5) : } r = k_5 [MCH_e - L][L] - k_{-5} [A_2 - L][H_b - L] \quad \text{Equation (V-25)}$$

The steps (1) to (4) are identical to those in the irreversible case. The elementary steps from (6) to (15) are developed for taking into account all the intermediate surface species at quasi-equilibrium state in the model :

$$\text{ES (15) : } K_{15} = \frac{P_{Tol}[L]}{[Tol-L]} \quad \Rightarrow \quad [Tol-L] = \frac{P_{Tol}[L]}{K_{15}}$$

$$\text{ES (14) : } K_{14} = \frac{P_{H_2}[L]^2}{[H_c-L]^2} \quad \Rightarrow \quad [H_c-L] = \frac{P_{H_2}^{0.5}[L]}{K_{14}^{0.5}}$$

$$\text{ES (13) : } K_{13} = \frac{[Tol-L][H_c-L]}{[A_{3(d)}-L][L]} \quad \Rightarrow \quad [A_{3(d)}-L] = \frac{[Tol-L][H_c-L]}{K_{13}[L]} = \frac{P_{Tol}P_{H_2}^{0.5}[L]}{K_{13}K_{14}^{0.5}K_{15}}$$

$$\text{ES (12): } K_{12} = \frac{[A_{3(d)} - L]}{[A_3 - L]} \Rightarrow [A_3 - L] = \frac{[A_{3(d)} - L]}{K_{12}} = \frac{P_{\text{Tot}} P_{H_2}^{0.5} [L]}{K_{12} K_{13} K_{14}^{0.5} K_{15}}$$

$$\text{ES (11): } K_{11} = \frac{[A_3 - L][H_c - L]}{[MCHde_{(r)} - L][L]} \Rightarrow [MCHde_{(r)} - L] = \frac{[A_3 - L][H_c - L]}{K_{11}[L]} = \frac{P_{\text{Tot}} P_{H_2} [L]}{\prod_{i=11}^{15} K_i}$$

$$\text{ES (10): } K_{10} = \frac{[MCHde_{(r)} - L]}{[MCHde - L]} \Rightarrow [MCHde - L] = \frac{[MCHde_{(r)} - L]}{K_{10}} = \frac{P_{\text{Tot}} P_{H_2} [L]}{\prod_{i=10}^{15} K_i}$$

$$\text{ES (9): } K_9 = \frac{P_{H_2} [L]^2}{[H_b - L]^2} \Rightarrow [H_b - L] = \frac{P_{H_2}^{0.5} [L]}{K_9^{0.5}}$$

$$\text{ES (8): } K_8 = \frac{[MCHde - L][H_b - L]}{[A_{2(r)} - L][L]} \Rightarrow [A_{2(r)} - L] = \frac{[MCHde - L][H_b - L]}{K_8 [L]} = \frac{P_{\text{Tot}} P_{H_2}^{1.5} [L]}{K_8 K_9^{0.5} \prod_{i=10}^{15} K_i}$$

$$\text{ES (7): } K_7 = \frac{[A_{2(r)} - L]}{[A_{2(d)} - L]} \Rightarrow [A_{2(d)} - L] = \frac{[A_{2(r)} - L]}{K_7} = \frac{P_{\text{Tot}} P_{H_2}^{1.5} [L]}{K_7 K_8 K_9^{0.5} \prod_{i=10}^{15} K_i}$$

$$\text{ES (6): } K_6 = \frac{[A_{2(d)} - L]}{[A_2 - L]} \Rightarrow [A_2 - L] = \frac{[A_{2(d)} - L]}{K_6} = \frac{P_{\text{Tot}} P_{H_2}^{1.5} [L]}{K_6 K_7 K_8 K_9^{0.5} \prod_{i=10}^{15} K_i}$$

Then the summation of all the coverage of active sites by surface species from above ES (1) to (15) and the vacant sites :

$$[L] + [MCH - L] + [A_1 - L] + [MCHe - L] + \dots + [Tol - L] = 1$$

$$\Leftrightarrow [L]^{-1} = 1 + K'_A P_{MCH} + K'_B \frac{P_{MCH}}{P_{H_2}^{0.5}} + K'_C \frac{P_{MCH}}{P_{H_2}} + K'_D P_{Tol} P_{H_2}^{1.5} + K'_E P_{Tol} P_{H_2} + K'_F P_{Tol} P_{H_2}^{0.5} + K'_G P_{Tol} + K'_H P_{H_2}^{0.5}$$

Equation (V-26)

With the new constants defined as :

$$K'_D = \frac{1 + K_6 + K_6 K_7}{K_6 K_7 K_8 K_9^{0.5} \prod_{i=10}^{15} K_i}, \quad K'_E = \frac{1 + K_{10}}{\prod_{i=10}^{15} K_i}, \quad K'_F = \frac{1 + K_{12}}{K_{12} K_{13} K_{14}^{0.5} K_{15}}, \quad K'_G = \frac{1}{K_{15}},$$

$$K'_H = \frac{1}{K_4^{0.5}} + \frac{1}{K_9^{0.5}} + \frac{1}{K_{14}^{0.5}}$$

Equation (V-27) ~ (V-31)

The new constants K'_G, K'_H can be regarded as the adsorption constants for toluene and all the atomic hydrogen from H_2 gaseous phase, respectively. K'_D, K'_E, K'_F can be treated as the combination product of several elementary steps. So if we replace the term $[L]$ in Equation (V-27) and the term $[MCHe-L]$ into Equation (V-26), the rate-determining step can be written as :

$$r = \frac{k_5 K'_C P_{MCH} - \frac{k_{-5}}{K'_I} P_{Tol} P_{H_2}^3}{P_{H_2} \left(1 + K'_A P_{MCH} + K'_B \frac{P_{MCH}}{P_{H_2}^{0.5}} + K'_C \frac{P_{MCH}}{P_{H_2}} + K'_D P_{Tol} P_{H_2}^{1.5} + K'_E P_{Tol} P_{H_2} + K'_F P_{Tol} P_{H_2}^{0.5} + K'_G P_{Tol} + K'_H P_{H_2}^{0.5} \right)^2}$$

Equation (V-32)

$$\text{With } K'_I = \prod_{i=6}^{15} K_i$$

Equation (V-33)

In this case, the initial reaction rate ($P_{Tol} = 0$ bar) can be expressed as :

$$r_0 = \frac{k_5 K'_C P_{MCH}}{P_{H_2} \left(1 + K'_A P_{MCH} + K'_B \frac{P_{MCH}}{P_{H_2}^{0.5}} + K'_C \frac{P_{MCH}}{P_{H_2}} + K'_H P_{H_2}^{0.5} \right)^2}$$

Equation (V-34)

The difference between the Equation (V-24) and (V-34) is simply the adsorption of hydrogen term K'_{H_a} and K'_H . Despite in the Equation (V-35), the initial reaction rate is limited by step (5), the steps (9) and (14) which occur after RDS are still explicitly implicated in the initial rate expression. This can be explained by the fact that we considered the rate-determining step is reversible and all the surface intermediates which are not relevant to the product toluene ($P_{Tol} = 0$) are still contributing to the reaction rate. In this case, the respective influences of hydrogen partial pressure and methyl-cyclohexane partial pressure on the initial reaction rate have the same shape as in Figure V-17. Instead, the rate scale calculated by Equation (V-34) is 10^5 times smaller than the experimental results, due to the term K'_H instead of K'_{H_a} . Nonetheless, the evolution of the surface species concentrations at the very beginning of the reaction ($P_{Tol} = 0$ bar), as a function of variable hydrogen pressure at same condition for a constant methyl-cyclohexane partial pressure, can probably provide us a clue on the explanation of the maximum rate discovered by the two models locating in a very narrow hydrogen pressure interval ($P_{H_2} < 0.1$ bar). This analysis is presented in the Figure V-18.

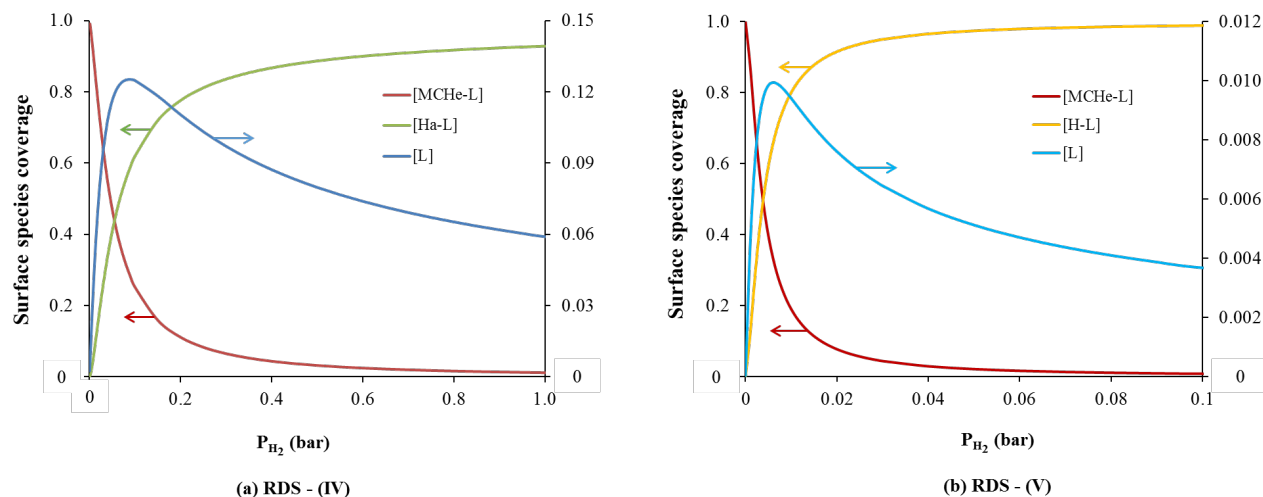


Figure V- 18 Evolution of the coverages of surface species methyl-cyclohexene (MCHe), hydrogen (Ha or H) and active sites (L) as a function of hydrogen partial pressure at constant methyl-cyclohexane partial pressure of 0.8 bar at 625 K for (a) RDS - (IV) model; (b) RDS - (V) model

The surface species coverages of the adsorbed methyl-cyclohexene (MCHe) and hydrogen atom (Ha or H) for both RDS-(IV) and RDS-(V) are depicted in Figure V-18, which present similarly the most abundant intermediates that are dominating the surface. All the other intermediate surface species coverages are very small. However, the amount of vacant site is also reported. As increasing the hydrogen partial pressure, [H-L] is logically enhanced for both models. This is a main difference with the model of Van Trimont, which supposed that the concentration in adsorbed hydrogen could be neglected. In the meantime, [MCHe-L] lowers, competing with hydrogen. Very interesting is the evolution of the concentration of vacant site [L]. It indeed exhibits a maximum, very similar to the rate for both models: its seems to be the key parameter to enhance the rate. At low hydrogen pressure, MCHe dominates and poisons all free sites, preventing the dissociation of MCHe into A_2 and H, which both need L sites to be formed. At very high hydrogen pressure, adsorbed H atoms dominate and give rise to the same limitation. Only at intermediate pressure where MCHe and H are competitors, can the proportion

of vacant site be high enough to make the dehydrogenation of MCHe possible. However, this crossing point in both case of reversible and irreversible steps appears at very low hydrogen partial pressure: 0.09 bar for RDS-(IV) model and 0.006 bar for RDS-(V) model. The fact that RDS-(V) model takes into all the three steps for hydrogen desorption, makes this crossing point even more severe at lower hydrogen partial pressure, comparing to RDS-(IV) model that only involves one hydrogen desorption step.

The evolution of the rate as a function of methyl-cyclohexane conversion to toluene at constant hydrogen partial pressure of 12.2 bar at 625 K is depicted in Figure V-19.

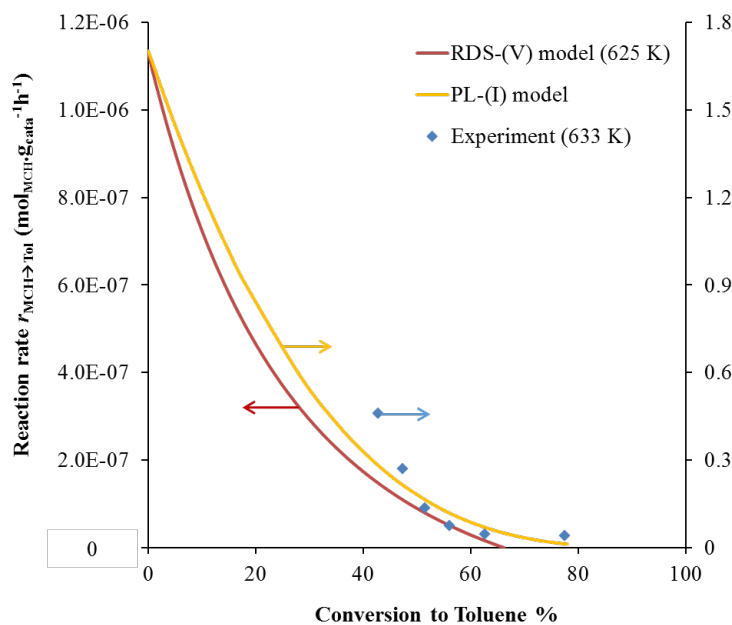


Figure V- 19 Reaction rates as a function of methyl-cyclohexane conversion to toluene for RDS-(V) model at 625 K and at $P_0(\text{H}_2) = 12.2$ bar and $P_0(\text{MCH}) = 0.8$ bar in comparison with PL-(I) model and experiments

Again, the model underestimates strongly the reaction rates (by a factor of 10^6). The curve shape, on the other hand, seems to fit very well to the PL-(I) model and not bad to the

experiments, either. The reaction at equilibrium exhibits an overall reaction rate tends to zero, the methyl-cyclohexane conversion to toluene is about 65%, same as that found for model RDS-(II).

The most abundant intermediates species on the surface during the reaction are shown in Figure V-20: hydrogen (H-L), toluene (Tol-L) and methyl-cyclohexadienyl ($A_{3(d)}$ -L, the precursor of toluene). By contrast, the surface methyl-cyclohexene (MCHe) is no more dominant once the reaction begins and toluene is formed. Once again, we reported also the surface coverage of vacant active sites (L), even it is at very low coverage. The coverage of the rest intermediates is omitted in this case. As the conversion increase, [Tol-L] increases and so does its precursor [$A_{3(d)}$ -L], which suggests us that during the reaction the step (13) can have an intrinsic co-dominant role with step (5). The [H-L] reduces to meet with the increasing [Tol-H] at a crossing point that is around 85% of conversion. At last, the [L] continues to decrease as conversion increases, which explains the fact that the reaction rates continue to decrease due to the lack of available reaction sites.

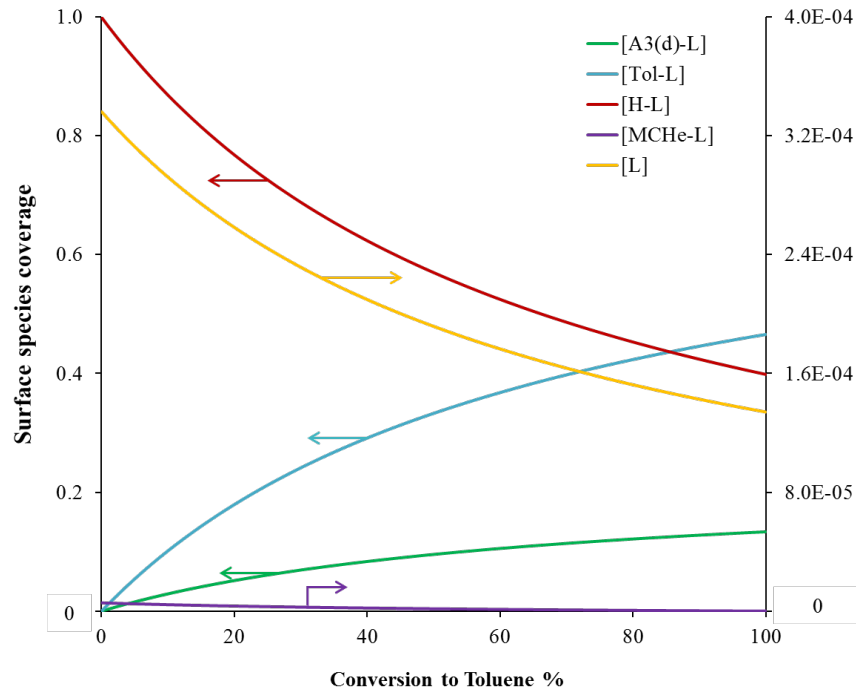


Figure V- 20 Evolution of the concentrations of relevant surface species Toluene (Tol), methyl-cyclohexadienyl ($A_{3(d)}$), Methyl-cyclohexene (MCHe), hydrogen (H) and active sites (L) as a function of methyl-cyclohexane conversion to toluene for the RDS-(V) model at 625 K and at $P_0(H_2) = 12.2$ bar and $P_0(MCH) = 0.8$ bar

2.4.3 RDS-(VI) model: reversible rate-determining step (13)

Now if we consider elementary step (13) as a reversible rate-determining step, the overall reaction rate can be expressed by :

$$\text{ES (13)} : r = k_{13} [A_{3(d)} - L][L] - k_{-13} [Tol - L][H_c - L] \quad \text{Equation (V-35)}$$

Once again, the equilibrium constants are established by assuming the step (13) as the reversible rate-determining step. The steps (1) to (4) remain identical as previous cases. The steps from (5) to (15) have to be re-expressed :

$$\text{ES (9)} : K_9 = \frac{P_{H_2} [L]^2}{[H_b - L]^2} \Rightarrow [H_b - L] = \frac{P_{H_2}^{0.5} [L]}{K_9^{0.5}}$$

$$\text{ES (5)} : K_5 = \frac{[A_2 - L][H_b - L]}{[MCHe - L][L]} \Rightarrow [A_2 - L] = \frac{K_5[MCHe - L][L]}{[H_b - L]} = \frac{\prod_{i=1}^5 K_i K_9^{0.5} P_{MCH}[L]}{P_{H_2}^{1.5}}$$

$$\text{ES (6)} : K_6 = \frac{[A_{2(d)} - L]}{[A_2 - L]} \Rightarrow [A_{2(d)} - L] = K_6[A_2 - L] = \frac{\prod_{i=1}^6 K_i K_9^{0.5} P_{MCH}[L]}{P_{H_2}^{1.5}}$$

$$\text{ES (7)} : K_7 = \frac{[A_{2(r)} - L]}{[A_{2(d)} - L]} \Rightarrow [A_{2(r)} - L] = K_7[A_{2(d)} - L] = \frac{\prod_{i=1}^7 K_i K_9^{0.5} P_{MCH}[L]}{P_{H_2}^{1.5}}$$

$$\text{ES (8)} : K_8 = \frac{[MCHde - L][H_b - L]}{[A_{2(r)} - L][L]} \Rightarrow [MCHde - L] = \frac{K_8[A_{2(r)} - L][L]}{[H_b - L]} = \frac{\prod_{i=1}^9 K_i P_{MCH}[L]}{P_{H_2}^2}$$

$$\text{ES (10)} : K_{10} = \frac{[MCHde_{(r)} - L]}{[MCHde - L]} \Rightarrow [MCHde_{(r)} - L] = K_{10}[MCHde - L] = \frac{\prod_{i=1}^{10} K_i P_{MCH}[L]}{P_{H_2}^2}$$

$$\text{ES (14)} : K_{14} = \frac{P_{H_2}[L]^2}{[H_c - L]^2} \Rightarrow [H_c - L] = \frac{P_{H_2}^{0.5}[L]}{K_{14}^{0.5}}$$

$$\text{ES (11)} : K_{11} = \frac{[A_3 - L][H_c - L]}{[MCHde_{(r)} - L][L]} \Rightarrow [A_3 - L] = \frac{K_{11}[MCHde_{(r)} - L][L]}{[H_c - L]} = \frac{\prod_{i=1}^{11} K_i K_{14}^{0.5} P_{MCH}[L]}{P_{H_2}^{2.5}}$$

$$\text{ES (12)} : K_{12} = \frac{[A_{3(d)} - L]}{[A_3 - L]} \Rightarrow [A_{3(d)} - L] = K_{12}[A_3 - L] = \frac{\prod_{i=1}^{12} K_i K_{14}^{0.5} P_{MCH}[L]}{P_{H_2}^{2.5}}$$

$$\text{ES (15)} : K_{15} = \frac{P_{Tol}[L]}{[Tol - L]} \Rightarrow [Tol - L] = \frac{P_{Tol}[L]}{K_{15}}$$

By treating in the same way as previously for the summation of all the coverage of active sites by surface species from above ES (1) to (15) and the vacant sites, the $[L]$ can be derived :

$$[L]^{-1} = 1 + K'_A P_{MCH} + K'_B \frac{P_{MCH}}{P_{H_2}^{0.5}} + K'_C \frac{P_{MCH}}{P_{H_2}} + \frac{K'_J P_{MCH}}{P_{H_2}^{1.5}} + \frac{K'_L P_{MCH}}{P_{H_2}^2} + \frac{K'_M P_{MCH}}{P_{H_2}^{2.5}} + K'_G P_{Tol} + K'_H P_{H_2}^{0.5}$$

Equation (V-36)

With the new constants defined as :

$$K'_J = \sum_{j=5}^7 \prod_{i=1}^j K_i K_9^{0.5}, K'_L = \prod_{i=1}^9 K_i + \prod_{i=1}^{10} K_i, K'_M = \left(\prod_{i=1}^{11} K_i + \prod_{i=1}^{12} K_i \right) K_{14}^{0.5}$$

Equation (V-37) ~ (V-39)

The other constants remain identical as for model RDS-(V).

So if we replace the term $[L]$ in Equation (V-36) and the terms $[A_{3(d)} - L]$, $[Tol - L]$ and $[H_c - L]$ into Equation (V-36), the rate can be written as :

$$r = \frac{k_{13} K'_N P_{MCH} - \frac{k_{-13}}{K'_p} P_{Tol} P_{H_2}^3}{P_{H_2}^{2.5} \left(1 + K'_A P_{MCH} + K'_B \frac{P_{MCH}}{P_{H_2}^{0.5}} + K'_C \frac{P_{MCH}}{P_{H_2}} + \frac{K'_J P_{MCH}}{P_{H_2}^{1.5}} + \frac{K'_L P_{MCH}}{P_{H_2}^2} + \frac{K'_M P_{MCH}}{P_{H_2}^{2.5}} + K'_G P_{Tol} + K'_H P_{H_2}^{0.5} \right)^2}$$

Equation (V-40)

$$\text{With } K'_N = \prod_{i=1}^{12} K_i K_{14}^{0.5}, K'_p = K_{14}^{0.5} K_{15}$$

Equation (V-41), (V-42)

In this case, the initial reaction rate ($P_{Tol} = 0$) can be expressed as :

$$r_0 = \frac{k_{13} K'_N P_{MCH}}{P_{H_2}^{2.5} \left(1 + K'_A P_{MCH} + K'_B \frac{P_{MCH}}{P_{H_2}^{0.5}} + K'_C \frac{P_{MCH}}{P_{H_2}} + \frac{K'_J P_{MCH}}{P_{H_2}^{1.5}} + \frac{K'_L P_{MCH}}{P_{H_2}^2} + \frac{K'_M P_{MCH}}{P_{H_2}^{2.5}} + K'_H P_{H_2}^{0.5} \right)^2}$$

Equation (V-43)

Therefore, the impacts of hydrogen and methyl-cyclohexane partial pressure on the initial reaction rate are also studied for RDS-(VI) (Figure V-21).

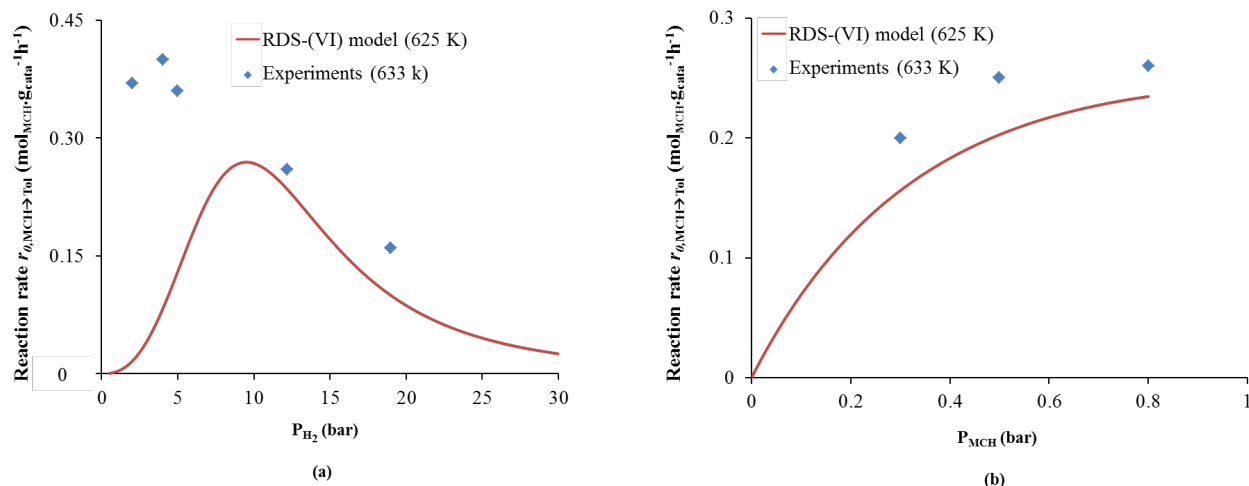


Figure V- 21 Initial reaction rates ($P_{\text{Tol}}=0$ bar) calculated by RDS-(VI) in comparison with experimental results (633 K), as a function of (a) H_2 partial pressure at constant methyl-cyclohexane partial pressure of 0.8 bar (b) Methyl-cyclohexane partial pressure at constant H_2 partial pressure of 12.2 bar at 625 K

In both cases, the order of magnitude of the rate is the same between the model and the experiments. In Figure V-21(a), the initial reaction rates as a function of hydrogen partial pressure indicates a maximum reaction rate at the intermediate hydrogen partial pressure of 10 bar. This is so far the best kinetic model that is achieved by our study to meet this kinetic phenomenon, by assuming step (13) as the rate-determining step. Nevertheless, this maximum reaction rate is found at 10 bar, against the experimental value found near 5 bar and the rate at the maximum is smaller than the experimental one. This point deserves a complementary analysis on the sensibility to each parameter in order to enhance the agreement with experiments, which will be done in detail in next section. In Figure V-21(b), the model fits very well with the experiments as the rates stop increasing rapidly at around 0.5 bar of methyl-cyclohexane.

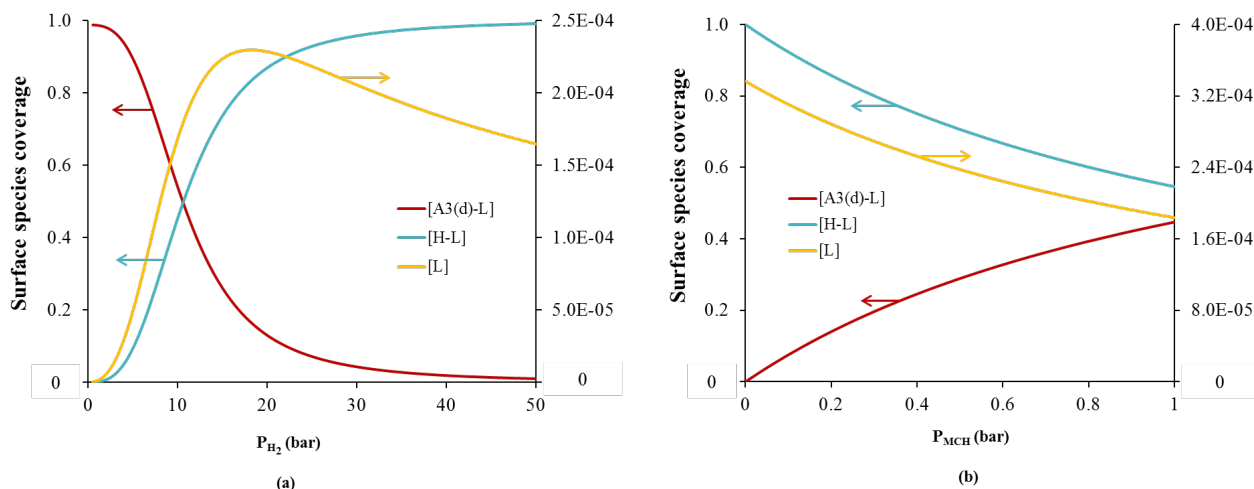


Figure V- 22 Evolution of the coverage of surface species methyl-cyclohexadienyl ($A_{3(d)}$), hydrogen and active sites as a function of (a) hydrogen partial pressure at constant methyl-cyclohexane partial pressure of 0.8 bar and of (b) methyl-cyclohexane partial pressure at constant hydrogen partial pressure of 12.2 bar, for the RDS-(VI) model at 625 K

Figure V-22 depicts the surface coverage evolution of the intermediate species as a function of hydrogen and methyl-cyclohexane partial pressures for zero conversion, which are: methyl-cyclohexadienyl ($A_{3(d)}-L$), hydrogen ($H-L$) and vacant active sites (L). In Figure V-22 (a), Once again, $[L]$ is the key to the reaction rates when hydrogen partial pressure increase, resulting in the maximal $[L]$ at hydrogen pressure of about 10 bar, corresponding to the maximum rate. At low hydrogen pressure, $A_{3(d)}-L$ dominates and poisons all free sites, preventing the dissociation of $A_{3(d)}-L$ into Toluene and H, which both need L sites to be formed. At very high hydrogen pressure, adsorbed H dominates and gives rise to the same limitation. In Figure V-22 (b), at low methyl-cyclohexane partial pressure and high hydrogen partial pressure (12.2 bar), the surface is covered by hydrogen (high $[H-L]$). With the methyl-cyclohexane partial pressure increasing, the surface is gradually being taken over by methyl-cyclohexadienyl ($A_{3(d)}-L$), where $[A_{3(d)}-L]$

enhances. However, $[L]$ decreases since the methyl-cyclohexane pressure starts to increase, which means that the reaction occurs on the vacant reaction sites. As $[L]$ continues to decrease, one can expect that the reaction rate will eventually tumble down. As a matter of fact, our model RDS-(VI) predicts that the initial reaction rate starts to decrease when $P_{MCH} > 1.5$ bar.

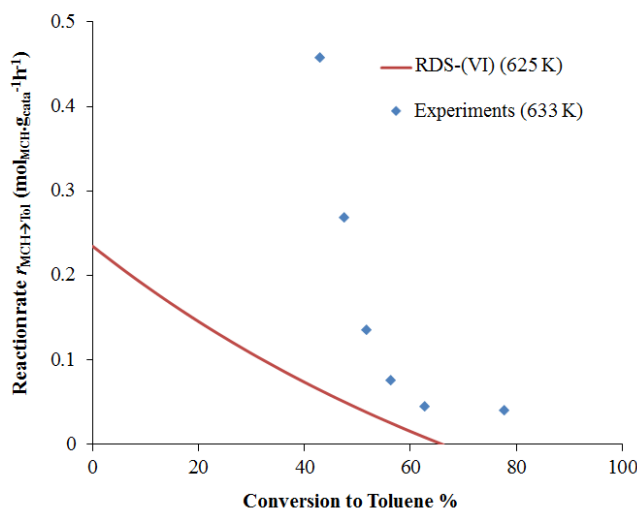


Figure V- 23 Reaction rates as a function of methyl-cyclohexane conversion to toluene for the RDS-(VI) model at 625 K and at $P_0(H_2) = 12.2$ bar and $P_0(MCH) = 0.8$ bar

Figure V-23 shows the reaction rates as a function of the conversion to toluene. The rates between the model and experiments remain comparable in terms of order of magnitude. However the curve shape is less satisfying. At low conversion, the reaction rate is too low, whereas the experiment results tend to suggest a very high rate but not infinite at zero conversion. Once again, the reaction reaches equilibrium at around 65% conversion. So the surface coverage evolution of the relevant intermediates species are traced as a function of the conversion, in Figure V-24. It is found that the most abundant surface species are toluene (Tol-L), hydrogen (H-L) and methyl-cyclohexadienyl ($A_{3(d)}$ -L, precursor of toluene production). The $[H-L]$ is weakened during the

formation of toluene. However, $[A_{3(d)}-L]$ reduces by producing toluene on the surface. The crossing point of $[A_{3(d)}-L]$ and $[Tol-L]$ is at 40% conversion and the one of $[H-L]$ and $[Tol-L]$ at 85%.

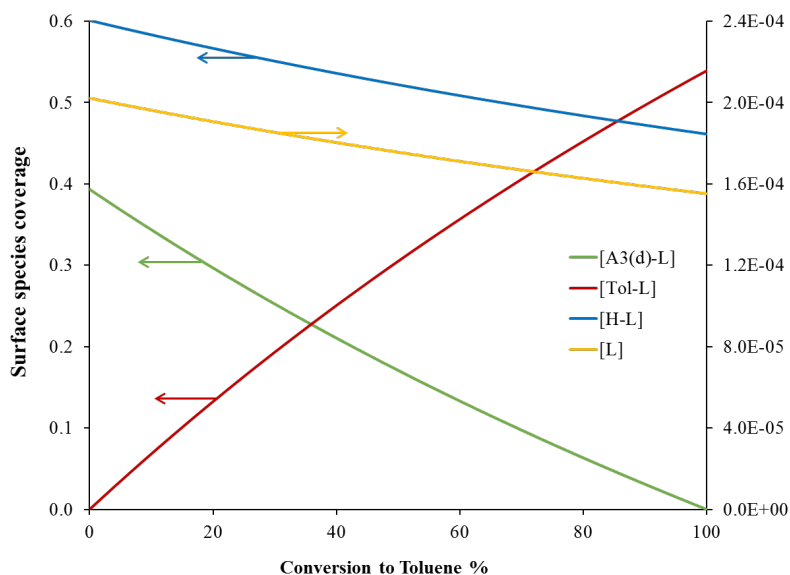


Figure V- 24 Evolution of the coverage of relevant surface species Toluene (Tol), methyl-cyclohexadienyl ($A_{3(d)}$), hydrogen (H) and active sites (L) as a function of methyl-cyclohexane conversion to toluene for the RDS-(VI) model at 625 K and at $P_0(H_2) = 12.2$ bar and $P_0(MCH) = 0.8$ bar

2.4.4 TDTS-(II) model: reversible rate-determining step (11)

Now, let us consider the global reaction step $H \rightleftharpoons I \rightleftharpoons J \rightleftharpoons K$ as rate determining step by using the energetic span theory. The new activation free energy $\Delta_r G^\ddagger_{H \rightarrow TS_j} = 115$ kJ/mol (see in Figure V-9). However, if we write the rate equation for this global rate determining step by the same mechanistic model giving rise to RDS-(IV), RDS-(V) and RDS-(VI) models in Table V-8, we find us trapped by the merging of step (9) in the RDS : $2 H_b-L \rightleftharpoons 2 L + H_{2(g)}$ ($H \rightleftharpoons I$), preventing any easy expression of $[H_b-L]$. Moreover, step (10) : $MCHde-L \rightleftharpoons MCHde_{(r)}-L$ ($I \rightleftharpoons$

J), exhibits a low activation and reaction free energies. So by these reasons, we simplified this global rate determining step $H \rightleftharpoons I \rightleftharpoons J \rightleftharpoons K$ by considering the elementary step (11) as the rds : $MCHde_{(r)}-L + L \rightleftharpoons A_3-L + H_c-L$, which appears to be the fifth C-H bond cleavage step. So the rate equation by assuming the step (11) as rate determining step can be written as :

$$r = k_{11} [MCHde_{(r)} - L][L] - k_{-11} [A_3 - L][H_c - L] \quad \text{Equation (V-44)}$$

As before, we can deduce the concentration of the surface active sites $[L]$:

$$[L]^{-1} = 1 + K'_A P_{MCH} + K'_B \frac{P_{MCH}}{P_{H_2}^{0.5}} + K'_C \frac{P_{MCH}}{P_{H_2}} + K'_J \frac{P_{MCH}}{P_{H_2}^{1.5}} + K'_L \frac{P_{MCH}}{P_{H_2}^2} + K'_F P_{Tol} P_{H_2}^{0.5} + K'_G P_{Tol} + K'_H P_{H_2}^{0.5} \quad \text{Equation (V-45)}$$

Then we have the reaction rate expression:

$$r = \frac{k_{11} K'_Q P_{MCH} - k_{-11} K'_R P_{H_2}^3 P_{Tol}}{P_{H_2}^2 (1 + K'_A P_{MCH} + K'_B \frac{P_{MCH}}{P_{H_2}^{0.5}} + K'_C \frac{P_{MCH}}{P_{H_2}} + K'_J \frac{P_{MCH}}{P_{H_2}^{1.5}} + K'_L \frac{P_{MCH}}{P_{H_2}^2} + K'_F P_{Tol} P_{H_2}^{0.5} + K'_G P_{Tol} + K'_H P_{H_2}^{0.5})^2} \quad \text{Equation (V-46)}$$

With:

$$K'_Q = \prod_{i=1}^{10} K_i, \quad K'_R = \frac{1}{\prod_{i=12}^{15} K_i} \quad \text{Equation (V-47), (V-48)}$$

In this case, the initial reaction rate can be written as :

$$r_0 = \frac{k_{11} K'_Q P_{MCH}}{P_{H_2}^2 (1 + K'_A P_{MCH} + K'_B \frac{P_{MCH}}{P_{H_2}^{0.5}} + K'_C \frac{P_{MCH}}{P_{H_2}} + K'_J \frac{P_{MCH}}{P_{H_2}^{1.5}} + K'_L \frac{P_{MCH}}{P_{H_2}^2} + K'_H P_{H_2}^{0.5})^2} \quad \text{Equation (V-49)}$$

Its evolution as a function of H_2 and methyl-cyclohexane partial pressures is depicted in Figure V-25.

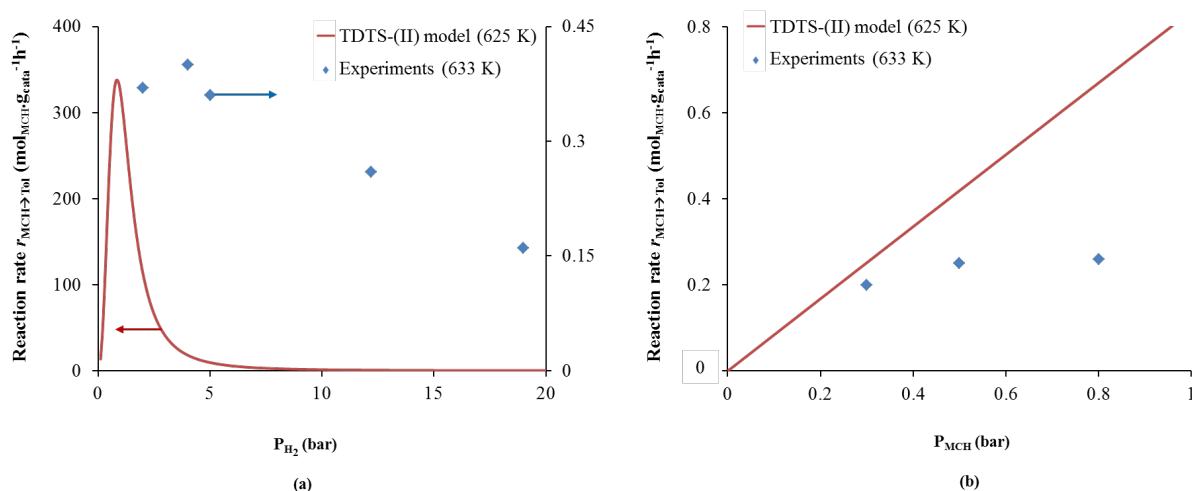


Figure V- 25 Initial reaction rates ($P_{Tot}=0$ bar) calculated by the TDTS-(II) model (reversible step (11) as RDS) in comparison with experimental results (633 K), as a function of (a) H_2 partial pressure at constant methyl-cyclohexane partial pressure of 0.8 bar (b) Methyl-cyclohexane partial pressure at constant H_2 partial pressure of 12.2 bar at 625 K

In Figure V-25 (a), the maximum initial rate appears at around 1 bar of hydrogen partial pressure. However, the reaction rates are much higher compared to the experimental results. Meanwhile, the shape of the curve is sharper than the experimental one. In Figure V-25 (b), the rates are of the same order of magnitude with the experiments but the plateau is not reproduced, which show no saturation of rates in the current conditions, especially at this high hydrogen partial pressure.

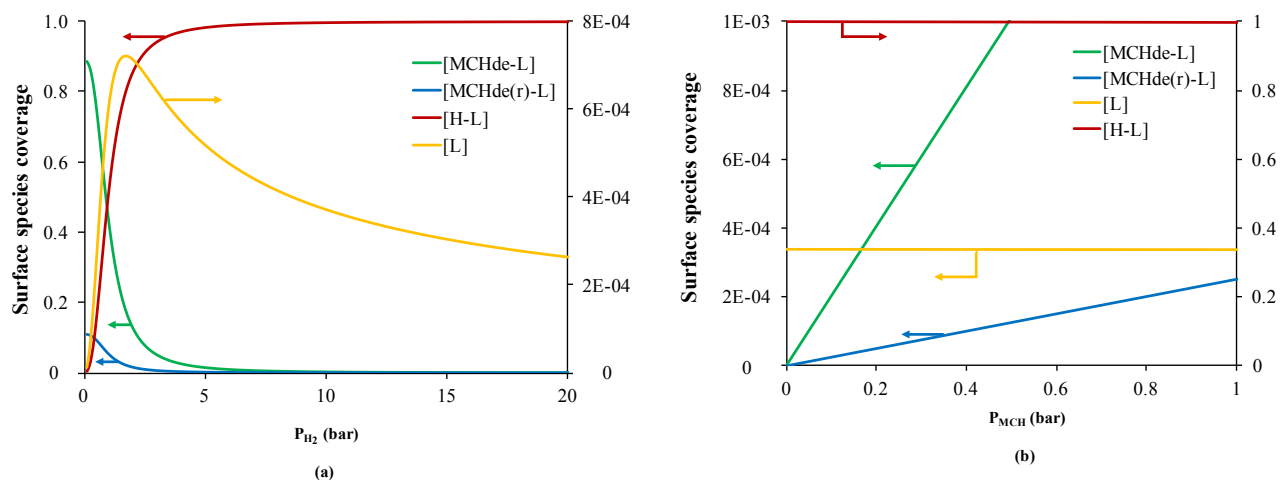


Figure V- 26 Evolution of the coverage of surface species methyl-cyclohexadiene (MCHde, MCHde_(r)), hydrogen (H) and free active sites (L) as a function of (a) hydrogen partial pressure at constant methyl-cyclohexane partial pressure of 0.8 bar and of (b) methyl-cyclohexane partial pressure at constant hydrogen partial pressure of 12.2 bar, for the TDTS-(II) model (reversible step (11) as RDS) at 625 K

Figure V-26 (a) depicts the surface species coverage of methyl-cyclohexadiene (MCHde, MCHde_(r)), hydrogen and active sites as a function of hydrogen partial pressure. The [MCHde-L] and [MCHde_(r)-L] decrease, when the hydrogen partial pressure increases. Particularly, instead of MCHde_(r)-L, the direct reactant of step (11), MCHde-L is more abundant, because of the low free energy barrier and similar free energy level of these two intermediates. [H-L] increases and very rapidly reaches saturation when hydrogen partial pressure increases above 4 bars. In contrast, the free active sites coverage [L] firstly increases while increasing the hydrogen pressure, then decreases, in agreement with the reaction rate evolution. The active sites coverage is directly related to the reaction rate, implying that the more available sites are given, the higher reaction rate can be reached. This phenomenon is not observed in Figure V-26 (b), because the constant hydrogen partial pressure is obviously too high in this case and the hydrogen coverage stays saturated despite the increase of methyl-cyclohexane pressure. Also, in Figure V-26 (b),

compared to Equation (V-45), one sees that the evolution of the rate is controlled by the evolution of $[MCHde_{(r)}-L]$ which increases as a function of P_{MCH} in this P_{H_2} regime.

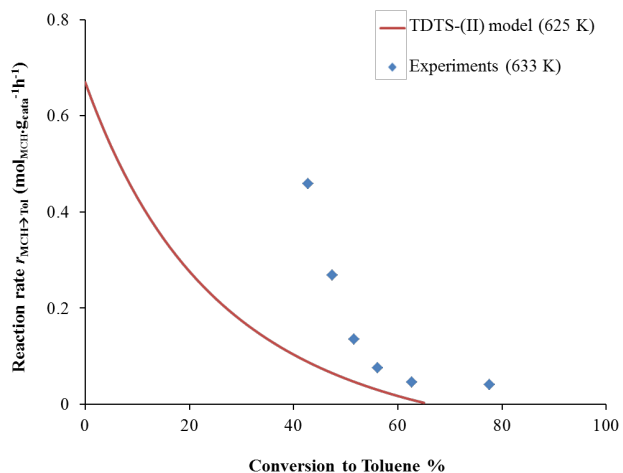


Figure V- 27 Reaction rates as a function of methyl-cyclohexane conversion to toluene for the TDTS-(II) model (reversible step (11) as RDS) at 625 K and at $P_0(H_2) = 12.2$ bar and $P_0(MCH) = 0.8$ bar

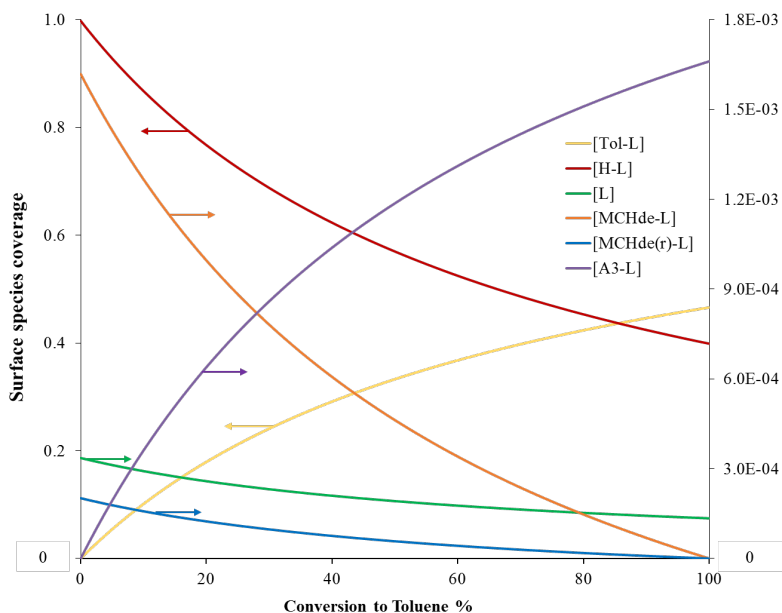


Figure V- 28 Evolution of the coverage of relevant surface species Toluene (Tol), methyl-cyclohexadiene (MCHde, $MCHde_{(r)}$), methyl-cyclohexadienyl (A_3), hydrogen (H) and active sites (L) as a function of methyl-cyclohexane conversion to toluene for the TDTS-(II) model (reversible step (11) as RDS) at 625 K and at $P_0(H_2) = 12.2$ bar and $P_0(MCH) = 0.8$ bar

Figure V-28 and V-29 show the reaction rate and relevant surface species coverage evolution in the course of the reaction (as a function of the conversion), respectively. This evolution on reaction rate this time is more coherent with the experimental results. If we now look at the surface species coverage, all the reactant intermediates MCHde-L and MCHde_(r)-L have a decreasing surface coverage and the product intermediates A₃-L and Tol-L have an increasing coverage. [H-L] and [L] also decrease during the reaction because of the formation of toluene on the surface.

2.4.5 TDTS-(III) model: reversible rate-determining step (15)

Another competitive total energy barrier obtained by energetic span is the total reaction step $M \rightleftharpoons N \rightleftharpoons \text{Tol}_{(g)}$ with total free activation energy $\Delta_r G_{M \rightarrow \text{Tol}_{(g)}}^\ddagger \approx \Delta_r G_{M \rightarrow \text{Tol}_{(g)}} = 115 \text{ kJ/mol}$. If we adopt these total reaction steps as rate-determining step, the two molecules desorption steps : hydrogen and toluene molecule, will be completely different from any model mentioned previously, while all of them consider one of the C-H bond cleavage steps as rate-determining. However, we encounter the same difficulty to express the rate equation when it comes to the H₂ desorption step: $M \rightleftharpoons N$, where intermediate concentration $[H_c-L]$ should be written independently from the global reaction rate equation. So, again the global rate-determining can be simplified as $N \rightleftharpoons \text{Tol}_{(g)}$, the elementary step (15). The rate equations by assuming step (15) as rate determining step can be expressed as :

$$r = k_{15} [\text{Tol} - L] - k_{-15} P_{\text{Tol}} [L] \quad \text{Equation (V-50)}$$

$$[L]^{-1} = 1 + K'_A P_{MCH} + K'_B \frac{P_{MCH}}{P_{H_2}^{0.5}} + K'_C \frac{P_{MCH}}{P_{H_2}} + K'_J \frac{P_{MCH}}{P_{H_2}^{1.5}} + K'_L \frac{P_{MCH}}{P_{H_2}^2} + K'_M \frac{P_{MCH}}{P_{H_2}^{2.5}} + K'_S \frac{P_{MCH}}{P_{H_2}^3} + K'_H P_{H_2}^{0.5}$$

Equation (V-51)

$$r = \frac{k_{15} K'_S P_{MCH} - k_{-15} P_{Tol} P_{H_2}^3}{P_{H_2}^3 (1 + K'_A P_{MCH} + K'_B \frac{P_{MCH}}{P_{H_2}^{0.5}} + K'_C \frac{P_{MCH}}{P_{H_2}} + K'_J \frac{P_{MCH}}{P_{H_2}^{1.5}} + K'_L \frac{P_{MCH}}{P_{H_2}^2} + K'_M \frac{P_{MCH}}{P_{H_2}^{2.5}} + K'_S \frac{P_{MCH}}{P_{H_2}^3} + K'_H P_{H_2}^{0.5})}$$

Equation (V-52)

Where,

$$K'_S = \prod_{i=1}^{14} K_i$$

Equation (V-53)

So, the initial reaction rate can be written as,

$$r_0 = \frac{k_{15} K'_S P_{MCH}}{P_{H_2}^3 (1 + K'_A P_{MCH} + K'_B \frac{P_{MCH}}{P_{H_2}^{0.5}} + K'_C \frac{P_{MCH}}{P_{H_2}} + K'_J \frac{P_{MCH}}{P_{H_2}^{1.5}} + K'_L \frac{P_{MCH}}{P_{H_2}^2} + K'_M \frac{P_{MCH}}{P_{H_2}^{2.5}} + K'_S \frac{P_{MCH}}{P_{H_2}^3} + K'_H P_{H_2}^{0.5})}$$

Equation (V-54)

Its evolution as a function of H₂ and methyl-cyclohexane partial pressures is depicted in Figure V-29. Remarkably, the evolution as a function of the H₂ partial pressure is not following a maximum, but monotonously decreases. The orders of magnitude of rates are very different from experiments. The shape of the evolution of the rate versus P_{MCH} is nicely reproduced but again not the order of magnitude. Figure V-30 reports relevant surface species concentrations, and demonstrates that the evolution of the rate is primarily driven by [Tol-L], in agreement with Equation (V-50).

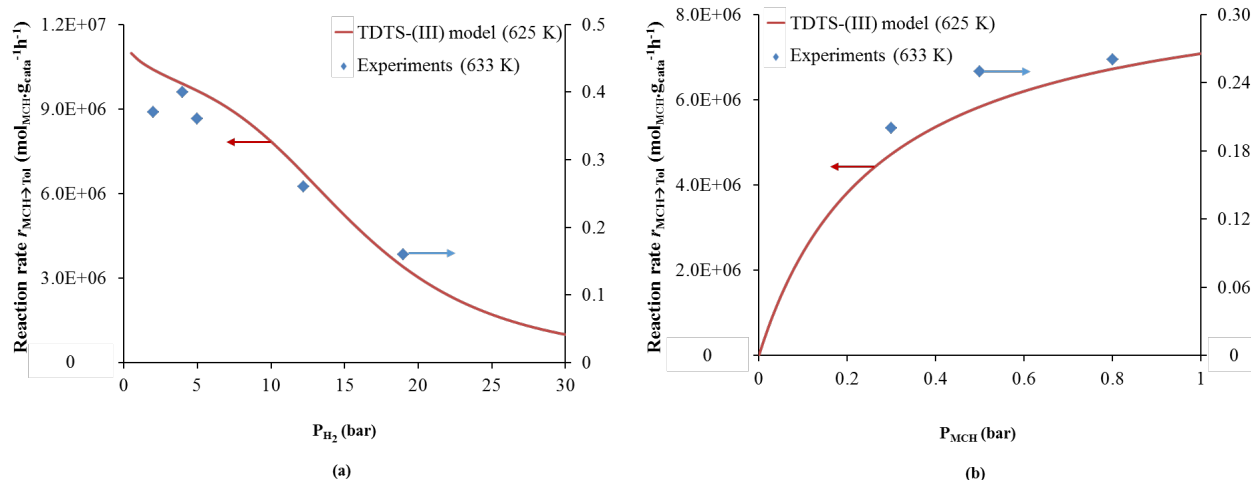


Figure V- 29 Converted initial reaction rates ($P_{\text{Tol}}=0$ bar) calculated by the TDTS-(III) model (reversible step (15) as RDS) in comparison with experimental results (633 K), as a function of (a) H_2 partial pressure at constant methyl-cyclohexane partial pressure of 0.8 bar (b) Methyl-cyclohexane partial pressure at constant H_2 partial pressure of 12.2 bar at 625 K

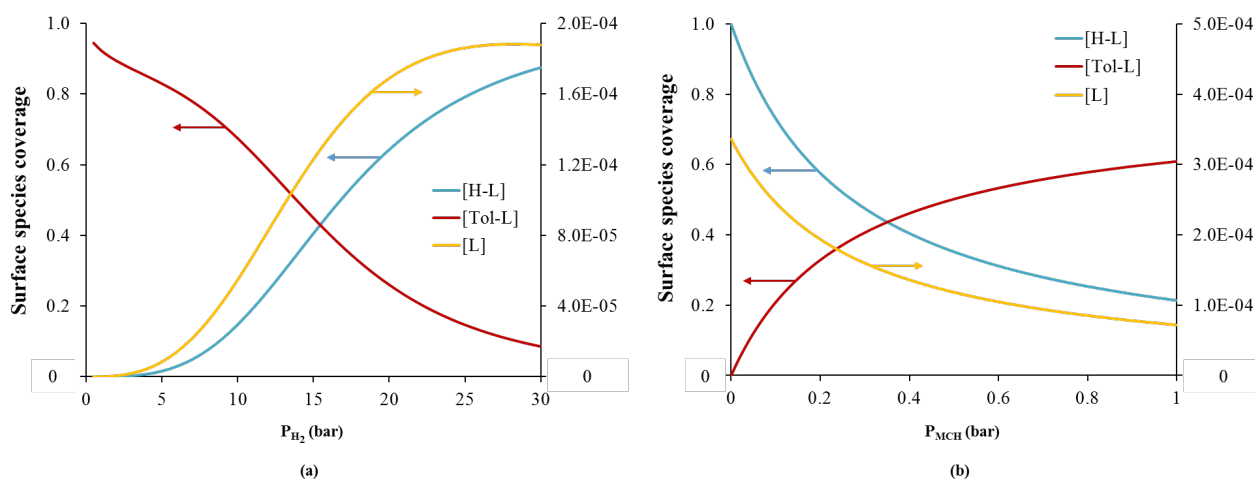


Figure V- 30 Evolution on the coverage of surface species toluene (Tol), hydrogen and active sites as a function of (a) hydrogen partial pressure at constant methyl-cyclohexane partial pressure of 0.8 bar and of (b) methyl-cyclohexane partial pressure at constant hydrogen partial pressure of 12.2 bar, for the TDTS-(III) model (reversible step (15) as RDS) at 625 K

Figure V-31 demonstrates a poor agreement with experiments for what regards the evolution of the rate as a function of the conversion, with a clear role of $A_{3(d)}\text{-L}$ and Tol-L on this evolution (Figure V-32).

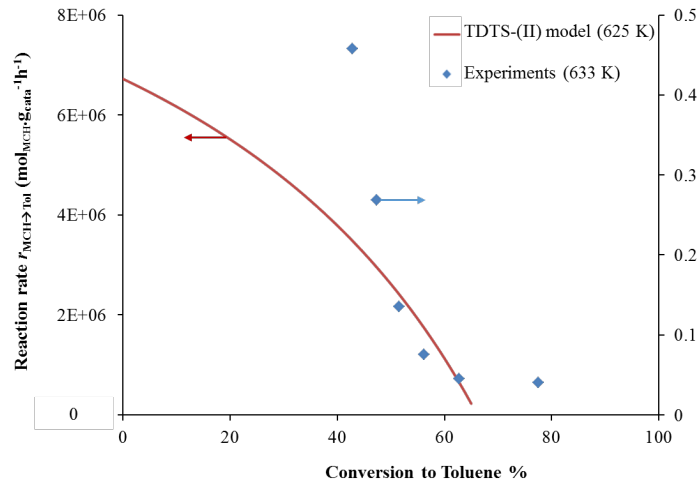


Figure V- 31 Reaction rates as a function of methyl-cyclohexane conversion to toluene for the TDTS-(III) model (reversible step (15) as RDS) at 625 K and at $P_0(\text{H}_2) = 12.2$ bar and $P_0(\text{MCH}) = 0.8$ bar

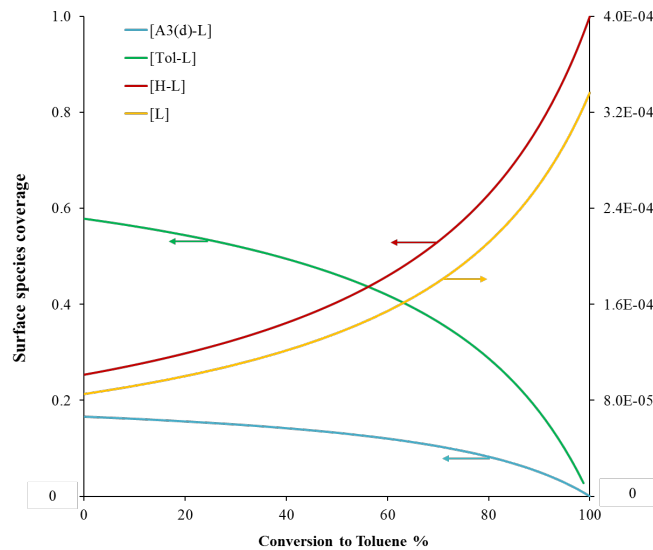


Figure V- 32 Evolution on the coverage of relevant surface species Toluene (Tol), methyl-cyclohexadienyl ($A_{3(d)}$), hydrogen and active sites as a function of methyl-cyclohexane conversion to toluene for the TDTS-(III) model (reversible step (15) as RDS) at 625 K and at $P_0(\text{H}_2) = 12.2$ bar and $P_0(\text{MCH}) = 0.8$ bar

2.4.6 Sensibility analysis for the RDS-(VI) model

So far, the RDS-(VI) model (reversible rate-determining step (13)) is the most relevant model confronting our experimental results, in terms of order of magnitude of reaction rates and in terms of evolution of the initial reaction rate as a function of the hydrogen and methylcyclohexane partial pressures. However, the hydrogen pressure at which the rate reaches its maximum is not perfectly reproduced. The evolution of the reaction rates as a function of methylcyclohexane conversion also behaves unsatisfyingly (Figure V-21 and V-23). So the question is asked that for this *ab initio* parameterized kinetic model, in which extent the deviations from our calculated thermodynamic and kinetic data (from free energy calculations) can affect the accuracy of the kinetic model. A sensibility analysis on these free energies and derived constant parameters is thus of great interest.

In order to identify the key parameters playing on the position of the maximum as a function of the hydrogen pressure, the rate expression in Equation (V-43) is analysed in case of $P_{H_2} \rightarrow 0$ and $P_{H_2} \rightarrow \infty$ to be able to parameterize the curve shape from the two sides. Then we have:

$$P_{H_2} \rightarrow 0, \quad r_0 \rightarrow \frac{k_{13} K'_N P_{H_2}^{2.5}}{P_{MCH} K'_M} \quad \text{Equation (V-55)}$$

$$P_{H_2} \rightarrow \infty, \quad r_0 \rightarrow \frac{k_{13} K'_N P_{MCH}}{P_{H_2}^{3.5} K'_H} \quad \text{Equation (V-56)}$$

It appears that the constants k_{13} , K'_N , K'_M , K'_H play a role on these two limit behaviours. The rate constant k_{13} , which is related to the activation free energy, is not varied in the following analysis. The strategy is to focus on the other constants K'_N , K'_M , K'_H that are calculated from

reaction free energy. These constants are the functions of several equilibrium constants for elementary steps (Equation (V-31), (V-39) and (V-41)). Moreover, the equilibrium constants in common of K'_N , K'_M , K'_H are K_4 , K_9 and K_{14} , which are the desorption constants of hydrogen from its various surface forms (H_a , H_b and H_c). So the free energy of elementary steps (4), (9) and (14) are operated as shown in Table V-12 by five most representative analysis after several trials. The tolerance for the deviation on these *ab initio* calculations are ± 10 kJ/mol.

Table V- 12 Relevant parameters operated for the sensibility analysis on the case of RDS-(VI) model (reversible rate determining step (13))

	Original	Parameters (a)	Parameters (b)	Parameters (c)	Parameters (d)	Parameters (e)
$\Delta_r G_{(4)}$ (kJ/mol)	29	39	29	29	38	39
$\Delta_r G_{(9)}$ (kJ/mol)	60	60	70	60	60	68
$\Delta_r G_{(14)}$ (kJ/mol)	65	65	65	75	57	55
K'_N	1.26E+06	1.72E+05	1.75E+05	4.85E+05	4.51E+05	9.18E+04
K'_M	1.28E+06	1.74E+05	1.77E+05	4.91E+05	4.57E+05	9.30E+04
K'_H	8.51E+02	8.78E+02	1.38E+03	1.69E+03	5.93E+02	9.36E+02

Table V-12 indicates the five analysis (parameters (a) to (e)) to examine the sensibility of the relevant parameters on the evolution of reaction kinetics, via simply modifying $\Delta_r G_{(4)}$, $\Delta_r G_{(9)}$ and $\Delta_r G_{(14)}$, standing for the reaction free energy of elementary steps (4), (9) and (14). The recalculated constants K'_N , K'_M , K'_H are also given, as a comparison to the original *ab initio* values. The evolution on the reaction kinetics of these five analyses is given in Figure V-33.

Figure V-33 (a) depicts the initial reaction rates as a function of hydrogen partial pressure, Figure V-33 (b) depicts the initial reaction rates as a function of methyl-cyclohexane partial pressure and Figure V-33 (c) describes the rates during the reaction varying the methyl-cyclohexane conversion. It appeared to be very difficult to find the ideal parameters that fit

properly the three types of data at same time. When increasing $\Delta_r G_{(4)}$, $\Delta_r G_{(9)}$ and $\Delta_r G_{(14)}$ individually (parameters (a), (b) and (c)), the intermediate hydrogen partial pressure corresponding to the maximum rate moves towards that observed experimentally in Figure V-33 (a). This can be explained by the fact that increasing these reaction free energies corresponds to preventing the desorption of H_2 , thus increasing the poisoning effect by adsorbed atomic hydrogen, e.g. making it appear at lower hydrogen pressure. However, the shape of the curve in the decreasing part is not satisfying. Moreover, these adjustments make the trends worse when considering the evolution of the rate as a function of P_{MCH} and of the conversion (Figure V-33 (b) and (c)). This again can be understood as the poisoning effect by hydrogen being stronger, the rate increases much more slowly than expected by increasing P_{MCH} . The set of parameters (d) gives the best compromise. It corresponds to the strong weakening of constants K'_N and K'_M , like all other parameters (a) to (e) do. However, the parameters (d) is the only one that achieves to weaken K'_H by increasing $\Delta_r G_{(4)}$ and reducing $\Delta_r G_{(14)}$. This means that the desorption of H_c has to be promoted, whereas the desorption of H_a has to be inhibited as compared to our original DFT calculations. Note however that 10 kJ.mol^{-1} is typical of errors made in the DFT calculation of free energies (Chapter III: *section 1.3.2*), so that the main conclusion we can reach here is that the model is very sensitive.

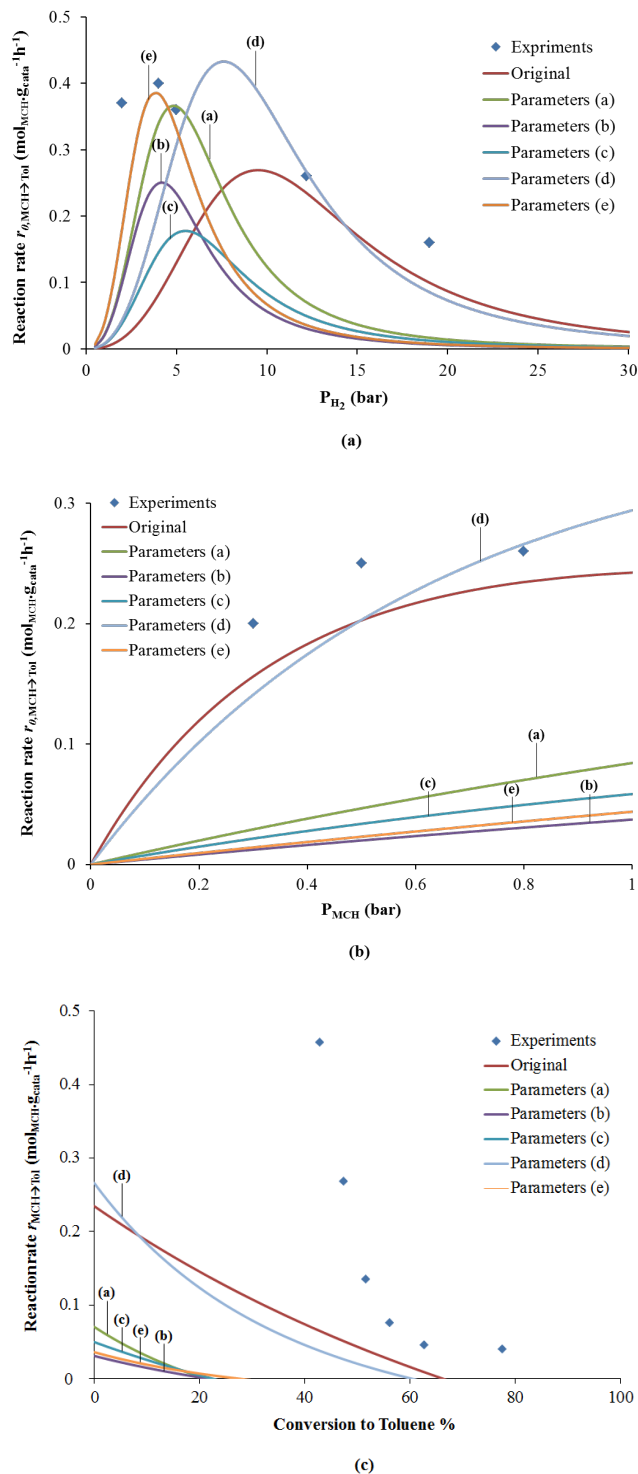


Figure V- 33 Evolution of the calculated rates in t sensibility analysis for model RDS-(VI) compared to the experimental results: (a) initial reaction rate as a function of hydrogen partial pressure at constant methyl-cyclohexane partial pressure of 0.8 bar (b) initial reaction rate as a function of methyl-cyclohexane partial pressure at constant hydrogen partial pressure of 12.2 bar (c) reaction rate as a function of methyl-cyclohexane conversion to toluene at $P_0(\text{H}_2) = 12.2$ bar and $P_0(\text{MCH}) = 0.8$ bar

2.4.7 Arrhenius plot and Eyring plot for the Langmuir Hinshelwood kinetic models

By the help of the kinetic parameters at different temperatures in Table V-9, the apparent activation energy and activation enthalpy are also calculated for these 5 LH kinetic models (RDS-(IV), (V), (VI); TDTS-(II), (III)). The results are summarized in Table V-13 for all the 8 models that have been established till now, as reference to the experimental results that we obtained as well. In term of activation energies and enthalpies, the model RDS-(IV), RDS-(V) and TDTS-(II) give the closest values compared to the experimental ones (2 kJ/mol of difference). However, none of these three models show satisfactory results on other kinetic aspects. The model RDS-(VI) and RDS-(III), on the other hand, exhibit a relative discrepancy on the activation energy and enthalpy, but they somehow succeed to fit some other reaction kinetic descriptors.

Table V- 13 Recapitulation of the activation energy and activation enthalpy exploited by Arrhenius and Eyring plot for all the kinetic models, as a comparison with the experimental values

Model	Experiment	LH kinetic model							
		RDS-(I)	RDS-(II)	RDS-(III)	RDS-(IV)	RDS-(V)	RDS-(VI)	TDTS-(II)	TDTS-(III)
Activation energy (kJ/mol)	200	202	202	133	191	220	169	202	208
Activation enthalpy (kJ/mol)	195	196	196	128	186	214	164	197	202

2.5. Conclusion and perspectives

In *section 2.*, the experimental results we reported in *section 1* are firstly fitted by a power-law kinetic model. We found the apparent reaction order for methyl-cyclohexane to be about 3 by fitting the reaction rates as a function of space time; the reaction orders were found to be 0.3 order (near 0) with respect to hydrogen and 1.5 with respect to methyl-cyclohexane by fitting the reaction rates as a function of methyl-cyclohexane partial pressure and hydrogen partial pressure. The fitting results suggest that more detailed models are required to assess the complexity of the mechanism.

Before building several types of Langmuir-Hinshelwood (LH) kinetic models from our *ab initio* calculations, the latter being used to set up the reaction scheme, choose relevant rate-determining steps and calculate each rate and equilibrium constant was needed in the integration of the model. It leads firstly to three “extended” Langmuir Hinshelwood kinetic models, for which each intermediate is a system embedding the cluster and the adsorbed species without considering competitive adsorption between hydrogen and dehydrogenated MCH molecules. Secondly, a complex mechanistic model including explicit site competition between atomic hydrogen and dehydrogenation intermediates was proposed and three new Langmuir Hinshelwood kinetic models were thus proposed. Finally, two extra LH models inspired by the energetic span concept, considering reaction step sequences as globally limiting step, were also studied by using the same formalism including explicit site competition with atomic hydrogen. The results can be summarized in Table V-14.

Table V- 14 Summary agreement between each kinetic model compared to experiments (T = reasonable agreement ; F = non-reasonable agreement), for various kinetic parameters.

Model	Initial rates as function of P(H ₂)		Initial rates as function of P(MCH)		Rection rates as funcion of conversion		Activation energy	Activation enthalpy
	Order of magnitude	Max. P(H ₂)	Order of magnitude	Shape of the curve	Order of magnitude	Shape of the curve		
RDS-(I)	T	F	T	T	--	--	T	T
RDS-(II)	T	F	T	T	F	T	T	T
RDS-(III)	F	F	F	T	T	T	F	F
RDS-(IV)	F	T	F	F	--	--	T	T
RDS-(V)	F	T	F	F	F	T	T	T
RDS-(VI)	T	T	T	T	T	F	F	F
TDTS-(II)	F	T	T	F	T	T	T	T
TDTS-(III)	F	F	F	T	F	F	T	T

We can conclude that it is very difficult to have one LH model that validates all these kinetic descriptors compared to experimental results at the same time. All these criteria are strongly related to the reaction mechanism that we assume. However, among all the imperfections, models RDS-(II), RDS-(VI) and TDTS-(II) behave reasonably and these three models also happen to have three different nature of RDS, step (5), (13) and (11), respectively. This suggests that the real complete reaction kinetics may be a combination of all these 3 steps, a simple RDS cannot simply achieve all the expectations.

As consequence, a micro-kinetic model parameterized by *ab initio* constants is strongly required in the future. At this point, according to our current results, the hydrogen coverage is a crucial parameter to take into account.

References

- (1) Sinfelt, H. J.; Hurwitz, H.; Shulman, R. A. *J. Phys. Chem.* **1960**, *64*, 1559–1562.
- (2) Maria, G.; Marin, A.; Wyss, C.; Muller, S.; Newson, E. *Chem. Eng. Sci.* **1996**, *51*, 2891–2896.
- (3) Alhumaidan, F.; Cresswell, D.; Garforth, A. *Ind. Eng. Chem. Res.* **2011**, *50*, 2509–2522.
- (4) Usman, M.; Cresswell, D.; Garforth, A. *Ind. Eng. Chem. Res.* **2012**, *51*, 158–170.
- (5) Van Trimont, P. A.; Marin, G. B.; Froment, G. F. *Ind. Eng. Chem. Fundam.* **1986**, *25*, 544–553.
- (6) Verstraete, J. Thesis : Kinetische Studie van de Katalytische Reforming van Nafta over een Pt-Sn/Al₂O₃ Katalysator, Universiteit Gent, 1997.
- (7) Bournonville, J. P.; Franck, J. P. *Hydrogen and catalytic reforming In : Hydrogen effect in catalysis*, 653-677; Marcel Dekker, Inc., 1987.
- (8) Leprince, P. *3 Procédés de Transformation. Chap.4 Reformage Catalytique*, 105-169; Technip, 1998.
- (9) Jossens, L.; Petersen E. E. *J. Catal.* **1982**, *73*, 377–386.
- (10) Amatore, C.; Jutand, A. *J. Organomet. Chem.* **1999**, *576*, 254–278.
- (11) Kozuch, S.; Shaik, S. *Acc. Chem. Res.* **2011**, *44*, 101–110.

CHAPTER VI – CONCLUSIONS AND PERSPECTIVES

1. Conclusions

The present work dealt with the reactivity of γ -alumina supported platinum subnanometric clusters, focusing on the mechanism of methyl-cyclohexane dehydrogenation to toluene as a model reaction for catalytic reforming. The goal was to unravel the reaction mechanisms, combining *ab initio* calculations, kinetic experiments and modeling, to provide guides for the control of catalytic properties and reaction conditions. Molecular aspects are indeed lacking in the literature to unravel these questions of high practical relevance.

1.1 *Ab initio* dehydrogenation mechanisms of methyl-cyclohexane over $\text{Pt}_{13}\text{H}_6/\gamma\text{-Al}_2\text{O}_3$ (100) cluster and Pt (111) surface

Firstly, by periodic Density Functional Theory (DFT) calculations at the PBE-dDsC and PBE levels, we chose the $\text{Pt}_{13}\text{H}_6/\gamma\text{-Al}_2\text{O}_3$ (100) system as a relevant model for the catalyst, and considered the Pt (111) surface as a reference system. We assumed that the reaction proceeds via sequential C-H bond cleavages and H_2 desorption steps, but in the case of the supported clusters with co-adsorbed hydrogen, reconstruction and H migration steps appeared to be necessary to consider. The overall Gibbs free energy profile was determined, with all the intermediates and transition states involved in the proposed reaction pathway.

From a technical point of view, accurate estimation of Gibbs free energies including vibrational contributions for condensed phases and adsorbed molecules showed a high sensitivity

towards calculation parameters. The investigation of this sensibility allowed us to choose our calculation parameters with a compromise on the calculation time. The importance of dispersion interactions was also emphasized, as estimated with PBE-dDsC (with respect to PBE), both for $\text{Pt}_{13}\text{H}_6/\gamma\text{-Al}_2\text{O}_3(100)$ and $\text{Pt}(111)$ systems. The dispersion corrections have significantly decreased the free energy profiles and also impact some adsorption structures, especially prominent for the first methyl-cyclohexane physisorption step of and methyl-cyclohexyl chemisorption. These dispersion forces are stronger on the $\text{Pt}(111)$ surface than on $\text{Pt}_{13}\text{H}_6/\gamma\text{-Al}_2\text{O}_3(100)$, with a free energy lowering of 80 kJ/mol on $\text{Pt}(111)$ against 30 kJ/mol on $\text{Pt}_{13}\text{H}_6/\gamma\text{-Al}_2\text{O}_3(100)$.

On $\text{Pt}_{13}\text{H}_6/\gamma\text{-Al}_2\text{O}_3(100)$, the fluctuonality of the cluster induces several steps of cluster reconstruction and hydrogen atom migration coming along with the sequential C-H bond cleavage steps. The highest energy barrier found so far on $\text{Pt}_{13}\text{H}_6/\gamma\text{-Al}_2\text{O}_3(100)$ corresponds to the third C-H cleavage step of methyl-cyclohexene into methyl-cyclohexenyl + H with a free activation energy of 95 kJ/mol at the PBE-dDsC level. However, the free activation energies for several steps are close: for instance, The last C-H cleavage step of methyl-cyclohexadienyl +H to toluene + 2H exhibits a free activation energy of 87 kJ/mol at the PBE-dDsC level. The cluster reconstruction steps and hydrogen atom migration steps are generally less activated than the C-H cleavage steps. Meanwhile, on the $\text{Pt}(111)$ surface, the second C-H cleavage step of methyl-cyclohexyl +H to methyl-cyclohexene + 2 H is found to be the most demanding step with a free activation energy of 79 kJ/mol, which is very close to that of the first C-H cleavage step with an free activation energy of 78 kJ/mol at the PBE-dDsC level.

Overall, our *ab initio* calculations reveal the complexity of the reaction pathway for the subnanometric clusters, but give rise to proposals for rate determining steps, which validity can be tentatively estimated thanks to kinetic modeling compared with experiments.

1.2 Kinetics for dehydrogenation reaction on γ -alumina supported platinum catalyst

In the second part of our work, the reaction kinetics has been studied by both experimental and kinetic modeling methods.

Catalytic methylcyclohexane dehydrogenation experiments were performed on a Pt/ γ -Al₂O₃ catalyst which characteristics are as close as possible to the *ab initio* system: high dispersion of monometallic platinum particles, dechlorinated support. The operating conditions were chosen to guarantee the absence of diffusion limitations and the access to intrinsic kinetics. The influence of parameters such as space time, temperature, partial pressure of hydrogen and methylcyclohexane, was investigated systematically. Notably, a maximum in rate was observed as a function of P(H₂), while it monotonously increases with P(MCH). The apparent activation energy and enthalpy were determined (200 and 195 kJ/mol, respectively).

These data were then used to confront with kinetic models that we built. A Power-law kinetic model was preliminarily constructed by solely fitting the experimental results in order to receive the information on reaction constant and reactions orders. However, considering the inconsistencies between reaction orders found, these fitting results suggested that more detailed models are required to assess the complexity of the mechanism.

Thus, we built Langmuir-Hinshelwood (LH) models, based on the stepwise dehydrogenation mechanisms and DFT kinetic constants. Two types of models were built : (1) LH kinetic models based on a single rate determining elementary step without explicit consideration of adsorption competition with adsorbed atomic hydrogen ; (2) LH kinetic models based on a single rate determining elementary step including explicit consideration of adsorption competition with adsorbed atomic hydrogen. The nature of the rate determining step was selected based on the rate constants of each individual elementary steps, or on the consideration of limiting step sequences, thanks to the energetic span concept. Among the 8 models that were built, three models performed better than the others in terms of different kinetic descriptors: reaction rates values, reaction rates dependence upon hydrogen partial pressure, methyl-cyclohexane partial pressure and conversion, finally the apparent reaction activation energy and enthalpy. The maximal reaction rate at an intermediate hydrogen partial pressure proposed in the literature^{1,2} was reproduced by the model based on the last C-H bond cleavage step (from methyl-cyclohexadienyl + H to toluene + 2H) as rate-determining step including explicit consideration of adsorption competition with adsorbed atomic hydrogen. A sensibility analysis on the free energies and derived constant parameters was done to promote this model. The conclusion was drawn by this analysis that the hydrogen desorption steps and thus the hydrogen coverage are very sensitive parameters. The best evolution of reaction rates dependence upon methyl-cyclohexane conversion was achieved by the model based on the fifth C-H bond cleavage step (from methyl-cyclohexadiene to methyl-cyclohexadienyl + H) as rate-determining step including explicit consideration of adsorption competition with adsorbed atomic hydrogen. This later one also succeeded to meet the activation energy and enthalpy with experiments, 202 and 197 kJ/mol, respectively, versus 200 and 195 kJ/mol experimentally. Another one that has very close values (202 and 196 kJ/mol, respectively) to the experimental activation energy and enthalpy is the

model based on the third C-H bond cleavage step (from methyl-cyclohexene to methyl-cyclohexenyl + H) as rate-determining step without explicit consideration of adsorption competition with adsorbed atomic hydrogen. These results suggest that the real complete reaction kinetics may be a combination of all these 3 steps, a simple RDS cannot simply achieve all the expectations with current LH kinetic approach.

2. Perspectives

The results reported in this thesis open perspectives for the better understanding of the catalytic system, of the reaction mechanism and more generally for the understanding and control of the behavior of the catalyst in catalytic reforming. Relevant parameters to investigate in the future are the following, in particular by *ab initio* calculations:

- The influence of the hydrogen partial pressure on the hydrogen coverage. Indeed, so far, a constant hydrogen coverage was considered as the starting point, whereas experimentally it may vary. For this, the various models established in the past by C. Mager-Maury³ will be useful starting points.
- Also, the influence of the facet of gamma-alumina. So far, the cluster considered is located on the (100) surface of alumina, whereas the (110) is the most abundant. The latter surface is partially hydrated in reforming-like conditions, which is expected to influence the electronic and reactive properties of the aggregates. The models established by A. Gorczyca⁴ describe the interaction of hydrogen with Pt₁₃ clusters with the hydroxylated (110) surface, which would be of interest to consider for further reactivity investigations.

- The effect of chlorine on rate constants, present on the real catalytic systems, could also be of interest. Mager-Maury et al.⁷ prepared models of platinum clusters supported on chlorinated alumina. The effect of chlorine on the affinity of the clusters for hydrogen would be a required preliminary step before engaging a reactivity study.
- In a more long-term research, it is also of great interest to investigate the behavior of bi-metallic nano-aggregates, particularly Pt_xSn_y/Al_2O_3 . Models for this bi-metallic catalyst have been using *ab initio* calculations combined with experimental work at IFPEN by A. Gorczyca.⁵ and Jahel et al..⁶ The atomic scale mechanism and kinetics of dehydrogenation of methyl-cyclohexane to toluene on such systems still need to be investigated.
- Finally, other reactions of interest in catalytic reforming, such as cyclisation, isomerization and hydrogenolysis should be undertaken.

Regarding kinetic modeling, a micro-kinetic model parameterized by *ab initio* constants is substantially required in the future, in order to give us a clear vision on the more detailed kinetics, such as rate-determining step and the reaction order and apparent constant. The advantage of such an approach with respect to the LH models proposed here is to avoid any assumption on RDS, considering explicitly all forward and backward rate constants for the integration of the rate equations. At this point, according to our current results, the hydrogen coverage is a crucial parameter to take into account. It will be also strongly necessary to have a micro-kinetic model on the case of Pt (111) system, in order to compare the reaction kinetics with cluster system. Finally, all the perspectives mentioned above for *ab initio* calculations could lead to dedicated kinetic modeling works.

Such works will be key to demonstrate the value of the multiscale simulation approach undertaken here, consisting in the feeding of kinetic models with ab initio data. They will also be important for bridging the gap between model approaches often undertaken in computational chemistry, and the real catalyst, with complex chemical composition, and the real process, involving a large set of reactants, products and reaction conditions.

References

- (1) Van Trimpont, P. A.; Marin, G. B.; Froment, G. F. *Ind. Eng. Chem. Fundam.* **1986**, *25*, 544–553.
- (2) Verstraete, J. Thesis : Kinetische Studie van de Katalytische Reforming van Nafta over een Pt-Sn/Al₂O₃ Katalysator, Universiteit Gent, 1997.
- (3) Mager-Maury, C.; Bonnard, G.; Chizallet, C.; Sautet, P.; Raybaud, P. *ChemCatChem* **2011**, *3*, 200–207.
- (4) Gorczyca, A.; Moizan, V.; Chizallet, C.; Proux, O.; Del Net, W.; Lahera, E.; Hazemann, J. L.; Raybaud, P.; Joly, Y. *Angew. Chem. Int. Ed.* **2014**, *53*, 12426–12429.
- (5) Gorczyca, A. Thesis : Caractérisation de catalyseurs métalliques supportés par spectroscopie XANES, apports du calcul quantique dans l'interprétation des spectres expérimentaux. research thesis, Université Joseph Fournier de Grenoble & IFPEN, 2014.
- (6) Jahel, A. N.; Moizan-Baslé, V.; Chizallet, C.; Raybaud, P.; Olivier-Fourcade, J.; Jumas, J. C.; Avenier, P.; Lacombe, S. *J. Phys. Chem. C* **2012**, *116*, 10073–10083.
- (7) Mager-Maury, C.; Chizallet, C.; Sautet, P.; Raybaud, P. *ACS Catal.* **2012**, *2*, 1346–1357.

Abstract: Catalytic reforming aims at transforming naphtha into high octane aromatics and producing simultaneously dihydrogen. The catalyst used is composed of platinum-based sub-nanometric clusters highly dispersed on a gamma-alumina support which behavior under reaction conditions is the subject of numerous questions. We investigate experimentally and theoretically one model reaction probing the metal sites, the dehydrogenation of methyl-cyclohexane into toluene. A detailed atomic scale understanding of the mechanisms involved, and their related kinetic parameters, is required. We undertook DFT calculations with PBE and PBE-dDsC functionals on a relevant Pt₁₃/γ-alumina model, in order to determine the intermediates, transition states and their free energies. The reaction mechanism was explored by assuming sequential C-H breaking steps. Reconstructions of the cluster and hydrogen migrations occur along the reaction pathway, highlighting its high fluxionality (also confirmed by molecular dynamics). Free energies of activation for C-H bond breaking, H migration and cluster's reconstruction were systematically determined at T=625 K. The highest activation Gibbs free energy ($\Delta_r G^\ddagger=95$ kJ/mol) is found for the third C-H bond breaking on methyl-cyclohexene, while the most stable intermediate is the {toluene+H₂} adsorbed product. However, other C-H bond breaking steps and eventually toluene desorption may compete. A comparison with the Pt (111) surface is also given. Rate constants of elementary steps estimated by DFT are introduced in 8 Langmuir-Hinshelwood (LH) kinetic models based on a single rate determining step (RDS) concept, or on a limiting steps sequence deduced from an energetic span analysis. We finally carried out experimental tests on Pt/γ-alumina catalysts (0.3 wt% Pt) at various temperatures, space times, hydrogen and methyl-cyclohexane partial pressures, to provide experimental kinetic data. The calculated apparent activation enthalpy is predicted to be 196 kJ/mol in close agreement with the experimental one (195 kJ/mol) for the best LH model (third C-H bond breaking as RDS). Moreover, the dependence of reaction rates on hydrogen and methyl-cyclohexane partial pressures are discussed with respect to experimental trends and models. Although the main trends are recovered by the kinetic model, some discrepancies are revealed. This work paves the way for a future microkinetic modeling.

Résumé: Le reformage catalytique vise à transformer les naphthas en aromatiques à haut indice d'octane et à produire simultanément du dihydrogène. Le catalyseur utilisé est composé d'agrégats sub-nanométriques à base de platine hautement dispersées sur un support d'alumine-gamma dont le comportement en réaction pose de nombreuses questions. Nous étudions expérimentalement et théoriquement une réaction modèle qui sonde les sites métalliques, la déshydrogénation du methyl-cyclohexane en toluène. Une compréhension détaillée à l'échelle atomique des mécanismes impliqués et des paramètres cinétiques est nécessaire. Nous avons mis en œuvre des calculs DFT (PBE et PBE-dDsC) sur un modèle pertinent Pt₁₃/alumine-gamma, afin de déterminer les intermédiaires, les états de transition et leurs enthalpies libres. Le mécanisme a été exploré via des étapes séquentielles de rupture des liaisons C-H. Une reconstruction des agrégats se produit le long du chemin réactionnel, mettant en évidence sa fluxionalité (confirmée par dynamique moléculaire). Les enthalpies libres d'activation de la rupture C-H, de migration d'hydrogène et de reconstruction de l'agrégat ont été systématiquement déterminées à T=625 K. L'enthalpie libre la plus élevée ($\Delta_r G^\ddagger=95$ kJ/mol) est trouvée pour la troisième rupture de liaison C-H sur le methyl-cyclohexène. L'intermédiaire le plus stable est le produit adsorbé {toluène+H₂}. Cependant, d'autres étapes de rupture C-H ou de désorption du toluène sont compétitives. Les constantes de vitesse des étapes élémentaires obtenues par DFT sont introduites dans 8 modèles cinétiques différents de type Langmuir-Hinshelwood (LH). La nature de l'étape déterminante de la vitesse a été choisie en fonction des constantes de vitesse de chaque étape élémentaire individuelle, ou de la prise en compte de séquences d'étapes limitantes, grâce à une analyse de type « energetic span ». Nous avons finalement expérimentalement réalisé des tests catalytiques sur Pt/γ-alumine (0.3 wt% Pt) à différentes températures, temps de contact, pressions partielles d'hydrogène et de méthylcyclohexane, pour obtenir des données cinétiques expérimentales. L'enthalpie d'activation apparente de 196 kJ/mol calculée par l'un des meilleurs modèles LH (3^{ème} rupture C-H limitante) est proche de l'expérience (195 kJ/mol). De plus, l'évolution des vitesses de réaction en fonction des pressions partielles d'hydrogène et de méthylcyclohexane est discutée au regard de l'expérience et des modèles. Même si les tendances sont recouvertes par les modèles, des écarts théorie-expérience sont mis au jour, ce qui ouvre des perspectives vers une modélisation microcinétique future.